CIRPASS: The Cambridge Infrared Panoramic Survey Spectrograph

Andrew Jonathan Dean

INSTITUTE OF ASTRONOMY
AND
HUGHES HALL

UNIVERSITY OF CAMBRIDGE

July 2002

A thesis submitted to the University of Cambridge
in accordance with the regulations for
admittance to the degree of Doctor of Philosophy.

CIRPASS: The Cambridge Infrared Panoramic Survey Spectrograph

Andrew Jonathan Dean

The Cambridge Infrared Panoramic Survey Spectrograph, CIRPASS, is an infrared spectrograph that operates in the 0.9 to 1.8 μm wavelength region. CIRPASS was developed entirely at the Institute of Astronomy, Cambridge, and the design, construction and performance of CIRPASS are presented in this thesis.

CIRPASS provides integral field spectroscopy (IFS). Spectra are simultaneously obtained from 499 contiguous spatial elements in a two-dimensional area of sky using an integral field unit (IFU). The construction of the IFU, which used a lenslet array and fibre optic bundle, is presented, as well as a review of IFS techniques.

The sensitivity of CIRPASS has been maximised by ensuring the background signal detected by the instrument is reduced to an absolute minimum. CIRPASS has the capability to remove, both in hardware and software, the dominant infrared sky background from OH emission in the upper atmosphere. The advantages that this offers, and the benefits of both suppression techniques are presented. The thermal background of CIRPASS was reduced by cooling the entire spectrograph to -40°C. The instrument was cooled using a conventional industrial refrigeration system and resulted in significant improvements to the instrument's performance. The characteristics of the HAWAII infrared detector array used were measured, to determine their impact on the instrument's sensitivity, and found to be within specification.

Software was written to reduce CIRPASS data that is applicable to any IFS instrument producing data in the Euro 3D format. A data reduction pipeline, that can be used for rapid data reduction at the telescope and for more detailed analysis afterwards, was implemented. The pipeline implementation and the techniques adopted for reducing closely packed spectral data on an infrared detector are discussed.

The performance of CIRPASS was quantified by observing the Cambridge night sky with CIRPASS attached to a small telescope. The results provide an accurate measure of the instrument's performance on a larger telescope and are detailed. The expected limiting magnitudes for 3 hour observations of a point source, on an 8 m telescope, resulting in a signal-to-noise ratio of 5 are J=21.3 and H=19.3. The equivalent limiting line fluxes are J=4.4×10^{-18} ergs/s/cm^2 and H=9.0×10^{-18} ergs/s/cm^2.

DECLARATION

The research described in this thesis was carried out under the supervision of Dr. Ian Parry at the Institute of Astronomy, University of Cambridge. No part of the thesis has already been, or is currently being submitted for a degree, diploma, or any similar qualification at any other university.

The thesis is the outcome of my own work, except when explicit reference has been made to the work of others.

Some of the work presented in this thesis has appeared in the following publications:

Parry, Ian R. *et al.* , 2000. *CIRPASS: a NIR integral field and multi-object spectrograph*, in Proc. SPIE Vol. 4008, p. 1193-1202, Optical and IR Telescope Instrumentation and Detectors, Masanori Iye; Alan F. Moorwood; Eds.

Parry, I. R., Dean, A. J. *et al.* , 2000. *CIRPASS: A Near-IR Integral Field Spectrograph*, Imaging the Universe in Three Dimensions. Proceedings from ASP Conference Vol. 195. Edited by W. van Breugel and J. Bland-Hawthorn. ISBN: 1-58381-022-6 (2000), p.191

This dissertation does not exceed the limit of 60,000 words.

Andrew Jonathan Dean
Cambridge
4th July, 2002

ACKNOWLEDGEMENTS

First and foremost, I would like to thank my supervisor, Dr. Ian Parry, for his guidance throughout the course of my PhD; for always being happy to answer any questions I had, no matter how naive; and for always buying me a pint on trips to the pub.

I would also like to thank the entire Instrumentation Group at the Institute of Astronomy. I had not expected to be working with such a friendly and amusing group of people, who helped to make my PhD thoroughly enjoyable. Thanks go to Rachel and Ram for numerous data reduction and software discussions, to Dave for helping me get to grips with optics, to Steve for help with all things electrical and mechanical, to Jim for much practical insight, and to Rob for giving up Friday nights to help with CIRPASS observations. Thanks are also due to Dr. Craig Mackay for his guidance on the operation and characteristics of infrared detectors.

Many friends in Cambridge have kept me sane throughout my PhD. My fellow students offer unrivalled lunchtime discussions about life, the universe, and everything, and I mean everything. Amongst these, I would particularly like to thank Lisa for being the group's social secretary and Jeremy for knowing Linux inside out.

Outside astronomy, I would like to thank Mike for ensuring I have an excellent sound system and for being a movie fanatic, and Toto, Milind, Alonso and Alex for making Wollaston 1 such a happening kitchen. Those times will not be forgotten.

Thanks also go to Zan, Amanda and the Creasys, Friday nights will never be the same again.

A special thank you to Radha, my own medic, who's shown me that there's so much more to life than science.

The acknowledgements would not be complete without mention of my family, who have encouraged and supported my education from the outset. I would like to thank Mum, Dad and James, for always being there; Nan, and Nan and Grandad, for the continual letters and for the many food parcels; and Aunty Em and my late Uncle Johnny for valuing my education so highly, and of course for the letters and cakes.

Andrew
4th July, 2002

CONTENTS

LIST OF FIGURES

LIST OF TABLES

CHAPTER 1

INTRODUCTION

1.1 Introduction

Contemporary scientific programs, by their very nature, push astronomical instrumentation to its limits. One focus of current research is faint, high redshift sources, which require observations with the largest telescopes. In turn, the recently available infrared optimised large telescopes demand spectrographs that can take advantage of their increased light collecting power. The Cambridge InfraRed PAnoramic Survey Spectrograph (CIRPASS) is an infrared spectrograph designed for use on 8-10 m class telescopes. The scientific motivation for building CIRPASS is given in Section 1.2.

At the time of writing, CIRPASS was en route to the Gemini South Telescope in Chile and its detector had just been upgraded to a higher quality HAWAII 1K device. First light on this 8 m telescope is expected in August, 2002. CIRPASS has been awarded time on the Anglo-Australian Telescope (AAT) to operate in multi-object spectroscopy (MOS) mode in October 2002, and discussions are in progress with the European Southern Observatory (ESO) to use CIRPASS on the Very Large Telescope (VLT) with the fibre positioner Oz Poz.

CIRPASS is versatile, combining many of the features offered by its contemporaries in a single instrument. CIRPASS provides integral field spectroscopy: a technique offering multiplex advantages over long slit spectroscopy, discussed in Section 1.3. CIRPASS has been developed from the Cambridge OH Suppression Instrument (COHSI) and is capable of avoiding the sky background produced by excited OH molecules in the upper atmosphere. OH background avoidance and removal is discussed in Section 1.4. A summary of currently available infrared spectrographs is given in Section 1.5, and an overview of CIRPASS and the thesis is given in Section 1.6.

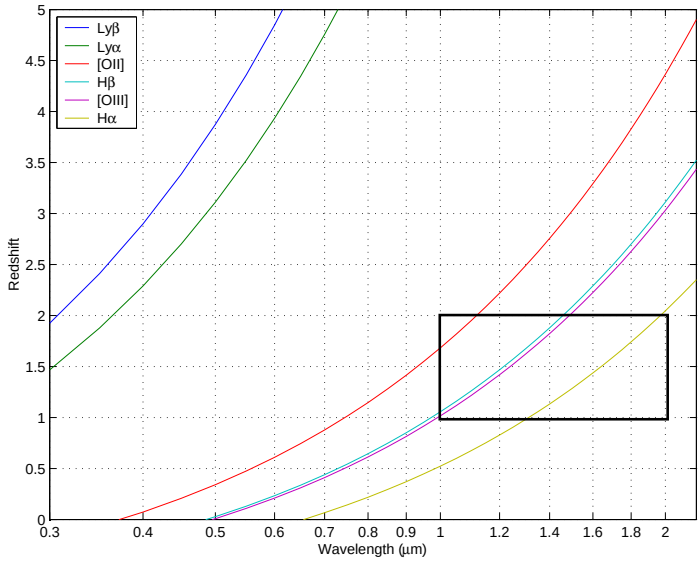

Figure 1.1: *Detected wavelength of a number of emission line features versus the redshift of the emitting object.*

1.2 Scientific motivation

1.2.1 Galaxy evolution

Spectroscopic observations in the optical waveband have allowed the study of a statistically complete sample of galaxies for redshifts z<1 (for example, Lilly et al., 1995; Glazebrook et al., 1995; Ellis et al., 1996). At redshifts z>1, however, most of the familiar, strong and well-studied star formation diagnostic lines for galaxies, have been redshifted into the near-infrared (NIR).

A galaxy's star formation rate (SFR) can be determined using a number of different techniques. Measurements of the UV continuum, the fluxes of primary lines (Hα), and the fluxes of secondary lines ([O II] and others) are commonly used. Figure 1.1 shows the wavelength of various diagnostic lines as a function of redshift, and highlights that the diagnostic lines detected at optical wavelengths for local galaxies will be seen in the infrared for galaxies with redshifts between 1<z<2.

The redshift range 1<z<2, corresponding to times when the universe was between 50% and 20% of its current age, is of great importance in galaxy evolution. Considerable evidence in the literature suggests that the cosmic star formation rate increases by about one order of magnitude from z=0 to z=1. (For example, measured SFRs are given by Gallego et al. (1995) for z=0 and Lilly et al. (1996) for z$\sim$1.) The SFR appears to reach a maximum at z$\sim$1.5 (Connolly et al., 1997), and then falls off slowly beyond z=2 (Steidel et al., 1999). This implies that the redshift range 1<z<2 is the

most important epoch in which to study the star formation history of the Universe.

[O II] fluxes are detectable in the optical to z$\sim$1.1 and have been used to compare evolutionary states of nearby galaxies (Cowie et al., 1996). However, the SFRs obtained from [O II] measurements may be misleading, as this line is produced in young stellar populations where dust extinction may have a significant effect. Measurements of the Hα/Hβ line flux ratio (the Balmer decrement), where both lines are in the infrared for z>1.1, quantify the amount of dust extinction and provide a direct measurement of the SFRs for these galaxies. Glazebrook et al. (1999) have presented results of near-infrared spectroscopy of a small sample of bright Hα emitting galaxies, and argue that for z$\sim$1 the Hα line emission measurement leads to higher SFRs than a consideration of the UV continuum. Rosa-González et al. (2002) have calculated SFR estimates for a sample of 31 nearby star-forming galaxies using Hα, [O II], UV and far-infrared fluxes. They find that SFRs deduced from the [O II] and UV measurements are systematically higher that those deduced from Hα and far-infrared measurements, and that this is due to an overestimation of the extinction correction. Furthermore, little is known about the redshift dependence of the [O II]/Hα and UV-cont/Hα flux density ratios, which are well established for the local universe (Bell & Kennicutt, 2001).

1.2.2 The nature of damped Lyman-α systems

Damped Lyman-α systems (DLAs) consist of high column density (N(HI)>2x10^{20}cm^{-2}) HI absorption line systems, detected by their imprint on spectra from background quasars. DLAs are a cosmologically important population, as for z>1 the majority of neutral hydrogen is locked up in these systems rather than in stars as observed locally (Storrie-Lombardi et al., 1996). Studies of DLAs give an independent view of the high redshift universe, as the sample is selected by gas cross-section rather than integrated starlight.

The exact relation between DLAs and galaxies, however, is not well established. One school of thought has high-z DLAs as thick gaseous disks, the progenitors of massive spiral galaxies (Wolfe et al., 1986). Another view is that DLAs are gas-rich dwarfs, potentially sub-galactic building blocks (for example, Pettini et al., 1990; Moller & Warren, 1998).

In order to determine the true nature of DLAs, a direct measurement of their SFR using hydrogen recombination lines is required. However, searches for Lyman-α emission have not provided useful measurements of the SFR, as extinction corrections for these lines are difficult or impossible to quantify. The use of the rest-frame

optical Balmer lines greatly reduces the problem of dust extinction, enabling star formation rates to be accurately determined (Pettini et al., 2001). As discussed above, these lines are in the infrared for z>1, where large numbers of DLAs are present.

1.2.3 The benefits of integral field spectroscopy

Integral field spectroscopy allows spectra to be simultaneously obtained for a number of contiguous areas across a two-dimensional field, and is usually achieved with an integral field unit (IFU) (Section 1.3). Spectroscopic observations of objects with a complex spatial structure are best studied with an IFU. The IFU provides both an image of the object as well as spectra for each spatial sample in the image. The spatially resolved spectroscopy allows the variation with position of object spectra to be measured. This information can be used, for example, to determine the object's internal kinematics, or the star formation rate across an object, providing insight into its process of evolution. Studies of high redshift and merging galaxies are amongst the numerous objects ideally suited to observation with an IFU, as summarised by Eisenhauer et al. (2000).

Galaxies typically have sizes of a few arc seconds for the redshift range 1<z<2, which is matched to the size of the CIRPASS IFU (Section 2.3.1). Figure 1.2 shows the CIRPASS IFU overlaid onto an image of the local galaxy NGC 4252 as it would appear at z=1.44 and Figure 1.3 shows the CIRPASS IFU overlaid onto a number of galaxies in a Hubble Space Telescope (HST) image.

An IFU is essential for the observations of DLAs discussed above. The location of the star forming regions in the galaxy associated with a DLA is usually unknown. The DLA observations only confirm that the sight-line to the background quasar passes through a large column of neutral hydrogen. Difficulties of point spread function subtraction of the quasar mean that broad-band imaging is unlikely to reveal the foreground galaxy in emission. Spectroscopy is vastly more effective for emission line searches because it is more sensitive, and any emission from the foreground DLA should be readily apparent against the continuum of the background quasar. There is a high probability that any star forming region would fall outside a narrow slit placed over the quasar. Indeed recent NIR long slit spectroscopy failed to detect Hα from star formation in 8 DLAs (Bunker et al., 1999), suggesting that their is no star formation associated with a DLA system, or that it was missed by the observations. The star forming regions are likely to be compact (as in local spirals, Figure 1.2) and are well matched to the size of the CIRPASS IFU, making it an ideal tool for determining if star forming regions are associated with DLAs.

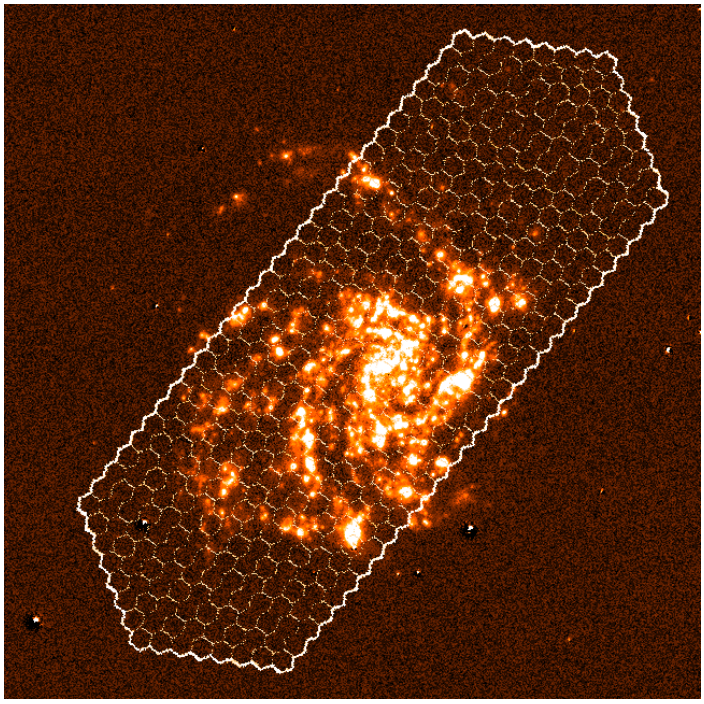

Figure 1.2: *A Hα image of the local spiral NGC 4254 as it would appear at z=1.44 with the CIRPASS integral field unit overlaid (0.25″ lenses). (Ferguson, private communication.)*

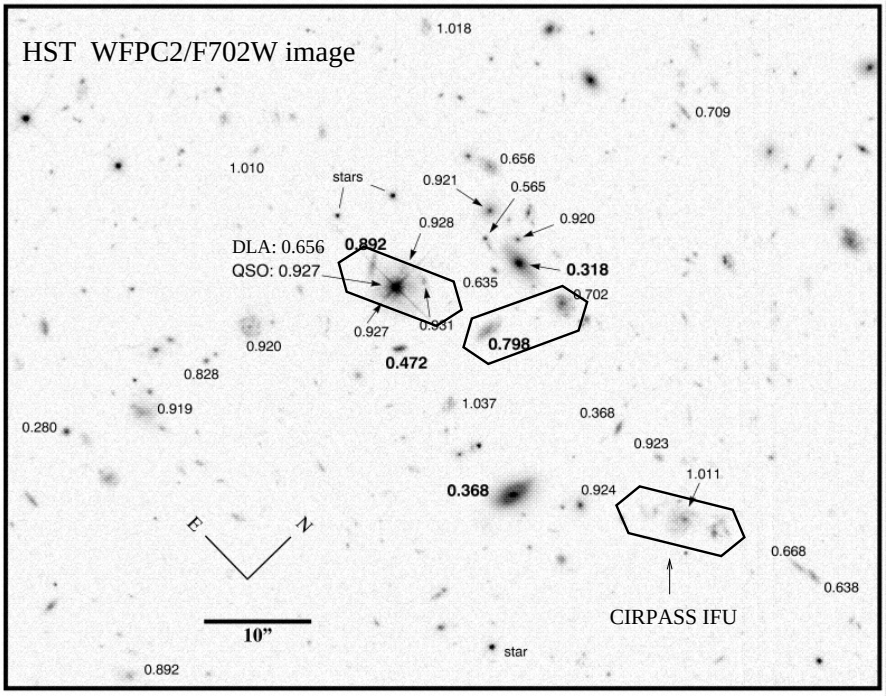

Figure 1.3: *A HST WFPC2 image of the field 3C336, with the CIRPASS IFU overlaid as it would sample three objects in the field. The IFU scale is 0.33″ lens, and the image was taken with the filter F702W (∼R band). (Bunker, private communication.)*

There are many other areas that can be addressed with an infrared integral field spectrograph. Some of these include:

- Studies of high redshift lensed galaxies and structure in gravitational lenses. Obtaining the redshifts of arcs from infrared surveys will allow constraints to be placed on the distribution of dark matter within clusters (Smail et al., 1995) and the dynamical properties of distant field galaxies to be studied.
- Studies of QSO environments, ULIRGs and LINERS.
- Studies of low mass stars, such as brown dwarfs.

A spectrograph with an IFU need not be solely used for studies of extended objects, but can also be used for observing programs typically employed on a conventional spectrograph. Although the addition of an IFU may reduce system throughput, it avoids slit losses and the IFU instrument remains as sensitive as a conventional spectrograph. This is particularly true for the case of poor seeing, where only a small fraction of the object may be on the slit in a conventional spectrograph, whereas the object would be fully sampled by an IFU, owing to its larger spatial size.

A multi-object spectroscopy mode is a planned upgrade for CIRPASS. This mode is targeted at redshift surveys and population studies of $1<z<2$ galaxies, where observational efficiency is clearly paramount.

1.3 Integral field spectroscopy

Traditionally, astronomical observations are made with a two-dimensional detector, sufficient for imaging programs. For spectrographic measurements, however, one spatial dimension of the sky is usually lost, to allow dispersion of the image across one axis of the detector. Spectrographs placing a long slit over the object lose spatial information parallel to the slit width.

Many astronomical programs require spectroscopic information over the whole of a two-dimensional field (Section 1.2.3). That is, they require wavelength information for each point in the image or three-dimensional data (commonly referred to as an (x,y,λ) data cube). Such data can be obtained by time scanning across one of the dimensions, examples include: wavelength scanning using a Fabry Perot (Taylor & Atherton, 1980) or a 2D Fourier transform spectrometer (Maillard, 1995); or spatial scanning of the slit across the sky (Wilkinson et al., 1986). Ideally however, an instrument simultaneously producing both two-dimensional image data and a

spectrum for each point in the image, would make best use of telescope time. An instrument fulfilling this criterion provides integral field spectroscopy (IFS). In IFS the two-dimensional sky data is reformatted into a one-dimensional slit using an integral field unit (IFU) allowing the data to be dispersed onto the detector without loss of spatial information.

A number of different techniques have been adopted to perform the reformatting of the sky image for the spectrograph, three of which are summarised in Figure 1.4. Lenses alone can be used to sample the telescope focal plane, as shown in the first column of the figure. The lenses form images of the telescope pupil, which are then dispersed by the spectrograph. The dispersion direction is chosen to maximise the wavelength coverage and to minimise the spectra overlap on the detector. Although this technique has relatively high throughput, it is difficult to achieve large wavelength coverage without the spectra overlapping. The first spectrograph to adopt this IFS technique was TIGER (Bacon et al., 1995), which uses a micro lens array to sample the telescope focal plane. TIGER is an optical spectrograph, although the IFS technique chosen is not dependent on the wavelength range of operation. Each of the techniques illustrated in Figure 1.4 is equally applicable to optical and infrared instruments. With the addition of optical fibres, the image tiles can be rearranged into a more conventional slit, as shown in the second column of the figure. The spatial information contained within the image is, therefore, reformatted before the image is dispersed, which avoids the problem of the spectra overlapping on the detector. Throughput losses, associated with the focal ratio degradation (FRD)[1] of fibres, can be minimised by suitable choice of lenses to sample the telescope focal plane and by matching the spectrograph optics to the fibre output focal ratio. The CIRPASS IFU follows this technique; the different options available for implementing a fibre fed IFU are discussed in more detail in Section 2.2. The CIRPASS IFU is based on that developed for SPIRAL (Kenworthy et al., 1998), other infrared instruments adopting the same approach for their IFUs include NIRMOS (Le Fevre et al., 2000) and SMIRFS (Haynes et al., 1998).

The third column illustrates the image slicing technique. An array of mirrors is used to segment the telescope focal plane, the light from each mirror being sent in slightly different directions to a second array of mirrors. The second array reformats the image segments to form the slit. When image slicing the spatial information in the image slice is maintained in the direction perpendicular to the dispersion direc-

[1]Focal ratio degradation is a property of optical fibres whereby light emerging from a fibre has a faster focal ratio than that entering it, and can be caused by light refracting from imperfections at the fibre-cladding boundary.

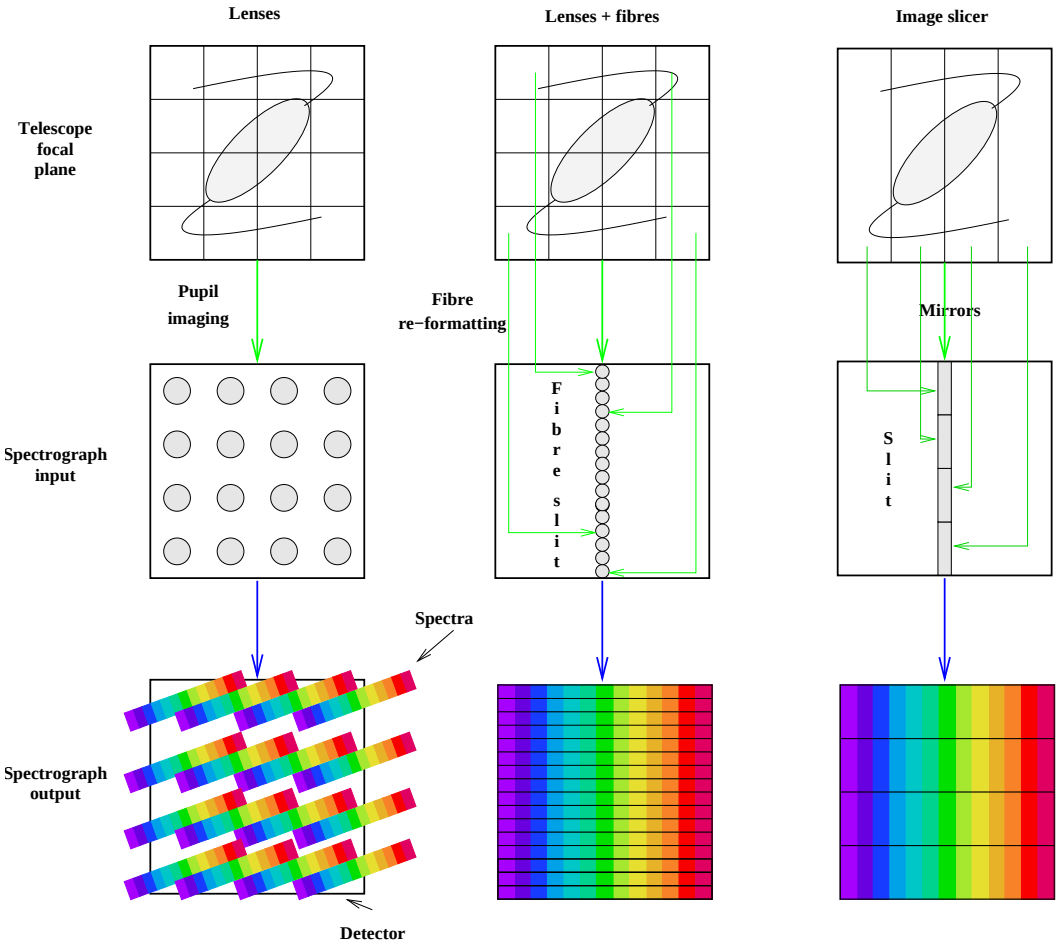

Figure 1.4: *Summary of the techniques available to perform integral field spectroscopy.* The top diagrams show the sampling of the telescope focal plane. The image at the telescope is then reformatted for the spectrograph as shown in the middle diagrams. The bottom diagrams show the output from the spectrograph at the detector. (After Dubbeldam et al. (2000).)

tion. FRD is avoided by not using fibres. IFUs of this design will operate at cryogenic temperatures, whereas the effects of cooling a fibre bundle coupled to a lens array are unknown, and differential contraction problems may be encountered. A fibre fed IFU would also suffer from thermal stress induced FRD. Image slicers containing many mirrors can, however, be bulky and difficult to fabricate. Examples of infrared instruments with image slicers include 3D (Krabbe et al., 1995), GNIRS (Dubbeldam et al., 2000) and UIST (Ramsay Howat et al., 1998).

1.3.1 Future integral field spectroscopy techniques

Integral field spectroscopy can be achieved using a detector that records the three-dimensional information directly. Such devices are still in an early stage of development, but are becoming available for use at optical wavelengths. Perryman & Peacock (2000) describes observations with a 6 x 6 array of super-conducting tunnel junctions (STJs) each with a wavelength resolution of about 100 nm. In an STJ based detector, the absorption position, arrival time and the corresponding energy (and hence wavelength) are measured for each detected photon.

Keller (2000) describes a Spectral Hole Burning Device (SHBD) with 5000 x 5000 spatial elements, each with a spectral resolution of 0.001 nm (over a 15 nm band centred at 634 nm). A SHBD uses an amorphous plastic film doped with a dye molecule. Each individual dye molecule has a very narrow absorption line, where the absorption wavelength is affected by the molecule's interaction with the film and other dye molecules. The doped film, therefore, exhibits a broad band of absorption wavelengths. When the film is exposed, incident photons prevent the film from absorbing more photons of the same wavelength. The spectrum and intensity of the incident photons is deduced after the observation using a tunable laser, which measures the intensity of light absorbed by the material at different wavelengths.

1.4 OH suppression

The dominant sky background in the infrared is produced by excited OH free radicals in the upper atmosphere. OH emission lines are observed between 0.61 and 2.62 μm, with the brightest lines seen above 1.5 μm. On a dark night, almost 98% of the background photons in the H band come from 69 distinct OH lines whose profile widths are spectrally unresolved at a resolution of R$\sim$17000, while 92-98% of the J background comes from 53 narrow OH, O_2, and N_2 emis-

sion lines (Herbst, 1994). Gravity waves[2] in the upper atmosphere cause the absolute and relative intensities of the emission lines to be strongly time and spatially dependent. The OH intensities have both short and long timescale fluctuations (periods of minutes and hours), and are spatially uniform over scales of a few arcminutes (Ramsay et al., 1992; Hecht et al., 1995). Their variation, both temporally and spatially, complicates sky background subtraction (Rousselot et al., 2000). The brighter lines have intensities of order 100 to 360 photons/s/m^2/arcsec^2 (Maihara et al., 1993), producing about 1000 times the flux that CIRPASS sees from a J=20 object in a spectral resolution element on an 8 m telescope.

A recent atlas of the OH lines, obtained using ISAAC (Cuby et al., 2000), has been published by Rousselot et al. (2000) for the wavelength range 1 to 2.25 μm. It extends the work of Oliva & Origlia (1992) and Osterbrock et al. (1996, 1997). Owing to their variation throughout the night and between sites, only relative intensities of the lines were given. Figure 1.5 shows the OH lines observed by ISAAC, and the transmission of the atmosphere[3], for the wavelength region 1.0 to 1.9 μm, encompassing the J (1.15 to 1.35 μm) and H (1.45 to 1.8 μm) passbands.

The wavelength composition of the OH lines present in the sky background has been studied in depth. The nature and intensity of the continuum between the lines is relatively unknown, however, and few measurements in the infrared region have been published. (The continuum is thought to be caused by zodiacal light, and scattered moonlight from aerosol particles in the atmosphere.) Maihara et al. (1993) measured the interline continuum as 590 photons/s/m^2/arcsec^2/μm at 1.65 μm (about one-fiftieth the average flux of the OH airglow emission), while Cuby et al. (2000) report a value four times higher than this, without offering explanation for the large value. Content (1996) summarises nine other measurements taken mainly between 0.4 and 1 μm. As the continuum is potentially very faint, contributions from the thermal background of the instrument, telescope and dome, as well as scattered light from the strong OH lines, can be significant. This renders accurate measurements of the continuum intensity difficult. The Maihara observation was taken with increased dust in the atmosphere, due to a volcanic eruption, increasing scattered moonlight. Thus, the continuum could be considerably fainter than that stated. The Cambridge night sky continuum was measured with CIRPASS and found to be

[2]A gravity wave is the name given to the periodic fluctuations seen in the density and temperature of the upper layer of the atmosphere (Hines, 1960).

[3]The atmospheric data is that predicted for Mauna Kea. The data, produced using the program IRTRANS4, was obtained from the UKIRT worldwide web pages and is for an altitude of 4200 m, an airmass of 1.0, a H_2O column of 1.2mm and a resolving power of R=3000.

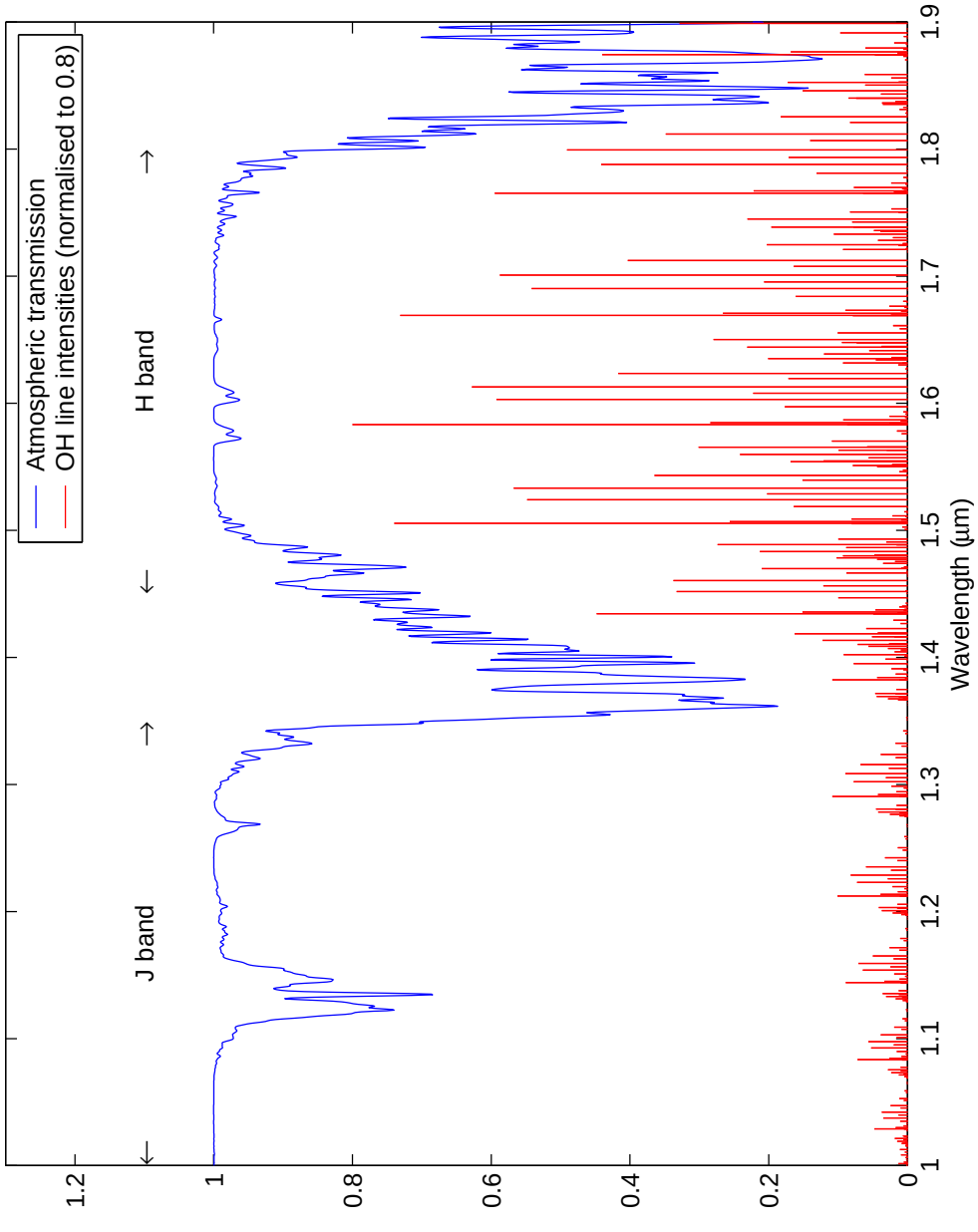

Figure 1.5: *Characteristics of the atmosphere in the infrared.* The OH lines and their relative intensities are shown. The strong water absorption by the predicted Mauna Kea atmosphere can be seen between the J and H bands.

960±128 photons/s/m^2/arcsec^2/μm, which was one thirty-third of the measured total OH flux (Section 9.2.2). The higher value was expected as the Cambridge sky suffers from considerable light pollution.

Given the potentially faint continuum versus the large flux present in discrete OH lines, removal of the OH flux to reduce instrumental scattering, and observation between the OH lines, can considerably improve an instrument's sensitivity. The OH flux can be removed by specific components in the instrument, a technique known as hardware suppression. Alternatively software suppression can be adopted whereby the OH flux in a spectroscopic instrument is allowed to reach the detector, but is then ignored (OH avoidance).

Instruments adopting an entirely hardware suppression technique include OHS for Subaru (Iwamuro et al., 2001) and COHSI (Ennico et al., 1998). Instruments that will offer a combination of hardware and software suppression (to maximise wavelength coverage) include FMOS (Maihara et al., 2000) and GOHSS (Lorenzetti et al., 2000). However, the availability of large infrared detectors has meant that the majority of new instruments have opted to avoid the OH background signal in software. Table 1.1 summarises the advantages offered by each OH suppression technique.

A combination of the two techniques is possible with CIRPASS. Hardware suppression has the advantage that the large quantity of OH light is removed early in the optical path, reducing instrumental scattering. Masking out all of the OH lines, however, may mean that otherwise recoverable object signal is lost, particularly for the fainter lines. Thus, the hardware suppression component of CIRPASS will only remove the brightest lines. The future use of the largest available 2K infrared array will also allow software suppression at R=3000, with a wavelength range of 0.4 μm per exposure. The suppression component of CIRPASS, methods of implementing hardware suppression, and the relative merits of the hardware and software suppression techniques are discussed in Chapter 4.

1.5 Currently available infrared spectrographs

The new 8-10 m class telescopes require spectrographs with large optics and fast cameras to make full use of their light collecting power (or A-Ω product), as illustrated by the following formulae (McLean & Chaffee, 2000):

$$(f/number)_{camera} = 206265 \left(\frac{d_{pix}}{D_{tel}\theta_{pix}} \right) \tag{1.1}$$

Hardware suppression	Software suppression
Bright OH light removed early in the optical path, which reduces the instrument background due to scattered light.	Does not require the additional optics necessary for hardware suppression, which reduce the instrument's throughput.
Spectral resolution at detector not limited to the high resolutions (R>2000) necessary for software suppression. Wavelength coverage for a given detector size need not be sacrificed to allow suppression of the OH.	Optical design of spectrograph simpler, hence spectrograph can be smaller, easier to build and less expensive.
Detector persistence problems are avoided.	

Table 1.1: *Summary of the advantages of hardware versus software OH line suppression.*

$$D_{collimator} = \frac{Rp}{206265\,(2tan\theta_B)}\theta_{pix} D_{tel} \tag{1.2}$$

Equation (1.1) relates the f-number of the camera required to match the image size θ_{pix} (arcsec), to the physical size of a detector pixel d_{pix} for a telescope of diameter D_{tel}. Equation (1.2) illustrates the dependence of the collimator diameter $D_{collimator}$, on the resolving power R (=$\lambda/\Delta\lambda$), of a spectrograph matched to p pixels each of size θ_{pix} (arcsec) (assuming a spectrograph used in Littrow or quasi-Littrow mode at a blaze angle of θ_b). Thus, as the telescope diameter increases, a faster camera and larger optics are required for the same image size and resolution at the detector. Consequently, spectrographs built for large telescopes require innovative designs in order to accommodate the larger optics; it is not a simple matter to upgrade from available spectrographs in use on 4 m telescopes.

Table 1.2 summarises the infrared spectrographs that are available, or will soon be available, for use on existing 6.5 to 8 m telescopes. Similarly, Table 1.3 lists infrared spectrographs on 4 m telescopes that are, or will be, available to UK astronomers.

The efficiency and diameter of the telescope used by a spectrograph have considerable impact on the limiting magnitudes available with the spectrograph. Instrument-specific factors that contribute to a spectrograph's performance are the efficiency of its optics, the characteristics of the detector used, the detected background signal and any systematic errors present when the data is reduced.

The percentage of detected photons compared with the number entering the instrument is quantified as the throughput. The throughput is set by the efficiency of the instrument's optics and the quantum efficiency of the detector. Clearly, the throughput should be maximised in order to obtain the best performance from the instrument. Background contributions, which add to the noise on the detected signal, may come from the thermal background of the telescope and instrument, scattered light within the instrument and the dark current of the detector. The readout noise of the detector, the number of detector pixels matched to a spectral resolution element (SRE) and the spectral dispersion also affect the sensitivity achieved.

As with any instrument, each of these areas has been addressed to ensure that the best possible performance has been obtained from CIRPASS. Table 1.4 compares CIRPASS's limiting magnitude with that of two other available infrared spectrographs. To allow fair comparison, an attempt has been made to ensure that the instrument configurations are similar. For this reason, the stated performance of NIRSPEC has been scaled down from a 10 m to 8 m telescope.

ISAAC uses its gratings in 4^{th} and 3^{rd} orders for J and H band coverage, respec-

Instrument	Telescope	First light	Telescope diameter	Spectral resolution	IFU elements	AO	MOS gain
CIRPASS	GEMINI	mid 2002	8 m	3,500-26,000	490	Yes	150
NIFS	GEMINI	mid 2003	8 m	5,000	1000	Yes	No
NIRI	GEMINI	2001	8 m	$<$1,650	No	Yes	No
PHOENIX	GEMINI	2002	8 m	50,000-75,000	No	No	No
FLAMINGOS-1	GEMINI	2002	8 m	350	No	No	$\sim$100
GNIRS	GEMINI	mid 2003	8 m	600-18,000	No	No	No
ISAAC	VLT	1998	8 m	500-3,000	No	No	No
NIRMOS	VLT	$>$2005	8 m	2,000	No	No	180
SINFONI	VLT	2004	8 m	1,000-4,500	1000	Yes	No
NIRSPEC	KECK	1998	10 m	2,000-25,000	No	Yes	No
NIRC-2	KECK	Late 2002	10 m	5,000	No	Yes	No
IRCS	SUBARU	2000	8 m	$<$20,000	No	No	No
OHS	SUBARU	2000	8 m	OH-supp	No	No	No
FMOS	SUBARU	2006	8 m	OH-supp	No	No	400
LUCIFER	LBT	mid 2004	8 m	5,000-36,000	Upgrade	Yes	25-50
FLAMINGOS-1	MMT	2001	6.5 m	$\sim$1000	No	No	$\sim$100
FLAMINGOS-2	MMT	2004	6.5 m	$\sim$1000	No	No	$\sim$100
FLAMINGOS	MAGELLAN	$\sim$2005	6.5 m	$\sim$1000	No	No	$\sim$100
EMIR	GTC	2005	10 m	4000	No	No	$\sim$100

Table 1.2: *Summary of the best near-infrared spectrographs available or soon to be available for use on 6.5-10 m telescopes.*

Instrument	Telescope	First light	Telescope diameter	Spectral resolution	IFU elements	AO	MOS gain
CGS4	UKIRT	1991	4 m	40-40,000	No	Tip/tilt	No
UIST	UKIRT	2003	4 m	1,500-3,500	172	Tip/tilt	No
IRIS-2	AAT	2001	4 m	1,500-2,500	No	No	50

Table 1.3: *Summary of the best near-infrared spectrographs available or soon to be available for use on UK 4 m telescopes.*

Wavelength (μm)	CIRPASS	NIRSPEC	ISAAC
1.25	20.7	19.5	19.6
1.65	19.8	18.5	19.3

Table 1.4: *Comparison of CIRPASS's performance with other infrared spectrographs: limiting magnitudes for $S/N = 3$ in $1/2$ hour on an 8 m telescope.* The values for CIRPASS assume a total throughput of 5.4%, a readnoise of 7.6 e^-/read and 18% scattering. The NIRSPEC values are based on its predicted performance on Gemini with 0.5″ seeing and R∼2000 (Geballe, 2001). The performance of ISAAC on the VLT was obtained from their exposure time calculator (ESO/DMD User Support Group, 2001) and are for their medium resolution grating (R∼5000), and a 0.6″ slit.

tively, whereas the CIRPASS grating operates in Littrow mode in first order. The CIRPASS grating should, therefore, be more efficient than ISAAC's. ISAAC uses a camera with a slower f-ratio to image the spectra than CIRPASS. A spectral resolution element on ISAAC, therefore, covers more pixels than on CIRPASS and hence contains a higher readout and background noise. The above two reasons are the likely cause of CIRPASS having fainter limiting magnitudes than ISAAC.

The HAWAII detector used by CIRPASS has $1/8^{th}$ the dark current of the ALADDIN array used by NIRSPEC. The NIRSPEC detector also suffers from a significant number of hot and unstable pixels (McLean et al., 2000) and its detector is the likely reason for CIRPASS slightly outperforming NIRSPEC.

CIRPASS is the only currently available spectrograph in the Tables, that can be used with an AO system and offers both IFU and MOS modes; OHS is the only other spectrograph currently available that offers hardware OH suppression.

1.6 Overview of CIRPASS

CIRPASS was designed and built by the Instrumentation Group at the Institute of Astronomy, Cambridge UK. CIRPASS has been developed from the COHSI spectrograph (Ennico, 1998) to take advantage of existing hardware, and has been redesigned to incorporate the latest available technology. It is a fibre-fed, infrared spectrograph, with an integral field unit for viewing the sky. The spectrograph potentially offers hardware removal of the OH sky background, or the entire spectrum can be sampled and the OH removed in software. The long term goal is to offer a combination of the two, with the strongest OH lines removed to minimise scattering.

A schematic overview of the entire instrument is given in Figure 1.6. Light from the telescope is imaged onto the IFU using two lenses, after which it is reformatted into a slit for the spectrograph using a fibre-optic bundle. The spectrograph follows

a conventional collimator-disperser-camera design, producing the spectra at a mask-mirror plane. Scattering is kept to a minimum in this part of the light path by having few optical surfaces. Light from the mask-mirror is re-collimated and then imaged onto the detector using a f/1.35 camera. The CIRPASS spectrograph uses a single mirror in three off-axis passes, rather than the three lenses shown in the figure. The mirror collimates the beam from the slit, images the dispersed light onto the mask surface, then re-collimates the beam for the camera. The use of this one mirror, rather than three lenses, results in a compact design that allows the grating to be used in reflection in near Littrow mode.

CIRPASS can be broken down into a number of major components. The focal plane unit (FPU) is the part of the instrument that is attached to the telescope and contains the IFU. The IFU has 499 hexagonal elements each feeding an optical fibre, the other ends of which are formatted into the one-dimensional fibre slit. The FPU is the only part of CIRPASS that operates at ambient temperatures. The FPU, IFU and fibre slit are described in Chapter 2.

Light contamination from thermal background radiation from a dome temperature ($\sim$2°C) instrument would be significant when observing at infrared wavelengths. To minimise the effects of this background, all other parts of CIRPASS are cooled to below ambient temperatures. The spectrograph optics and hardware suppression optics operate in a cold room cooled to -40°C. The reasons for cooling to -40°C, CIRPASS's filter complement and the cooling implementation are discussed in Chapter 3.

The spectrograph component of the instrument is essentially unchanged from the COHSI spectrograph, and can use the hardware OH removal mask technology developed for COHSI (Ennico, 1998). Changes have been made to accommodate the larger fibre slit and to allow operation in a cooled environment. The spectrograph optics are discussed in Chapter 4.

The spectra are viewed with a cryogenic camera, whose optics and the infrared detector are cooled using liquid nitrogen. The camera is entirely new for CIRPASS and operates in the cooled suppressor, which raised new design challenges. An important component of the camera design was to ensure that manufacturing delays would be minimal, allowing the camera to be rapidly built. This meant that a chromatic design was adopted and the chromatic aberrations were corrected by tilting the detector. The design and construction of the camera is discussed in Chapter 5.

CIRPASS currently uses a HAWAII 1K infrared detector, whose performance and characteristics are presented in Chapter 6. The instrument has been designed, how-

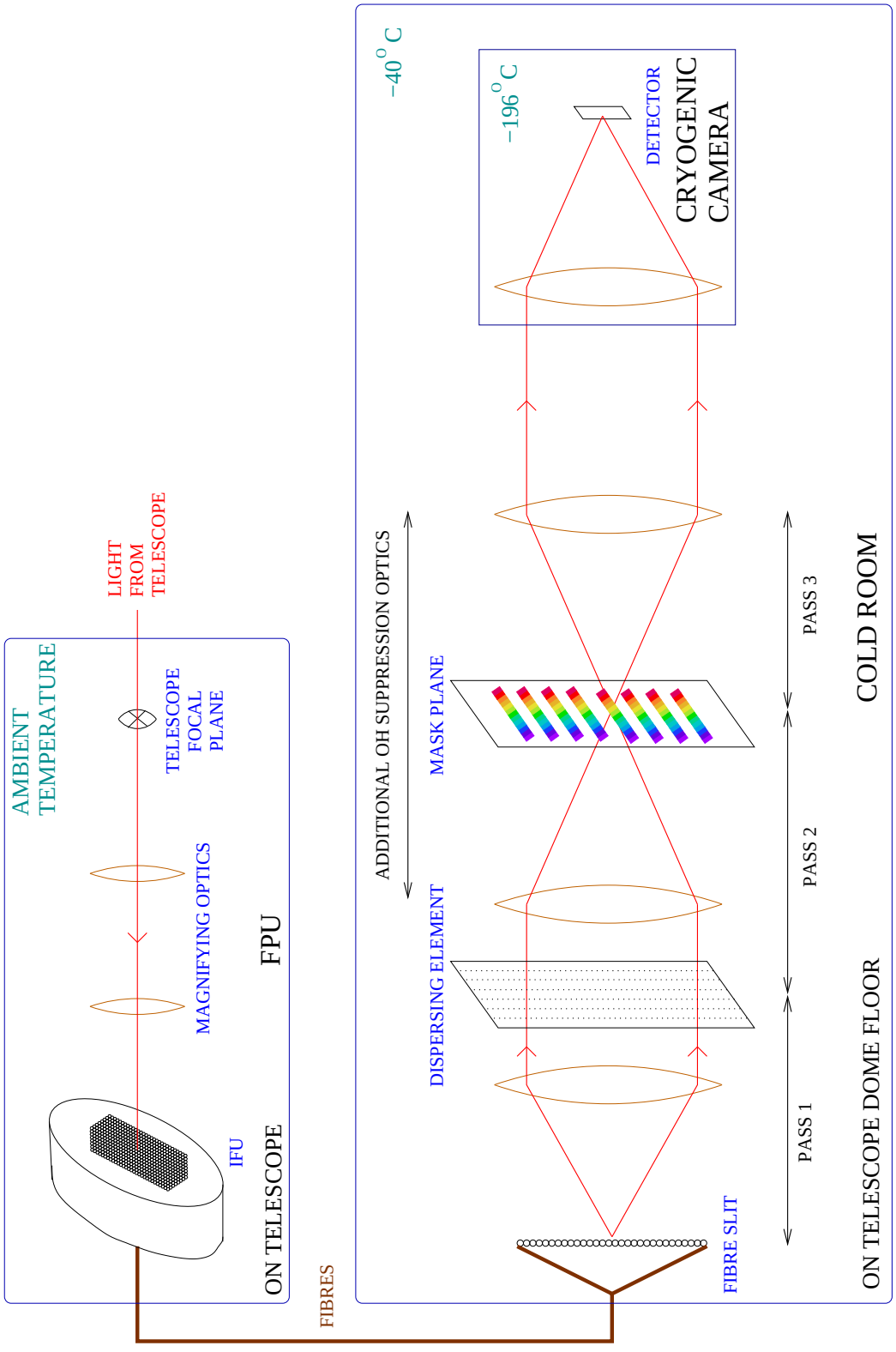

Figure 1.6: *Schematic overall representation of CIRPASS's components.*

ever, for use with a larger HAWAII 2K array. It is a relatively simple matter to replace the 1K detector with a 2K, when available, giving twice the wavelength coverage in one exposure.

CIRPASS is a stand-alone instrument designed to require minimal support when used. Instrument control software and data reduction software have been written specifically for the instrument. The instrument control software, presented in Chapter 7, allows the user to select wavelength range and filter combinations and to initiate the data taking process. Quick-look data reduction software, developed for use at the telescope, allows immediate assessment of the quality of the data obtained and fast reconstruction of the image incident upon the IFU. Pipeline software has also been developed for further data reduction away from the telescope. The data reduction software is presented in Chapter 8.

The performance of CIRPASS has been tested both in the laboratory, and by using a small telescope viewing night sky objects from Cambridge. The results of these test observations and the overall performance of CIRPASS is presented in Chapter 9.

CHAPTER 2

FIBRE FEED AND FOCAL PLANE UNIT

2.1 Introduction

The CIRPASS spectrograph resides on the telescope dome floor and is connected to the telescope focal plane by an optical fibre bundle. At the telescope end of the fibre bundle is the focal plane unit (FPU), while at the spectrograph end the fibres are formed into a slit to feed the spectrograph.

The FPU is attached to the telescope. It contains re-imaging optics to sample the telescope focal plane at several different magnifications, and an integral field unit (IFU) of 499 lenslets onto which the telescope focal plane is projected to feed the optical fibres. Mechanisms are provided for remote alignment and magnification changes, as well as a pupil-viewing TV system to check the accuracy of alignment. Calibration sources are provided at the pupil position and a shutter is provided close to it.

The fibre feed was newly built for CIRPASS, incorporating design improvements and more fibres than were used for the original COHSI fibre feed. The CIRPASS fibre feed consists of the IFU, a 17.5 m fibre run, and a fibre slit to feed the spectrograph, the design and construction of which are presented in Section 2.2.

The mechanical design of the FPU, and a small part of the optical design are telescope dependent. The optical design of the FPU, for use at the Gemini South Telescope, is presented in Section 2.3.1, and its mechanical design is presented in Section 2.3.2.

2.2 Integral field unit

2.2.1 Integral field spectroscopy with fibres

In integral field spectroscopy (IFS), spectra are simultaneously formed for contiguous parts of a two-dimensional field (Section 1.3). The IFS capability of CIRPASS was implemented using lenses to sample the telescope focal plane, where each lens was coupled to an optical fibre. The lens and fibre array formed the integral field unit (IFU). The other ends of the fibres were reformatted into a one-dimensional slit to deliver light to the spectrograph (Figure 1.4).

In general, the number of fibres in the slit is set by the detector size and the desired pixel spacing between adjacent fibre spectra. Increasing the number of fibres allows a larger area of sky to be sampled by the IFU in one exposure. Maximising the number of fibres used is, therefore, desirable. The COHSI IFU contained 100 fibres that were imaged onto 256^2 PICNIC arrays. The use of a larger 1024^2 (and possibly 2048^2) HAWAII detector, and optimal spacing of the fibres on the detector allowed CIRPASS to have a 508 fibre slit. The fibres have a full width half maximum (FWHM) of two pixels at the detector and their centres are two pixels apart. Allington-Smith & Content (1998) discuss the spacing of spectra from adjacent IFU elements and conclude that overlapping the spectra only has a small effect on spatial resolutions; furthermore, the ability to allow overlapping spectra from adjacent IFU elements can be exploited to maximise the number of elements and hence increase the field of view, as was done for CIRPASS. The CIRPASS optics were designed to fit all 508 fibres onto a 1K array. If the detector were upgraded to a 2K device, although the wavelength coverage would be increased, the fibre spacing would not change, thus, only half of the 2K array (perpendicular to the dispersion direction) would be used.

The telescope focal plane could have been directly sampled using the polished ends of the optical fibres, without any additional lenses. There are, however, two arguments against this. First, without lenses the packing fraction (that is the ratio of the light gathering area of the fibres to the total area covered by the fibres) would be much less than 100%. By using closely packed square or hexagonal lenses to feed light into the fibres, the effective packing fraction can approach 100%. Secondly, telescope f-ratios typically vary from f/8 to f/36, whereas optical fibres have 75% better throughput at f/3.5 than f/10 as was measured by Kenworthy (1998). Lenses were used, therefore, to convert the telescope f-ratio to a value appropriate for the fibres. Micro and macro lenses are commonly used for this purpose. (Micro lenses have diameters below $\sim$1 mm while lenses with larger diameters are macro lenses.) A

micro lens array is formed directly from one substrate, rather than by adding lenses individually as is done for macro lens arrays. Micro lenses are used when the telescope focal plane scale is such that direct sampling requires small lenses. Micro lens arrays are, however, difficult to manufacture and have problems with accurate fibre alignment, compared with macro lens arrays. Micro lens arrays also have intrinsic losses (Lee, 1998) and have problems with non-telecentricity[1]. By magnifying the telescope focal plane, larger, or macro lenses can be used. Macro lenses tend to have better cosmetic quality than micro lenses (as they can be handpicked for quality control) and are close to telecentric. Accurate fibre alignment is also easier to achieve with larger lenses. The optical arrangement used for magnifying the telescope focal plane is discussed in Section 2.3.1. The additional optics give added flexibility as the scale at the lens array surface can be adjusted by changing the magnifying lens used. The advantages of macro lens arrays over micro lens arrays, as summarised above, is discussed in more detail by Kenworthy (1998). Other instruments offering integral field spectroscopy using fibre fed integral field units include TEIFU (Murray et al., 2000), which uses a micro lens array, and INTEGRAL (García-Lorenzo et al., 2000) whose fibres directly sample the telescope focal plane.

CIRPASS uses a macro lens array of 499 hexagonal lenses (2.6 mm across flats) to feed the fibres, arranged as shown in Figure 2.1. COHSI (Ennico et al., 1998) and SPIRAL (Kenworthy et al., 1998) also used macro lens arrays. The sizes provided for the CIRPASS IFU, as it would appear on the sky at the Gemini f/16 focus, are given in Table 2.1. Galaxies typically have sizes of a few arcseconds for the redshift range $1 \leq z \leq 2$ and are well matched to the size of the IFU. (Roche et al. (1996) reports the distribution of angular sizes of 5384 faint galaxies measured using the Hubble Space Telescope to $I \simeq 26$, and states that their diameters vary between ~ 0.2 to 3 arcsecs.)

2.2.2 Assembly procedure

The CIRPASS IFU was built by Dr. David King, following similar techniques to those developed by Kenworthy et al. (1998) for the SPIRAL and COHSI IFUs. The procedure is summarised here to record the differences and improvements made for the CIRPASS IFU.

A 17.5 m fibre run was used for CIRPASS, long enough to reach between the Gemini focus and the telescope dome floor. Ultra-low OH silica optical fibres from Polymicro, with an attenuation of less than 3 dB/km for the J and H bands, a core

[1] Non-telecentricity is discussed in Section 2.3.1.

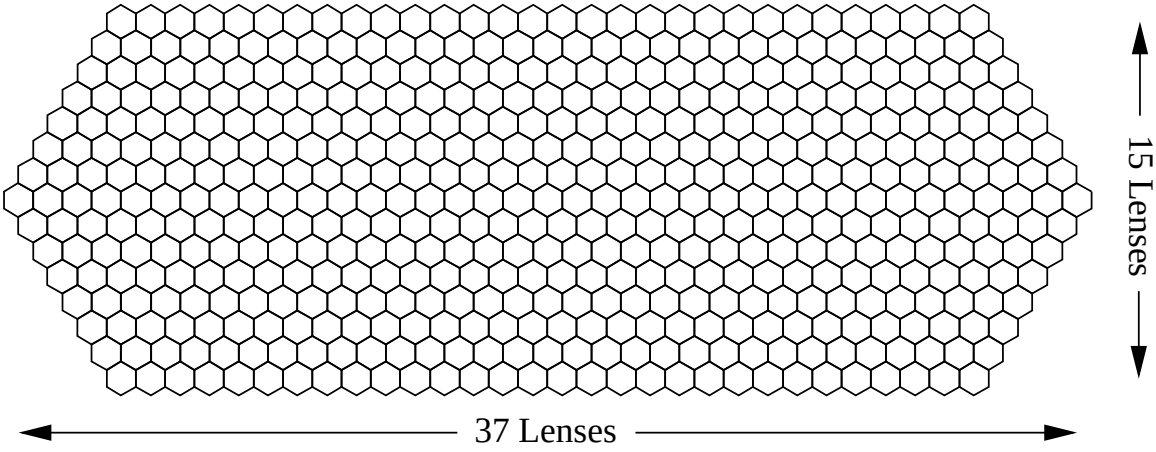

Figure 2.1: *The tessellating arrangement of hexagonal lenses used to form the macro lens array, which samples the telescope focal plane.*

diameter of 104 μm and a core to cladding ratio of 1.2 were used. The fibres were housed in a PVC-coated, flexible steel conduit for protection. The first part of the assembly procedure was to feed 18 m long fibres into the conduit. 508 fibres were used for our 499 element IFU to allow for a few broken fibres and to provide calibration fibres separate from the IFU.

The IFU ends of the fibres were glued into 3 steel ferrules for support during polishing and IFU assembly. A slow-setting, two-part adhesive was used for this purpose, as it does not shrink when cured. Contraction of the glue on setting can stress the fibre, increasing its focal ratio degradation (FRD)[2], and may have adversely affected the COHSI IFU.

An aluminium jig was made to hold the fibres during polishing. The front surface of the jig was circular and had 550 3 mm diameter holes parallel to its cylindrical axis (10 mm deep). The fibres were held in these holes using a heat resetting resin that melts at 100°C. Thus the fibres could be polished and then removed from the block by heating. The fibres initially protruded from the block's surface by a few millimetres. The fibre surfaces were polished on a standard polishing jig using progressively finer powders, to a final grade of 1 μm.

For the CIRPASS slit, the bare fibres were held between two BK7 glass substrates, each of dimensions $30 \times 7 \times 82$ mm. One substrate had a 0.14 mm depth recess on its top surface to accept all 508 fibres. This allowed the fibres to be closely packed, that is, touching each other, and meant that the slit was only 1.2 times bigger than the COHSI slit for 5 times more fibres. The desired spacing of the fibres on the detector was two pixels, which projected to 150 μm at the slit. This is just larger than a fibre's

[2]FRD is summarised in the footnote on page 7.

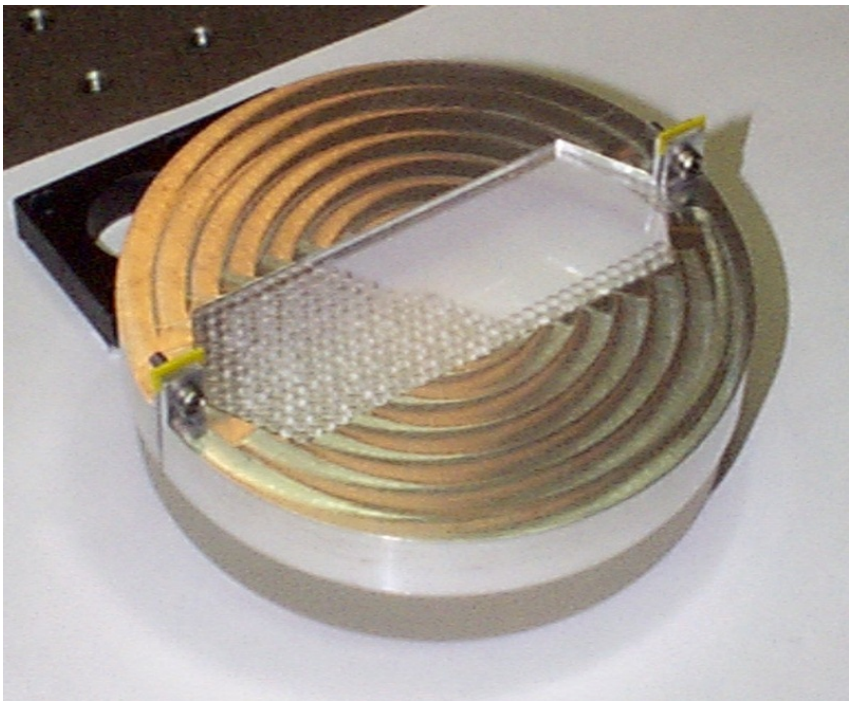

Figure 2.2: *Macro lens array assembly process.* Lenses being added to the glass substrate and constrained by an aluminium mask.

diameter, hence their close-packed arrangement. The same slow-setting adhesive as used for the ferrules was then flowed around the fibres, and another similarly shaped piece of BK7 glass (but without the recess) placed on top of the fibres to form the slit assembly. The fibres were left protruding from the front face of the slit and were not polished until the IFU had been made, as it was easier to illuminate individual fibres for identification purposes with this arrangement.

The macro lens array was formed on an optically flat SF2 glass substrate of thickness equal to the focal length of the macro lenses (29.7 mm) and diameter 109.1 mm. An aluminium mask with a cutout of the final lens array geometry was made to fit over the substrate and hold the lenses in place during assembly (Figure 2.2). Each lens was hand-picked and checked for optical quality, dabbed with UV curing glue and then placed on the substrate. This was repeated for all the lenses with the substrate at a slight angle, so that gravity maintained them in a close-packed arrangement. Once all the lenses had been added the glue was hardened using a UV lamp. The aluminium mask was then removed and the lens surfaces were anti-reflection coated. The completed lens array is shown in Figure 2.3.

The fibres were then individually attached to the glass substrate on the opposite side to the lens array. The same technique as for the COHSI IFU construction was used. The macro lens array and field lens (Section 2.3.1) were placed in a vertical

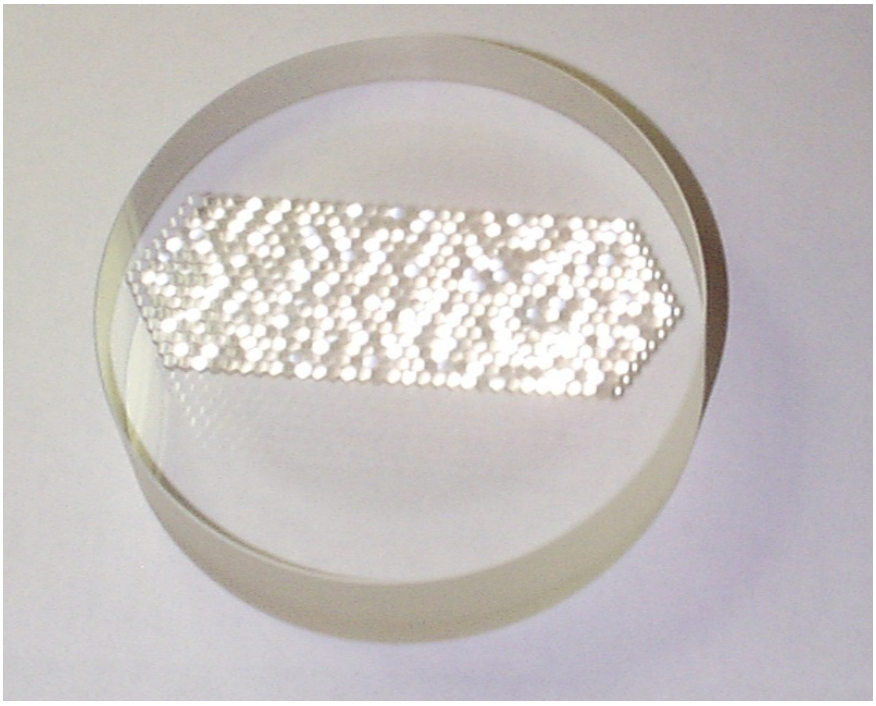

Figure 2.3: *Macro lens array completed.* All 499 macro lenses attached to the glass substrate.

optical bench, so the fibres could be attached from above. A graticule was placed at the position of the fibre image formed by the field lens and macro lenses and was viewed using a TV camera. Fibres were identified by illumination from the slit end. The fibre's slit position and the macro lens to which is was attached were recorded. The fibre was then checked for optical quality and placed in an x-y-z stage for positioning on the back of the macro lens array. The alignment of the fibre image with the graticule was viewed on the TV screen and adjusted accordingly. The fibre was then backed off from the substrate (in the z direction), UV setting glue applied to its face and then moved back into contact with the substrate. Final improvements to the alignment of the fibre image and graticule were made before illuminating the substrate with UV light to cure the glue and hold the fibre in place. This process was repeated for all 499 lenses and took approximately 15 minutes per fibre; the whole assembly took about 1 month to complete. As more fibres were added, the position of the graticule was frequently checked by re-illuminating the first fibre and adjusting the graticule so that it was centred in the first fibre's image. Figure 2.4 shows the back of the IFU as the fibres were being added and Figure 2.5 shows the IFU with all the fibres attached. The fibres were then supported and secured in

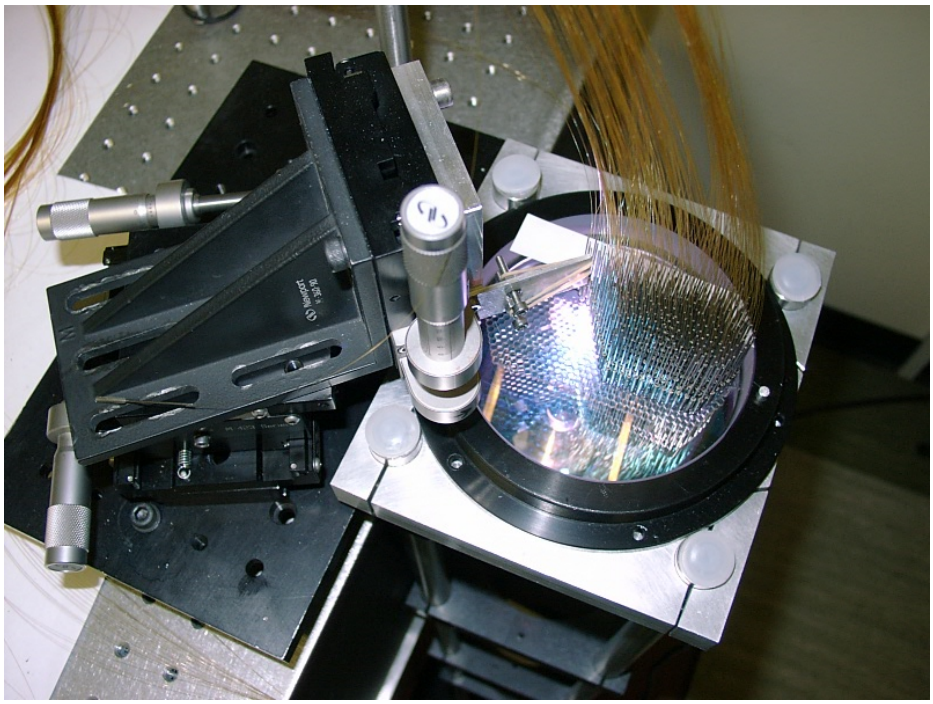

Figure 2.4: *The semi-completed IFU, showing the positioning of fibres on the glass substrate containing the macro lens array.*

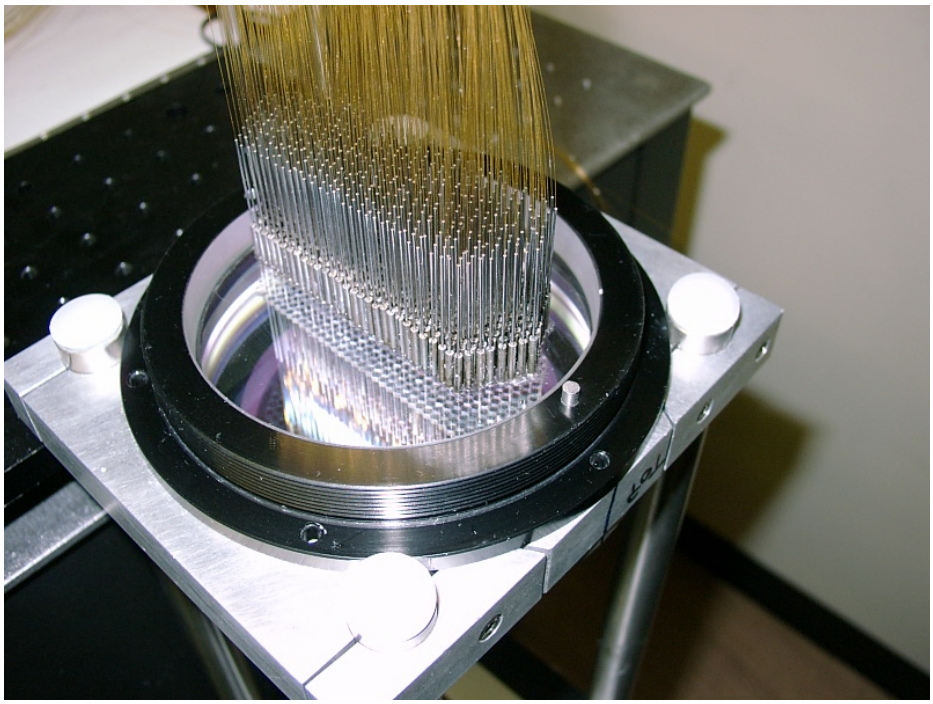

Figure 2.5: *View of the IFU showing all 490 fibres attached to the macro lens array glass substrate.*

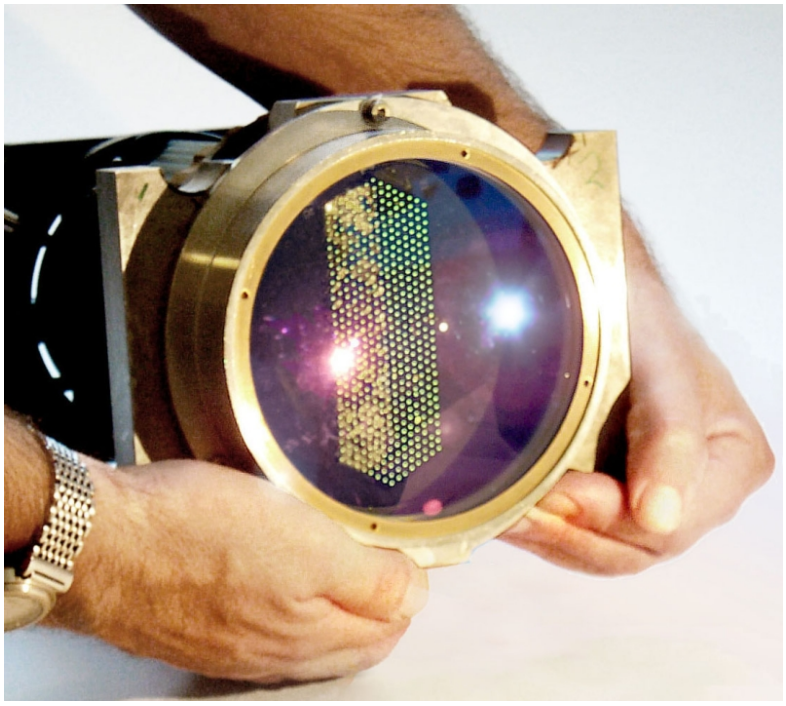

Figure 2.6: *The finished IFU.* The picture shows the macro lens array being illuminated by light shining down the fibres from the fibre slit. The field lens is in place.

place on the back of the glass substrate using a potting compound[3]. Re-enterable polyurethane was used for this purpose. The fibres in the slit whose IFU ends had not been attached to the IFU were brought together and formed into a small bundle. These fibres can be illuminated via a small hole in the side of the IFU metal casing and form the calibration fibres. The completed IFU is shown in Figure 2.6.

The fibre slit was then polished to an accuracy of 1 μm and a slit lens of Schott SFL57 glass cemented to the slit substrate. The slit lens was necessary as the light beam from each fibre had to be launched at a slightly different angle from its neighbours. This was not required for COHSI or SPIRAL as each of their fibres lay in a groove cut at the required angle. The close packing of the fibres in the CIRPASS slit, however, made this approach impossible. The slit lens ensures that the beam from all parts of the slit is directed to the grating (after reflection in the primary mirror), is incident on the mask mirrors, and hence is directed onto the detector.

The fibre slit to IFU mapping, that is, the fibre number in the slit that is attached to a given lens in the IFU, was later checked as part of the data reduction software

[3]Potting compounds are usually used to encapsulate electrical devices, protecting them from the surrounding environment. They are slow setting resins that can be flowed around the device before hardening. Re-enterable compounds remain malleable when set, thus allowing the fibres to be removed if necessary. The compound supports the fibres but does not inflict any lateral forces.

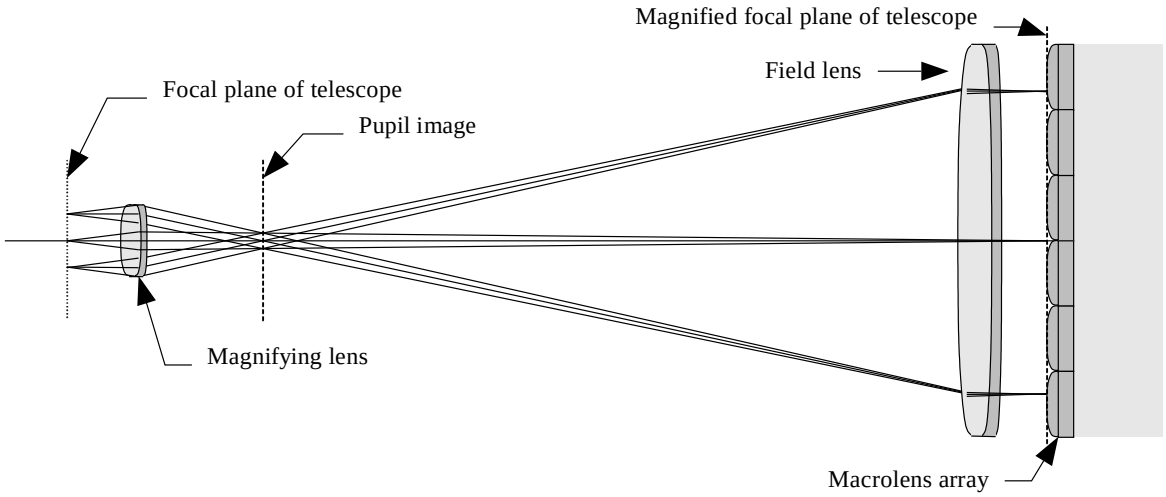

Figure 2.7: *Schematic outline of the fore-optics optical layout.*

testing and is presented in Section 8.3.1. There were 7 fibres that broke during assembly and 11 calibration fibres were provided, spaced throughout the slit, leaving 490 that were attached to a lens in the IFU. The breakdown of calibration and broken fibres is given in Table 8.2.

2.3 Focal plane unit

2.3.1 Optical design

The CIRPASS fore-optics uses two lenses to magnify and re-image the telescope focal plane onto the IFU. This fore-optics design was successfully used for both the SPIRAL and COHSI instruments (Kenworthy, 1998) and the arrangement is depicted in Figure 2.7. The magnifying lens forms an image of the telescope pupil and an enlarged image of the telescope focal plane on the surface of the lenslet array. The field lens images the pupil at infinity, so that the pupil images formed by the lenslet array all fall on the optical axes of the lenslets and thus onto the end of each fibre. That is, the field lens provides telecentric correction. Telecentric correction eliminates throughput losses caused by light rays entering the fibres at steep angles (and hence fast focal ratios).

Another potential FRD problem is illustrated in Figure 2.8, which shows a micro lens fed optical fibre. The on-axis input focal ratio of this system is the lenslet's focal length divided by its diameter, which is correct for the black rays. As can be seen, however, rays from the edge of the pupil enter the edge of the fibre (the dotted rays) at a larger angle than the on-axis (black) rays. The mean focal ratio derived from

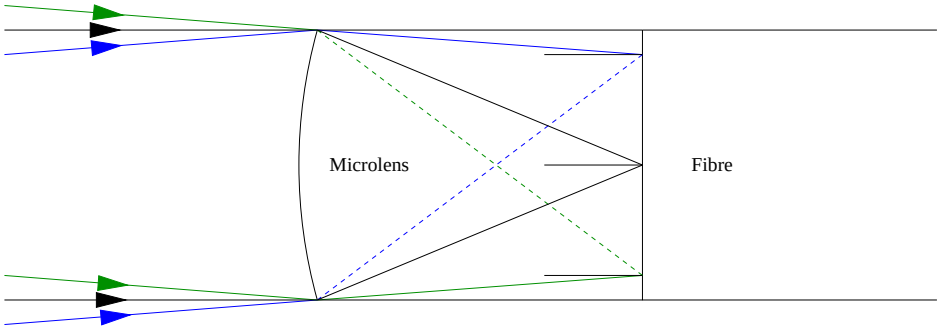

Figure 2.8: *Light paths for a micro lens fed optical fibre, to illustrate geometric FRD.* The dotted rays have a higher angle of incidence (and hence input focal ratio) than the telecentric ray shown in black.

Magnifier focal length (mm)	Scale per lens (″/lens)	Field size (″)
68.73	0.36	13.3 x 4.8
47.73	0.25	9.3 x 3.3
22.90	0.12	4.4 x 1.6
14.25	0.05	1.9 x 0.7

Table 2.1: *The different scales available with the IFU at Gemini.* The lens scale is the distance between two parallel edges of the lens, the field size is for the two longest dimensions of the IFU.

all rays that are accepted by the fibre is higher than that derived from the on-axis rays. This effect is known as geometric FRD and is an important consideration when designing an IFU that uses a micro lens array to feed optical fibres. The amount of geometric FRD is proportional to the ratio of the diameter of the lens feeding the fibre to the fibre diameter, and inversely proportional to the focal length of the lens. It is, therefore, intrinsically less for macro lenses than micro lenses, if the same size fibres are used.

Four magnifying lenses are provided for use on Gemini giving four different scales on the IFU as stated in Table 2.1. The three larger scales are for use directly at the Cassegrain focus and reside in the FPU described here. The finest scale matches the improved seeing provided by the Hokupa'a adaptive optics system (Roth et al., 2001) and is not currently available as it requires a different FPU to connect to CIRPASS.

The macro lenses feed the fibres with an f-ratio of 6.5 (f/6.5); this becomes a faster beam upon leaving the fibre slit owing to FRD. The spectrograph optics are designed for an f/5.5 beam.

2.3.2 Mechanical assembly

The FPU provides CIRPASS's interface to the telescope. It is attached at the Cassegrain focus of the Gemini telescope and is mounted from a Gemini instrument support structure (ISS).

The FPU assembly is based around a rigid, lightweight Kanya framework[4]. This frame provides our interface to the Gemini ISS and supports an aluminium bread-board on which the CIRPASS optical and mechanical components are mounted. An ICU is also attached to the frame (Section 7.4), providing the electrical interface to the mechanisms and allowing remote control of them. The FPU is unusually light compared with most instruments that are entirely mounted from the telescope; this is corrected with ballast weights to ensure that the telescope is balanced.

The IFU and its associated fore-optics are mounted on the aluminium optical base plate (which has dimensions of $901 \times 700 \times 16$ mm). The position of the telescope focal plane is fixed relative to the table, however, the requirement of a number of different image scales on the IFU means that the position of the IFU and field lens relative to the table are not fixed. In order to change scale three magnifying lenses are provided and the desired lens is moved into the light path using an x-y stage. The linear position (or z position) of the magnifiers in the x-y stage is set such that their foci coincide on the telescope side of the optical axis, and alignment of their common focus with the telescope focus can be achieved by moving the entire stage using a manual linear actuator. This mechanism was not motorised as it should not need adjustment once aligned. Changing magnifiers results in a change in position of the telescope pupil, which can be accommodated by moving the field lens and IFU. The IFU and field lens are mounted using a Linos Photonics macrobench four rod system, which is attached to a motorised linear translation stage. These rods also house a shutter and a remote pupil viewing mechanism. The telescope pupil is viewed by driving a pellicle into the light path, between the magnifier and shutter, and is imaged using a small CCD camera. Figure 2.9 shows a picture of the completed FPU assembly and Figure 2.10 shows a schematic of the FPU's optical and mechanical components.

Three arc lamps and a continuum source are provided on the optical table. A small fibre optic run was made for each lamp, which injects light into the IFU from the centre of the x-y stage assembly that holds the magnifying lenses. The light from

[4]The Kanya system provides custom sized aluminium bars. These can be attached together in a number of ways to allow easy fashioning of a custom framework, which can be readily assembled and disassembled. The UK distributor of this system is AluSett.

the continuum lamp is also connected via another fibre optic run to the calibration fibre port on the side of the IFU.

2.3.3 Alignment procedure

Initial alignment of the fore-optics was performed in the laboratory, away from the telescope. The IFU was removed and a laser installed in its place. The optical axis of the fore-optics was then defined by aligning the laser with the mechanical axis along the Linos Photonics rail system. The positioning of the magnifiers was then set. The magnifiers are held in tubes of the correct length to ensure that their foci are coincident on the telescope side, and their placement in the tubes was set to the nearest 10 μm using a depth gauge. There are four such tubes on the x-y stage, three for the magnifiers and one that has a screen for viewing the telescope focal plane. Centration of the magnifiers was achieved by observing the back reflections and interference patterns of the laser on a perforated screen, and the x-y position of each magnifier was noted.

The pupil screen is a silica disc with a small dot marked at its centre. The screen was positioned, once driven into the beam, using shims, so that it was coincident with the laser beam. Its z position was set by measurement from the field lens to an accuracy of 1 mm.

The laser was then replaced with the IFU and the fibre slit illuminated to form a pupil image close to the screen. The IFU was then adjusted to centre the pupil onto the dot on the pupil screen.

Alignment at the telescope was first achieved by ensuring that the telescope focal plane was correctly aligned with the magnifiers' focal plane. The magnifier screen was moved onto the optical axis and viewed using the TV camera (and beam splitter). The z position of the x-y stage could then be adjusted until a star image was focussed on the screen. This is a manual adjustment that should not need changing during an observation.

The z location of the telescope pupils formed by each magnifier was then matched with the fibre pupils' location as defined by the pupil screen. The telescope's primary mirror was illuminated by viewing the twilight sky, allowing the telescope pupil to be viewed behind the magnifiers. The z position of the IFU stage was then adjusted until the telescope pupil image on the pupil screen was focussed (that is, at its smallest size). The z position of the IFU stage was recorded and the x-y position of the magnifier stage refined, so that the telescope pupil was accurately centred on the pupil screen for each magnifier.

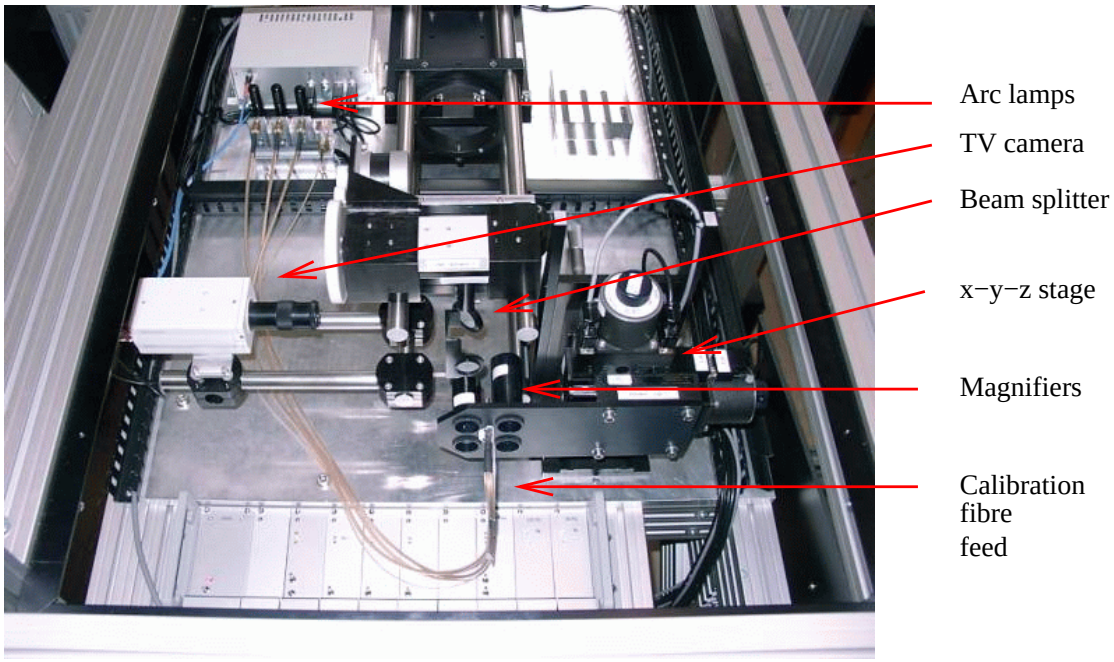

Figure 2.9: *Picture of the completed FPU.*

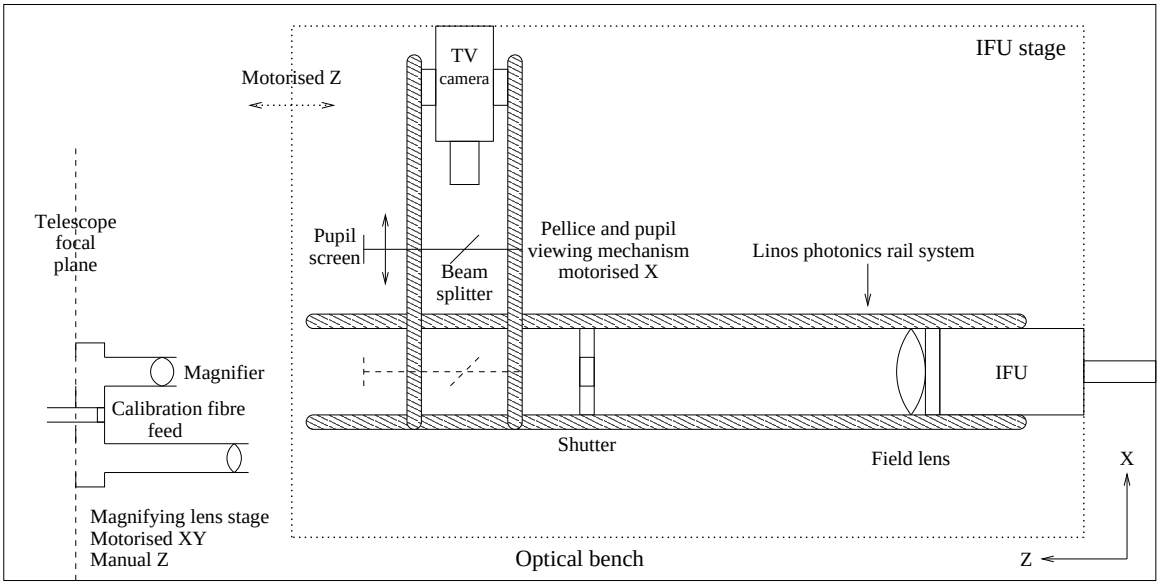

Figure 2.10: *Schematic outline of the FPU's optical and motorised components.*

Once the alignment had been achieved, x, y magnifier and IFU z positions were stored in the instrument control software, for each magnifier. The software could then move all of the mechanisms to the correct positions for each IFU image scale. Changing scale during an observation then only requires selection of that scale.

CHAPTER 3

THERMAL BACKGROUND PERFORMANCE: FILTER SPECIFICATION AND REFRIGERATION SYSTEM

3.1 Introduction

Infrared instruments, such as the CIRPASS camera, are commonly operated at cryogenic temperatures to achieve low thermal backgrounds and acceptable detector performance. However, CIRPASS's large spectrograph optics are located outside the cryogenic camera. These large optics are operated in a cold room maintained at $-40°C$, rather than at room temperature, as was the case for COHSI. The reasons for cooling the large optics to this intermediate temperature, the cold room design and its refrigeration system are presented in this chapter.

A model, based on blackbody emission from the spectrograph optics, was developed to predict the thermal background that would be detected by our camera system. The model, which is discussed in section 3.2, was used to define our filter performance requirements and is what drove us to cool the entire optical assembly. Using this model, new filters were specified and procured for CIRPASS. The performance of the new filters and the background performance of the cooled system is presented in Section 3.5.

A commercially available cooling solution was adopted, with slight customisation to improve its performance and stability. The system used is presented in Section 3.3 and its performance is given in Section 3.4. Both the FMOS (Maihara et al., 2000) and GOHSS (Lorenzetti et al., 2000) spectrographs plan to cool their large optics with a system similar to that designed for CIRPASS.

3.2 Thermal background and filter specification

The HAWAII detector used by CIRPASS is sensitive to light from 0.85 to 2.5 μm, defining the maximum available wavelength range for astronomical observations with CIRPASS. (The detector's sensitivity as a function of wavelength is presented in Section 6.3.7.) However, thermal emission of infrared radiation from the instrument itself is significant when working in this wavelength region. Although the background can technically be subtracted using off target observations (by employing a beam-switching or nodding technique), its large magnitude means that its noise contributions are significant. Large backgrounds can also rapidly saturate the detector, making observations of faint sources impossible. Considerable effort has been made with CIRPASS to reduce the thermal background produced and hence detected by the instrument. This has allowed us to achieve the stated limiting fluxes in the J (1.15 to 1.35 μm) and H (1.45 to 1.8 μm) passbands.

Planck's law, stated in equation (3.1), describes the intensity of radiation from a blackbody source, where I is the intensity of the radiation in photons/s/str/m^2/m, if all other constants are in SI units, c is the speed of light, h is the Planck constant, k is the Boltzmann constant, T is the temperature (k) and λ is the wavelength of the radiation.

$$I = \frac{2c}{\lambda^4 \left(e^{\frac{hc}{\lambda kt}} - 1\right)} \tag{3.1}$$

Figure 3.1 shows the blackbody radiation from an object at room temperature for the H and K (2.0 to 2.4 μm) bands. As can be seen, the intensity of thermal emission increases exponentially with increasing wavelength and starts to become significant above 1.8 μm. Significant improvements can therefore be made by filtering out light from wavelength regions outside that being observed. The total flux emitted is also a function of the temperature of the blackbody source, increasing with temperature as illustrated in Figure 3.2. Thus, by cooling the instrument, the background due to the instrument can be considerably reduced. As an illustration of the benefits of cooling, the blackbody background that would be detected by the CIRPASS camera at 1.8 μm is 3 e$^-$/pix/s at 27°C, and 0.003 e$^-$/pix/s at −33°C, a factor of 1000 improvement (using Equation (3.1), given that the HAWAII detector has square pixels of side 18 μm and a quantum efficiency of 60% at 1.8 μm, the camera's solid angle is 0.43 str and the resolution is 2 Å per pixel).

The CIRPASS camera is cryogenically cooled, thus the amount of thermal background light generated within the camera is negligible. (The dewar contains cold

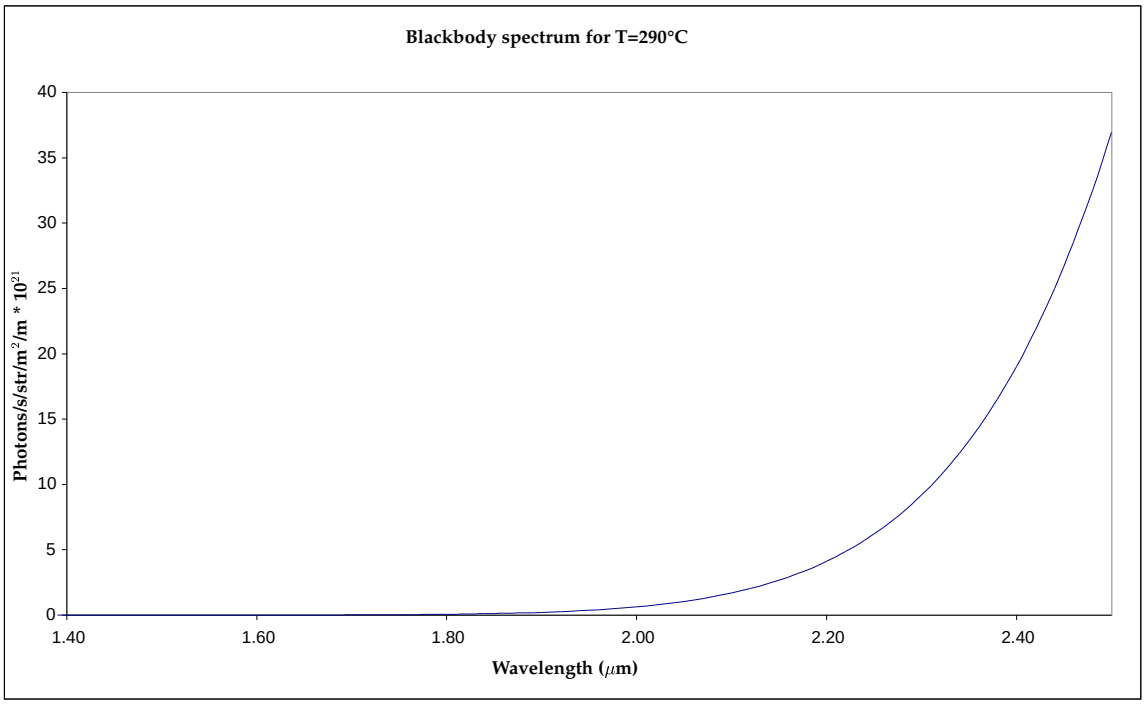

Figure 3.1: *Photons produced via blackbody radiation at room temperature, in the infrared region, as a function of wavelength.*

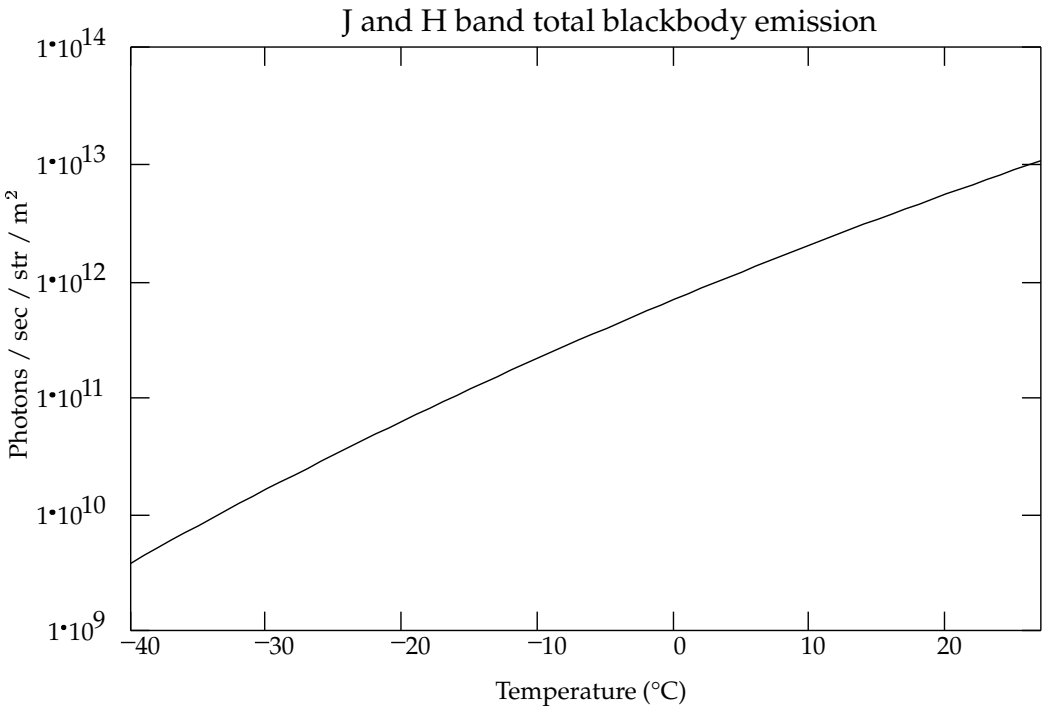

Figure 3.2: *Integrated J and H band photon flux from a blackbody source as a function of temperature.*

baffles to prevent the detector from seeing the warm dewar walls. Section 5.2.) The camera, however, has a very fast f-ratio or f# (f/1.35) and highly efficient optics, consequently it could see a large background from either the dewar window or the dispersing optics, both of which are warm by comparison. To keep this background to a very low level (i.e. the order of the detector dark current of 0.05 e^-/pix/s), the two approaches suggested above have been implemented:

- The light is filtered as close to the detector as possible, using a cold, short-pass filter with a substantial optical density for wavelengths above the longest observed.
- The dispersing optics and dewar window are cooled to reduce their intrinsic blackbody emission.

Given the size of CIRPASS's dispersing optics, it is impractical to cool them to the cryogenic temperatures necessary for acceptable performance in the K band. The optical fibres used to feed the spectrograph also have very poor transmission in K. It was decided from the outset, therefore, that CIRPASS would only offer J and H band coverage, allowing the large amount of K band background light to be removed by using a suitable filter, without affecting the instrument's performance. It was also hoped that by using suitable blocking filters it would be possible to operate the dewar window and spectrograph optics at ambient temperatures.

A spreadsheet was set up to model the thermal background produced by the CIRPASS optics and enclosure before the dewar. The spreadsheet assumes that the number of detected background photons, per second, in a pixel is given by:

$$\begin{matrix}\textit{background}\\ \textit{photons}\end{matrix} = \begin{matrix}\textit{blackbody}\\ \textit{photons (I)}\end{matrix} \times \begin{matrix}\textit{blackbody}\\ \textit{emissivity}\end{matrix} \times \begin{matrix}\textit{camera}\\ \textit{throughput}\end{matrix} \times \begin{matrix}\textit{camera solid}\\ \textit{angle}\end{matrix} \times \textit{pixel area} \times \begin{matrix}\textit{pixel}\\ \textit{wavelength}\\ \textit{coverage}\end{matrix} \quad (3.2)$$

The black body emissivity is essentially a scaling factor, and was determined to be 0.2 by measuring the thermal background at room temperature, with no filters in the camera. Its value was later checked as a function of temperature once the cold room was constructed and found to be consistent. The modelling was also carried out with an emissivity of unity as a worst case scenario. The camera throughput includes the detector quantum efficiency, as well as the transmission of the optics and filters, as a function of wavelength. The camera solid angle is given by $\pi/(2f\#)^2$. The modelling was carried out over the wavelength range 1.0 to 2.8 μm. Wavelengths below 1 μm were not considered as their is very little contribution to the thermal background at

the shorter wavelengths. The modelling was extended slightly beyond 2.5 μm as the thermal emission is very strong at the longer wavelengths and the precise detector cut-off wavelength was not well known. This approach ensured that conservative results would be obtained: the resulting performance figures would underestimate the performance of CIRPASS. A summary of the results is presented in Table 3.1.

The analysis showed that, with no filtering at ambient temperatures, the background is about 1.4 million times greater than the desired 0.05 e^-/pix/s, and that cooling to −101°C would be necessary for acceptable performance with no filters.

Three filters were designed and added to the model in order to reduce the background. One short pass filter, permanently in the beam, with a cut-off at 1.8 μm to remove the very strong K band radiation. In addition two short pass filters are available, one to be used when observing in J (1.15 to 1.35 μm), and another for observing in short H (1.45 to 1.6 μm).

The three filters were designated camblock 1, 2 and 3 and were manufactured by IR Engineering. The specified profiles of these filters is given in Figure 3.3 and Figure 3.4 shows the actual measured optical density profiles, as provided by the manufacturer, for each of the delivered filters. Camblock 1 is a 60 x 60 mm filter located in the detector box (Section 5.2.3), that is, camblock 1 is the filter closest to the detector and is always in the light beam. It is the K band blocking filter. With just camblock 1 in the camera, acceptable performance in the long H band (1.6 to 1.8 μm) is achieved if the cold room is operated at −45.5°C.

For operation in short H, camblock 3 is used. This is a 170 mm diameter, short-pass filter with a cut-off at 1.65 μm, and located in one of the filter wheels. (Section 5.2.2). As can be seen from the table, it is only necessary to cool to −26°C with this filter combination for operation in short H. Cooling of the instrument is definitely required, though, for acceptable performance in the H band.

For observing in the J band camblock 2 is used. Again, it is a 170 mm diameter, short pass filter, located in one of the filter wheels, but with a lower cut-off at 1.4 μm. The combination of camblock 1 and 2 in the beam theoretically allows observations in the J band, with the dispersing optics at room temperature, although in practice the cold room is always operated at about −40°C during an observing run.

It is relatively easy to enclose the dispersing optics in a cold room, though the fibre feed is still left at room temperature. Thus, the thermal background from the fibres was calculated to ensure that it would not be significant, given the improved background performance of the cold room. The dark performance of optical fibres was tested using the COHSI spectrograph and the fibres were found to behave as a

Cold room temperature	*Emissivity*	*Filter near detector*	*Filter in wheel*	*Usable wavelength range (μm)*	*Detected thermal background (e^-/pix/s)*	
					specified	*delivered*
4	1.0	none	none	0.85-1.80	71,802	
−101.2	0.2	none	none	0.85-1.80	0.05	
−40.0	0.2	none	none	0.85-1.80	281.5	
4	1.0	Camblock 1	none	0.85-1.80	142.3	262.6
−45.5	0.2	Camblock 1	none	0.85-1.80	0.05	0.11
−40.0	0.2	Camblock 1	none	0.85-1.80	0.12	0.25
4	1.0	Camblock 1	Camblock 3	0.85-1.65	7.5	16.5
−25.7	0.2	Camblock 1	Camblock 3	0.85-1.65	0.05	0.12
−40.0	0.2	Camblock 1	Camblock 3	0.85-1.65	0.004	0.01
4	1.0	Camblock 1	Camblock 2	0.85-1.35	0.11	0.26
12.1	0.2	Camblock 1	Camblock 2	0.85-1.35	0.05	0.14
−40.0	0.2	Camblock 1	Camblock 2	0.85-1.35	0.0003	0.0001

Table 3.1: *Predicted thermal backgrounds for CIRPASS, as a function of temperature and filter combination.* The background contribution for each pixel is a blackbody spectrum summed over the wavelength range 1 to 2.8 μm. Backgrounds using the specified filter profiles are given as well as the backgrounds obtained using the measured profiles of the delivered filters.

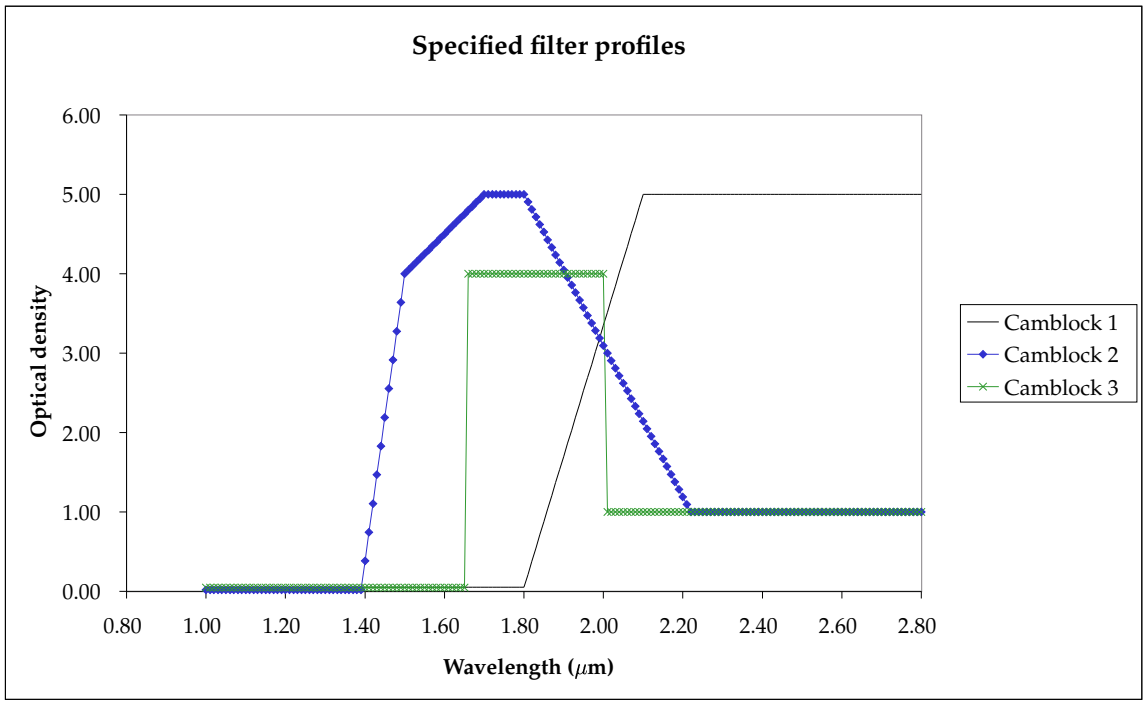

Figure 3.3: *CIRPASS filter profiles.* Specified optical density plots for filters camblock 1, 2 and 3.

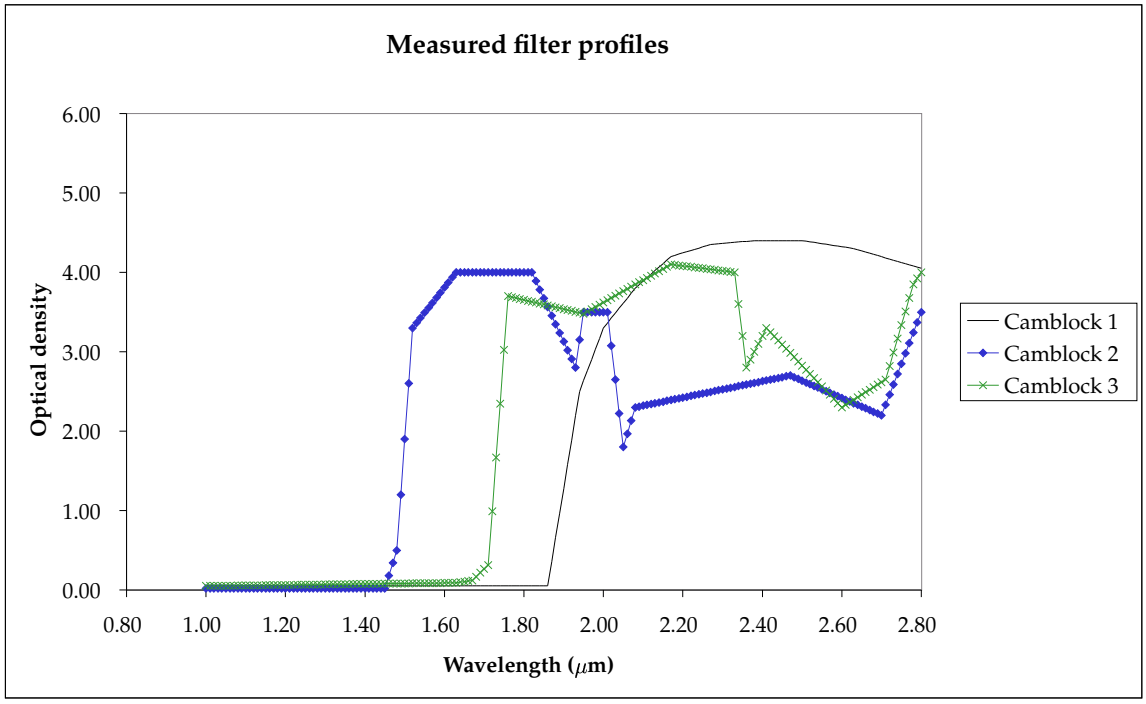

Figure 3.4: *CIRPASS filter profiles.* Measured optical density plots, as provided by the manufacturer, for the delivered camblock 1, 2 and 3 filters.

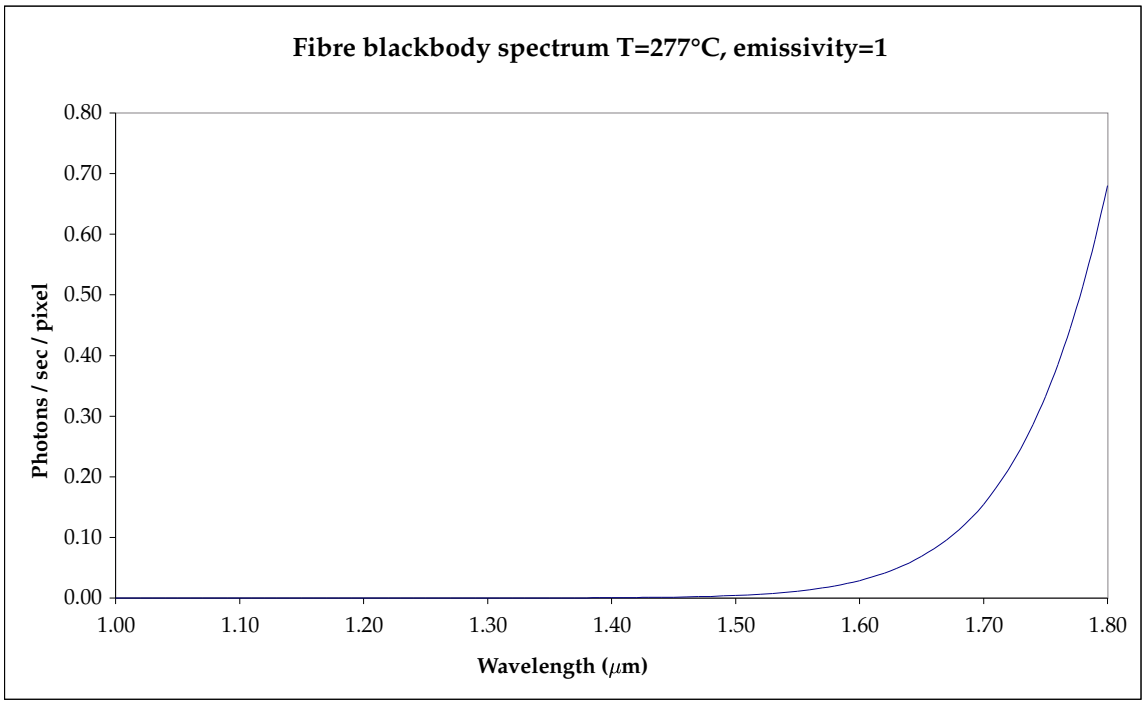

Figure 3.5: *The blackbody spectrum produced by the CIRPASS optical fibres at 4°C.*

grey body source with an emissivity of about 0.3. To be certain of acceptable performance, the CIRPASS fibre spectrum was added to our background model using a fibre emissivity of 1. The derived spectrum is shown in Figure 3.5 for a temperature of 4°C, and shows that the background from the fibre itself is below 0.05 e^-/pix/s for wavelengths below 1.64 μm.

3.3 Cooling implementation

The desired background performance dictated that the dispersing optics should be cooled to −46°C. As a result, a commercially available cooling solution was sought. Small refrigeration plants are frequently used by life science laboratories and were readily available. A system was purchased from Barber and Clarke Ltd. with the following specifications:

- An insulated chamber with internal dimensions of 1880 x 2510 x 1300 mm and hatches for easy access to the assembled spectrograph inside the chamber.
- A refrigeration plant, to cool the chamber to -45 ± 1°C with an ambient temperature below 30°C. (Two separate plants were required: one to operate in Cambridge, thus running from a U.K. electricity supply, and with a cooling fan

designed for operation at the atmospheric pressures typically experienced at sea level; and another to operate in Hawaii, thus from a U.S. electricity supply and the ∼60% atmospheric pressure present at 14,000 feet.)

The chamber was constructed of several 150 mm thick polyurethane sections clad with plastic coated galvanised steel. The sections are fastened together with quick-release locks, allowing easy assembly and dismantling, and have a black internal finish. 3 large (600 x 1250 mm) and 4 small (400 x 200 mm) access hatches were cut into the walls. The large hatches have doors and provide easy access to the optics. The smaller hatches act as feed through panels for the electrical, vacuum and liquid nitrogen connections. This chamber forms the CIRPASS cold room and Figure 3.6 is a picture of the finished assembly. The heat load through the walls, if the cold room is at -40°C with an ambient temperature of 20°C is about 350 W, given that the thermal conductivity of polyurethane is 0.032 W/m/K and the outside surface area of the cold room is approximately 27 m^2. The access hatches have galvanised steel connecting the inside and outside of the room, however, and the electrical feed-throughs provide additional conduction paths into the room. The actual heat load was, therefore, expected to be higher than this and was estimated at 500 W. (Table 7.1 details all of the heat loads on the cold room, present in the completed instrument.)

The cold room is cooled using a two-cycle system. A Copeland compressor with a cooling capacity of 2 kw is the primary cooling agent. To avoid placing excessive heat into the telescope dome, the compressor's heat exchanger is cooled using a conventional refrigeration line. Gemini has a 0°C glycol line for this purpose, and a water chiller was used to provide a coolant line in Cambridge. The primary cooling line uses R404a refrigerant, capable of cooling the room to -50°C at full capacity with the compressor. A conventional cooling cycle is used and a schematic outline of the system is given in Figure 3.7. In addition to the evaporator there is a 180 W fan inside the cold room to ensure an even temperature throughout.

3.4 Cooling performance and stability

The cold room performed to specification as delivered. However, the design and control system were optimised for a typical cold storage chamber, in contrast to the stable temperature required for CIRPASS. Thus a number of changes were made to the system.

The system was set to run with the compressor permanently on, temperature regulation being achieved via the hot gas line, rather than by on-off control of the

Figure 3.6: *Picture of the CIRPASS cold room assembled in the laboratory in Cambridge.*

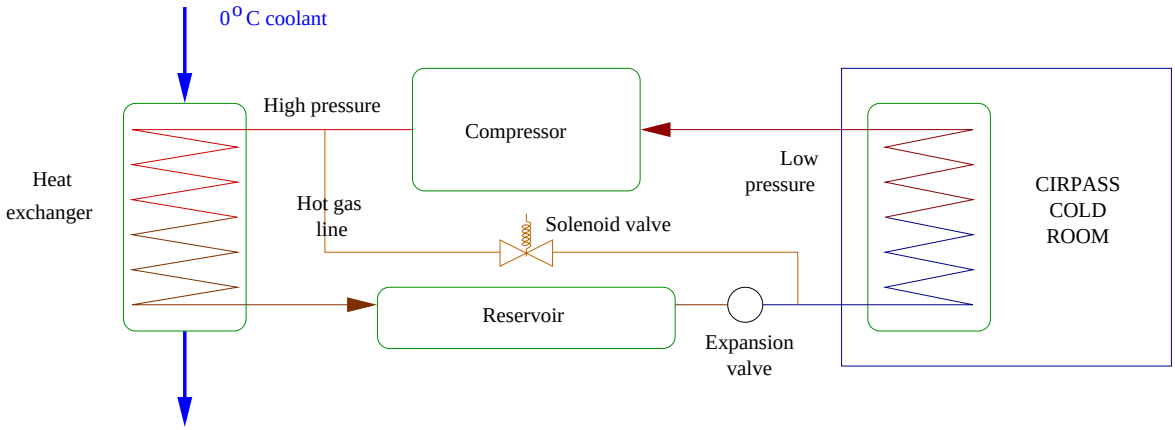

Figure 3.7: *Schematic outline of the refrigeration system.*

compressor. A small amount of hot refrigerant is mixed with the cold refrigerant before it reaches the cold room. This gave a one degree temperature cycle, as the hot gas injection into the cold line was switched on and off by the cold room temperature controller. This could be detected, however, as a 0.2 pixel shift in the position of spectra on the detector. A Eurotherm controller[1] was added, and the original Dixell[2] controller supplied with the refrigerator set to run the system at -50°C giving the Eurotherm executive control. This new controller has a much finer temperature resolution and reduced the temperature fluctuations inside the cold room to <0.1°C, resulting in an undetectable change in position of spectra on the detector.

The cold room temperature is maintained at -40 ± 0.1°C, which is slightly higher than the desired -45°C. This is to allow us to confidently maintain a stable temperature, as we are not at the limit of the refrigeration system's cooling ability. The cold room should not be affected by external fluctuations, such as changes in the laboratory or dome temperature. It therefore provides a very stable temperature environment in which to operate CIRPASS, avoiding the problems experienced with COHSI at UKIRT as the dome temperature dropped throughout the night (Ennico, 1998).

The time it takes from initial switch on, to the cold room internals reaching a stable temperature (the cool down time) is about 14 hours. If switched on early in the morning, CIRPASS can be ready for observing the same evening, although ideally it should be used the next day. The time it takes from switching the cold room off, to being able to open the doors with minimal ice forming on the internal components (the warm up time) is about 24 hours. However, this can be speeded up, if required, using the system's inbuilt defrost heaters. Using the defrost heaters, however, can result in large amounts of ice forming inside the cold room. Figure 3.8 shows the variation of the cold room temperature from switch-on to warm up over a four day period.

It was initially thought that preventing ice from forming on the optics, i.e. humidity control, during operation may be a problem. Care was taken when assembling the cold room to ensure that it was air tight. The liquid nitrogen boil off from the dewar is fed directly into the cold room, to maintain a low humidity inside the room once it is sealed. This slightly pressurises the room above atmospheric pressure, preventing ingress of moisture from the outside. With this arrangement, small amounts

[1]This is their proportional-integral-derivative (PID) controller, model number 2216, with more information available at `http://www.eurotherm.co.uk`

[2]The modelled supplied with the refrigeration system was XR370C, their web-page is `http://www.thermofrostcryo.co.uk/home/dixell.html`

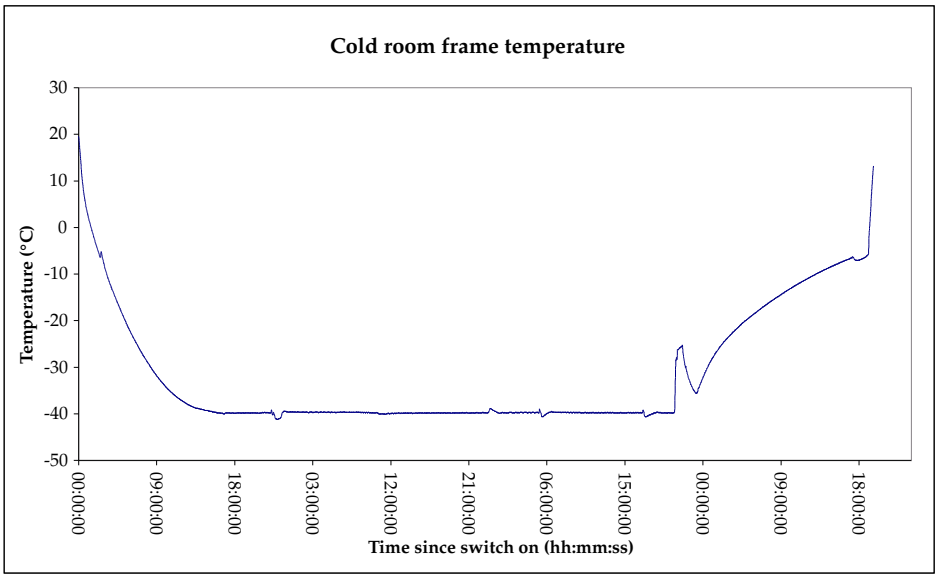

Figure 3.8: *Temperature stability of the cold room.* The temperature of the aluminium framework inside the cold room over four days of operation. The small glitches are a result of filling the dewar with liquid nitrogen. Heaters are used during a fill to stabilise the temperature, which is why the glitches are to both higher and lower temperatures. The rapid increase in temperature at the start of the warm up period is due to the defrost heaters, which were switched on to decrease the warm up time.

of ice form only on the coldest parts inside the room, which are the evaporator coils. The optics have been seen to remain clear for a two month period with the cold room kept permanently on. Small amounts of ice sometimes form elsewhere, however, when the refrigeration system does a periodic defrost cycle. To allow any ice that may have formed on the cooling elements to melt and drain away, the refrigerant flow is stopped for a few minutes each day and 100 W heaters, located next to the evaporator coils, are switched on. During this time the evaporator is at a higher temperature than other components inside the room, as a result ice occasionally forms on the optics. The ice quickly sublimes, however, once the defrost cycle finishes.

Operating CIRPASS in a cold room required the new cryogenic camera to operate with an ambient temperature of −40°C. Problems were encountered with the performance of the camera's O-rings as its external walls cooled, and this is discussed in Section 5.4.

3.5 Filter performance

New filters were designed and developed for CIRPASS by IR Engineering, thus it was important that the performance of the filters delivered was checked and to spec-

Filter	Wavelength range blocked (μm)	Background (e^-/pix/s) 15°C	-40°C
None	none		825.23
Camblock 1	>1.8	23	5.68
Camblock 2	1.4→1.8	1014	5.65
Camblock 3	1.6→1.8	622	4.84
Camblock 1 + 2	>1.4	2.6	0.15
Camblock 1 + 3	>1.6	3.5	0.16
Camblock 1 + metal plate	all	0.20	0.03

Table 3.2: *CIRPASS background measurements through various filter combinations at 15°C and at -40°C.* The values do not have the dark subtracted, which is 0.03 e^-/pix/s as determined from the camblock 1 + metal plate observation. The value for camblock 1 alone is with camblock 1 located in a filter wheel.

ification. After initial problems with the filter's protective coatings a set of camblock 1,2 and 3 filters were delivered and fitted in CIRPASS.

Extensive measurements of the backgrounds obtained with the new filters were carried out, with the cold room operating at various temperatures. A summary of the results is given in Table 3.2.

The background seen with just camblock 1 in the beam was higher than the expected 0.05 e^-/pix/s predicted by our model at -45°C and it was suspected that this filter may be faulty. As we do not have the facility to fully characterise a filter's optical depth from 1 to 2.5 μm (the detectors operating region), an indirect approach was taken in order to investigate the filter's response. A matt black metal plate was fitted to the front dewar window and background measurements taken as its temperature was varied. These results were combined with the background measurements taken through various combinations of camblock 1, 2 and 3, with the detector observing the cold room at different temperatures. The optical arrangement was again modelled with our blackbody spreadsheet, initially using the measured optical density profiles of the filters. These profiles were then adjusted to try to reproduce the background data seen and to determine the wavelength region where the majority of our background signal was originating.

The analysis and the measured filter transmission suggest that camblock 1 is the prime filter at fault. Camblock 1 does not begin to have significant optical density (OD) until 1.85 μm, whereas the filter was requested to start blocking from 1.80 μm. This has an impact when observing in long H, although both camblock 2 and 3 can be used to reduce this gap in blocking when observing in J or short H. Camblock 1 is also below specification across the whole wavelength range, its OD is around 4, whereas an OD of 5 was requested. The analysis also highlighted the importance

of camblock 1's blocking for large angles of incidence. Camblock 1 is located closer to the detector than the other filters, hence it must block light at a faster f-ratio than the other filters to ensure that the light doesn't reach the detector. The measured OD of camblock 1 given in Figure 3.4 is for light parallel to the filter's normal and it is suspected that the filter's blocking is much poorer for steeper angles of incidence.

Camblock 2 and 3 were performing close to specification, as can be seen by the significant drop in background radiation when either of these filters is in the light path. Their ODs are below specification at the shorter wavelength ranges, although they are slightly better than requested for the longer wavelengths (above 2 μm), making up, to some extent, for the poor performance of camblock 1 in this region. The significance of the thermal background at the long wavelength range of the spectrum (above 1.8 μm), can be seen in the background measurements with just camblock 2 or camblock 3 in the beam. The higher background observed, particularly at room temperature, with camblock 2 rather than camblock 3, is due to camblock 2's poorer blocking at the longer wavelength end of the spectrum.

The design of camblock 1 was checked and revised with IR engineering and we are awaiting a replacement filter. As a result, it was not possible to achieve our desired sensitivity in J with the cold room at ambient temperature. As an intermediate solution, however, the background performance can be recovered by observing with the cold room at -40°C for all wavelengths. As can be seen in Table 3.2, the J band performance at -40°C with camblock 1 and 2 is acceptable, although the background seen when observing in long H (with just camblock 1 in the beam) is about 50 times higher than was expected. Cooling to -70°C would be necessary to achieve the desired 0.05 e^-/pix/s, with just this filter. Thus, the backgrounds obtained with the current filters are not quite as good as hoped for, but are still low enough not to have a significant impact on the instrument's sensitivity. Figure 3.9 shows the background from the cold room through camblock 1 and 3 as a function of temperature.

3.6 Cold room versus vacuum chamber

The CIRPASS spectrograph is a large assembly, requiring a cooled enclosure with an approximate internal volume of 6 m^3. The cold room adopted was cost-efficient and readily available, when compared to a more traditional dewar design using a liquid nitrogen (LN_2) cooled vacuum chamber.

The temperature performance of the cold room was sufficient to achieve the thermal backgrounds required for CIRPASS. Current telescopes operate at $\sim$2°C. Little

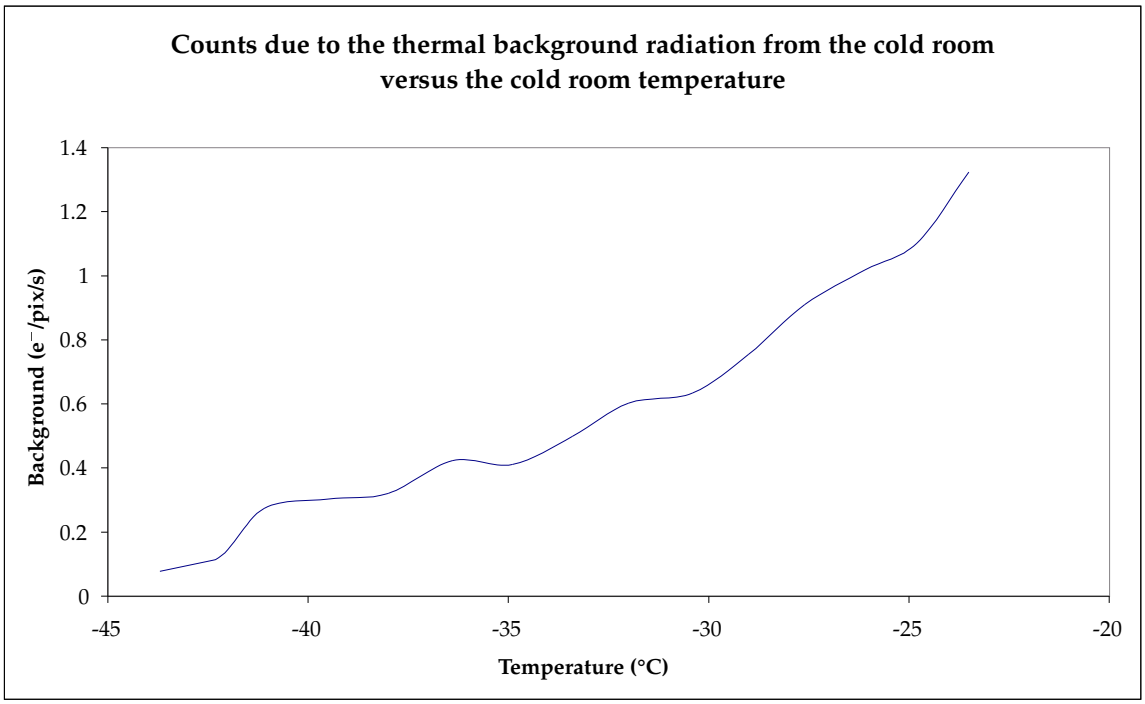

Figure 3.9: *Variation of the thermal background from the cold room with temperature, measured through filters camblock 1 and camblock 3.*

benefit would, therefore, be obtained from reducing the cold room temperature below ~ -70°C, as the thermal background from the telescope would become dominant. If desired, the current cold room could operate to -70°C by increasing the thickness of its walls and by using a two stage refrigeration process. This lower temperature would significantly reduce the thermal background from wavelengths above 1.8 μm, allowing K band operation. The ability to cool to cryogenic temperatures offered by a more conventional dewar is, therefore, not required.

The cold room offers a number of advantages over a dewar. The presence of the air and fan inside the room ensure that the internal temperature gradient is small, which is essential when trying to achieve a minimal thermal background. This would not be the case with a conventional dewar. The internal dewar walls would be close to ambient temperature and heat shielding would be required to keep the dewar internals cold. Also, coupling the optics to the cooling medium of the dewar would require a considerable redesign of the CIRPASS spectrograph's framework and mounts. The cold room intrinsically provides a light-tight and thermally dark environment. Again, the dewar internals would require careful light shielding to ensure that the optical elements could not see the warm dewar walls. Furthermore, a vacuum tight cold enclosure constructed from steel or aluminium would be considerably heavier than the current room, for the same size enclosure.

The cold room has a larger cooling power than a conventional LN_2 cooled dewar, and it is possible to cool the entire system in under 24 hours. The time required for a dewar the size of the CIRPASS cold room to reach equilibrium temperatures could be considerably longer.

An advantage of using a cold vacuum enclosure is that it would circumvent the vacuum problems experienced when the camera was operated at $-40°C$ (Section 5.4). The air-free environment would also avoid the potential problem of ice forming on the optical surfaces, although ice formation does not affect the performance of CIRPASS.

In general, any form of cold room enclosure would be too large and too heavy to be directly attached to a telescope. Their use is, therefore, restricted to instruments where they can be mounted on the telescope dome floor or Nasmyth platform.

The cold room solution adopted for CIRPASS has worked well, and certainly imposed fewer technical challenges than would have been experienced with a more conventional cold room design using a dewar. The DAZLE instrument (Parry et al., 2002), currently being built by the Institute of Astronomy Instrumentation Group, will also use a cold room similar to that designed for CIRPASS.

CHAPTER 4

SPECTROGRAPH AND HARDWARE SUPPRESSION CAPABILITY

4.1 Introduction

The CIRPASS dispersing optics are fed by a fibre slit, and reside on the telescope dome floor in a cooled enclosure (as discussed in Chapters 2 and 3). The optics follow a Schmidt design, with the light from the slit passing through a traditional collimator - grating - camera arrangement to produce a R$\sim$3100 spectrum on a mask surface. The spectra formed on the mask are then viewed with a cryogenic camera. The design of the dispersion optics is presented in Section 4.2.

The spectrograph contains a number of mechanisms that allow the optical system to be aligned remotely: the spectra can be focussed on the masks, or their position on the detector altered. Remote changes of the wavelength range observed are also possible. Both the mechanisms and the spectrograph support structure were required to operate reliably when cooled to -40°C. The mechanical design is discussed in Section 4.3 and the procedure for aligning the spectrograph optics is given in Section 4.4.

CIRPASS has the capability to remove, via the mask surface, the predominant sky background in the infrared region caused by OH emission lines. The spectral resolution at the detector is also high enough to allow observations between the OH lines. CIRPASS, therefore, employs both hardware and software OH suppression. The advantages of each technique and the optimal suppression scheme adopted for CIRPASS are discussed in Section 4.5.

4.2 Optical design

The CIRPASS spectrograph is essentially the COHSI spectrograph (Ennico, 1998) with the recombination optics removed, but the OH suppression capability main-

tained. The optical layout of the CIRPASS spectrograph is based around a Schmidt design, and is depicted in Figure 4.1. The fore-optics deliver light to the fibres at f/6.5 and the spectrograph is designed for an f/5.5 beam from the fibre slit, to account for focal ratio degradation (FRD). An off-axis Schmidt follows, in double-pass. The first pass acts as the collimator for the grating, and the second as a camera, forming a spectral image on the mask mirrors. The mirrors are curved to match the focal plane produced by the Schmidt camera.

The option for hardware suppression is provided by the mask mirrors. The mirrors have non-reflecting lines (0.5% reflectance) across them in the slit direction, at the wavelengths corresponding to the OH sky lines. These suppression lines have a top hat profile in the dispersion direction. The mirrors are, however, highly reflective (98%) at the positions corresponding to the gaps between the OH lines. CIRPASS was commissioned with entirely reflective masks, to measure the actual OH sky profile. The optimal OH rejection profile could then be used to make the masks (Section 4.5).

The simplicity of the collimator arrangement, from the fibre slit to the masks, keeps scattering to a minimum in this part of the system. This allows the mask to reject a very large fraction of the total OH light coming in from the sky.

Although a number of grating options are available, CIRPASS was commissioned with that providing the instrument's lowest spectral resolution, to allow faint observing. A reflection grating working in first order was used, which provides spectra on the mask at a resolution of R$\sim$3100 at 1.4 μm. This is high enough to allow observations between the OH lines or to suppress them in hardware. The beam diameter of 150 mm allowed a standard large grating, supplied by Thermo RGL, to be used; it has 400 l/mm and is blazed at 1.2 μm. The grating gives a spectral resolution of 4.4 Å at the detector over 2 pixels.

The f/5.5 spectrum at the mask is physically reduced to the size of the detector by a third pass through the Schmidt (which collimates the beam) and a cryogenic f/1.35 camera. The camera is described in Section 5.3.

Operation of the spectrograph optics in a cooled environment was not expected to cause any problems, although the optics may require re-alignment if set at room temperature, to operate at -40°C. The fibre slit was the largest unknown from a cooling point of view. COHSI, however, had a fibre slit cooled to liquid nitrogen temperatures and Lee et al. (2001) found that operating fibres at cryogenic temperatures had negligible impact on their performance.

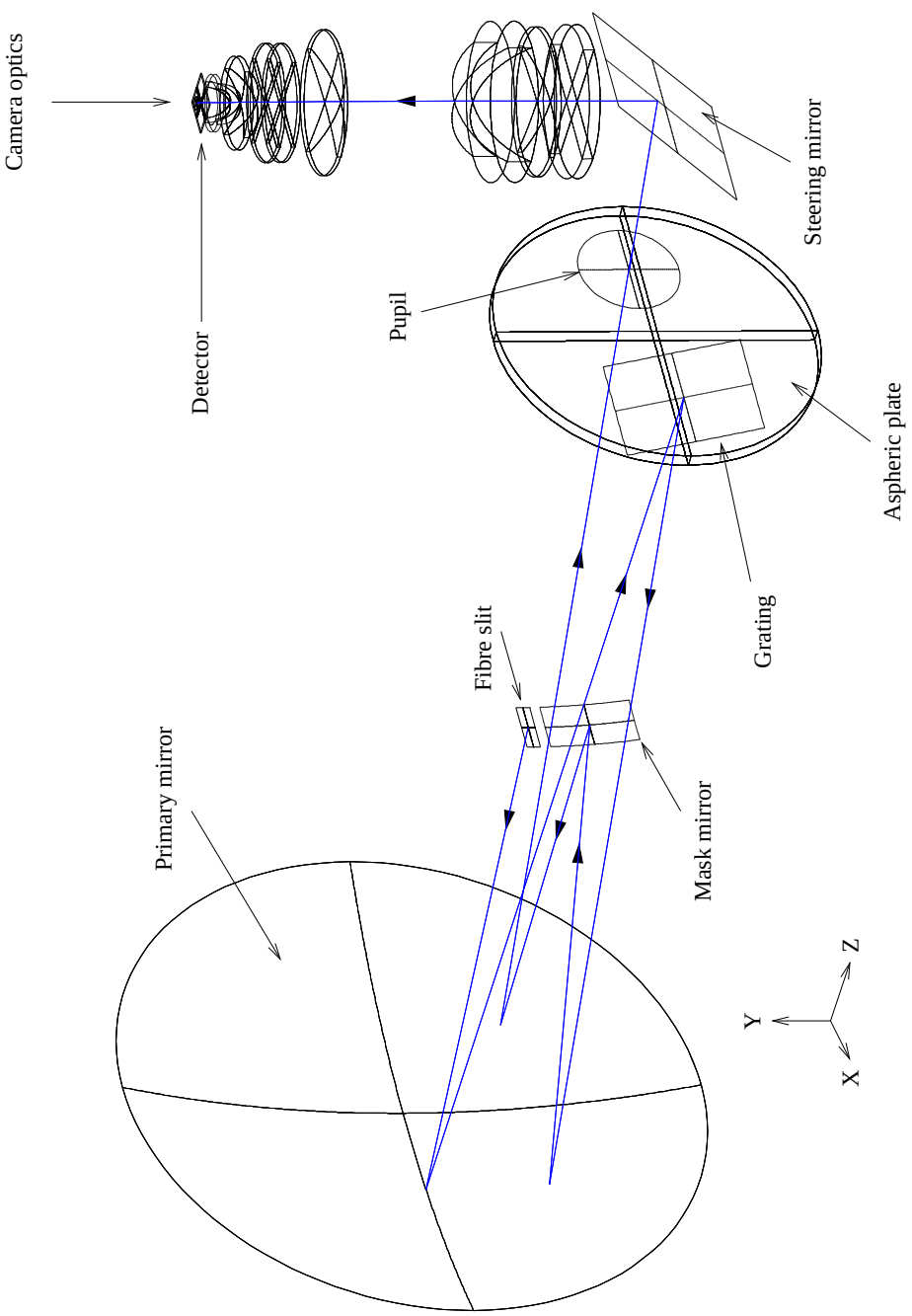

Figure 4.1: *The spectrograph and hardware suppression optical layout.* Only the J mask mirror is shown for simplicity. The H band mask mirror would be located above the fibre slit. The ray shown is for a wavelength of 1.2 μm.

4.3 Mechanical design

The spectrograph was built around a Kanya frame, as was the focal plane unit (FPU). The frame supports the cryogenic camera and all of the spectrograph optics, namely: the fibre slit and mask mirror assembly, the primary mirror, the aspheric, the grating and the steering mirror. Figure 4.2 gives a schematic overview of the mechanical layout of the spectrograph. A picture of the assembled optics, inside the cold room, is given in Figure 4.3.

The primary mirror was mounted on an aluminium shoe and secured in position with three foam padded brackets. Manual alignment was provided via five screws, terminated by pads that press against the mirror.

The fibre slit and mask mechanisms were mounted on a motorised translation stage (in z). The slit position and y position of the masks was fixed relative to the stage. The angle of each of the masks can be manually adjusted via a three point kinematic mount[1] (rotation about x and y).

Motorised mounts, that allow rotation about the x and y axes, were provided for the grating and steering mirror. Rotating the grating about x moves the spectra up and down (y) on the mask surface, to align the OH lines on the mask with those in the spectra. Rotating the mirror about x changes the wavelength range observed, as the viewing window at the mask surface is moved in y. Rotating the grating about y moves the spectra in the slit direction on the mask; the same motion with the steering mirror moves the viewing window in x. These two movements can be used as part of a dither observing sequence, to minimise the effects of imperfections on the mask surface and detector bad pixels on the quality of the output data.

The five motorised mechanisms (mask z, grating x and y, and steering mirror x and y) were required to operate inside the cold room and hence at -40°C. Stepping motors were purchased to meet this requirement (Section 7.3.2) and sufficient clearances (to accommodate differential contraction on cooling) were ensured in setting up the mechanisms to allow reliable operation when cold. Any greases used were specified to -40°C. No problems were experienced with the suppressor mechanisms at room temperature or at -40°C.

[1] Kinematic mounts are described in Section 5.2.3

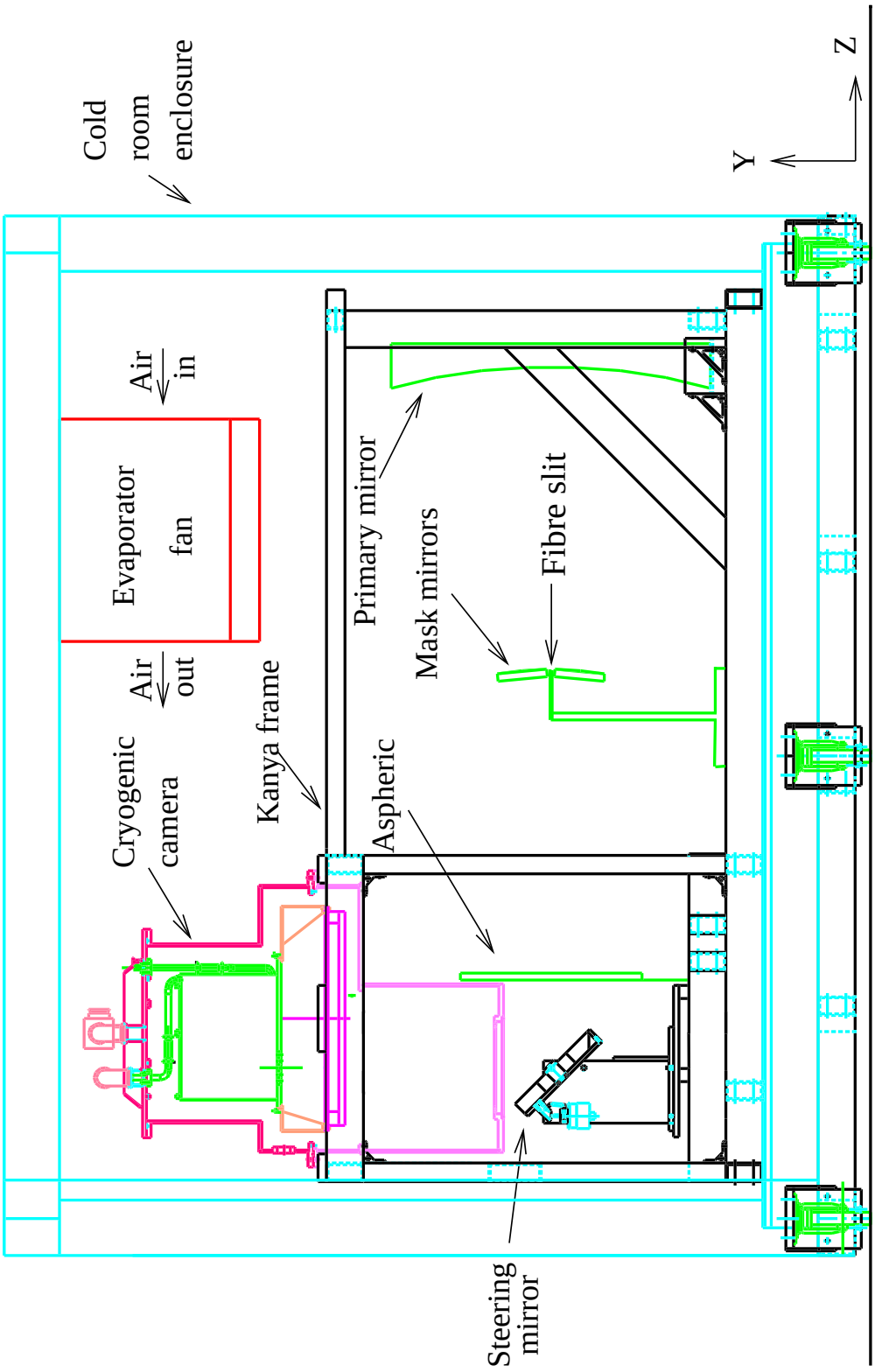

Figure 4.2: *Schematic drawing showing the layout of the spectrograph's optical and mechanical components.*

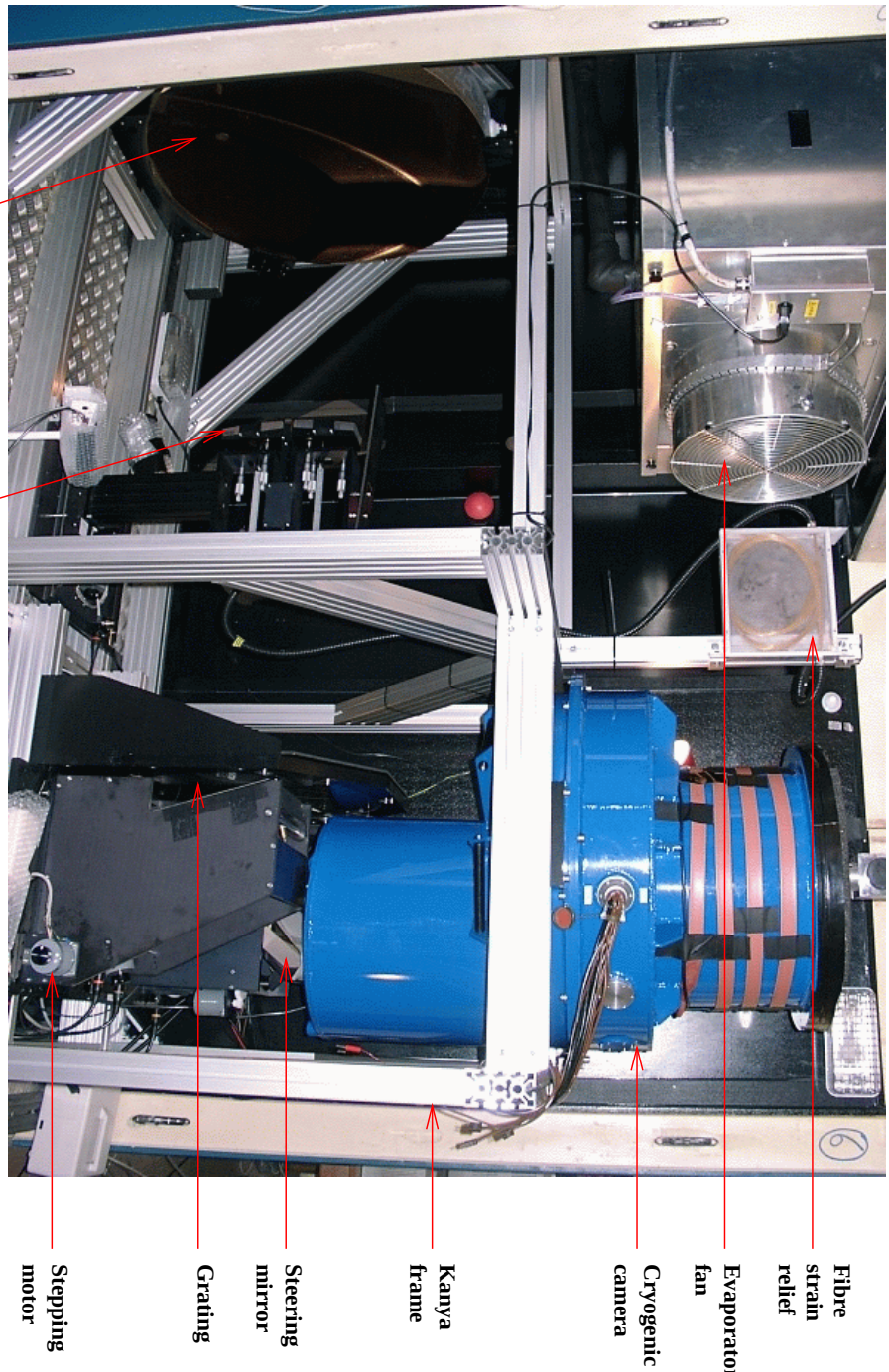

Figure 4.3: *Picture of the assembled dispersion optics inside the cold room.*

4.4 Assembly and alignment procedure

The first stage of assembly, once the Kanya frame had been constructed, was to add the cryogenic camera. The optical axis of the spectrograph was then defined by placing two posts at either end of the Kanya frame, centred width wise and with pins attached whose tips were at the desired height for the optical axis. The tips were then exactly illuminated with a laser, its beam defining the optical axis.

The primary mirror was then added and adjusted so its centre coincided with the laser beam. The mirror's centre was found using cotton thread attached across two diameters. The angle of the mirror was adjusted so that the reflected spot from the laser beam fell back on itself, ensuring that the mirror was aligned with the optical axis. The aspheric plate was added and aligned in a similar fashion. It was centred by measurement against the Kanya frame and its tilt adjusted to ensure that the laser beam was reflected back onto itself. A pupil plate was placed in front of the aspheric, with holes of the Schmidt pupil's diameter in front of the grating and steering mirror positions, to reduce the effects of scattered light on the system. (The size of the pupil is set by the f-ratio of the light from the fibres, and the distance from the fibres to the primary mirror.)

The slit unit was added next. Auto-collimation ensured that the beam was correctly launched into the spectrograph. A plane mirror was placed in the grating position and the IFU illuminated from its pupil position, hence illuminating the slit. The slit was then moved in the z direction until its image fell back on itself. The angle of the fibres in the slit (in the xz plane) was preset to ensure the light went through the centre of the pupil in front of the grating, with the slit in the auto-collimation position. The height of the slit was adjusting using shims to ensure this was also true in the xy plane.

The steering mirror and grating were then added in their nominal alignment positions. The mirror turn (rotation about the y axis) and tilt (rotation about the x axis) were adjusted until the fibre slit could be viewed centrally on the detector. The grating turn was then adjusted so that the fibre spectra fell centrally on the masks as seen on the detector.

It was then necessary to ensure that the camera was optimally focussed and that the detector was flat. The IFU was illuminated with monochromatic light with the detector viewing the un-dispersed image of the fibre slit. The detector's tilt was adjusted to focus the slit image across it. The slit image was then moved in the dispersion direction on the detector, by changing the steering mirror's tilt, and the

detector was adjusted to ensure that it was also flat in this direction.

Once it was certain the detector was flat, the position of the masks could be adjusted to align them with the fibre slit. The grating tilt was adjusted so that the (small) spectra from the monochromator were moved across the mask surfaces. The orientation of the masks was then adjusted to focus the spectra in the dispersion direction and the direction orthogonal to it for the entire mask surface.

The detector then required tilting to match the achromatic nature of the camera. The IFU pupil was illuminated with an arc lamp, and the detector's tilt adjusted so that the lines were in focus across the detector in the dispersion direction.

The arc lines were also used to ensure that the grating tilt was correct, i.e. that the J and H bands were correctly positioned on the masks. Finally the steering mirror tilt was moved so that the desired wavelength range was observed.

In order to perform OH suppression, it is essential that the spectra are focussed on the masks' surfaces, hence their location via auto-collimation. If plain mirrors are used instead of mask mirrors then this is no longer necessary and the mirrors can be moved in the z direction to focus the spectra on the detector (or the detector itself can be moved). Refocussing was necessary after cooling the spectrograph, and was usually achieved via the detector focus mechanism.

4.5 OH suppression techniques

The predominant background signal detected by CIRPASS originates from line emission from OH molecules in the upper atmosphere. Removing these emission lines at an early stage in the optical train of the instrument (hardware suppression), or by dispersing the light sufficiently to allow observations between them (software suppression or OH avoidance), can result in considerable gains in an instrument's sensitivity (Section 1.4).

Hardware suppression can be achieved using filters designed to block wavelength bands in which large amounts of OH flux are present. Alternatively, as in CIRPASS, if the input spectrum is dispersed onto a physical surface within the spectrograph, at a high enough resolution, the parts of the spectrum contaminated with OH lines can be removed or masked out by this surface. The spectrum can then be recombined, if necessary, to give the desired wavelength coverage at the detector.

Numerical simulations of both these hardware suppression techniques have been carried out by Herbst (1994). He concluded that the most significant sensitivity improvements can be achieved using the masking technique, dispersing the back-

ground to between R=2000-4000 resolution, and that this generally outperforms suppression devices using band pass filters. Martini & DePoy (2000) calculated the optimal resolution for software suppression and also concluded that, for a 2 pixel resolution, a dispersion of R=2000-4000 provides optimal OH rejection for a wide range of detector noise and source signals. Software suppression requires detectors that are large enough to allow acceptable wavelength coverage at the medium resolutions required for OH suppression, whereas for hardware suppression the dispersion can be reduced after the OH has been removed, allowing a larger wavelength range to be observed per exposure.

Software suppression has the advantage that the resolution of the spectrograph can easily be changed by using a different grating (assuming the resolution is still high enough to allow software suppression). A hardware suppression instrument, that does not recombine the light after the suppression optics, would require new suppression masks that matched the changed dispersion, complicating the procedure.

The performance advantage offered by hardware suppression over software suppression, depends on the amount of input light that is scattered within the spectrograph. In a software suppression instrument, a fraction of the total OH flux will be spread out over the entire detector, increasing the instrument's background and degrading its performance. In a hardware suppression instrument the OH flux is removed, limiting the amount scattered across the entire detector.

The amount of scattering was quantified for CIRPASS using continuum source observations of the 11 calibration fibres. The total signal in a background-subtracted calibration fibre frame was compared with the total signal in the detector regions where the calibration fibres are focussed. Measurements were taken at seven different intensity levels to minimise the effects of poor background subtraction and numerous darks were taken in-between frames to reduce any persistence signal (Section 6.3.4). It was found that 18$\pm$1% of the input light is scattered in CIRPASS. When observing between 1.4 and 1.6 μm, the total OH signal detected is 166,148 e^-/s, which equates to 0.03 e^-/pix/s due to scattered OH for a 1024^2 array, comparable with our dark current. The theoretical performance gain for CIRPASS with 0% scattered OH, rather than 18%, is presented in Section 9.6.1 and gives an improvement in limiting magnitude of J=0.2 and H=0.03.

Clearly, masking the OH lines would be beneficial for CIRPASS J band operation. The lower performance gain in H, although the H band OH emission is stronger, is due to the instrument's higher thermal background in H (Section 9.6.1). In order to

determine the optimal masking profile CIRPASS will be commissioned with entirely reflective masks, to allow measurement of the night sky spectrum. The CIRPASS masks will then be made using this data and may be different from those used for COHSI. Only the brightest lines and possibly even then, only the line cores will be masked out. This will allow some of the suppression to be carried out in software, preserving signals that may be recoverable from the fainter lines. Bright emission lines from O_2 and N_2 may also have sufficient intensities to warrant masking.

As well as reducing scattering, hardware suppression ensures that the OH lines do not saturate the detector, particularly when long observations are required for faint sources. This is advantageous as the HAWAII arrays suffer from a considerable amount of persistence (Section 6.3.4). Residual OH lines are present in darks, or other images, taken after an on-sky exposure. This presents a problem if the observing procedure is to move the image over the detector. This would typically be done to allow removal of bad pixels or cosmic ray hits during the data reduction process. Such a scheme could only be employed in a software suppression instrument if the image were shifted solely in the slit direction, and if the slit were perfectly straight, so that the positions of the OH lines remained fixed on the detector.

The cost of hardware suppression is the additional optics necessary to produce the spectrum at a mask plane, these additional optics reduce the throughput of the spectrograph. Furthermore the additional optics increase the size of the spectrograph, which is undesirable as for CIRPASS the entire spectrograph has to be cooled.

The optics that could be removed are illustrated in Figure 1.6. For the CIRPASS optical design shown in Figure 4.1, the OH suppression optics equate to two additional passes through the Schmidt system, after the first pass that delivers light to the grating. Hence, three, gold coated mirror surfaces and 4 air-glass SLAR coated surfaces could be removed. These surfaces have a measured total efficiency of 79%.

The optical design chosen to provide OH masking for CIRPASS incorporates a grating in a near-Littrow configuration, which minimises losses due to anamorphism and allows large grating angles (and high spectral resolutions). The masking layout also includes a white pupil, which made the design of a high throughput camera simple to achieve. As a result, it is difficult to conceive of a design using a conventional reflection grating that would be $1/0.79\times$ more efficient, as these designs would have to deal with anamorphism, groove shadowing and larger light beams.

4.6 Future suppression techniques

Hardware suppression using filters is generally limited by the width of the filter blocking profiles. It is difficult to manufacture filters that block a large number of very narrow wavelength regions, as would be requisite for an OH suppression filter. The DAZLE instrument (Parry et al., 2002) circumvents this by specifically targeting an individual gap between the OH lines for observations, and blocking the remainder of the J and H bands.

An OH tailored filter for use in the J band may be obtainable, owing to recent advances in filter technology. Offer & Bland-Hawthorn (1998) discuss the application of rugate filters to OH suppression instruments. Rugate filters consist of a thin film deposited on a transparent substrate. The refractive index of the film varies continually throughout the coating and the final filter is made up from a number of thin-film materials with different refractive indices. By tailoring the refractive index profile variation throughout the coating, it is possible to design filters with complex and varying transmittance curves. The rugate design theoretically allows filters with a small number of transmittance minima at any chosen wavelength and for any desired width. Such a filter could be exploited for OH suppression at wavelengths of less than 1.4 μm where the OH lines are grouped into distinct and non-overlapping bands, allowing considerable gains in signal-to-noise to be achieved for imaging or low resolution spectroscopy programs.

An exciting new hardware suppression filter may be obtainable with the materials used for spectral hole burning discussed in Section 1.3. The gaps between the OH sky lines could be burnt into the material before an evening's observing. It would then absorb the OH background light, but be transparent for the remainder of the spectrum.

CHAPTER 5

THE CIRPASS CRYOGENIC CAMERA: DESIGN, CONSTRUCTION AND PERFORMANCE

5.1 Introduction

CIRPASS takes advantage of state-of-the-art infrared detector array technology. The HAWAII 1K or 2K arrays, for which CIRPASS was designed, provide four and sixteen times more detector area respectively than the PICNIC devices used by COHSI. These larger arrays allow a wide wavelength coverage in a single exposure (the whole of the J or H band), at sufficient resolution to observe between the OH sky lines. As the high resolution spectrum can be imaged directly with these devices, the reformatting of the spectral resolution performed by the COHSI dewar and second fibre bundle was no longer necessary. The extra optics required to recombine the light and provide the lower resolution spectrum reduce system throughput. Hence they were removed and replaced with a new camera for CIRPASS.

As CIRPASS worked to a tight schedule for project completion the simplest design incorporating the most readily available optics was adopted. A chromatic camera was built using five lenses (of F2 and SFL57 glass) and is described in Section 5.3. The chromatic aberrations were corrected by tilting the detector in the dispersion direction. The tilt required depends on the spectral resolution (that is, the grating being used) and thus needs to be adjustable. This was achieved with a combined detector focusing and tilt mechanism and is discussed in Section 5.2.3.

To achieve the lowest possible signal backgrounds for all the wavelength ranges in which CIRPASS will operate, several different filter combinations are necessary. To keep the size of the dewar[1] acceptable, thirteen different filter combinations are pro-

[1]The dewar refers to the camera's outer casing and its vacuum and LN_2 mechanical components.

vided using two filter wheels, each accepting four different filters. The filter wheels are discussed in Section 5.2.2.

Paradoxically, operating the dewar in a cold room at -40°C placed additional constraints on its mechanical design, causing problems that are not present in dewars operated at room temperature. The mechanical aspect of the dewar is discussed in Section 5.2, and its operation in the cold room is discussed in Section 5.4.

5.2 Mechanical design and performance

5.2.1 Dewar

Figure 5.1 shows a schematic outline of the CIRPASS camera and Figure 5.2 is a photograph of the constructed dewar. The dewar height is 1024 mm and it contains four major internal assemblies: the liquid nitrogen (LN_2) can, the detector mount and focussing mechanism, the filter wheels and the camera optics. These components constitute the camera's cold assembly.

The dewar and all its major sub-assemblies were constructed entirely from aluminium, to avoid problems induced by differential contraction as they are cooled. Aluminium has a high thermal conductivity (120-190 W/(m.K), compared with 16-47 W/(m.K) for steel) and a density approximately $3/8$ that of steel. Hence it provides a good cooling path for the dewar optics and gives a lighter dewar than if steel had been used.

The dewar body was constructed from three cylindrical sections of different diameters. The top section houses the liquid nitrogen chamber and its associated plumbing. The larger middle section contains the detector assembly, focussing mechanism, filter wheels and some of the camera optics. All of the electrical feedthroughs are also made through this section. The final section houses the remaining camera optics. Each of the walls of the cylindrical sections was rolled from a single sheet and has a single welded seam. The cylindrical walls fit into grooves on flange plates that make up the horizontal sections and these joints were also welded. Ribs were welded to the body at the joints of the horizontal and vertical sections for added rigidity.

As depicted in Figure 5.1, the cold assembly inside the dewar is supported by G10 trusses at the top and stabilised by further G10 supports around the filter wheel. The filter wheel supports can flex (in the vertical direction only) to allow for differential contraction between the cold assembly and the dewar walls. The inner cold struc-

ture, including the optical tower, is hidden from the outer dewar walls by aluminium heat shields. To further reduce radiative heat losses, all internal surfaces of the dewar were covered with mylar sheeting and any remaining gaps were filled with mylar tape.

External access to the dewar internals was provided using O-ring sealed ports; the O-rings were specified to work at our cold room temperature of $-40°C$. The dewar casing splits into two halves at the middle cylindrical section, via an O-ring sealed flange. O-ring sealed ports were also provided for the detector electronics and the auxiliary electronics (including temperature sensors, filter wheel and detector focusing mechanism). 55 and 41 way electrical feed-throughs were used, conforming to the Mil-C-26482 specification, which includes reliable operation to $-55°C$.

The pipework connecting the liquid nitrogen can to the fill ports on the outside of the dewar was constructed from stainless steel. This has a much lower thermal conductivity than aluminium and thus reduces the heat load on the nitrogen can. Stainless steel bellows form part of this pipework to accommodate the different contraction rate of the stainless steel and aluminium, particularly during a LN_2 fill. All joints were welded except for the aluminium to steel joint at the nitrogen can, which was sealed using stycast. Stycast was chosen as it is a hard joint material that will bond aluminium and stainless steel, and will operate at cryogenic temperatures. Three pipes were provided to the can: two terminate at the top of the can and are used for filling and venting nitrogen, while one goes to the bottom of the can and is used for level sensing. The volume of the nitrogen can is 25 litres, sufficient to keep the camera cold for 30 hours when it is operated inside the cold room. However, about 30 litres of LN_2 are usually required to refill the can owing to LN_2 evaporation during a fill. The camera internals are held at a vacuum of $5x10^{-5}$ mbar and cooled to approximately 90 K by the LN_2.

Ease of assembly and disassembly, from both a mechanical and an electrical point of view, were essential criteria of the dewar design. A brief outline of the assembly procedure follows. The nitrogen can and its associated heat shields were the first components to be added to the dewar. The can was attached by trusses to the dewar top and the O-ring sealed LN_2 feed-throughs were then fastened. These are the only feed-throughs in which air pressure acts to force the joint apart; this design is unavoidable if the whole system is to be dismantled and reassembled as necessary. The nitrogen can's radiation shields were then added before the dewar top lid was attached to the top cylindrical section; the dewar was then inverted and the rest of the cold assembly built up from the cold surface of the LN_2 can. The detector assem-

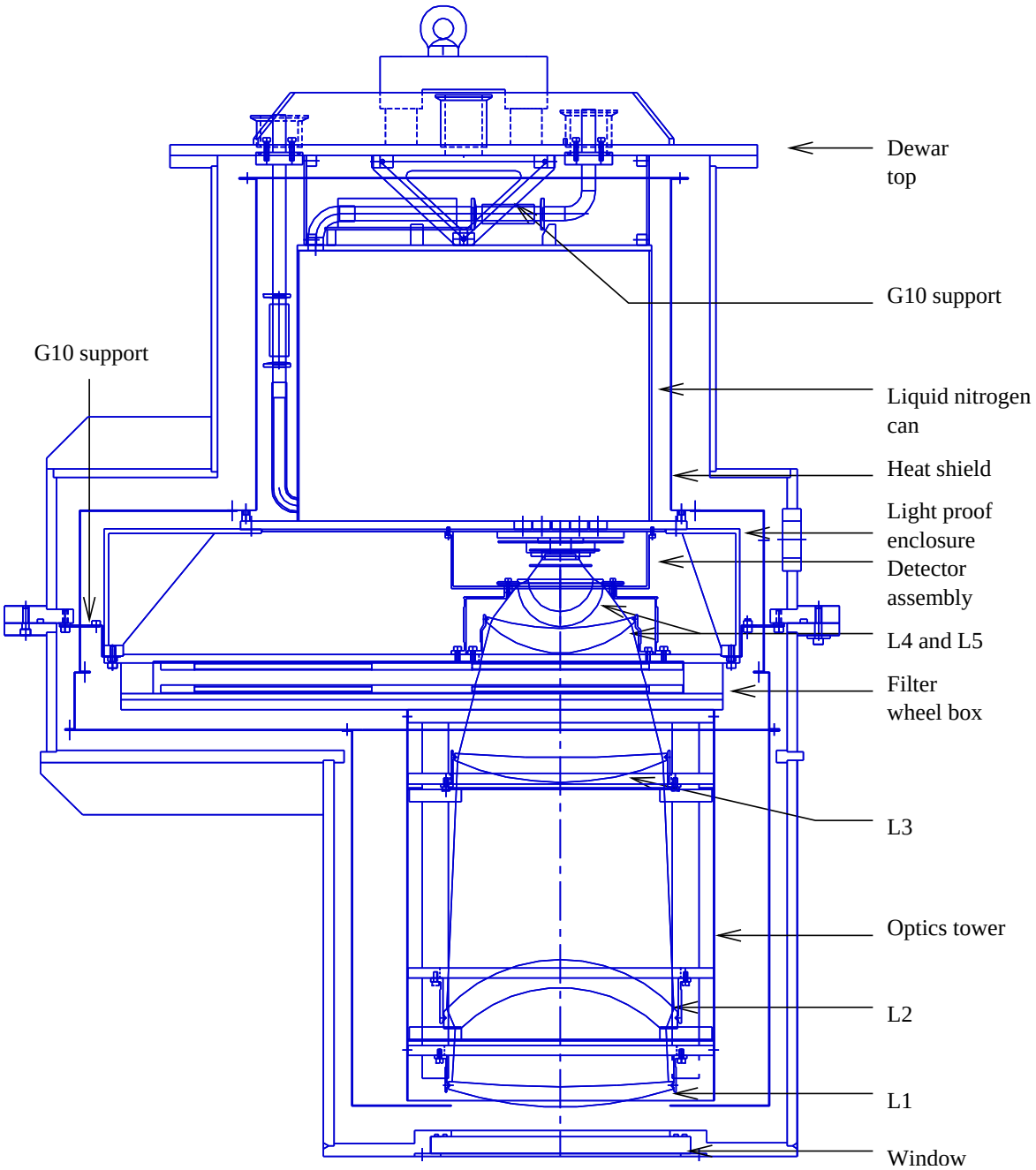

Figure 5.1: *Schematic outline of the CIRPASS camera.*

Figure 5.2: *Picture of the completed CIRPASS dewar.*

bly and focussing mechanism were then added. The filter wheel box and optics were assembled outside the dewar, with the optics aligned prior to addition (Section 5.3). The optics assembly was then lowered in and the remainder of the heat shielding added, before lowering on the final outer dewar walls.

5.2.2 Filter wheels

The CIRPASS camera contains two filter wheels in a single assembly, located two optical elements upstream of the detector. At this point the light beam is still quite wide, and not too fast to make the filter design impractical. Circular filters of diameter 170 mm were used. Several filters and masks were anticipated for CIRPASS to operate with acceptable backgrounds throughout J and H. Placing these in one wheel would have increased the size of the dewar considerably and would not allow filters to be used in combination with one another; hence two wheels were decided upon with four filter positions in each. A clear position was necessary in each wheel and a blank (non-transparent) in one, giving a total of thirteen different possible combinations. With this arrangement the filter wheels are the largest elements in the dewar and constrain its overall width.

The wheels are located on the same central axis and are separated with phosphor-bronze thrust washers. The axis is composed of a torlon cylinder mating with brass bushes on the wheels. The wheels are driven by cryogenic stepping motors from the outside edge. Each motor turns a small spur gear that mates with teeth cut into the perimeter of each wheel. The gear ratio is 48:1. In order to ascertain the position of the wheels as they are moved within the dewar, a feedback system was incorporated into the design. Three concentric grooves, whose depth was stepped with angular position, were milled into each wheel. The height of the grooves is read using micro-switches that report back to the instrument control software (Section 7.3.2). Figure 5.3 shows a picture of one of the filter wheels.

The filter wheels and their feedback system were found to operate reliably once the feedback micro-switches had been properly adjusted. The heights of the micro-switches above the grooves in the wheel were altered until each of the sectors was correctly identified, when the dewar was in its operational orientation. This was done by trial and error. A slight cross-talk exists between the two wheels, as the top wheel rests on the lower one. This cross-talk is only minimal as the wheels are held by the stepping motor's detent torque, limiting it to the backlash of the spur-teeth interface. Moving the lower wheel can cause the top wheel to move slightly, but not vice versa, so the lower wheel is always moved into position first. The wheels are

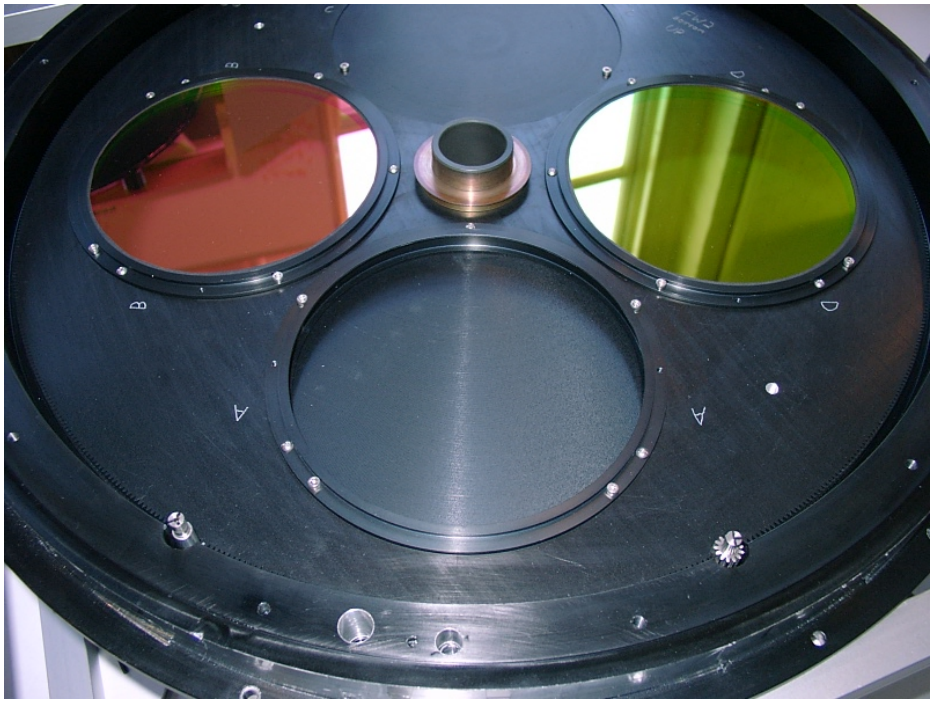

Figure 5.3: *Picture of a CIRPASS filter wheel. Camblock 2 and camblock 3 can be seen.*

always driven in the same direction to ensure repeatable positioning.

5.2.3 Focusing and tilt mechanism

The detector and its associated printed circuit board (PCB) sit on an aluminium base plate that has a cold finger in direct contact with the back of the detector. The detector is held against the cold finger by compression springs between a pressure plate and the top of the detector's radiation shield (the detector box). The detector box also houses the main blocking filter, but is otherwise impervious to light.

The detector box is mounted on an adjustable, three-point kinematic mount. Such a mount has precisely one constraint or actuator for each independent degree of freedom, so that motion in any one direction is only restricted by one mechanism. This type of mount offers stability, distortion-free mounting, and removable and repeatable re-positioning. The mount allows the detector to be moved along the optical axis for focussing and to be tilted with respect to the optical axis to accommodate the camera's change in focal length with wavelength. Cryogenic stepping motors are used to move the detector box.

The detector box sits on three lifting pins which mate with the conventional groove, centre and flat on the detector box, to form the kinematic mount. Lever

arms are used to translate the horizontal motion of a trunnion along a lead screw, as the stepping motor turns, into a vertical movement of the pin. The box is held in contact with the pins using fixed tension springs. Schematic representations of the assembly are given in Figures 5.4 and 5.5. Figures 5.6 and 5.7 are pictures of the completed assemblies.

Micro-switches are used to provide a fixed datum for the position of the detector assembly. Crude positioning is done by step counting from this reference, the image quality on the detector provides more accurate positional information.

The quality of the machining and alignment of the focus mechanism's components were critical for it to work well at LN_2 temperatures. The surfaces of the lifting pins were lapped and polished to achieve a highly smooth finish. Particular care was also taken to ensure that the lead screws were parallel to the direction of travel of the lifting arms, otherwise the mechanism would tighten as the box was raised. Each individual assembly was checked for operation at LN_2 temperatures by submerging it in LN_2 in the laboratory, and a number of iterations were required before the mechanism worked reliably in the dewar. As a result, it is likely that a simpler design will be used for the HAWAII 2K assembly, with fewer moving components. A wire design is currently favoured, in which the wire is wound around the motor shaft and attaches to either side of the detector assembly. The wire is supported by two cogs and suitable gearing employed. This technique has been used successfully by Hofmann et al. (2000).

The detector box can be driven into direct contact with the cold face of the LN_2 can. This configuration provides maximum cooling power for the detector. When the detector box is driven away from the cold face, it remains thermally coupled to the can by copper braids.

5.3 Optical design and alignment procedure

The CIRPASS camera optical design was carried out by Dr. Ian Parry and Dr. David King using Zemax[2]. Figure 5.8 shows a schematic of the optical arrangement. The camera has a very fast f-ratio (f/1.35) and consists of five lenses, L1 to L5, where L5 is the lens closest to the detector. Light enters the camera via the dewar window. The window and L1, L2 and L3 are made from F2 glass. L4 and L5 are SFL57 glass, the largest lens is 224 mm in diameter.

[2]Zemax is an optical design software package by Focus Software, detailed at `http://www.focus-software.com`.

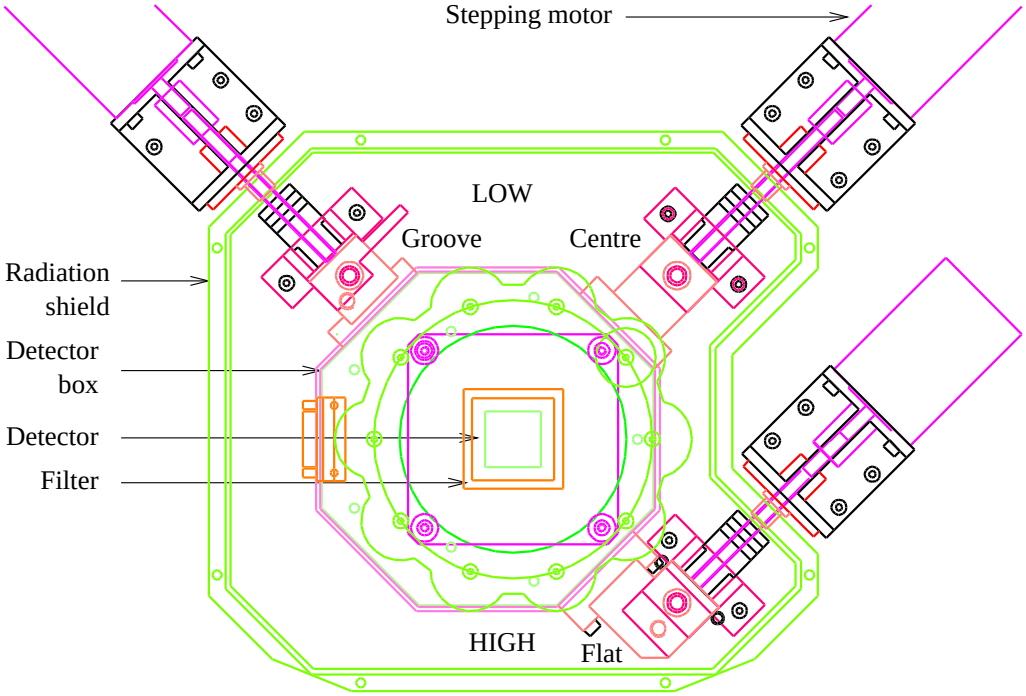

Figure 5.4: *Schematic view of the top of the detector assembly and focussing mechanism.*

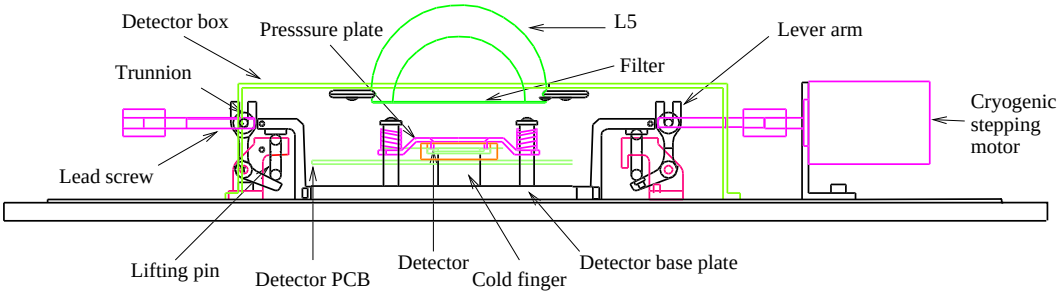

Figure 5.5: *Schematic view of the side of the detector assembly and focussing mechanism.* This view is inverted with respect to Figure 5.1.

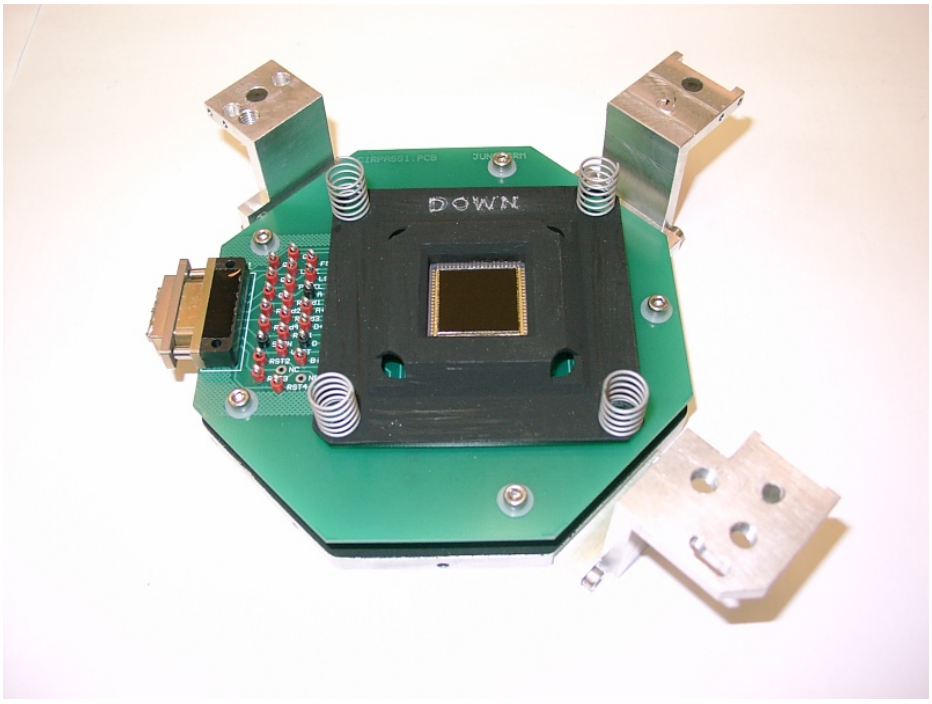

Figure 5.6: *The HAWAII 1K detector PCB and mount.*

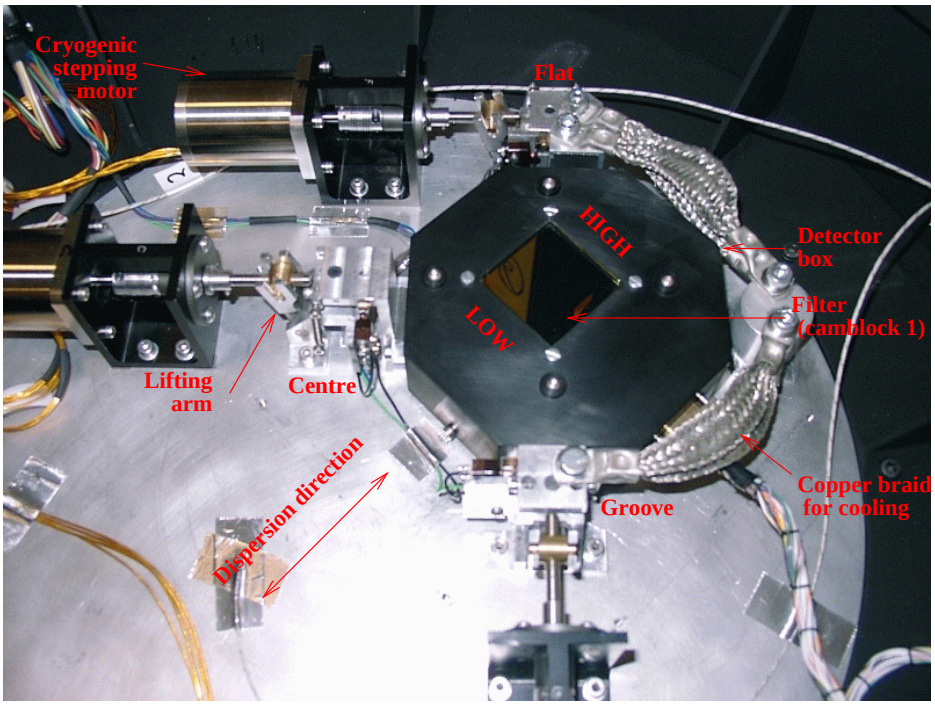

Figure 5.7: *The detector box fitted to the focussing and tilt mechanism.*

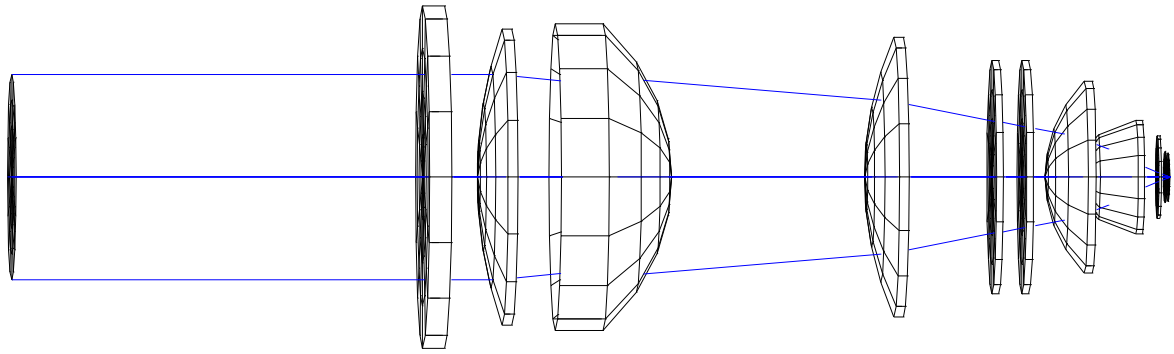

Figure 5.8: *Cryogenic camera optical layout.* Shown from left to right are: the camera pupil, the collimated beam, the dewar window, L1, L2, L3, the two filter wheels, L4, L5, the blocking filter, and the detector.

The camera has the possibility of including three filters before the detector, as already discussed:

- There is one filter permanently in the beam, close to the detector, through which all light that reaches the detector must pass. It is a blocking filter that blocks wavelengths longer than 1.8 μm (Section 3.2).
- Two more filters are available for operation at different wavelength ranges, via two filter wheels located between lenses 3 and 4 (Section 5.2.2).

All the lenses have spherical surfaces and are made from standard Schott glasses[3], resulting in a camera uncorrected for chromatic aberrations. The chromatic design was chosen as it is simple and allows the lenses to be made from readily available glasses, thus ensuring that the instrument could be developed in a short time. Barium fluoride or calcium fluoride could have been used to produce an achromatic camera. These glasses, however, are extremely expensive and are very fragile. The camera has a consequent change in focus with wavelength, but as it only ever operates in a spectrographic mode, focussed spectra can be obtained by tilting the detector in the dispersion direction.

The lens assembly can be split into two sections, both of which attach to the filter wheel box. Lenses L1, L2 and L3 are mounted on the underside of the filter wheel box (closest to filter wheel 1), using 4 aluminium support tubes. The lens mounts can be slid up and down these tubes in order to align the camera. Figure 5.9 shows a picture of the optics tower with L1, L2 and L3 attached to the aluminium support tubes. The last two lenses, L4 and L5, are mounted directly from the top side of the filter wheel box (closest to the detector), and are adjusted with shims.

[3]The lenses were purchased from Optical Surfaces Limited.

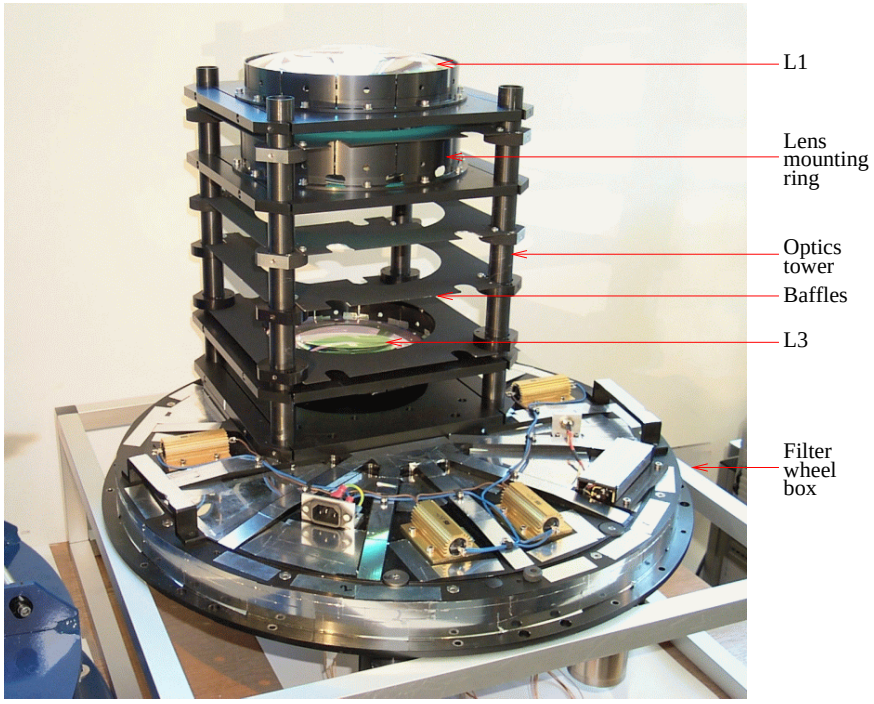

Figure 5.9: *Picture of the camera optics tower.* The mounting of L1, L2 and L3 on the filter wheel box can be seen. The filter wheel is inverted with respect to Figure 5.1.

Each of the five lenses is mounted in a slotted aluminium ring, so that when the lens and the mount are cooled, the ring can flex to accommodate the differential contraction of the two materials. This flexing should be concentric with the optical axis and should not introduce any de-centres or tilts. The mounts can be shimmed to correct for de-centring and tilting of the lenses during initial alignment.

The initial setting of the lens spacing was carried out via measurement and spacer tubes. The tubes were cut to the correct length to fit between L1, L2 and L3. Zemax was used to determine the lengths of the tubes at room temperature, so that once cooled to LN_2 temperatures the camera would be correctly focussed. This procedure worked well and the expected optical quality was achieved when the camera was cold (Section 9.3).

A brief outline of the alignment procedure follows:

- A vertical laser beam was set up to define the optical axis of the camera. The laser was mounted on a support frame above an optical table. The beam was directed downwards towards the table by a 45° flat mirror. Another flat mirror was placed on the optical table below this. The 45° flat was adjusted so that the laser beam reflected onto itself. A perforated target was installed just below the folding flat.

- The flat mirror was removed from the optical table and the filter wheel assembly clamped onto its handling frame below the 45° flat, with the L4 and L5 mount uppermost. The filter wheel was positioned so that the laser beam was passing approximately centrally through the open apertures in the filter wheels.

- The method of alignment involved defining the optical axis of the camera as being the optical axis of the most steeply curved lens, setting the laser through this axis and bringing all other lenses to this axis.

- Lens 5 was the first lens to be mounted onto the filter wheel assembly. The holes through its mount are over-sized by about 1 mm and its mount was adjusted (relative to the filter wheel) so that there was equal freedom around each fixing bolt. This allowed the lens to be centred over the aperture through the filter wheel assembly before being fastened in place.

- The complete filter wheel assembly, on its mounting frame, was then adjusted so that the back reflections of the laser beam from L5's surface and the interference fringes were centred on the laser beam (as witnessed on the perforated target). This assumes that L5's mount correctly aligns its optical axis with that of the filter wheel. This was checked by rotating the entire filter wheel to ensure that the back reflection from L5 did not precess about the optical axis. Once the back reflections were centred on the laser, the filter wheel assembly handling frame was clamped to the bench. The optical axis of the system was then defined by the laser beam and further optical elements were brought into alignment with it.

- L5 and its mount were then removed, and L4 on its mount installed, centred onto the laser beam, and tightened down. L5 was then replaced, centred and tightened down. This was necessary as L4's mount fits between L5's mount and the filter wheel assembly.

- The filter wheel assembly needed to be reversed to install lenses L1, L2 and L3. The handling frame was rotated and adjusted so that the back reflections from L4 and L5 were centred, before everything was again clamped down. The optics tower was then installed onto the filter wheel and the lenses L1, L2 and L3 added. The spacing between the lenses was defined by the pre-made spacing rods, which were placed between the lens mounting plates. L3 was installed and centred, followed by L2 and then L1.

5.4 Operating the dewar in the cold room

The performance of the dewar in a room temperature environment was as expected. A typical vacuum of 5x10^{-6} mbar was achieved and the detector reached a stable temperature of 90 K. The cool down time was approximately 12 hours and the warm up time was about 24 hours. The achieved temperature stability was better than 0.5 K over 10 hours. Some problems were encountered, however, when the dewar was operated in the cold room at −40°C.

As the temperature of the cold room dropped, the vacuum began to degrade and fluctuate. The first time the dewar was refilled with LN_2, with the cold room operating at about −40°C, the vacuum rapidly degraded to about 5x10^{0} mbar whilst the fill was in progress and did not recover until the cold room was switched off. The specification of the O-rings used was checked. Although we had asked for O-rings specified to −40°C (Buna-N or medium nitrile), contacting the manufacturer revealed that high nitrile O-rings, only rated to −30°C, had been provided. The most rapidly available replacement O-rings from the same supplier were silicone O-rings specified to −60°C, with which all of the dewar O-rings were replaced.

The room temperature vacuum performance with the new O-rings was slightly worse at 1x10^{-5} mbar, as silicone O-rings are generally used for hydraulic, rather than vacuum, seals. (The permeation constant against N_2 for silicone is 13 times that of nitrile, Singh & Thomas III (1998).) With the dewar under vacuum in the cold room, but not containing any LN_2, the vacuum was monitored as the room's temperature dropped. The vacuum degraded to 4x10^{-5} mbar with the cold room at −40°C and remained fixed at this value. The dewar was then filled with LN_2 and maintained a vacuum of 4x10^{-5} mbar throughout four LN_2 refills. However, on the fifth fill the vacuum deteriorated quite markedly, accompanied by a decrease in temperature of the dewar body and a build-up of ice on the dewar window. On inspection of the temperature logs, it became apparent that the vacuum had started to degrade once the dewar walls reached −42°C and that this had already happened once before on the night before the fifth fill. Subsequent LN_2 fills caused the vacuum to degrade still further and it became necessary to switch off the cold room completely to allow the vacuum to recover.

The vacuum deterioration seemed to correlate well with the temperature of the dewar top reaching −42°C. Once this happened the loss of vacuum caused the dewar top to cool more rapidly, exacerbating the problem. Brief excursions were made into the cold room with our helium leak detecting system. Leaks were found at the LN_2

feed-throughs on the dewar top, which rapidly went away as the dewar warmed up. The feed-throughs were the expected cause of the problem, given the prior evidence and the fact that they are our only joints that atmospheric pressure forces apart. Thus their design was reconsidered. The silicone O-rings, rated to −60°C, were kept at the LN_2 feed-throughs; while Belleville spring washers were added to the screws clamping the LN_2 feed-throughs to increase stability at this joint. Two 100 W heater resistors were placed on the dewar top, close to the LN_2 feed-throughs, and extra insulation added to the top of the dewar. Finally, all the other O-rings were changed back to nitrile, rated to −40°C, as nitrile O-rings have better vacuum performance. A supplier (Barnwell Services Ltd.) has since been found offering low nitrile O-rings with a minimum temperature of −60°C. It is hoped to replace the current nitrile O-rings with these the next time the dewar is available for modification.

With the new configuration and the cold room at a steady −40°C, a stable vacuum of $1x10^{-5}$ mbar was achieved. This vacuum would still start to degrade during a LN_2 fill, so the heater resistors were used to counter this. A PID controller was used to maintain the dewar top at −30°C during a LN_2 fill. With this addition, only occasional glitches in the vacuum are now seen and these recover quickly. Using this arrangement, the cold room has been operated continuously for two months at −40°C with the dewar also kept cold at LN_2 temperatures, for two months. The LN_2 hold time, with the dewar in the cold room, is in excess of 30 hours. LN_2 fills are usually performed at 9 am to minimise any adverse effects on the system stability when observing at night. The detector temperature achieved is 86 K, again with a stability of better than 0.5 K over 10 hours.

Given the above experience with the LN_2 feed-through seals, it is unlikely that plastic O-rings would be used in a future design of this feed-through joint. The joint experiences large temperature changes when the dewar is refilled with LN_2, and the O-rings are likely to experience temperatures of −80 to −100°C. These temperature are well beyond the operating temperatures of commercially available O-ring materials. The use of a metal seal would be the most likely replacement, either of CF Flange type or elastic metallic O-rings.

Finally, a fan was added to continuously blow air across the dewar window. The window can potentially be colder than the refrigerator's cooling element, as one side of it sees the nitrogen can. Ice slowly builds up on the cooler elements inside the cold room. The fan maintains the dewar window at the air temperature of the cold room, preventing ice from forming on it.

CHAPTER 6

DETECTORS

6.1 Introduction

CIRPASS exploits the latest available infrared detector array technology, using HAWAII 1K detectors manufactured by Rockwell Scientific (Kozlowski et al., 2000). These contain 1024x1024 infrared detecting elements, or pixels, and are sensitive to light in the range 0.85 to 2.5 μm. They typically have a quantum efficiency of about 60% in both the J and H wavelength bands, dark currents of order 0.03 e^-/pix/s and a readnoise of 10 e^-/read. The performance of the detector has a major impact on the performance of the instrument as a whole. For this reason its characteristics have been studied in detail and will be presented in this chapter.

CIRPASS is in the fortunate position of having early access to one of the latest HAWAII 2K Science grade detector arrays. These detectors are essentially equivalent to the 1K devices except that they have four times as many pixels. CIRPASS has been manufactured with the intention of using a 2K detector. However, until the performance of these detectors has been fully quantified, CIRPASS will continue to use a 1K detector. With the 1K, the wavelength coverage of the system in one exposure is half that intended, owing to the lower number of pixels in the dispersion direction. A review of the 1K and 2K arrays is given by Hodapp (2000).

The HAWAII detector is a hybrid device: it consists of a light sensitive layer, made from mercury cadmium telluride, electrically bonded on top of the read out integrated circuit (ROIC) or multiplexer. This allows electronic access to individual pixels within the detector array. Each pixel can also be followed as it integrates, without disruption of the detection process, unlike a CCD. Thus, the detector can be operated in a non destructive read (NDR) mode, which has advantages for data processing and is discussed further in Chapter 8.

The detector is driven by an Astrocam 4100 controller. This is a CCD controller which connects to a windows PC running PixCel software. The infrared detector is

made to appear as a CCD to the controller, using an in-house built interface board. More detailed information is presented in Section 7.5.1. The operation of the detector is presented in Section 6.2 and its performance is given in Section 6.3.

6.2 HAWAII detector operation

In its most reduced form, the HAWAII detector is simply a collection of capacitors that lose charge when photons are incident upon them. The detector material used in the HAWAII array is mercury cadmium telluride; this light-sensitive layer is bonded to the readout electronics or 'multiplexer' beneath it by indium columns. Each unit cell, or pixel, of the detector consists of the light-sensitive component and three other transistors. One of these buffers the output voltage from the 'capacitor' and another gates it to the detector output terminal. The third is used as a switch and allows an input voltage, VRESET, to be applied to the capacitor to provide the initial charge. VRESET can be adjusted externally. The multiplexer also contains a number of gates and registers which allow each of the pixels to be addressed individually. Figure 6.1 gives a schematic outline of the detector's electronic arrangement.

The output from the unit cell is buffered by another transistor, before being presented to the external detector readout electronics. The bias level of this output amplifier, provided by a further transistor on the substrate, can also be adjusted externally.

CIRPASS uses a CCD controller to drive and read out the detector. An electronic interface is used to make the HAWAII detector compatible with the controller. A custom built interface box is used and takes advantage of the correlated double sampling available with a CCD controller. The interface box turns the timing waveforms from the controller into those expected by the detector. It also provides the detector's power supplies, tunable voltage levels and two reference voltages.

The two reference voltages are used as comparison levels for the detector output, to reduce the noise on the final output signal. The CCD controller switches between one of these, REF, and the actual output from the device, on the pixel clocking time scale. The signal from the detector is the difference of these two voltages. In practice, this difference is obtained by integrating on each signal for a fixed amount of time (the clocking time), before passing the output signal to a fast analogue-to-digital converter (ADC). This method smoothes out high-frequency noise and limits the effects of $1/f$ noise for frequencies lower than the overall signal-processing time.

The other reference voltage, the Dummy Output Source (DOS), provides the base

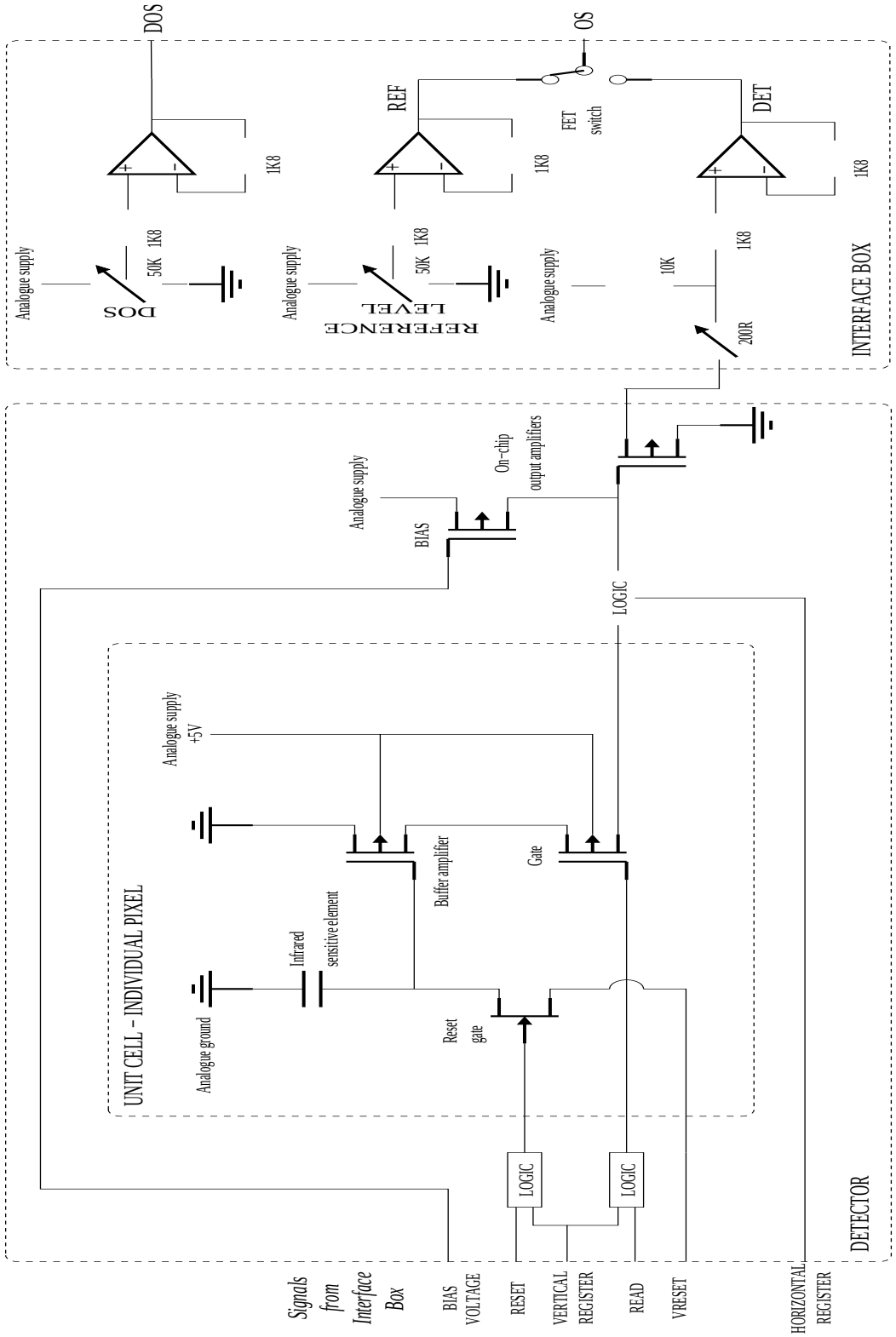

Figure 6.1: *HAWAII detector unit cell and readout circuitry schematic.*

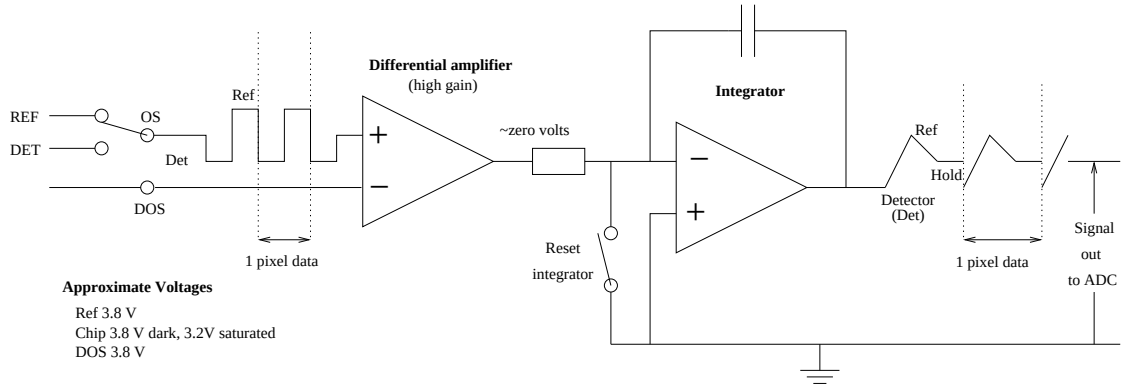

Figure 6.2: *Schematic layout of the CCD controller used to drive the IR arrays.*

level against which the detector output voltage is compared. This removes problems associated with drifts in any of the DC supply levels and further reduces the effect of noise spikes on the output from the detector. A schematic diagram of the controller electronics is given in Figure 6.2. OS (Output Source) and DOS are the signals generated inside the interface box and presented to the CCD controller. The interface box performs the switching between REF and DET (the buffered detector output voltage) to generate OS.

There are three voltages provided by the interface box that affect the performance of the detector: VRESET, BIAS and REF. VRESET is the initial voltage applied to a pixel at the start of an integration and affects the overall integration capacity (the well depth). The higher VRESET, the more charge initially applied and the greater the integration capacity. However, if VRESET is too large the device will not integrate linearly as the first few photons arrive. Increasing BIAS improves the linearity of the device but reduces the overall readout range (that is, reduces the effective well depth). REF determines the blacklevel, or 'no light' level, of the pixels. It is used to slightly offset all the pixels positive, as the ADC in the controller can only convert positive voltages. (CIRPASS currently has a 14 bit ADC in the controller.) These voltages were optimised for the 1K array and those used are given at the end of this chapter (Section 6.5). CIRPASS has a low photon arrival rate, thus well depth is not a limitation. For this reason, the voltages chosen ensure that the detector always integrates linearly, sacrificing some of the available integration capacity.

6.2.1 Typical readout procedure

When the detector is first switched on, the software automatically performs a 'Hardware Initialise' routine. This causes the controller to read out a few rows of data

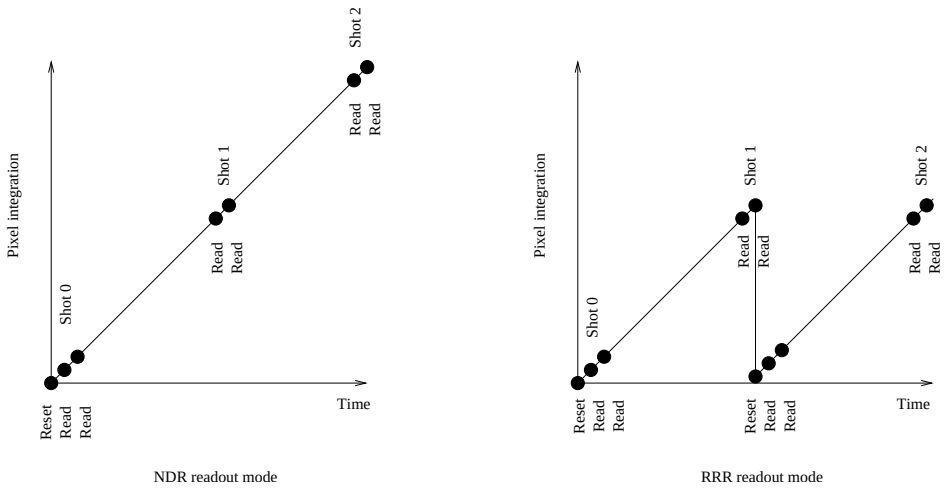

Figure 6.3: *Illustration of NDR versus RRR readout modes.* Both graphs are for a 2 shot, 2 reads per shot configuration. In NDR mode the detector is allowed to integrate for the total exposure time and successive shots do not affect the charge accumulated on the detector. In RRR mode the detector is read out before and after a reset, for every shot.

from the detector, which it then uses to adjust its internal voltage levels. This is to optimise the double correlated sampling (DCS) readout method and to set the device zero level appropriately.

There is then the choice of two readout modes: non destructive read (NDR) and read reset read (RRR). Both modes are characterised by the number of shots, the number of reads and the exposure time. The number of shots specifies the number of times the pixels are sampled in the total exposure time. The number of reads specifies how many times the pixels are read out at each shot. There is no time delay between successive reads, but there is a time delay between successive shots.

In NDR mode the pixels are sampled, or read, as they integrate without affecting their integration. The detector is reset using a process called pre-flushing (discussed in Section 6.3.2). The first shot follows and consists of a series of reads. The detector is then allowed to integrate before the next shot, of the specified number of reads, occurs. This continues for the total number of shots and the detector continues to integrate for the total exposure time. CIRPASS typically uses NDR mode.

The RRR mode creates data similar to that obtained from a CCD, whereby each time the pixels are read they are reset and then read again, starting another integration. The number of shots specifies the number of separate integrations required in the total exposure time. If more than one read is specified, the detector is read out that number of times before and after each reset. The two modes are illustrated in Figure 6.3.

Thus, for CIRPASS, an exposure consists of a series of shots, with a fraction of the total exposure time between each shot. In turn, each shot consists of a number of reads with no delay between them. The shot index is 0 based so a 10 Shot, 2 Read, 100 second exposure would mean reading out the array 22 times (11 total shots x 2 reads), with 10 seconds between each shot. The detector readout procedure adopted for CIRPASS is discussed in more detail in Section 8.4.

6.3 HAWAII 1K detector performance

CIRPASS was developed and tested using a HAWAII 1K device, which was the best available detector at the time of development. Its characteristics and behaviour are presented here. A better quality 1K detector recently became available and will be used for the forthcoming run on Gemini South. The replacement detector is expected to have a significantly higher quantum efficiency and fewer defective pixels.

6.3.1 Reset anomaly

The output signal from the HAWAII array shows some transient behaviour the first time it is read out after a reset. It appears that the system takes about a second to settle down after the reset has been performed. The effect is illustrated in Figure 6.4. For this figure, a small section of the array was read out 99 times in under 2 seconds, the detector then integrated (in a dark environment) for 60 seconds, and was then read out rapidly again. Hence, this was a 1 shot 99 read observation. The x axis of Figure 6.4 is read number and not time, and the jump at read 100 is due to the 60 second integration between reads 99 and 100. Thus, it can be seen that for the first shot (reads 1 to 99) the detector exponentially approaches its true value, whereas for the second shot (reads 100 to 198) the output is approximately constant. Subsequent shots also give a constant signal.

This behaviour is also seen when the device is operated in RRR mode, where the read after each reset has a large amount of structure across pixels. The structure is evidence of the system taking time to settle after a reset. The effect is minimised in RRR mode by pre-reading the device after the reset, but not actually storing the data. This, however, takes time and can be a problem for instruments observing bright sources. The time for the reset level to stabilise appears to be fixed. Thus, reading the array more slowly (at a lower pixel rate), means that less reads of the device are required before consistent results are obtained. The behaviour is thought

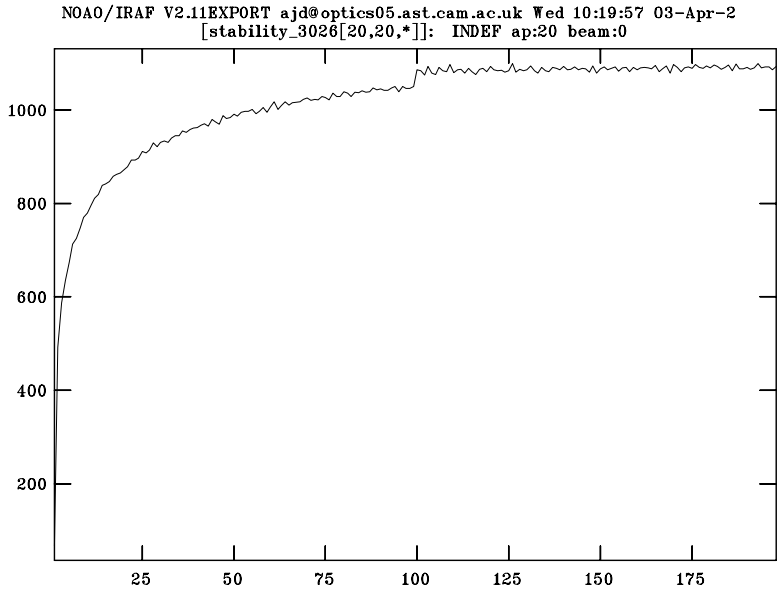

Figure 6.4: *Graph depicting the initial readout transient behaviour.* The x axis is successive readouts of the detector, with no time delay between readouts. There is a 60 second gap between reads 99 and 100. The y axis is counts (DN) measured from the detector, using a gain of 3.1 e^-/DN. The transient behaviour can be seen in the first 99 readouts with the detector exponentially approaching its true value, in contrast to the last 99 reads which give an approximately constant signal.

to be caused by trapped charge in the unit cell that is only removed by reading the device (Mackay, private communication).

In the normal NDR readout mode used by CIRPASS, where the entire detector is read out, the reset anomaly is only present in the first read of the first shot of the device; the device settles in the time it takes to read the detector once. Figure 6.5 shows a histogram of the image obtained by subtracting read 2 from read 1 in a dark exposure; these reads were contiguous. By contrast Figure 6.6 shows the histogram obtained by subtracting the last two consecutive reads of the detector. The average signal in the subtraction of the first two reads (from the first shot) is 8 times that in subsequent adjacent read (from the same shot) subtractions.

Thus, to avoid the transients the very first time the detector is read out, it is usually operated in a two-read mode. Each time information is required from the array (a shot), two successive reads are taken and only the second is used. Other groups, such as Finger et al. (2000), also report a similar reset anomaly, whereby the detector is nonlinear after a reset.

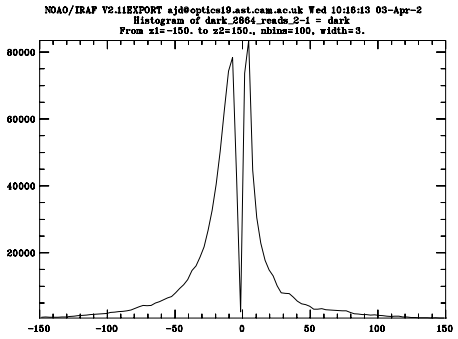

Figure 6.5: *Initial readout transient behaviour.* Histogram of the image obtained by subtracting the 1$^{\mathrm{st}}$ read of the detector from the 2$^{\mathrm{nd}}$, with no time delay between reads.

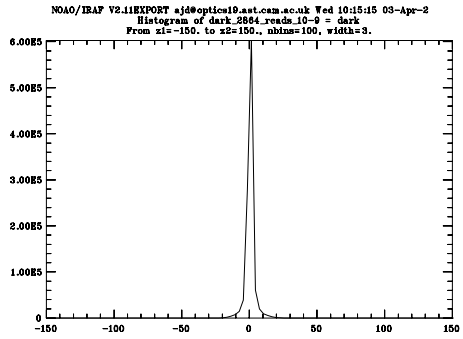

Figure 6.6: *Initial readout transient behaviour.* Histogram of the image obtained by subtracting the 9$^{\mathrm{th}}$ read or the detector from the 10$^{\mathrm{th}}$.

6.3.2 Reset level

At the start of an integration, it is necessary to apply a reset voltage to each pixel. The multiplexer allows an entire row of pixels to be addressed at once; thus, each row is reset in turn and the rows are rapidly clocked through. Given that each pixel has a finite capacitance and that a reset sequence can be completed in a few milli-seconds, considerable current demands are placed on the reset line. Hence, all the rows may not be reset to the same voltage, resulting in a fixed pattern in the reset (or bias) image. To minimise this, the reset sequence is performed more than once. A process called pre-flushing, where each pre-flush is actually a reset. Figure 6.7 shows the initial output signal from an individual pixel as a function of the number of resets. It is apparent that the pixel and its associated readout electronics do not reset to the true reset level unless more than 12 pre-flushes are performed (CIRPASS usually operates with 16 pre-flushes). It is also evident from Figure 6.7 that the shape of the pixel integration over time remains unaffected by the number of pre-flushes. Thus, pre-flushing the detector does not cause the reset anomaly described in Section 6.3.1.

6.3.3 Dark current

The expected photon arrival rate for CIRPASS is less than 1 photon/s. The detector dark current should be much less than this for the majority of the detector, in order to obtain an acceptable signal-to-noise ratio. The dark current was measured with the detector in the CIRPASS dewar, which was maintained at liquid nitrogen tempera-

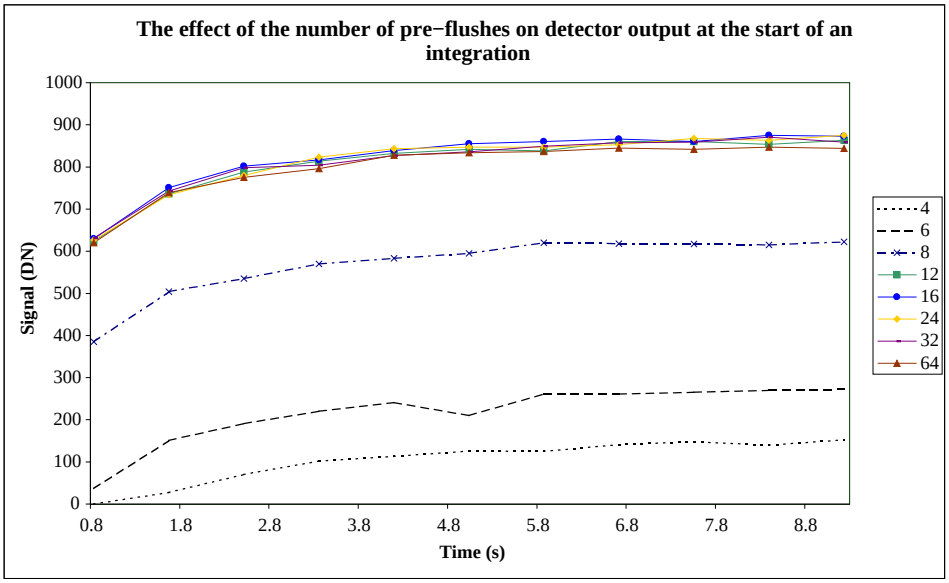

Figure 6.7: *Detector output level as a function of the number of resets.*

tures and was itself in the −40°C coldroom. The measured detector temperature was 86 K. The metal plate, located in one of the filter wheels, was used to prevent light from reaching the detector. Figure 6.8 shows a histogram of the dark current for each pixel obtained with this arrangement. The average dark current is 0.025 e^-/pix/s, 18% of pixels have a dark current in excess of 0.04 e^-/pix/s and 0.4% of pixels have a dark current in excess of 1 e^-/pix/s.

Preliminary measurements of the dark current were made with the HAWAII 1K detector in a small test dewar. These measurements revealed that the detector temperature must be kept constant to <0.1 K for reliable operation of the device. Initially, to make the detector as cold as possible, the liquid nitrogen chamber was placed under a partial vacuum to reduce its temperature. This process caused about 3 K fluctuations in the detector's temperature, as the nitrogen cooled or was replaced with warmer, room-pressure nitrogen. (The test dewar has a low capacity nitrogen chamber and hence a short hold time.) The detector output was seen to fluctuate in exact phase with its temperature, at times showing a decreasing signal of order 1 e^-/pix/s as the detector cooled. This was assumed to be due to the gain of the on-chip amplifiers varying with temperature. A temperature controller was used to stabilise the detector temperature to 92±0.1 K and a linear dark was again seen of magnitude 0.3 e^-/pix/s. When in the CIRPASS dewar, the detector temperature fluctuates by less than 0.1 K, as this dewar is much larger than the test dewar, has more cold mass (and hence a much larger thermal inertia) and is itself in a temperature regulated cold room.

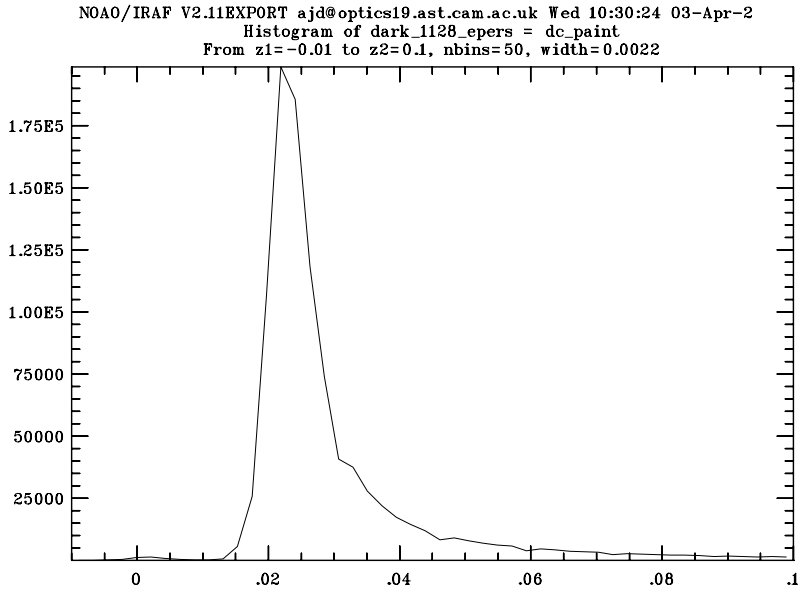

Figure 6.8: *Histogram showing the pixel distribution of dark currents for the CIRPASS HAWAII 1K array.* The x axis is the dark current in e^-/pix/s and the y axis is the number of pixels with that dark current.

6.3.4 Persistence

The HAWAII array shows a considerable amount of persistence: if exposed to a high light level, that is, one which causes the pixels to saturate in a few minutes, the detector subsequently shows an increased dark current.

An attempt was made to quantify this effect. A light source was used which gave non-uniform illumination, so the persistence signal could be compared with that from a non-illuminated part of the detector. A 1 hour dark was taken, followed by a 60 s illuminated exposure that took the detector to saturation point and a subsequent 1 hour dark. The number of times the detector was read out, the readout length and light brightness were varied.

The set-up used had a 'clean' dark of 0.29 e^-/pix/s (measured viewing the masks through camblock 2, with the cold room at room temperature). The detector was then exposed to 1137.13 e^-/pix/s for 60 seconds, bringing it close to saturation. The following 1 hour exposure had a dark current of 0.58 e^-/pix/s, double that seen prior to the detector being exposed to light.

By adjusting the exposure sequence and light level, the following observations were also recorded:

- When the number of shots in an exposure was doubled, the same persistence signal was obtained per shot, but as there were more shots the persistence de-

cayed more rapidly.

- Powering down the detector removed all persistence. If this was done by disconnecting the power supply lines to the detector, no adverse effect was evident in the subsequent dark. However, if this was done by powering down the CCD controller, the first shot of a subsequent dark exposure showed a significantly higher signal than in the remaining shots of that exposure. This effect had a similar appearance to a persistence signal, except that the same increased signal was seen in all pixels of the detector.

- If the intensity of the light source was increased, but the exposure time reduced so that the detector received the same total flux, then the persistence signal was also increased.

- Reading the detector many times after a strong persistence signal removed the persistence, but increased amplifier glow. 20 full detector readouts halved the measured persistence signal. 40 full detector readouts resulted in approximately one quarter of the signal being recorded, which brought the persistence signal into the noise region for these observations.

- If the detector was powered, but not being used, it slowly acquired a persistence signal proportional to the amount of time and light intensity to which it was exposed. After 24 hours with the detector in a dark environment of 0.025 e^-/pix/s a persistence signal of 20 times the dark was seen in the first shot. Exposing the detector to 1 minute of light, that would saturate the detector in a few seconds if it were being read out, resulted in a persistence signal of 30 times the detector's dark in the first shot.

- The detector always showed a slightly higher dark in the first shot of approximately three times the true dark.

6.3.5 Gain

The system gain is the number of detected electrons that corresponds to one data number (DN) recorded by the software. It is an important parameter, affecting amongst other things the deduced throughput of the optics. The gain, however, is difficult to measure accurately.

The gain of the detector can be determined by examining the noise in an image and comparing it to the mean signal in the same image. The technique used is based

on the fact that the electrons generated in the detector follow Poisson statistics. The recorded signal, however, is in data numbers, which is not electrons but electrons times a scaling factor, the gain (expressed in e^-/DN). Thus, the data numbers do not follow a Poisson distribution and the relation between the mean and variance for the data numbers allows the gain to be determined.

As stated by McLean (1997), if p is the photon noise in electrons, r is the readnoise in electrons and g is the gain in electrons/data number (e^-/DN), then the noise in electrons in the image will be given by, $\left(\frac{noise}{g}\right)^2 = \left(\frac{p}{g}\right)^2 + \left(\frac{r}{g}\right)^2$. The left hand side of the equation is just the observed variance V in DN and $p = \sqrt{gS}$ where S is the mean signal observed in DN, as the photons follow Poisson statistics. So the equation can be rewritten as:

$$V = \frac{1}{g}S + \left(\frac{r}{g}\right)^2 \tag{6.1}$$

Thus, a graph of variance against mean signal has a slope of $1/g$. The noise in the unprocessed data will contain contributions from the Poisson noise and readnoise, as suggested by the above equation. Other noise sources, however, such as flat field noise and a contribution from bias variations, may also be present. If these are not minimised and accounted for during the data reduction process, they may affect the accuracy of the gain measurement.

Typically, determining the gain of a CCD system involves taking a series of flat field exposures at different light levels, then measuring the mean and variance of the counts present in each of these images. In order for this to work well, the quantum efficiency of all the pixels needs to be very similar and the illumination should be flat across the entire CCD. This ensures that each pixel produces the same number of electrons following Poisson statistics. It is usual to remove the slight flat field pixel variation by dividing each intensity level by a good quality flat field image. This means that the gain determined is actually the average gain of all the pixels.

The situation for infrared arrays is slightly different. The 'flat field' images show much more variation as individual pixel gains and quantum efficiencies can vary by more than 10%. It is also difficult to produce a truly flat illumination across the entire detector using the CIRPASS spectrograph optics. Thus, a slightly different method was chosen for determining the gain of our system. The method chosen takes advantage of the fact that an infrared array can be non-destructively read out and allows the gain of every pixel to be determined independently.

A stable light source was used to illuminate the CIRPASS mask mirrors. The light reflected from the mirrors reached the camera after passing through a diffuser,

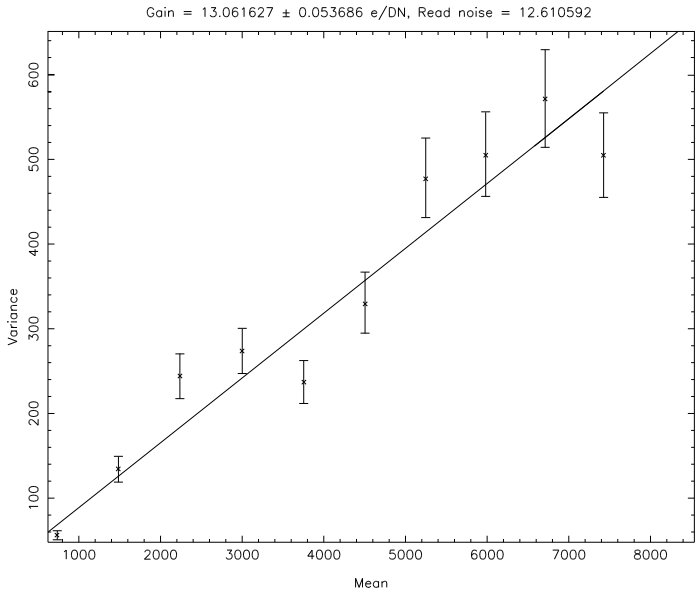

Figure 6.9: *A typical fit to the mean-variance data for one pixel in order to determine its gain.*

to ensure a reasonably flat illumination. The light intensity was then adjusted so that it brought the detector close to saturation in a two minute exposure, to ensure that the photon source provided the dominant signal and noise source detected at the detector. 100 consecutive observations were then made of this source using a 10 shot, 2 read, 120 second NDR sequence. Each successive shot gave a measurement of an effectively brighter source. Thus, for each pixel, observations were obtained at 10 different intensity levels, and there were 100 such observations at each intensity level. This allowed calculation of the mean and variance signal for each pixel at 10 different intensity levels and, therefore, the pixel's gain.

A CIRPASS pipeline script was written to perform all necessary reduction steps on data taken in the above fashion. The mean and variance were found for every pixel at each intensity level. A least squares fit was then performed on the data for every pixel, giving the gain and readnoise for each pixel. The results are shown in Figures 6.9, 6.10 and 6.11. The median gain in the image shown in Figure 6.10 is 12.5 ± 4 e^-/DN, which is slightly higher than the 8.1 e^-/DN quoted by the detector control software.

The usual source of inaccuracies with this method is due to over-estimation of the variance. If the variance were too large, the gradient of the mean-variance plot would be too high, and the deduced gain would be too low. It was, therefore, important that noise sources other than the Poisson variation in the photon signal were minimised when making the gain measurements. Thus, if anything, the measured

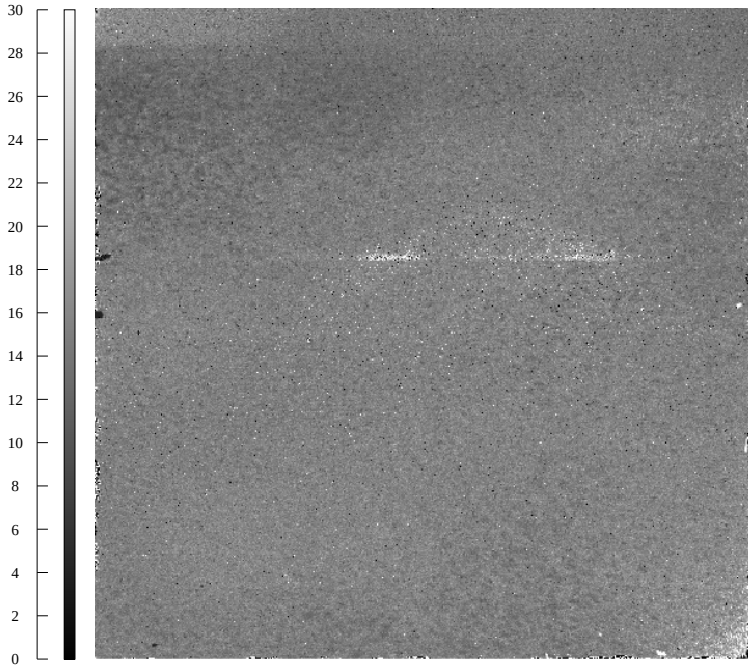

Figure 6.10: *Image of the individual pixel gains (e^-/DN) for our HAWAII 1K array.*

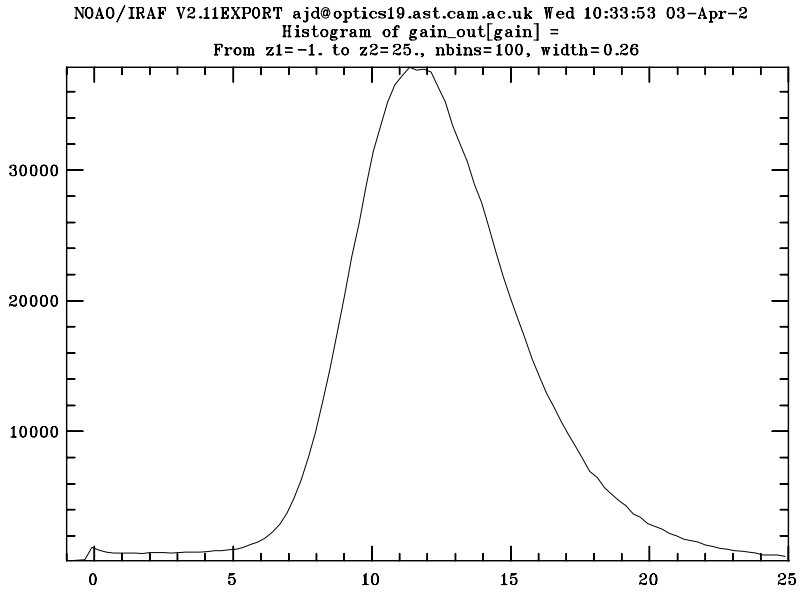

Figure 6.11: *Histogram of the individual pixel gains for the CIRPASS HAWAII 1K array.* The x axis is the gain in e^-/DN and the y axis is the number of pixels with that gain.

gain was expected to be lower than the true gain.

This method requires that the entire system is stable for the duration of the 100 observations. For this reason, the cold room and detector temperatures were carefully monitored when the gain data was taken. The light source also needed to remain constant for the duration of the exposure. To check this, the average measured intensity for a small section of the detector was plotted versus exposure number and found to be flat.

It is also conceivable that the gain of the readout system and detector could vary with time. To test this a small section of the detector was examined and illuminated with a bright light source, that would cause the detector to saturate in a 3 second exposure. Repeated 2 second exposures were then taken. These always had the same number of counts, for two separate $1/2$ hour periods, spaced 3 hours apart, suggesting that the gain does not change with time.

No dark current subtraction was performed on the data. However, given that the dark current is of order 0.03 e^-/pix/s, and photon arrival rates of approximately 490 e^-/pix/s were used, the errors caused by this should be negligible.

In theory, it is also possible to deduce the readnoise from the above procedure. However, a more direct method was chosen for determining the readnoise and is discussed in Section 6.3.6. For reference, the median readnoise obtained from the above gain data was 7 ± 7 DN.

6.3.6 Readnoise

The readnoise quantifies the error in the measured signal output from the detector readout system, compared with the number of electrons actually detected. Clearly, the readnoise should be as low as possible to maximise the signal-to-noise ratio available with CIRPASS.

In principle, it is possible to determine the readnoise of the detector from the gain measurements made above. This method is, however, fairly inaccurate as small errors in the gain or gradient of the mean-variance plot can produce large errors in the readnoise deduced from the data. Thus, a different technique was used.

A small section of the detector, typically a box of 10×10 pixels, was targeted, as it can be read out in a very short time. This box was then read successively 100 times (taking under a second), with the detector viewing a metal plate that was close to liquid nitrogen temperatures. Thus, the intrinsic detector dark current should have been the only contributing signal, and was negligible at 0.03 e^-/pix/s. A linear fit was then made to each individual pixel integration across these 100 reads, with the

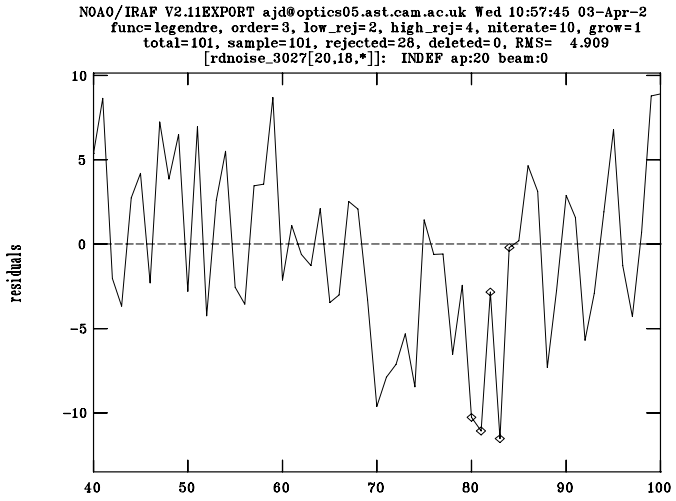

Figure 6.12: *The residuals from a linear fit to a single pixel's dark integration, used to determine the pixel's readnoise.* The x axis is pixel number and the y axis is the difference from the fit.

error on the fit being a measure of the readnoise per read. Figure 6.12 shows a typical fit to some data, with the gain set at 3.1 e^-/DN. The stated readnoise was then the average readnoise of all the pixels in the box. Using this technique the readnoise of the system was found to be 17 e^- per read which is a little higher than Rockwell's stated value of 10 e^- per read (Kozlowski et al., 2000), but still low enough to allow CIRPASS to reach its specified sensitivity (Section 9.6).

The high readnoise is thought to be caused by the 2 m of cable connecting the detector output to the interface box, where the output is subsequently amplified. This length is unavoidable if the readout electronics are operated outside the cold room. Amplifying the detector output directly on its PCB inside the dewar, and moving the readout electronics inside the cold room may significantly reduce the readnoise. Both of the above modifications are likely improvements to be made to CIRPASS after the commissioning observations.

The readnoise was also investigated as a function of the pixel clocking rate. From the results shown in Figure 6.13, it appears that the readnoise is fairly constant for a readout rate of <500 kpix/sec, but begins to increase approximately linearly for faster readout rates. The readnoise for a speed of 2000 kpix/sec was 1099 e^-, as the device no longer responds properly at these high clocking frequencies. For observations with CIRPASS, the detector is normally operated at 334 kpix/sec.

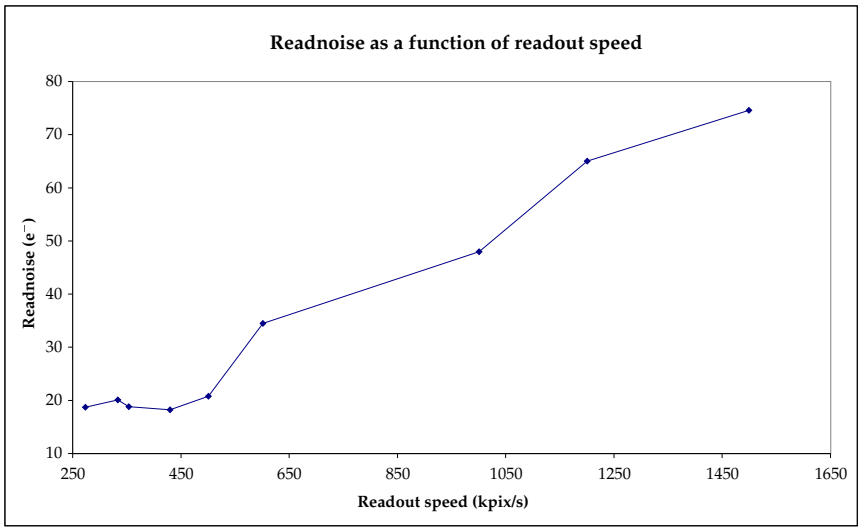

Figure 6.13: *Readout noise as a function of detector readout speed.*

6.3.7 Quantum efficiency

The quantum efficiency (QE) is the percentage of detected photons (that is, those photons that produce an electron in the light sensitive element), compared with the number incident upon the device. The QE is difficult to measure accurately, as it requires a stable and calibrated flux source and an optical arrangement with known throughput. For these reasons it has not been directly measured in Cambridge. Figure 6.14 is a typical QE plot for the HAWAII 1K detectors, as provided by Rockwell Scientific. The performance of CIRPASS, based on the throughput measurements presented in Section 9.2, is in agreement with the QE data presented in Figure 6.14. Measurements by the QUIRC group (Hora, 1997) have extended the wavelength range of the Rockwell QE measurements, and suggest that HAWAII 1K detectors continue to be sensitive to light to 0.7 μm. They do not, however, give the QE at 0.7 μm and it is expected to be below 20%.

6.4 Cosmic rays

Cosmic rays from data read out in NDR mode can be easily identified and removed since they manifest as an abrupt change in integration rate for one of the shots. This is discussed further in Section 8.4. On average, we observe 10.8 cosmic ray events per minute per square centimetre; a histogram of the cosmic ray energy distribution is given in Figure 6.15.

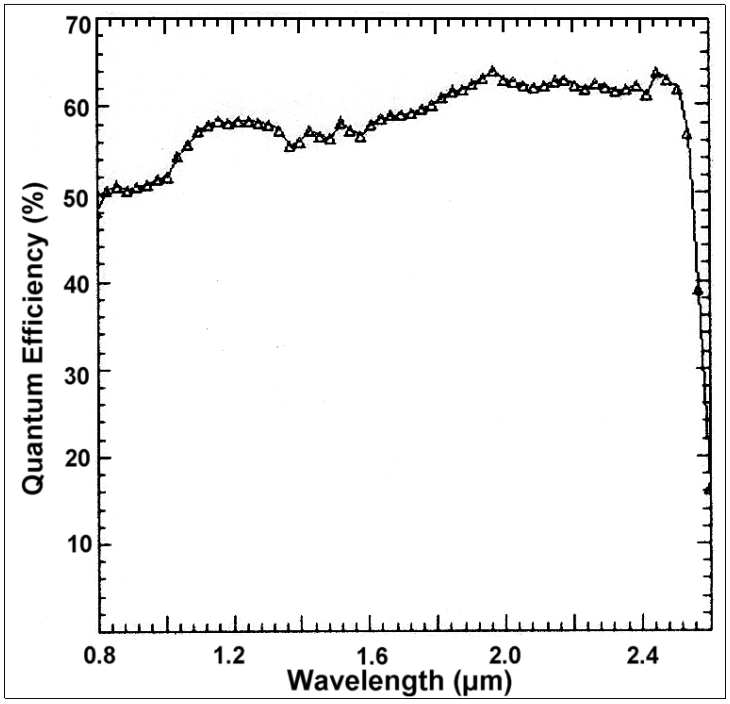

Figure 6.14: *Quantum efficiency plot for a HAWAII 1K infrared array, as provided by Rockwell Scientific.* The plot is for an array at a temperature of 78 K, has peak QE at 1.970 μm and cuts off at 2.579 μm.

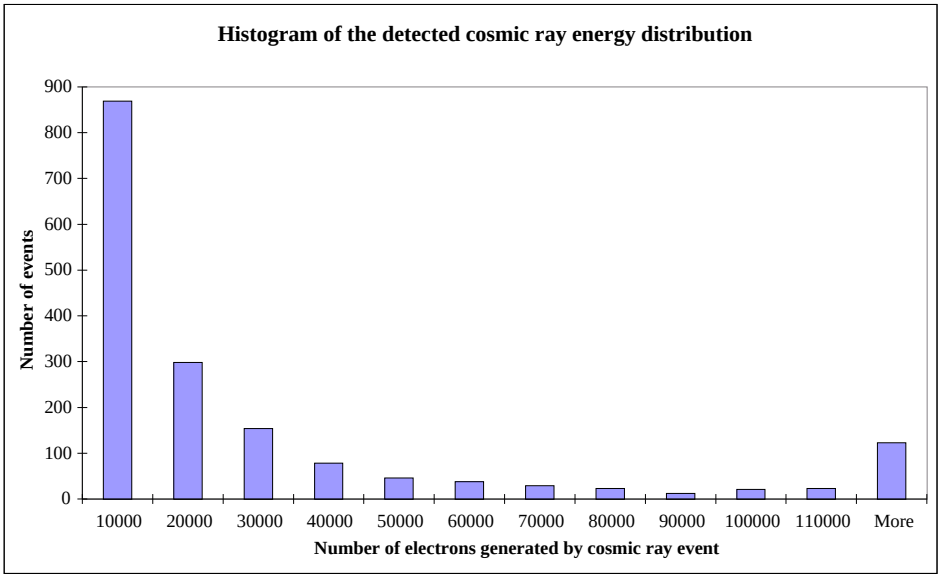

Figure 6.15: *Histogram showing the distribution of cosmic ray energy's detected by the CIRPASS HAWAII 1K array.*

6.5 Voltages used to drive the HAWAII 1K detector

Voltage Rail	*(V)*
Analogue supply	5.000
Digital supply	5.000
BIAS	3.495
VRESET	0.649
REF	4.13
DOS	3.72

CHAPTER 7

INSTRUMENT CONTROL

7.1 Introduction

CIRPASS is a complex instrument with several mechanisms under remote control. Most of these mechanisms will be adjusted between observations, for example to change wavelength range or image scale on the IFU. The observer is also required to initiate the data taking and data reduction process, and to monitor feedback from the instrument and telescope. Ideally, this should be as simple and automated as possible and performed from one central program, rather than each aspect of the instrument requiring its own application. The control system implemented for CIRPASS, following this design objective, is presented here.

The instrument is primarily driven by three personal computers (PCs), two in the control room and one in the dome. A controller and supporting software are used to run the detector and stepping motors are used to drive the various mechanisms. The combined hardware system which drives the instrument is presented in Section 7.3.

CirICS is the graphical user interface (GUI) program with which the CIRPASS user interacts and is discussed in Section 7.6. CirICS runs the detector data taking and control software PixCel, communicates with the telescope control software (TCS), and moves the various mechanisms in CIRPASS. It also provides a continuously updated display of the instrument status. CirICS was coded by A. N. Ramaprakash; the author was jointly involved with the software specification, overall functionality and testing.

7.2 CIRPASS control overview

The CIRPASS control system has been designed in a modular fashion, with all the separate systems being accessed from one program using a standard interface, CirICS. CirICS provides the central communication point between all the separate sys-

tems and is used for overall control during an observation. CIRPASS is intended to be a visitor instrument; as such it can operate stand-alone. CIRPASS does not rely on any pre-existing architecture at the telescope. Should telescope control be available, however, CirICS has an associated module that can interact with the Gemini telescope interface. CIRPASS can, therefore, be operated for an evening's observing by one person. The observer can alter the hardware configuration, for example to change wavelength range, initiate the data taking process and see a preliminary reduction of the data obtained using a few simple steps.

CIRPASS has four distinct systems to be controlled: the infrared detector, the data taking and reduction process, the mechanisms in the instrument and the telescope itself. Each of these systems uses a different interface and hardware arrangement and will be discussed below.

Primary communication between the various systems is via the CIRPASS local ethernet, the one exception being an RS232 serial link for mechanism control with an in-house built instrument control unit (ICU). A schematic overview of the instrument control system is given in Figure 7.1.

Additional feedback from the instrument is available on the same computer as the one running the CirICS software. CIRPASS has three video cameras inside the cold room and one camera on the fore-optics. It also has numerous temperature sensors and a humidity sensor, which are monitored and logged using commercially available software.

7.3 Instrument control hardware

7.3.1 Computer hardware

Three 500 MHz PCs, cirpass1, cirpass2 and cirpass3, are used to run CIRPASS. Cirpass1, which runs the Linux operating system, is used for data reduction and storage. It also manages the internal 100 Mbs ethernet network which connects the three computers. Cirpass2 is the instrument control computer. It has two displays: one for the CirICS program and one for remote display of the detector readout, so the user can be certain that the detector is operating correctly. Cirpass2 controls the stepping motors via three ICUs (Section 7.4) and monitors various instrument parameters. Cirpass3 is used to drive the HAWAII detector via an Astrocam 4100 controller and it is the output from this machine that is seen on the second monitor of cirpass2. Both cirpass2 and cirpass3 run the Microsoft Windows 98 operating system. Data is trans-

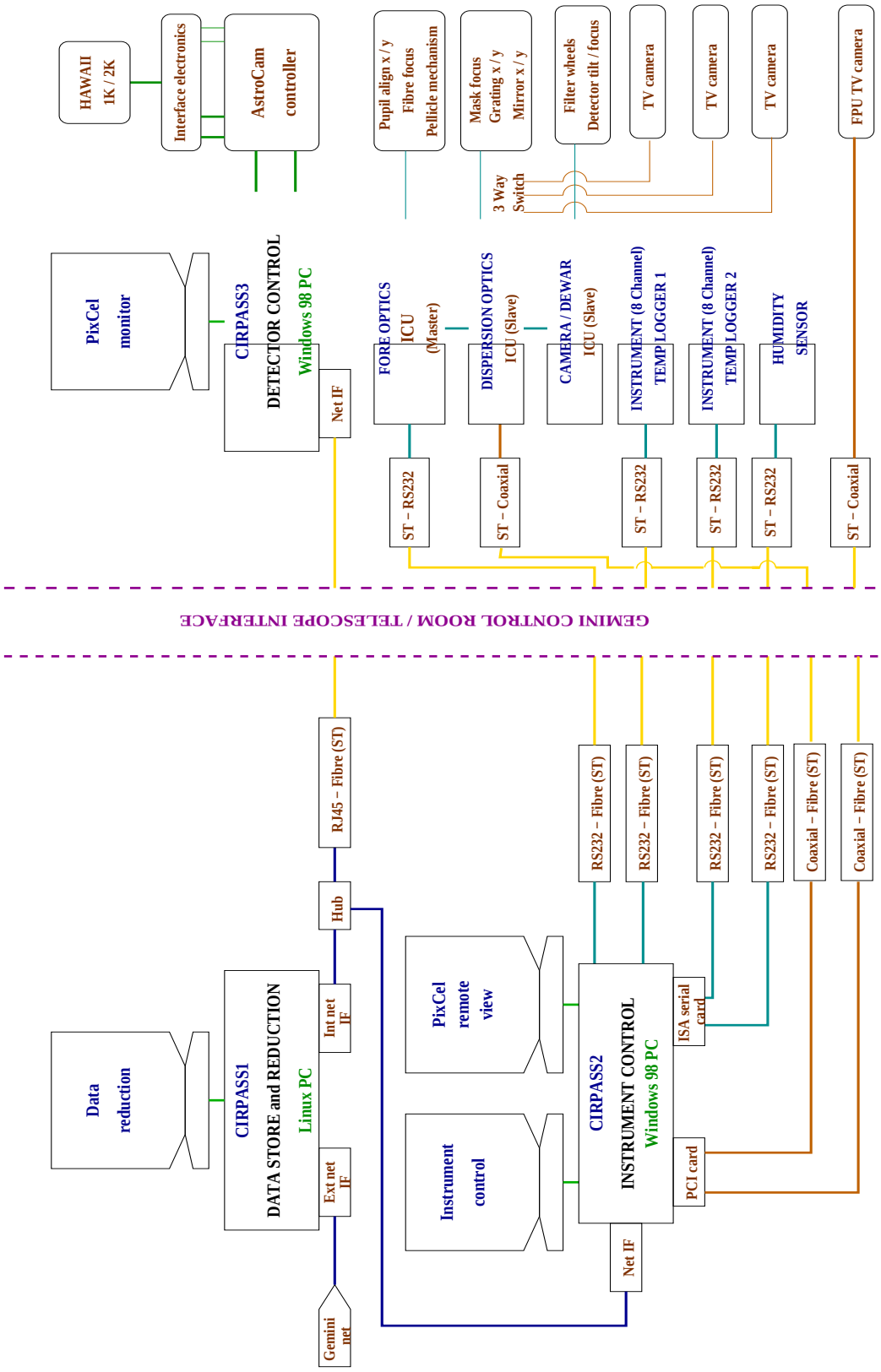

Figure 7.1: *Instrument control schematic.*

Figure 7.2: *The 'control room' arrangement used when testing CIRPASS in Cambridge.*

ferred directly, at the time of taking, from cirpass3 to the data reduction machine using the samba protocol.

Cirpass1 and cirpass2 reside in the telescope control room. Cirpass3 and the associated detector hardware and the stepping motor controllers are rack-mounted in the telescope dome. Communication between the telescope control room and dome is over fibre-optic links, which carry TCP (ethernet) and RS232 ASCII data via suitable converters.

The entire control system was assembled in the laboratory in Cambridge when CIRPASS was undergoing preliminary testing. Figure 7.2 is a picture of the arrangement used. The 19″ rack on the far left, which houses cirpass3 and the two slave ICUs, would normally reside in the telescope dome. The data reduction machine and the computer running CirICS are on the table in the middle. The table on the right is for the additional computer, needed in Cambridge, that controls the telescope guider.

7.3.2 Mechanism control

CIRPASS can be broken down into three separate assemblies, the fore-optics, the dispersing optics and the cryogenic camera. Each contain mechanisms requiring remote control and each operates at a different temperature. Three types of stepping

motors are used to drive the various mechanisms, each with appropriate operating temperature ranges. Within these, different sizes of motors are used depending on the torque required and available space.

Dewar

There are three assemblies to be moved in the dewar: the two filter wheels and the detector focussing mechanism. Five motors were required which would operate at liquid nitrogen temperatures. Phytron cryogenic motors were used, specified to work to 4 K in a vacuum environment. They are dry motors (that is, they have no lubricants). Feedback was achieved with micro-switches. There are three micro-switches at the edge of each wheel, which ride in three grooves cut into the wheel. The depth of the groove changes with the angular position of the wheel. The filter wheel positions were encoded using Grey code, so that only one micro-switch changes state when the filter moves between each encoded position, thus eight distinct states are available. As there are four filters in each wheel it is possible to encode each of the off-filter positions individually as well as all the on-filter positions. The grooves are arranged such that the on-filter sector is located to 1^o and the in-between filter sectors span 89^o. In practice the filter can be relocated in position more accurately than 1^o by the CirICS software. CirICS moves the wheel to the nearest half step of the motor (0.02^o) and the feedback is used to check that the system is behaving as expected. If a filter is not correctly located when the wheel has been driven by the specified number of steps, for example if the motor stalls, then CirICS will use the feedback to correctly find the requested filter. (There is a software limit of a maximum of a 50^o motion either side of the expected filter position when searching for the correct filter. This is to ensure that the wheel is not continually driven in the case of a mechanical failure.)

The three motors of the focussing mechanism (Section 5.2.3) each have an associated micro-switch which acts as a mid-range reference position and provides a rough indication as to the height of the mechanism. The actual image quality on the detector, however, provides a more accurate feedback of the detector's position.

Dispersing optics

The dispersion optics operate at -40°C, thus we did not need the space grade motors used in the dewar. Stebon stepping motors, which are greased and specified to operate to -42°C, were used. These motors were found to work well and showed

no signs of failing, even when the cold room was operated at −45°C. There are five motorised mechanisms, which are responsible for optical alignment and focussing. Micro-switches on all mechanisms ensure that their motion stays within limits. The tip-tilt mirror and grating can each be moved in two planes, one of these planes giving a change in observed wavelength, the other ensuring accurate alignment. The distance of the mask mirrors from the primary mirror can also be adjusted to ensure that the OH lines are accurately focussed on them, for optimal suppression.

Fore-optics

The fore-optics operate at ambient temperature, placing no special requirements on the stepping motors. Linos Photonics motors were used along with Hall Effect limit switches. There are four driven mechanisms for changing scale and image focussing on the IFU, there is also a shutter and four test lamps (Section 2.3.2).

7.4 Mechanism control electronics

In total, the electronics hardware for CIRPASS has to operate fourteen different stepping motors, fifteen micro-switches, two shutters and four test lamps. The large number of mechanisms required three separate instrument control units (ICUs), one for each major assembly of the instrument. Each ICU drives the stepping motors and reads the switches for the appropriate assembly. The first ICU is the master unit. It is connected to a serial port on cirpass2 and communicates using the RS232 protocol. The two remaining ICUs are slave devices and are daisy-chained from the first using further RS232 connections.

Each ICU contains a stepping motor controller card. We have used a standard Euro card manufactured by Cortex. This card generates the TTL signals necessary to drive the stepping motors, has four bit input and output lines and limit sense inputs. The card is controlled via RS232 protocol communication using the serial link of a PC (cirpass2). These cards can be daisy-chained, as each card will pass on any commands intended for a card further down the chain to its output serial link. The cards are expensive at £400 each and only have a 0.6 A output capability, so rather than using one card per motor, there is just one card per ICU. Additional circuitry is present in each ICU that allows the Cortex card to drive more than one motor. It was decided to limit the number of motors per ICU to six. As a result, each ICU contains six motor drive (PCB) modules, one for each motor at a cost of £100

each. These modules are capable of driving bipolar motors at current ratings of up to 2.5 A per phase. The additional circuitry and the instrument controller interface card (or decoder card) are responsible for enabling the appropriate driver module for the motor requested by the software. The user selects a motor by sending an appropriate command to the Cortex card, which causes a number to appear on the Cortex card's four bit output line. This number is read by the decoder card and the appropriate motor channel is then enabled. As a result, the waveform output from the Cortex card only causes the appropriate motor to move. The decoder card also connects the selected mechanism's limit switches to the inputs on the Cortex card. These limits are made just before a mechanism reaches an end-stop; once made, the Cortex card will not drive the stepping motor any more to prevent damage to the mechanism.

As well as driving stepping motors, each ICU can switch up to 6, 12 V lines on and off. This was achieved via the decoder card. The appropriate number on the four bit output will select a latched circuit operating an appropriate device. These are used to control the arc lamps and shutter.

Thus, the ICU has little intelligence but allows a wide variety of mechanisms to be controlled using its four bit output and some additional decoding circuitry. It is the responsibility of the driving program on the PC to operate the ICU correctly, hiding its underlying structure from the end user.

7.5 Device readout

7.5.1 Detector readout

The CIRPASS detector control hardware can drive either a 1K or 2K HAWAII infrared focal plane detector array. The instrument is currently operating with a 1K detector and upgrading to the 2K would require little change to the detector control hardware. The detector is driven by an Astrocam 4100 controller[1], which is a fourteen bit CCD controller. An interface box was used that makes the HAWAII array appear as a CCD to the controller. Different interface boxes will be needed for the two detectors, as the clocking waveforms for the two devices are slightly different. The CCD controller has the advantage that a double correlated sampling readout scheme is available that reduces the detector readout noise (Section 6.2 has a detailed description of the HAWAII array control electronics). The controller is run via Astrocam's

[1]The Astrocam 4100 controller was purchased from PerkinElmer Life Sciences Ltd.

PixCel software, which has had code modifications by Beckett (1995) to optimise its use for infrared arrays. The chip may be read out successively in a non-destructive manner allowing 'up the slope sampling' (non destructive read mode, NDR), or continually read and reset allowing shorter integration times for bright sources (read reset read mode, RRR) which may otherwise saturate the detector (Section 6.2.1). CIRPASS is generally operated in NDR mode as faint sources are normally observed and our data reduction pipeline is optimised for this readout scheme (Section 8.4).

7.5.2 Temperature and humidity sensing

T-type thermocouples are universally used throughout CIRPASS as they are reliable, readily available and can measure low temperatures. Fourteen temperatures are monitored, ranging from the liquid nitrogen can to the hot gas outlet of the refrigeration system. Picolog temperature logging hardware and software are used to read the thermocouples, and a Picolog relative humidity sensor (which operates to $-40°C$) is used in the cold room.

7.5.3 Video monitoring

Three cameras are used in the cold room and one is used on the fore-optics. The cold room cameras are to check the optics for signs of condensation, monitor the liquid nitrogen vent pipe and check that the mechanisms are moving reliably. Lamps, controlled by the ICUs, illuminate the cold room. The fore-optics camera views the telescope / IFU pupil and is used for alignment purposes. Standard cameras were used throughout, with those in the cold room provided with extra insulation. The cold room cameras are left permanently on so that their internally generated heat ensures that they continue to operate at $-40°C$. Composite video-to-fibre optic converters are used so that the video signal can be transmitted via a fibre-optic link to the control room. The images are viewed on cirpass2 using a PCI card and software designed for security monitoring systems. The software allows simultaneous monitoring of all four cameras and allows alignment images to be easily recorded for future reference. The device readout and instrument monitoring system therefore required items to be placed in the cold room, increasing the heat load placed on the refrigeration system. The additional heat input by these devices is summarised in Table 7.1 and is, however, negligible compared to the estimated 680 W heat load for which the refrigeration system was designed (Section 3.3). Table 7.1 also includes heat sources that are not permanently present. The power output from the dewar

Heat source	Estimated heat load (W)
Intrinsic to the cooling system	
Conduction through walls	500
Evaporator fan	180
Additional electronic items (permanently on)	
3 cameras	10.5
Picolog humidity sensor	1.5
Dewar window fan	9.5
Additional electronic items (occasionally on)	
Dewar heater resistors	20
3 lights	210
Stepping motors (per motor)	20

Table 7.1: *Heat sources on the cold room refrigeration system.*

heater resistors is controlled to maintain the temperature of the dewar walls slightly above that of the cold room air. The heater resistors are insulated from the cold room and ideally should only heat the dewar (and hence the LN_2 within it), not loading the cold room refrigeration system. The resistors are rated at 200 W full power, the figure quoted in the table is an estimate of the heat escaping to the cold room during normal operation. The cold room lights are rarely on, and the stepping motors are used for approximately five minutes total running time, during an evening's observing, making their impact on the cooling system negligible.

7.6 CirICS: the CIRPASS GUI

The CirICS software provides a graphical user interface to the control mechanisms previously mentioned. It operates on a number of different levels: user, engineer and advanced. At the user level, only a limited number of options are available. At this level the result of changing a setting may move a number of mechanisms without the user requiring any prior knowledge of the instrument. For example, to change wavelength range the tip-tilt mirror, detector focus and detector tilt need to be changed. CirICS will take care of this, moving each required mechanism by the correct amount.

At the user level three windows are used. The main application window (screenshot Figure 7.3) acts as a status window. From this the instrument control tool, Figure 7.4 and PixCel tool, Figure 7.5, may be opened. At the bottom of the status window are a text box and progress bar. The text box provides a history of the commands issued. The progress bar provides a continuously updated display of the

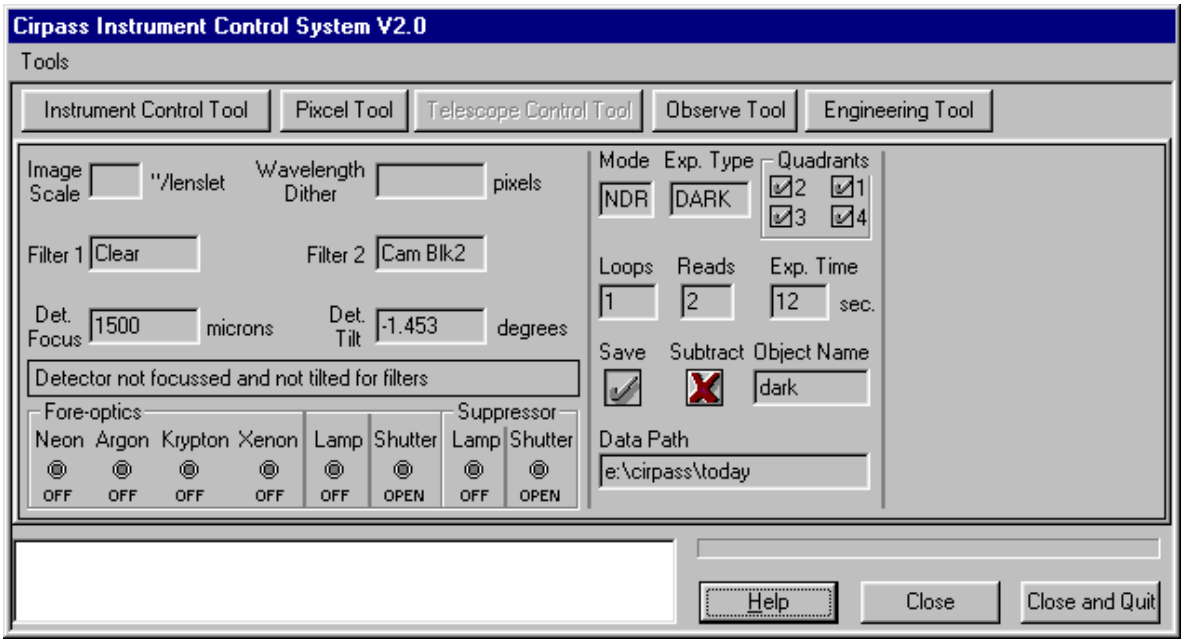

Figure 7.3: *CirICS user interface.*

completion status of the last command.

The instrument control tool is used to adjust the various mechanisms and operate the lamps and shutters. From here, different filters and focus positions may be selected, as well as different image scales. This is a 'one-click' process; the user selects the desired change and the software moves all necessary mechanisms.

There is a pull-down menu to select filters. When moving the wheels, the software first reads the wheel's position from the micro-switches and checks that its position is correct. It then moves the wheel just less than the specified number of steps to reach the next position, the wheel's position is read from the micro-switches and the wheel is then stepped forward or backwards as necessary, repeatedly reading the switches until the new position is found. The number of steps the software will move during this 'hunting' process is limited in case of a mechanical problem. As it is highly unlikely that the wheel will go beyond the new position, we almost always approach the new filter from the same direction, ensuring accurate re-positioning of a filter each time it is selected.

The instrument control tool also has a box where the detector focus and tilt are set. The user enters the detector focus position in millimetres or tilt in degrees and the software will then move the mechanisms as necessary. Changing focus requires a piston motion, moving each of the three detector focus motors by the same amount. Changing tilt is done by keeping the centre of the detector at a fixed height, so this also requires all three motors to be moved. CirICS has the geometry of our arrange-

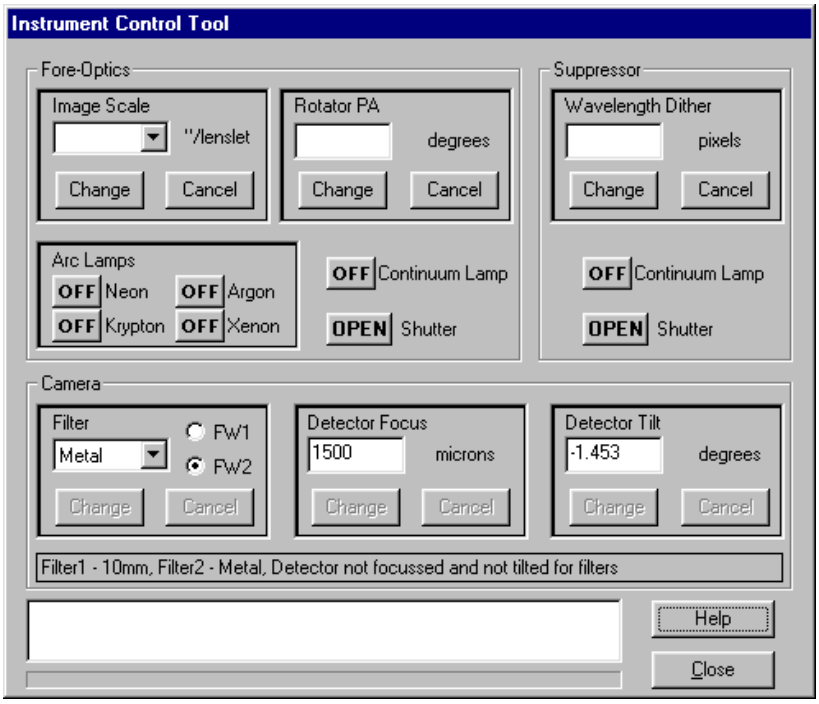

Figure 7.4: *CirICS instrument control tool.*

ment built in and thus calculates the required number of steps needed to move each mechanism. The change is only carried out when none of the limit switches have been made and if the motion will not move the mechanism beyond its software end stops.

The PixCel tool is used to start an exposure and provides a simple interface to the detector control software, presenting only the options necessary to take a data sequence. It also has a selection of check buttons for the data reduction pipeline. An observer can decide which tasks should be carried out by default when the pipeline is run. Checking these buttons causes CirICS to instruct PixCel to write various header keywords into the image data it outputs. These header keywords are subsequently read by the data reduction software. This is discussed more fully in Chapter 8.

An observe tool (screen-shot Figure 7.6) is also provided, which allows observing sequences to be pre-defined. All options which may be set in any of the above tools can be defined and stored as a particular observation. Many separate observing scenarios can thus be defined and saved. CirICS can then perform an entire observing sequence automatically by just selecting a pre-defined observation type. Numerous observations can also be strung together or the same observation repeated a fixed number of times.

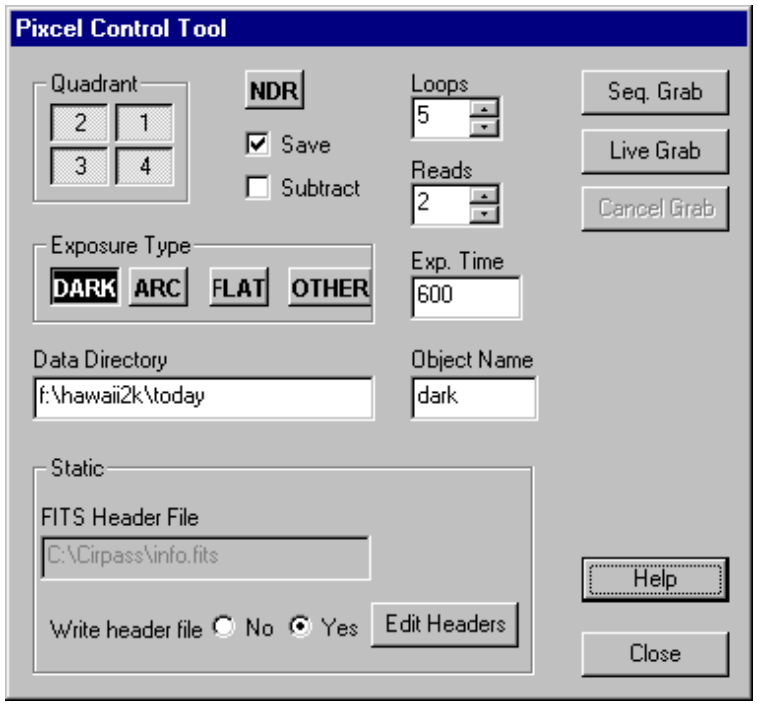

Figure 7.5: *CirICS PixCel control tool.*

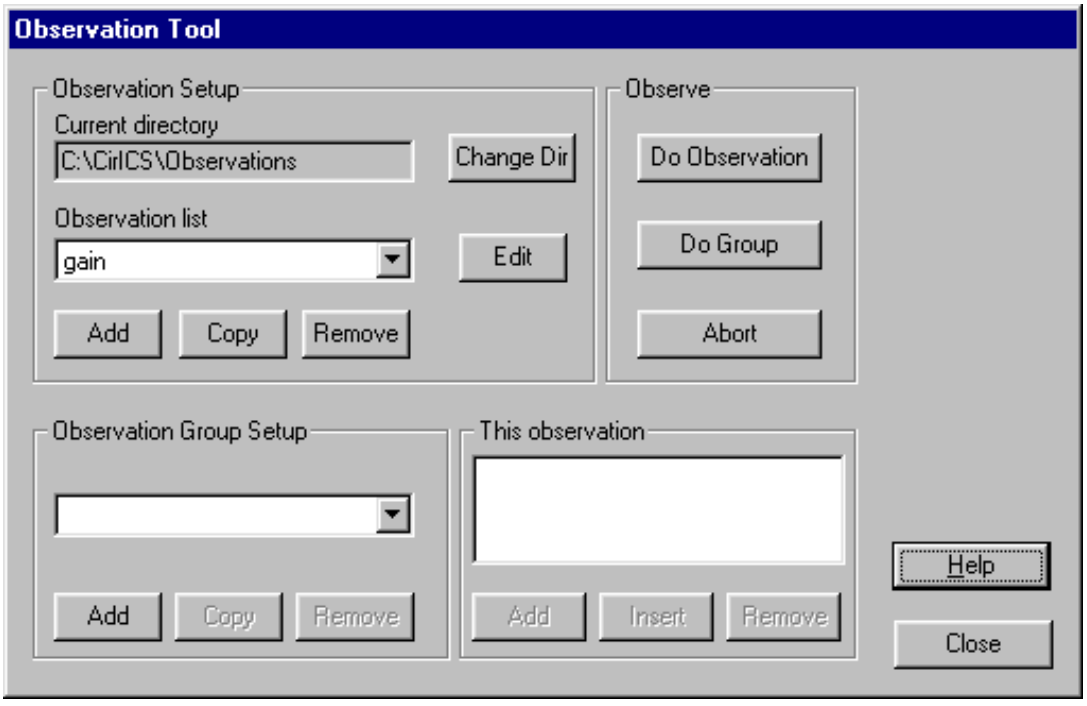

Figure 7.6: *CirICS observe tool.*

An observer has access to all of the above windows and they may be used concurrently.

To access the engineering window, all of the user level windows must be closed, except the main window. From the engineering window, it is possible to move each mechanism individually by a calibrated amount as in user mode; it is also possible to move each mechanism by any number of steps so that initial alignment can be achieved. Once alignment has been obtained it is 'set' in the engineering window. From then on, the user interface will be able to move the mechanisms using input parameters which should be obvious to an observer, rather than stepping motor steps which are more familiar to the engineer. The engineering tool provides a common interface for moving all of the mechanisms for CIRPASS and there is a separate tab for each of CIRPASS's assemblies.

The advanced mode, accessed from the engineering level, allows basic stepping motor parameters such as their maximum speed, acceleration and deceleration to be set. The software limits are also set in the advanced section. These numbers define the range of steps over which the mechanism can be driven. The software limits for CIRPASS were set to be just inside the limit switch positions, that is, the software will refuse to move a mechanism just before the Cortex card senses that the mechanical limits have been made and it itself stops driving. This ensures that we do not lose the step counting and hence, the absolute position of the motor, when the Cortex card starts to ignore movement commands that the software may send. Further to this, CirICS always checks that the limit switches have not been made before attempting to move the motor. An error message will be reported by the software in the event that a limit switch is unexpectedly made.

CHAPTER 8

DATA REDUCTION TECHNIQUES

8.1 Introduction

The CIRPASS data reduction software is an integral part of the instrument. It ensures that the instrument is fully exploited, both at the telescope when the quality of the observations needs to be checked, and afterwards when making scientific conclusions from the data. New software was developed for CIRPASS.

CIRPASS is one of a growing number of instruments that produces 3D data (Section 1.3). Whilst the initial stages of the software are CIRPASS specific, the later stages are applicable to any 3D instrument. For this reason, the CIRPASS data format, discussed in Section 8.2, was chosen to match the emerging standard for 3D data (Euro 3D, Allan et al., 2001).

The CIRPASS software runs under IRAF[1] (Tody, 1993) and is a collection of IRAF scripts and C programs. The pipelining and housekeeping is handled by IRAF cl tasks, while the C programs deal with the numerical aspects of the data reduction.

The spectra from individual fibres in CIRPASS are closely packed on the detector and extracting these spectra presented a significant data reduction challenge. Once extracted, the spectra can be combined to produce the image incident upon the IFU. The new software developed for both of these tasks is presented in Section 8.3.

Instrument-specific pipeline software was developed, which performs generic data reduction steps, such as bias subtraction and cosmic ray rejection, that are necessary for infrared arrays. The software also collates the raw data into a user-friendly format and is discussed in Section 8.4. Non-instrument-specific pipeline software, discussed in Section 8.5, was also developed. This software combines information from 3D data to perform tasks such as wavelength calibration and flat fielding.

[1]IRAF is a general purpose software system for the reduction and analysis of scientific data. It is written and supported by the IRAF programming group at the National Optical Astronomy Observatories (NOAO) in Tucson, Arizona and includes a good selection of programs for general image processing and graphics applications.

The CIRPASS data reduction pipeline is flexible, allowing it to run in a minimal mode. This minimal or 'quick-look' mode is intended for use at the telescope and is discussed in Section 8.7.

8.2 The CIRPASS data format

CIRPASS uses a data format similar to that proposed by the European 3D integral field working group (Boehm, 2001), as this format was still being refined at the time we needed our data reduction software. The CIRPASS data format was also strongly influenced by the format used by the STSci group for NICMOS data (Bushouse, 1996). CIRPASS uses multi-extension FITS (MEF) files. These are similar to ordinary FITS files (Cheung, 2001) except that they allow the combination of many individual FITS files into one file, each original file having its own extension in one master file. Extensions containing only ASCII data or data organised into tables are also allowed. Thus the MEF file format has the advantage that all data associated with one observation can be contained in one file, making the data on disk more manageable. Any CIRPASS data produced by the pipeline will be in the MEF file format described below.

The first two extensions of a CIRPASS MEF file contain observation and instrument configuration information. The first extension (0) consists only of a standard FITS header and contains a number of ASCII strings detailing observation parameters, such as the filters used and the exposure time. Keywords defining the data reduction path and history are also written. The second extension is a binary table that specifies the IFU to fibre slit configuration and is discussed in Section 8.3. There then follow sets of four image extensions, where each set is called an *imset*. A particular *imset* contains information associated with one readout of the detector. Typically, in NDR mode, the detector is read out many times during an exposure and there will be one *imset* for each of these readouts.

An *imset* is composed of science (*sci*), variance (*var*), data quality (*dq*) and time (*time*) image extensions. The science extension contains the actual image from the detector, while the variance image has its associated errors and is updated as the science data is reduced. The data quality image is used to flag pixels if they are unusual, for example, if they have had a cosmic ray hit or have high dark currents, using a binary coding scheme. The time array contains the actual exposure time for each pixel. Pixels may have different exposure times if, for example, they have had a minor cosmic ray hit, resulting in part of their integration time being removed by the

	Extension number	Extension type	Extension name	Extension version	Dimensions	Bits per pixel
	0	Header file				
	1	Binary table			3x517	
1^{st} *Imset*	2	Image	*sci*	1	1024x1024	−32
	3	Image	*var*	1	1024x1024	−32
	4	Image	*dq*	1	1024x1024	−32
	5	Image	*time*	1	1024x1024	−32
2^{nd} *Imset*	6	Image	*sci*	2	1024x1024	−32
	7	Image	*var*	2	1024x1024	−32
	8	Image	*dq*	2	1024x1024	−32
	9	Image	*time*	2	1024x1024	−32

Table 8.1: *Example structure of a CIRPASS multi-extension FITS file.*

cosmic ray rejection software. The science extension also contains a standard FITS header with entries relevant to that particular readout of the detector, namely, which shot and read of the detector it is from and its exposure time. Table 8.1 gives the typical structure of a CIRPASS MEF file, where a readout of the detector, or *imset*, is identified by the extension version. The last readout of the detector is placed first, that is in *sci,1*. Typically, the MEF file is reduced to just 6 extensions at the end of the pipeline, containing the final reduced image data in extension version 1.

Once the spectra have been extracted, a 6 extension MEF file is produced, the format of which is the same as detailed above except that the image extensions are now in IRAF multi-spec format. Each line of a multi-spec image corresponds to one extracted spectrum or, in IRAF terms, one aperture. Thus, the final science extension has dimensions of detector width by number of fibres. For backwards compatibility with the IRAF apextract package APNUMn keywords are also added into the science extension header. (These keywords give the y pixel value of the spectrum in the image and its aperture number, where n is the aperture number and the value of the keyword is y.)

8.3 Spectra extraction and IFU image reconstruction

In order to take full advantage of the spatially resolved spectroscopy offered by an IFU, software is required that translates the spectra on the detector into the image that was present on the IFU. Other translations, such as a velocity map deduced from the spectra and overlaid onto the IFU format, are also desirable for interpretation of the data.

The first stage in this process is extraction of the spectra associated with each fibre. The aim when designing CIRPASS, as with any other instrument, was to make

maximum use of the available detector area, which meant packing as many spectra onto the detector as possible. However, this can lead to crosstalk between adjacent spectra on the detector with the light from one fibre adding to that of its neighbours. For CIRPASS, the full width half maximum (FWHM) of the spectra varies between 0.8 and 1.2 pixels and the separation of their centres is between 1.25 and 2.75 pixels, resulting in significant crosstalk from the two nearest spectra. In this situation, distinct rows of the detector do not correspond to the spectra from particular fibres and it is not possible to simply sum rows across the detector in order to obtain the spectra from individual fibres. The variation in FWHM is caused by the detector not being exactly aligned with the focal plane and can be corrected by adjusting the detector focussing (tip-tilt) mechanism. The variation in the centre spacing is fixed and is due to the variation in physical spacing of the fibres in the CIRPASS slit.

To account for crosstalk when extracting CIRPASS spectra an optimal extraction algorithm, similar to that used by MPFS (Becker et al., 2000) and SAURON (Bacon et al., 2001), was developed by Johnson et al. (2002). The chosen mathematical model assumes that the pixel centres of the spectra on the detector are known and that the spectra have a known shape in the spatial (or cross-dispersion) direction (Gaussian for CIRPASS). The unknowns then are the heights of the profiles that produced a given intensity distribution across the chip (in the spatial direction). A model pixel intensity distribution, which is a function of the profile height, can be made. It is then possible to calculate the heights of the profiles that minimise the difference between the model intensity distribution and the observed intensity distribution, provided the profiles are such that the crosstalk is from fewer than two spectra either side of the central spectrum. The full mathematical details are presented by Johnson et al.

The technique assumes that the true centres of the spectra are accurately known before extraction. Thus, the errors induced by not accurately knowing the centres are an important consideration and were also investigated by Johnson et al. For the error on a extracted spectrum to be $<10\%$, the pixel centres have to be known to an accuracy of <0.3 pixels. It is, therefore, very important that these positions are accurately determined for CIRPASS and the procedure used is described in Section 8.3.1.

8.3.1 Fibre mapping and centring technique

The CIRPASS slit was assembled and each fibre in the slit numbered sequentially from 1 to 508. The IFU was then made and a record kept of which fibre was attached to which lens in the IFU (that is, the x,y position of the lens in the IFU to which the fibre was attached), as well as which fibres were used as calibration fibres and which

were broken. However, with the large numbers of fibres involved it is possible that a few mistakes in the numbering were made. Thus, when the fibre centres on the detector were found, it was also necessary to check that the mapping of fibre number in the slit to position in the IFU was correct. Given that a very good approximation to the IFU configuration was known, three masks were made to fit in front of the macro lens array on the IFU. Each mask only allows light through every third fibre in the slit. Thus the illuminated masks produce spectra on the detector separated by approximately six pixels, making it easy to find their centres and allowing the identification procedure to be automated to some extent. Just three images are necessary to characterise the whole slit. Images with just the calibration fibres illuminated were taken at the same time as the mask images, so that their positions could be used as reference positions for the spectra in subsequent observations. The configuration of the masks used is given in Figure 8.1, where the white lenses indicate holes in the masks used to illuminate specific fibres.

The masks were placed behind the field lens. Uniform illumination of the masks was provided using a light source at the pupil position. An example of the data obtained with one of the masks in front of the IFU is given in Figure 8.2. The top image shows the fibre spectra (from the fibres where there are holes in the mask) on the detector. The bottom image is a vertical cut across a few of the spectra illustrating that their peaks, and hence the fibre centre positions, can be resolved.

A Gaussian centring program was used to automatically find the peaks in the mask images for the central column of the detector. The results were then checked by hand as the software did not find all of the peaks. Using a calibration fibre image, an approximate mapping was determined between pixel y value and fibre number. The y values determined automatically were then converted to fibre numbers and compared with the list of fibre numbers that should be in the relevant masks. This made it easy to spot any centring errors or mistakes in the fibre slit to IFU mapping. The peaks were re-centred interactively as necessary. This procedure was carried out for each of the three masks and the calibration fibres, and resulted in an accurate fibre positions file containing fibre number and its pixel value, for the current arrangement. This file is a representation of the physical spacing of the fibres in the slit. If the fibres start at 1 in the slit and increase linearly along it, then the corresponding IFU map is given in Figure 8.3. Note that fibre position versus number is not an exactly uniform pattern across the IFU (see, for example, fibres 106 to 110). The spacing of adjacent fibres in the slit can also be calculated from the positions file and a histogram of this data is given in Figure 8.4. The calibration fibres and fibres

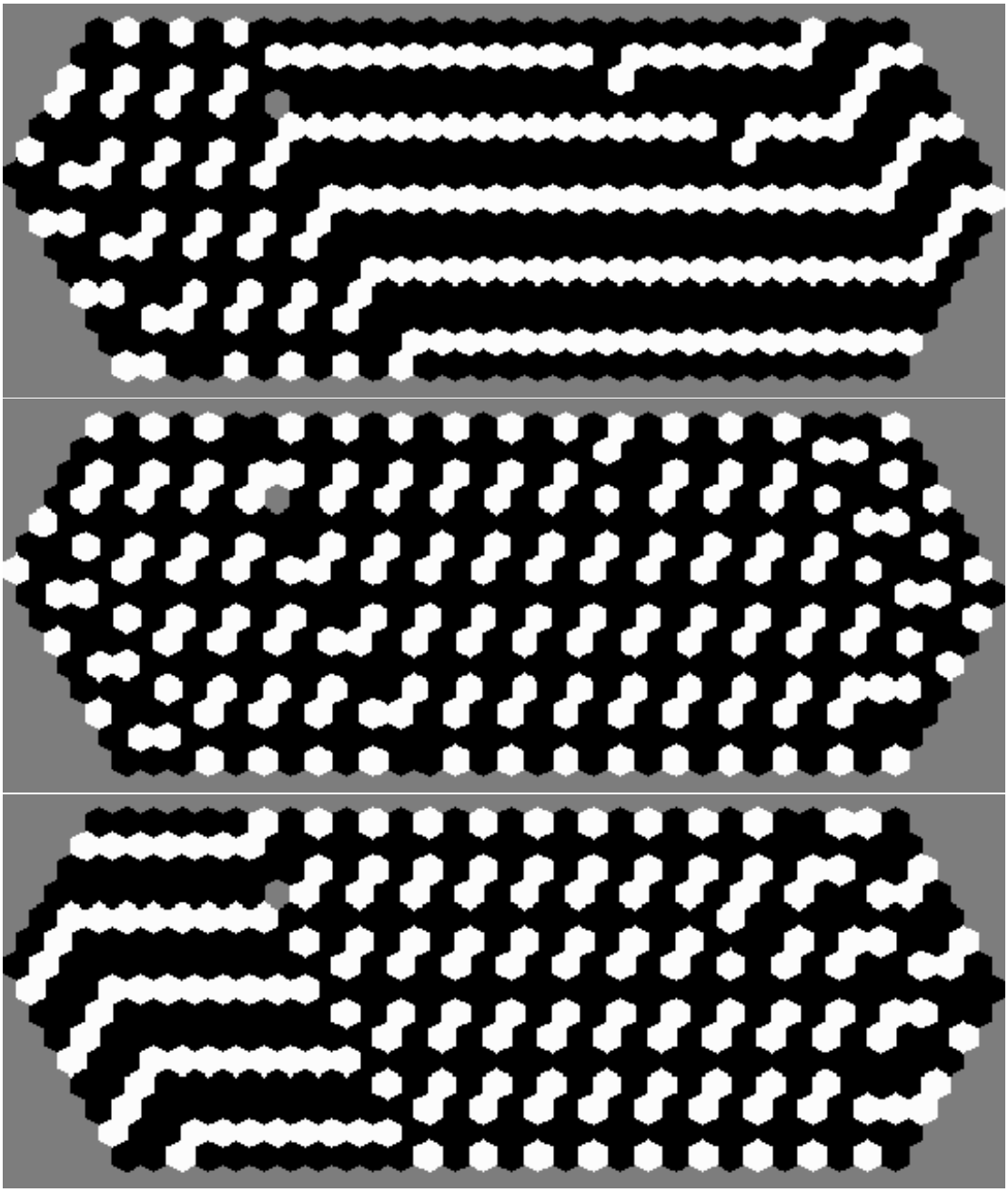

Figure 8.1: *Images showing the positions of the holes in the IFU masks* The white hexagons correspond to holes in the masks, that is, the illuminated fibres in the IFU.

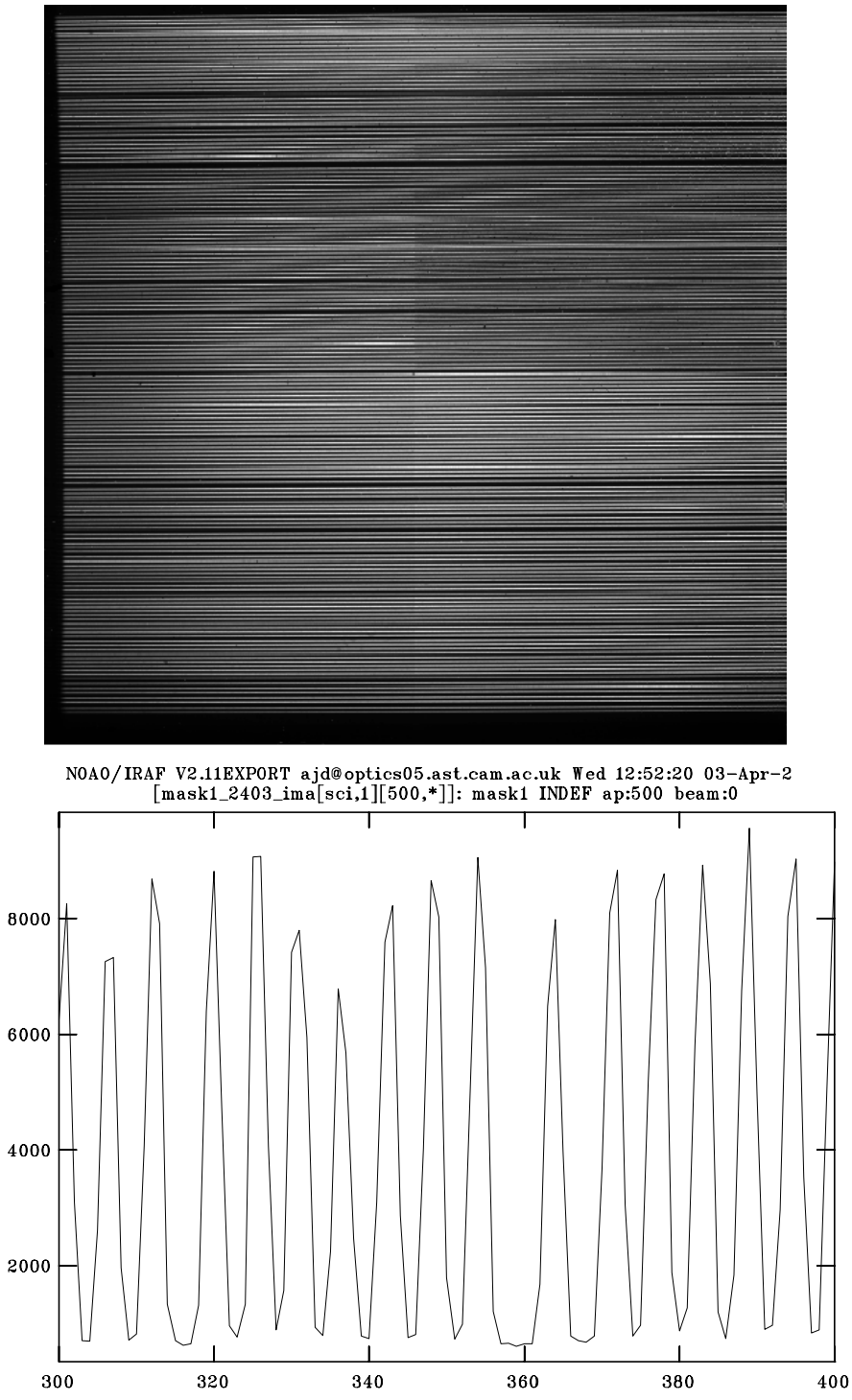

Figure 8.2: *Mask image data used for fibre centring.* Top: Fibre spectra on the detector, the dispersion direction is across the x axis and the fibres are separated along the y axis. Bottom: Close up vertical cut showing the fibre profiles in the y (spatial) direction.

Calibration fibres	7, 8, 23, 55, 96, 122, 167, 169, 172, 312, 424
Missing or broken fibres	1, 117, 127, 134, 145, 248, 417
Unusually close fibres	149,150 155,156 340,341 358,359
	435,436 468,469 474,475 494,495
Fibres on top of one another	7,8 335,336 503,504
Unusually far apart	13,14 148,149 289,290

Table 8.2: *Calibration, broken and unusually spaced fibres in the slit.*

Entry number	*FibreID*	*xcord*	*ycord*	*apnum*
1	1	−999	−999	−999
2	2	36	0	−999
3	3	35	1	−999
4	4	34	2	1
5	5	33	3	2
6	6	32	4	3
7	7	−999	−999	4
8	8	−999	−999	5
⋮				
358	358	−14	2	355
359	359	−15	3	356
360	−999	−16	4	−999
361	360	−17	5	357
⋮				
517	−999	−36	0	−999

Table 8.3: *Example fibre to IFU mapping information contained in a CIRPASS MEF file binary extension.*

whose spacings are unusual are given in Table 8.2. There are 490 lenses in the IFU with a fibre attached and 18 calibration or broken fibres, giving 508 fibres in the slit in total. There are a further 9 lenses in the IFU without a fibre attached.

The above fibre mapping information is contained in the binary table extension of any CIRPASS MEF file. This extension has three or four columns, depending on how far through the pipeline the image has been processed, and 517 entries (508 fibres in the slit and 9 lenses without a fibre). It contains an entry for every lens, even though a lens in the IFU may not actually have a fibre attached, plus an entry for every fibre in the slit that is not in the IFU, which may be a calibration fibre or just a broken fibre. A typical entry for CIRPASS is given in Table 8.3. *FibreID* specifies the fibre's number in the slit. The position of the fibre's lens in the IFU on a regular grid is given by *xcord* and *ycord*, where the geometry of the grid is specified by the keywords described below. *Apnum* is added by the extraction part of the pipeline

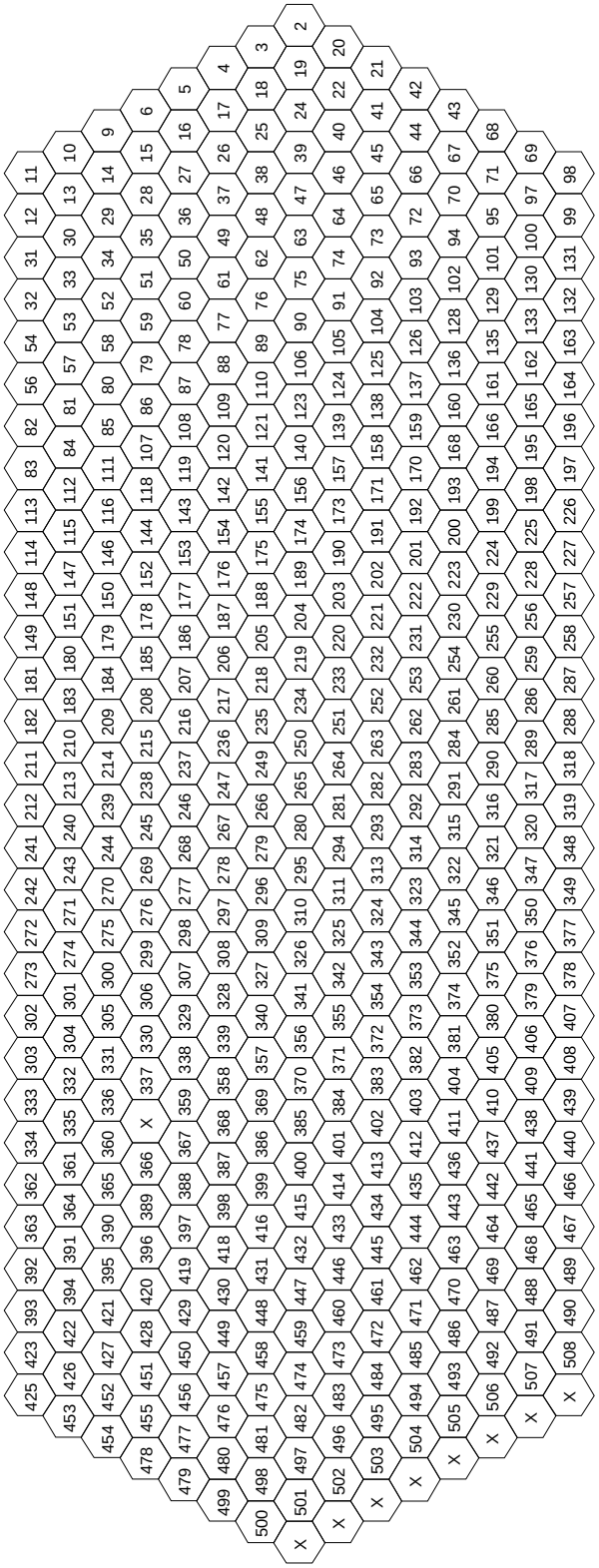

Figure 8.3: *Graphical depiction of the lens positions in the IFU showing the fibre number attached to each lens.* An X indicates a lens that does not have an attached fibre.

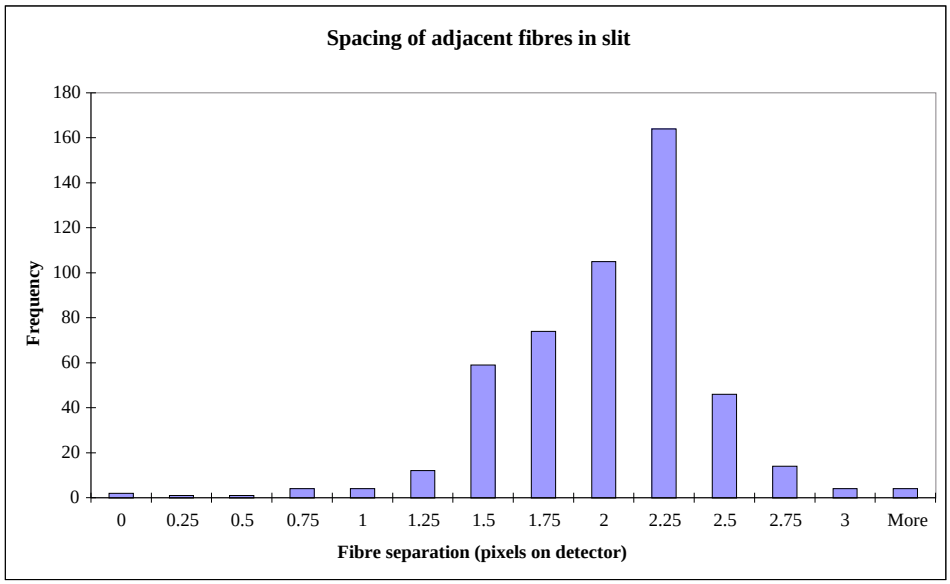

Figure 8.4: *Histogram showing the spacings between adjacent fibres in the slit.*

and is the extracted spectrum number in the multi-spec file for that fibre. An entry of -999 indicates that a fibre is not present in the IFU, slit or extracted spectrum. Thus, row 1 has a fibre in the slit that is not in the IFU; this is a calibration fibre but could also be a broken fibre. Row 360 represents a lens in the IFU which does not have an associated fibre in the slit. Rows 1 to 3 have -999 for their *apnum* as these fibres were off the edge of the detector and were, therefore, not extracted. This would not normally be the case for CIRPASS when properly aligned, and apnum is usually equivalent to *FibreID*.

The table extension also contains two header keywords to specify the geometry of the IFU grid and its lenses, these are YOVERX and MAXDIST. YOVERX is the y grid spacing divided by the x grid spacing. MAXDIST is the maximum distance, in terms of the x coordinate, that a lens can be from a lens centre position. By adjusting these two parameters it is possible to reproduce any tessellating pattern for the IFU and also allows the IFU display program to require no prior knowledge of the geometry of the IFU. For example, for square lenses on a uniformly spaced grid, YOVERX is 1 and MAXDIST is $\frac{\sqrt{2}}{2}$ (half the length of a lens's diagonal). For CIRPASS the grid positions are defined as the centres of the lenses in the IFU, thus YOVERX is $\sqrt{3}$. MAXDIST is the radius of a hexagon, in terms of the x grid spacing, which is $2\frac{\sqrt{3}}{3}$.

`Idisplay` is the IFU image reconstruction program written specifically for CIRPASS. It has the same goals as `ldisplay` written for COHSI and SPIRAL (Kenworthy, 1998). `Idisplay` was mainly coded in C, making it fast, even for instruments with many fibres. `Idisplay` works by deciding which grid centre a pixel is closest

to and assigning it the value of the corresponding grid point. The MAXDIST parameter is needed to ensure that lenses at the edge of the array are dealt with correctly, and results in these lenses having curved edges. In quick-look mode `idisplay` knows that CIRPASS has hexagonal lenses and ignores the MAXDIST parameter. In this mode it runs more quickly but may deal with the boundary between lenses less accurately. In practice, `idisplay` usually produces good quality images in quick-look mode and is always used in this mode for CIRPASS. It would, however, be necessary to recode this version for IFUs with different lens geometries. Once the IFU image has been displayed the user can interactively change wavelength range, click on lenses to see their spectra, or click on lenses to mark them as containing science data for later extraction.

As a demonstration of the functionality of the reconstruction software, a cardboard cutout of a galaxy was fitted over the IFU in the same place as the masks used to determine the fibre positions. Figure 8.5 is the multi-spectrum image produced by the extraction software when this galaxy mask is illuminated. Each line corresponds to an extracted spectrum (this is a J band image) and water absorption can be seen at the longer wavelengths. Figure 8.6 is the reconstructed IFU image obtained from the multi-spectrum data using `idisplay`.

8.3.2 Determining fibre positions when observing

The fibre positions determined using the masks provide a reference data set that allows their positions to be re-determined when the instrument configuration changes. The calibration fibres are used to establish the new positions as they are well separated on the detector, making it easy to determine their position and trace automatically. Refocussing CIRPASS causes the spacing between fibres to change and adjusting the wavelength range viewed can cause small shifts in the fibre positions on the detector. Thus, once the calibration fibre positions have been obtained they are compared with their expected positions from the mask data. The relationship between the two is fitted by a linear function, which is then applied to the positions in the reference file to determine the new positions of the science fibres. Previously, with the 100 IFU and with COHSI, the fibre positions had been found by linearly interpolating from the first and last fibres on the detector (Kenworthy, 1998). Figure 8.4 shows that this would be inadequate for CIRPASS as our fibre separations have considerable variation.

The trace of the fibres in the wavelength direction (that is, the variation in y pixel value with x pixel of the detector) is also required for the optimal extraction soft-

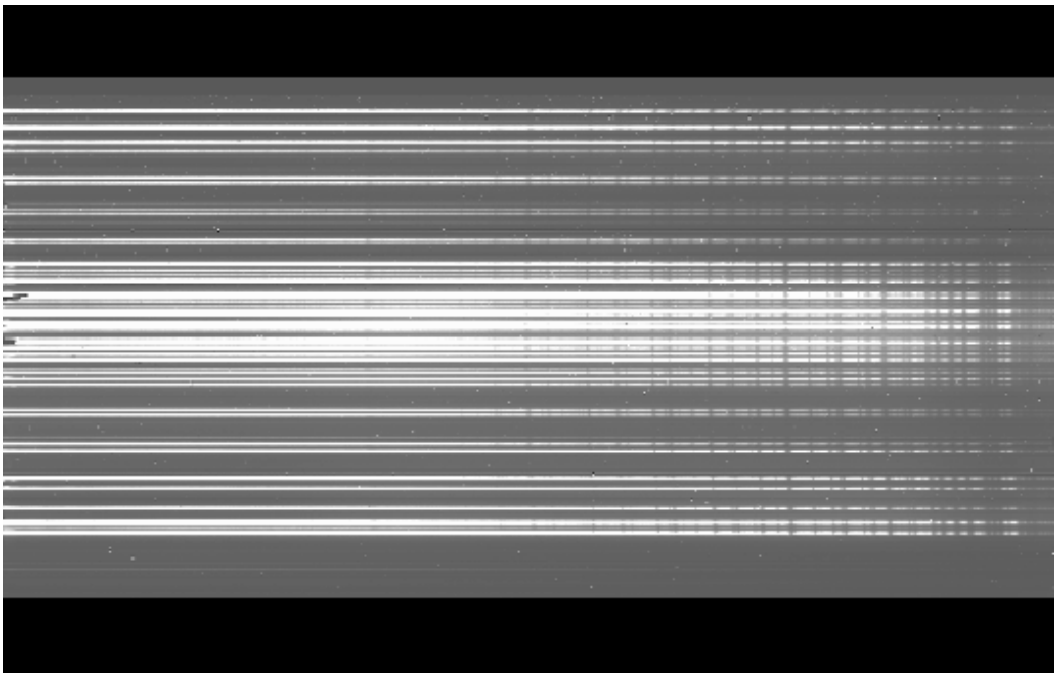

Figure 8.5: *Spectral data obtained from a galaxy mask placed in front of the IFU.*

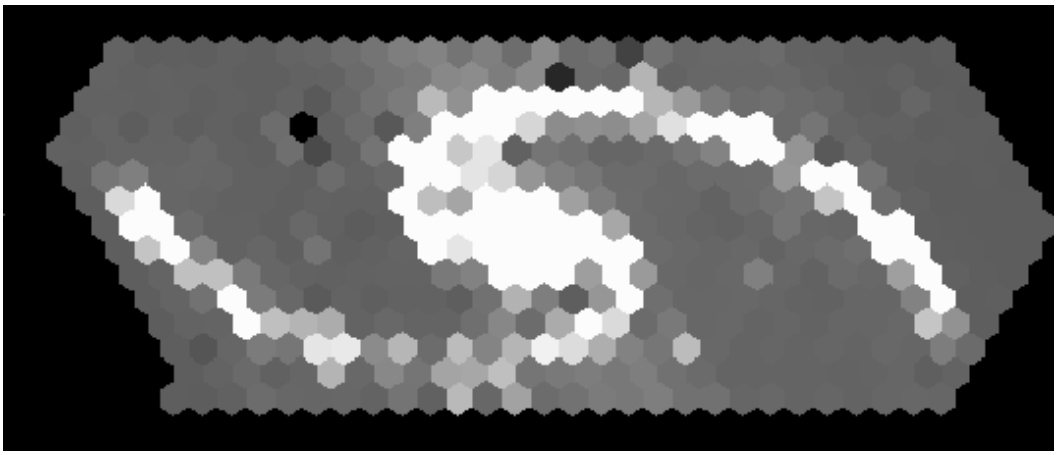

Figure 8.6: *IFU image reconstruction of the spectral data shown in Figure 8.5.*

ware, as the fibre positions need to be known at every pixel value across the detector. Again, this is done using the calibration fibres. A second order polynomial is used to define the trace of each of the calibration fibres across the detector. As the calibration fibres are reasonably evenly spaced throughout the slit, it is possible to determine the variation of the trace with position in slit, or the y pixel direction on the detector. A linear fit is used to determine the relationship between the first and second order terms of the trace with y position on the detector, and is then used to predict the trace of the science fibres.

Software was written to perform this procedure automatically. A new fibre positions file can be quickly obtained by running the software on a calibration fibre image. The accuracy with which the fibre positions can be determined is crucial to the performance of the optimal extraction software, so the position finding software was tested on some simulated data. The centring and tracing code both use a centroiding algorithm to establish the spectrum position and the returned positions agree to better than 0.015 pixels with that set in the simulated data. The software was also tested on real data. One of the masks used to establish the positions file was covered to leave only a few remaining holes. This allowed the use of independent IRAF tasks to establish the traces of a few fibres. The calibration fibres were then observed and our software used to predict the fibre positions. The interpolating of the traces reproduced the fibre positions to an accuracy of better than 0.3 pixels for 95% of the trace positions, and a typical fit is given in Figure 8.7.

As a final test of the accuracy of the positional data and image reconstruction, the spectra obtained from the masks were reconstructed and the results are given in Figure 8.8. These images should be compared with Figure 8.1 and show that the reconstruction software is working well. (Note that Figure 8.1 has the far left diagonal of lenses set to the background colour and hence they are not visible.)

To summarise the fitting technique mathematically, we assume that a fibre trace is given by:

$$y(f) = a(f) + a_1(f)x + a_2(f)x^2$$

where y is the y pixel of the trace on the detector, x is the dispersion direction detector pixel value, and f is fibre number in the slit, and that:

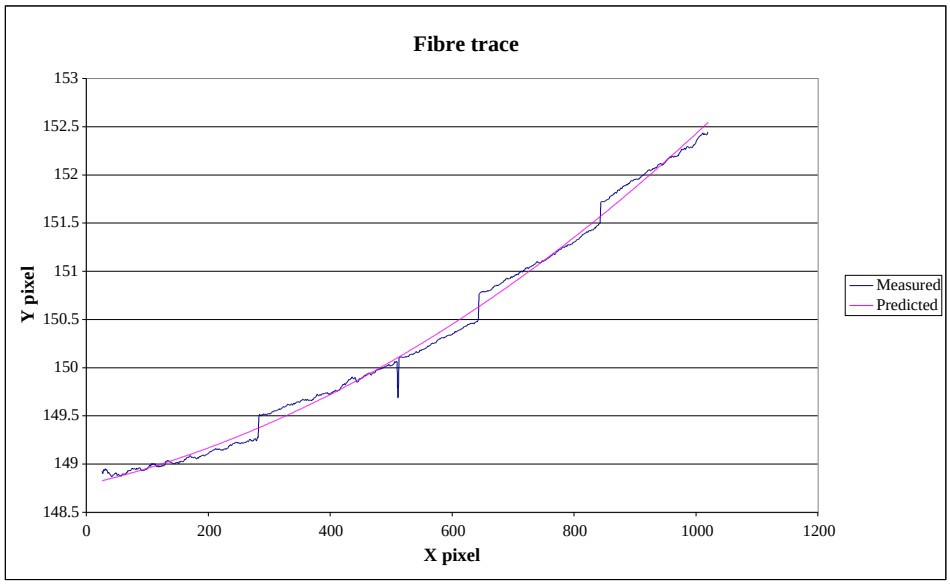

Figure 8.7: *Comparison of the predicted and measured fibre trace.* The predicted trace is obtained from the calibration fibres. The measured trace is the measured centroid positions for the fibre in question. The jumps seen in the measured trace are a real effect, and not a problem with the centroiding algorithm, caused by the HAWAII detectors having a non-uniform intra-pixel response.

$$
\begin{aligned}
a &= m \times ref\_pos(f) + c \\
a_1 &= m_1 a + c_1 \\
a_2 &= m_2 a + c_2
\end{aligned}
$$

where the coefficients for a are determined by comparison with the reference position (ref_pos) for a fibre, and for a_1 and a_2 by interpolation from the calibration fibre trace. This assumes that the above three equations are not correlated, which is reasonable for CIRPASS.

The tracing algorithm highlighted an interesting feature of the HAWAII detector's pixels. The steps in the position of the measured trace visible in Figure 8.7 are real features and not artefacts of the tracing algorithm. This can be verified by closely examining an image from the detector where it can be clearly seen that the trace does appear to 'jump' between pixels. This suggests that the detector's pixels do not have a uniform cross-sectional response to light and are more sensitive to light that falls close to their centres. This effect is also seen in CCDs (Jorden et al., 1994).

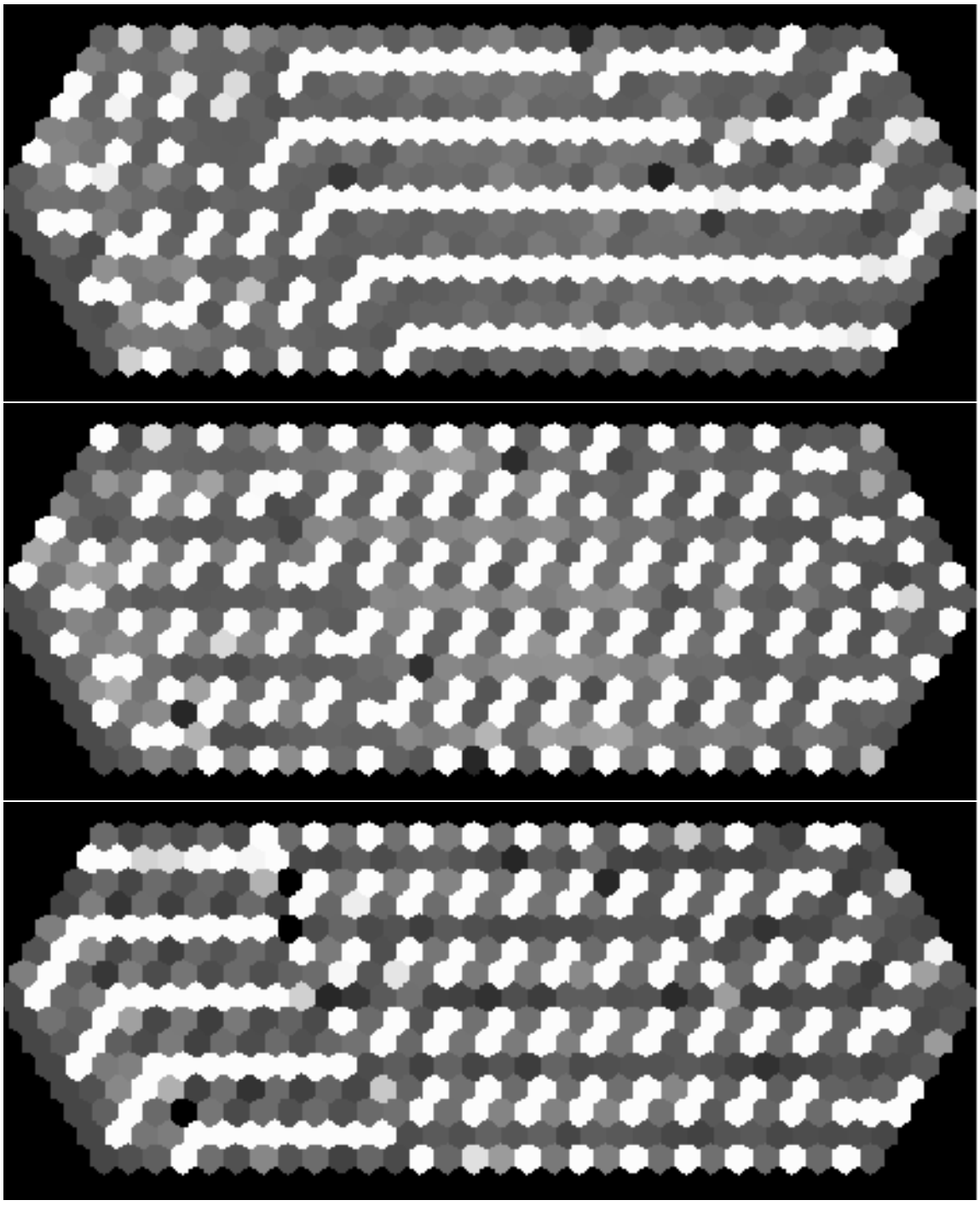

Figure 8.8: *Reconstructed images of the three masks used to identify the fibre positions.*

8.4 Basic pipeline: `docirpass`

A flowchart of the complete CIRPASS data reduction pipeline is given in Figure 8.9. The pipeline tasks employed for any one data set are driven by header keywords in the raw data, set at the time of writing the image data from the infrared array. The default data reduction to be performed can thus be specified before the observing commences, allowing observers to decide which data reduction steps they would like carried out at the telescope. These can later be changed, allowing more detailed reductions to be performed on the same data.

The initial stages of the pipeline are CIRPASS specific and are incorporated into the task `docirpass`. PixCel outputs plain FITS images for each read of the detector. The pipeline stacks these into a single MEF file for subsequent data reduction, and adds in the unpopulated error, time and data quality extensions. It also adds the table extension containing the IFU to fibre slit configuration.

The raw data from infrared detectors is cosmetically poor, as they tend to have large flat field variations and large numbers of aberrant pixels. Figure 8.10 shows a typical unprocessed image directly read out from the detector. The first few stages of the pipeline are standard, essential tasks used to produce a clean image from an infrared array. Bias (or reset level) subtraction and cosmic ray rejection are performed automatically by `docirpass`.

The cosmic ray rejection task takes advantage of the NDR mode of the detector, and is very similar to the NICMOS task cridcalc (Bushouse et al., 1998). A slope is fitted to the pixel integration with time, and readings that deviate from the slope by more than a user definable threshold are rejected as cosmic ray hits. The procedure then reiterates on the same pixel until no more spikes are found. The task also rejects large negative shifts as noise spikes. Figure 8.11 shows images typically obtained by the basic pipeline, and is Figure 8.10 after it has been processed through `docirpass`. At this point the data is in a form which should be more easily manageable by an observer.

The cosmic ray rejection software only functions if the chip has been read out as it integrates, a technique known as follow up the ramp (FUR) sampling. Alternative readout techniques are double correlated sampling and Fowler sampling (Fowler & Gatley, 1990). In double correlated sampling the detector is read out once at the start of the integration and once at the end of the integration. Fowler sampling extends double correlated sampling in that the detector is read out n times at the start of the integration and n times at the end, where n>1. The measured signal is then

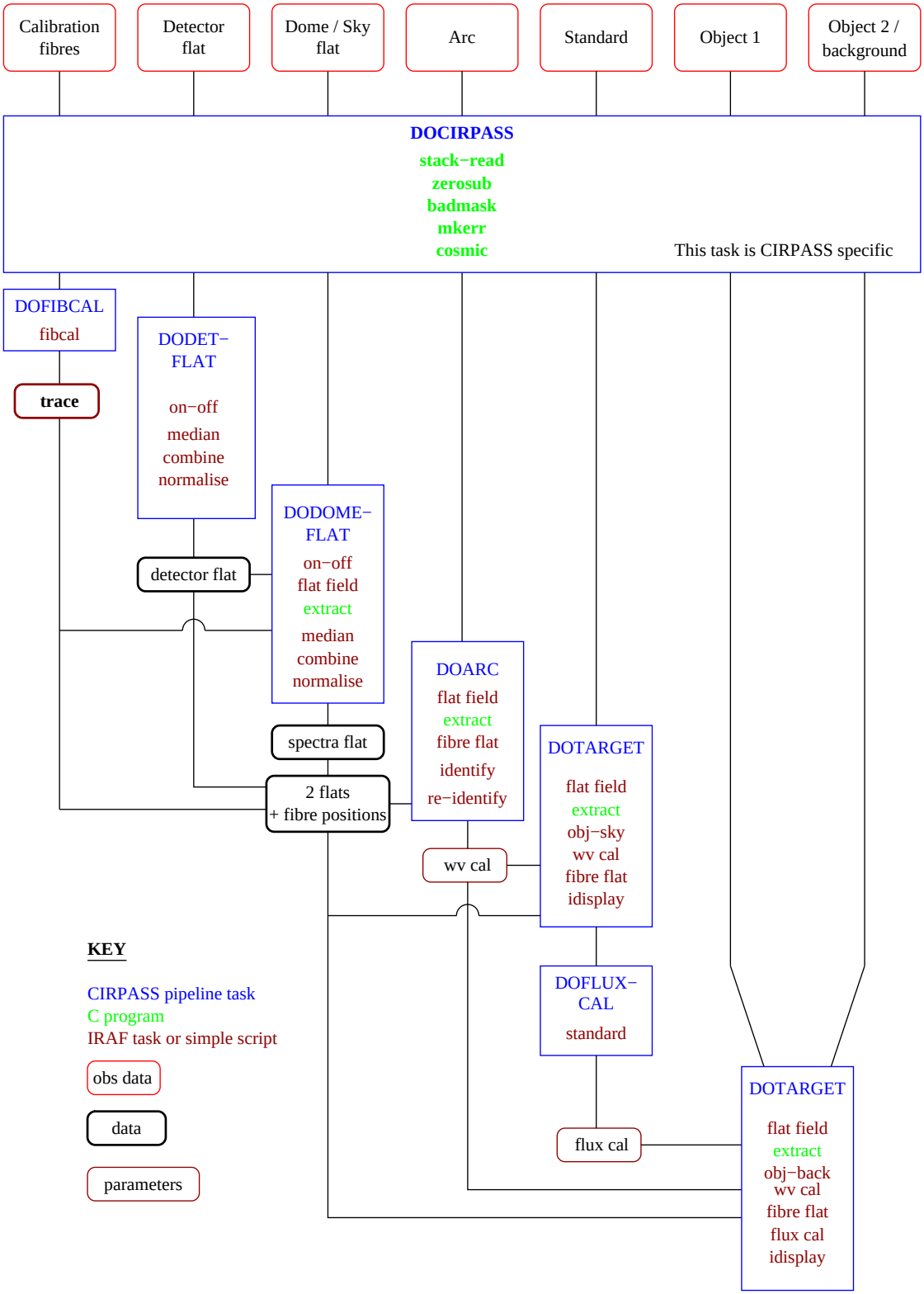

Figure 8.9: *Flowchart showing the expected data reduction steps for CIRPASS observations.*

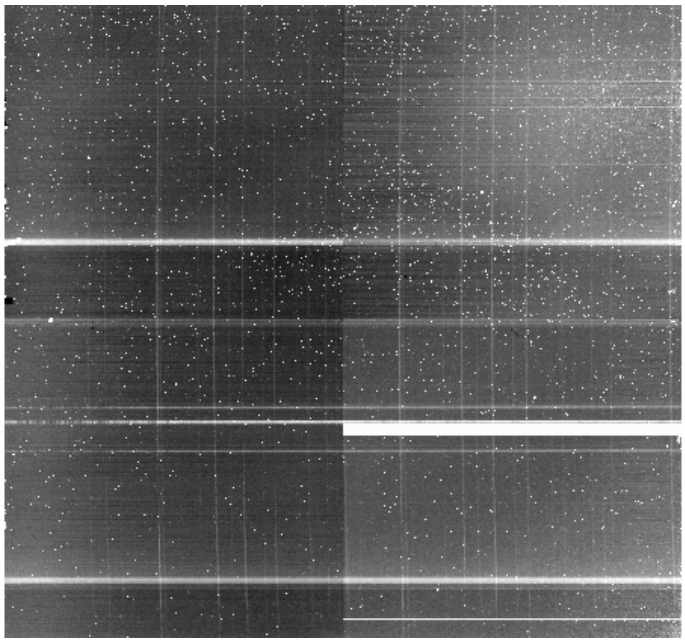

Figure 8.10: *Unprocessed sky image read directly from the HAWAII 1K detector.* The x axis is the dispersion direction and the y axis is the slit or fibre spatial direction. The horizontal bars are detector features and mask the weaker Polaris spectra that are present in this observation.

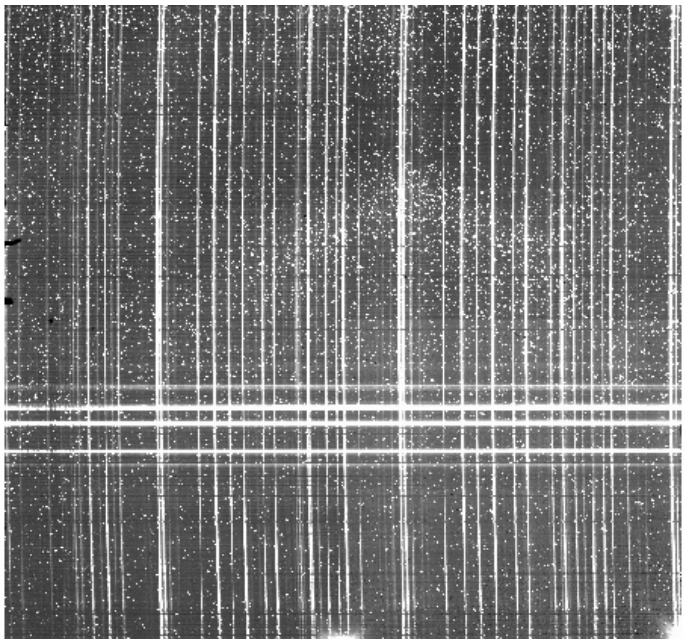

Figure 8.11: *Basic pipeline reduced image.* This is a dark-subtracted sky image. The horizontal spectra are from Polaris illuminating 5 lenses on the IFU. The vertical lines are from the OH sky background present in every fibre.

the average over the n reads. (This can also be viewed as averaging n integration slopes, each slope being obtained by subtracting equivalent reads from the start and end of the observation, or a Fowler pair. For example, read 3 of shot 0 and read 3 of shot 1). The sampling technique that gives the best signal to noise has been determined by Garnett & Forrest (1993), and has been shown to depend on whether the observation is background or readnoise limited, as summarised below:

- *Readnoise limited*: FUR sampling gives a higher signal to noise ratio than Fowler sampling, which in turn is better than double correlated sampling.
- *Background limited*: Double correlated sampling is better than both FUR and Fowler sampling.

CIRPASS was expected to be readnoise limited for J band observations below 2009 s (Section 9.6.1), hence FUR sampling was adopted for the detector readout scheme. This scheme has the advantage that double correlated sampling is available with the same data, if the background performance is not as expected. CIRPASS also uses more than one read for each ramp point, so that Fowler sampling also remains available.

FUR sampling assumes that the signal from the object is linear. This may not be the case for the object if atmospheric conditions are not perfect and is unlikely to be the case for the OH background in long exposures. In this situation the FUR data will be used by the quick-look pipeline to remove cosmic rays. The more detailed analysis will, however, use the double correlated data points or the Fowler points depending on the actual noise performance (ignoring the samples taken as the detector integrated). In this case, multiple exposures will be median combined to remove cosmic rays, before the spectra are extracted.

8.5 Further reduction: `dotarget`

The `dotarget` pipeline task reduces target object data. It expects a CIRPASS MEF file that has been produced by `docirpass` and outputs an (x,y,λ) MEF file (in Euro 3D format). The main component of the `dotarget` pipeline is the spectral extraction software. `Dotarget` optionally performs a number of other data reduction steps. Once the spectra have been extracted, wavelength calibration, flat fielding and flux calibration are available, if the appropriate pipeline calibration tasks have already been run. Background subtraction can also be incorporated into the pipeline if the

necessary data exists. Finally `dotarget` displays the reconstructed image of the IFU using the `idisplay` program.

8.5.1 Background subtraction

Sky subtraction is best achieved using two exposures, each with the object on a different part of the IFU. The two exposures form a beam-switch observation. In this way, the same fibre is used for both the object and background signal, which avoids systematic errors that may be induced by using different fibres. `Dotarget` optionally subtracts a background image, which will usually be part of a beam switched pair and will already have been reduced by `docirpass`. CIRPASS typically uses 30 minute observations comprising the total beam-switched pair (15 minutes per exposure).

8.5.2 Deviant pixels

The raw data suffers from both 'hot' and 'dead' pixels. About 1% of pixels are defective in this way. Hot pixels may have excessive dark currents or high quantum efficiencies (both of which can be corrected for), or they may simply be saturated from the outset. Dead pixels have unusually low signals that do not change over the course of an observation (within the limits of the readnoise). To prevent these pixels from impacting on the object signal, the spectra are recorded using several different parts of the detector array. This can be implemented using a dither observing pattern on the detector. In practice, however, the spectra are usually moved around the detector by moving the object on the IFU. The extracted spectra are then combined, rejecting spurious measurements.

8.5.3 Wavelength calibration

Wavelength calibration is performed by `doarc` and is obtained from observations of a standard arc lamp. The fibre spectra are extracted and arc lines identified in one fibre, to determine the wavelength scale for that fibre. The calibration is then reapplied and automatically scaled to the remaining fibres. The wavelength calibration for each fibre is written to the image header (in extension *sci,1*) of the multi-spec MEF file, for use by subsequent pipeline tasks. Wavelength calibration can also be obtained from the OH sky lines, present in every observation, if purely reflecting masks have been used.

8.5.4 Flat fielding

Two flat fields are required, a detector flat and a fibre flat. The detector flat removes pixel to pixel variations in sensitivity, and is necessary to ensure correct operation of the optimal extraction software. The illumination for this flat field should have the same pixel variation with wavelength as the observation, as pixels may have different sensitivities at different wavelengths. This flat field is obtained by illuminating the IFU with a continuum source, then slowly scanning the spectra across the detector in the direction parallel to the slit, whilst the detector is integrating (by moving the steering mirror yaw, Section 4.3). The scanning smears out the fibre profile in the slit direction, the total illumination across the detector should then be uniform.

The fibre flat field is used to remove variations in fibre throughput. Ideally these would be made from twilight flat fields to ensure that the spectrograph pupil is correctly filled, although observations of the illuminated telescope dome should provide an adequate approximation. If the fibre throughput is not a function of wavelength, then fibre flats can be obtained from observations of the OH night sky lines. The flux in each fibre from these lines should be identical for the small region of sky observed by the IFU. Thus the total OH flux detected by each fibre is an accurate measurement of the relative fibre throughputs.

The detector flat is primarily to allow correct operation of the optimal extraction software. It is not, therefore, imperative that the illumination is uniform over large pixel scales, provided that the same detector flat is used when generating the extracted fibre flat field spectra and extracted object spectra.

8.5.5 Telluric line removal, flux correction and calibration

Telluric absorption features from the Earth's atmosphere are very prominent in infrared spectra. The telluric lines do not scale linearly with airmass, thus to remove them, it is necessary to observe a standard star at roughly the same airmass as the science target. Hot (B) stars, which have relatively featureless spectra, or a solar analogue with a well known spectrum are good telluric standards. If different airmasses are used for the standard and object, it may be necessary to modify the spectrum of the telluric standard so that the centre and strength of its telluric lines match those of the object spectrum.

The telluric standard is, therefore, the best choice for the flux calibration standard, although a separate flux standard could be used and would require identical telluric correction before further use.

The flux calibration spectrum has units of flux-units/counts, where counts is the signal before flux calibration. `Dofluxcal` produces this spectrum in ordinary FITS image file format, based on the known spectrum of the standard and that observed. It is a single spectrum that should be the same for each fibre after the fibre flat fielding has been applied.

This reduction step may also be necessary to obtain the correct relative flux across a spectrum, as it removes, for example, the fibre, grating and detector response from the data. This would only be necessary if the fibre flat used was not a wavelength dependent flat field. However, the same fibre should then be used for observations of both the object and standard.

8.6 Current data reduction procedure

`Docirpass` and `dotarget` are the currently written and functioning pipeline tasks. Further reduction steps are currently up to the observer. The flow chart in Figure 8.9 shows the expected final data reduction pipeline, but contains as yet unwritten pipeline specific tasks. However, similar tasks are available in IRAF, and can be used on CIRPASS data outside of the pipeline. As experience with the instrument and reducing data from it grows, CIRPASS specific versions of these tasks will be written and added to the pipeline, and the pipeline will be refined to match the most commonly adopted data reduction procedure. The techniques used for reducing the commissioning observations in Cambridge are summarised below.

The observing procedure was to step the object across different lenses of the IFU. Typically, six positions of the object on the IFU were obtained, with the object light going down approximately three fibres owing to poor seeing and poor telescope tracking. Background subtraction was performed by subtracting adjacent observations, resulting in three beam-switched pairs. As the OH intensity varies on short time scales, particularly in Cambridge where the atmosphere is very unstable, it was not entirely removed by beam-switching. Thus an un-sharp masking technique was employed to further remove the background contribution from the OH. A rectangular median filter was applied over the image, having 20 pixels in the slit direction and 1 pixel in the dispersion direction. The median filtered image contains only signal from the OH lines, which can then be subtracted from the original beam-switched observation.

Wavelength calibration was performed on the OH image obtained above, using the OH lines, and stored for subsequent use on the object.

The resulting OH cleaned beam-switched pairs were then run through `dotarget`, using optimal fibre extraction, allowing the reconstructed IFU images to be displayed using `idisplay`. `Idisplay` allows the user to select lenses by clicking on them. When a lens is selected the relevant spectra is copied out of the multi-spec MEF file to a standard FITS file, and has the wavelength calibration contained in the corresponding OH image applied to it. Negative spectra are automatically multiplied by -1. Thus lenses with object data for all of the beam-switched pairs were selected, and then scaled, weighted and median combined, taking into account the wavelength calibration, using the IRAF task `scombine`. This process removes hot and dead pixels and cosmic rays from the data. It was used to produce all of the spectra given in Chapter 9.

8.7 Quick-look mode data reduction

In quick-look mode, `docirpass` and `dotarget` are run automatically with both pipeline scripts operating in a minimal mode. Optimal extraction of the spectra is not performed. Rather, the spectra are extracted by summing pixels perpendicular to a fibre's trace, which takes one sixtieth of the computational time. Raw images from the detector are quickly turned into an IFU image with minimal processing. This mode is especially useful when setting up CIRPASS. For example, when aligning the telescope field with the IFU, or focussing on the IFU it is helpful to see any changes in the IFU image quickly. It is also reassuring to see an image of the object on the IFU at the end of an observation. Jpeg images of the spectra obtained and the IFU image are created automatically. These images have names derived from the object and provide a convenient way to scan through an evening's observations when trying to locate data. Figure 8.12 is one such image.

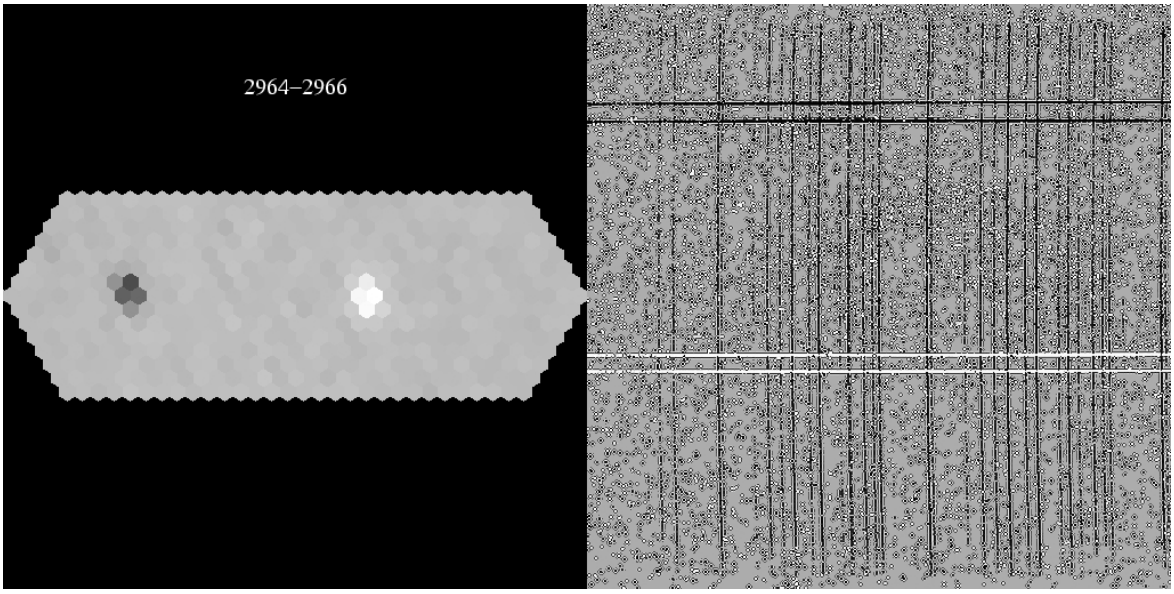

Figure 8.12: *A bookkeeping image automatically generated by the data reduction pipeline.*

CHAPTER 9

INSTRUMENT PERFORMANCE

9.1 Introduction

The performance of CIRPASS was quantified in the laboratory as part of its acceptance tests for use on the Gemini South telescope. The results of these tests are presented in this chapter.

The throughput of the instrument, that is, the percentage of detected photons compared to the number of photons entering the instrument, was determined using three independent techniques. Observations of a standard lamp, the night sky OH lines and Polaris were used, and the results are presented in Section 9.2. The throughput varies with lens on the IFU, mainly due to varying fibre throughputs; the relative performance from the elements that sample the telescope focal plane is presented in Section 9.2.4.

The optical performance was quantified using spot profiles obtained from argon lamp observations and is summarised in Section 9.3. The temperature stability of CIRPASS was determined from observations of the OH sky lines, whose positions on the detector should remain fixed. The thermal background performance and the temperature stability of the instrument are summarised in Sections 9.4 and 9.5.

The expected sensitivity of CIRPASS was modelled, using the measured performance figures presented in this chapter and throughout the thesis. The model and CIRPASS's expected limiting magnitudes are presented in Section 9.6. The analysis highlighted the sources of the instrument's noise, and showed that masking the OH skylines could potentially lead to an improvement of the instrument's sensitivity. The breakdown of the noise performance of CIRPASS is given in Section 9.6.1.

Observations were made with CIRPASS attached to a small telescope viewing the Cambridge night sky. The spectra obtained were used to quantify the instrument's sensitivity, independently of the measured performance of CIRPASS's various components. The data obtained and the deduced limiting magnitudes are presented in

Item	Efficiency
Magnifying lens (2 MLAR coated surfaces)	0.96
Field lens (2 MLAR coated surfaces)	0.96
IFU	0.70
Spectrograph collimator (1 mirror, SLAR coated surfaces)	0.91
Grating (wavelength dependent)	0.5 - 0.78
Spectrograph hardware suppression pass	0.79
Camera and steering mirror (1 mirror + 12 MLAR coated surfaces + filter)	0.65
Detector quantum efficiency (device and wavelength dependent)	0.5 - 0.8
Total	***7.5 - 18.8 %***

Table 9.1: *Throughput breakdown of CIRPASS's individual components.* The values for the IFU and grating were measured in the laboratory. The detector performance is as specified by Rockwell. The throughputs for the remaining optical components are based on the known performance of the relevant surfaces.

Section 9.7.

9.2 Throughput

The predicted performance of CIRPASS was initially based on a model combining the throughputs of each of CIRPASS's sub-assemblies. Once assembled, the throughput of the completed system was measured to check that it agreed with the model. Table 9.1 gives a breakdown of the throughput values used to determine CIRPASS's expected performance (for the telescope-independent components). The values used for each sub-item are based on measured performance figures before assembly. As a result, the values for the optical components are slightly less than any available manufacturer's specifications. A throughput of 0.97 for mirror surfaces, 0.967 for single-layer anti-reflection (SLAR) coatings and 0.98 for multi-layer anti-reflection (MLAR) coatings was assumed.

CIRPASS's throughput was checked using a standard lamp in the laboratory (Section 9.2.1), observations of the night sky lines in Cambridge (Section 9.2.2), and observations of Polaris using a small telescope in Cambridge (Section 9.2.3).

9.2.1 Throughput measurement from a standard lamp

The experimental set-up used to measure the throughput of CIRPASS from observations of a standard lamp is depicted in Figure 9.1. A minimal optical arrangement was deliberately used in order to avoid systematic errors or uncertainties. CIRPASS

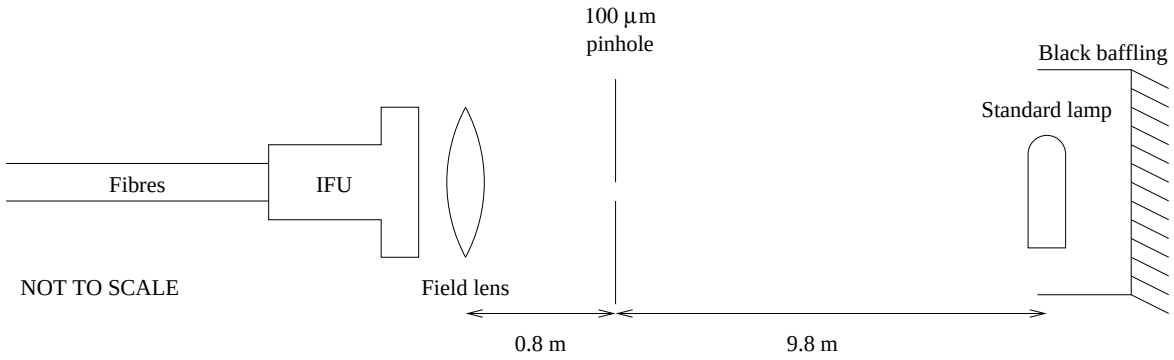

Figure 9.1: *Schematic outline of the experimental set-up used to determine the throughput of CIRPASS, from observations of a standard lamp.*

was operated in its final configuration inside the cold room. A standard lamp illuminated the field lens (on the front of the IFU), via a 100 μm pinhole. The lamp was a flux-calibrated source and was operated from a stabilised power supply. The pinhole size and pupil-to-lamp distance were chosen to avoid saturating the detector.

The experimental set-up was essentially a pinhole camera, with an image of the lamp formed on the IFU. The size of the pupil formed by the fibres at the pinhole position was 4.3 mm, and the image of the lamp on the IFU was smaller than the IFU. Thus, all light from the lamp passing through the pinhole would be detected (if the throughput were 100%). With this arrangement it is possible to 'beam-switch' the lamp image on the IFU, allowing the data reduction process to be very similar to that used on an astronomical object. An observation with a stop placed in front of the pinhole was also taken to provide an alternative background subtraction technique. This technique, however, has the disadvantage that light from sources other than the standard lamp could contribute to the detected signal. The experiment was carried out with the laboratory in darkness to minimise any unwanted signal, which would be orders of magnitude fainter than the signal from the lamp. The black baffling was to ensure that only light from the front of the lamp passed through the pinhole. Angling the baffling away from the IFU further reduced the chance of any reflected light reaching the IFU via the pinhole.

The throughput in J was measured with the cold room at room temperature (15°C), and in H with the cold room both at 15°C and at -40°C, in order to determine if the throughput was affected by operating the spectrograph in the cold room.

The throughput obtained in J (1.3 μm) was 7.0$\pm$0.5% using both a beam-switched pair and a background subtracted image. For H (1.54 μm), using both techniques, the throughput was 7.0$\pm$0.5% at room temperature and 6.9$\pm$0.2% with the refrigerator running. This is at the lower end of the predicted performance and is believed to be

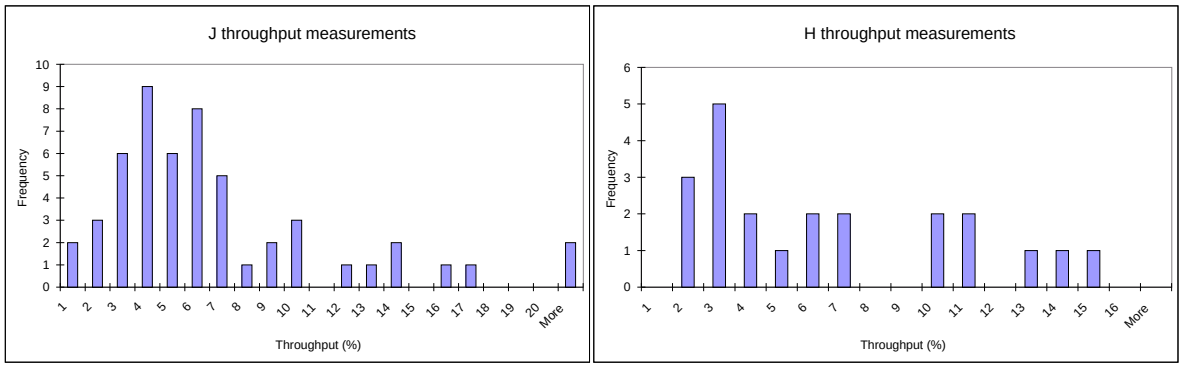

Figure 9.2: *Histograms showing the deduced throughput values from observations of the night sky OH lines.* The frequency is the number of OH lines that gave the corresponding throughput.

due to our detector operating at the lowest quantum efficiency (QE) value.

9.2.2 Throughput measurement from OH skyline intensities

The Cambridge night sky was observed through one of the laboratory windows. The experimental arrangement simply had the field lens in front of the IFU, directly viewing the night sky. The measured intensities of the OH lines were compared with the intensities published by Maihara et al. (1993), for all of the OH lines in the range 1.15 to 1.35 and 1.45 to 1.65 μm. Figure 9.2 shows histograms of the resulting throughput values. This technique is slightly inaccurate as the intensities of the lines in Cambridge may be quite different from those obtained by Maihara et al. from a clear Hawaiian sky, and is compounded by the fact that the intensities of the sky lines vary throughout the night. Furthermore, the J data was taken through the glass of the laboratory window, and the H data was taken on a slightly cloudy night. However, the data is in reasonable agreement with that obtained from the standard lamp.

The above data allowed an approximate estimate of the inter-line continuum to be made. As the fibre spectra do not cover the whole of the detector, the regions of the detector not directly illuminated by the fibres were used to quantify the scattered signal, which was then subtracted from the remainder of the image. This allowed the true continuum signal to be measured. For the H band Cambridge sky the measured continuum was 960 ± 128 photons/s/m^2/arcsec^2/μm which, when summed over the entire image, equated to $1/33$ of the total OH flux detected. This should be compared with the 590 photons/s/m^2/arcsec^2/μm equalling $1/50$ of the total OH flux, stated by Maihara et al. A higher continuum was expected to be observed in Cambridge as

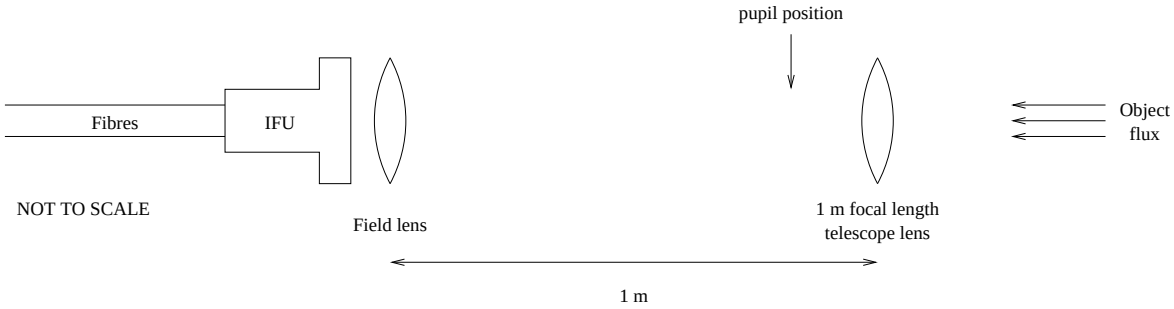

Figure 9.3: *Schematic outline of the simple telescope arrangement used to determine the throughput of CIRPASS from observations of Polaris.* The IFU entrance pupil projects to a 5.5 mm aperture at the telescope lens.

there is a considerable amount of light pollution, not least from very bright infrared lights used by security cameras outside the laboratory.

9.2.3 Throughput measurements from Polaris observations

Preliminary observations of Polaris were made with CIRPASS attached to a 5.5 mm telescope, with the cardinal aim of determining CIRPASS's throughput. The experimental arrangement is depicted in Figure 9.3. Although this was an extremely small telescope, it provided realistic test data as the full A-Ω product of the instrument was used. The scale on the IFU with this telescope was about 8 arc-minutes per lens, allowing the use of a static mount, with no need for tracking on Polaris. The IFU and the telescope (a simple plano-convex lens) were located in the CIRPASS laboratory looking out of a window. Two 1000 second exposures were taken and subtracted from each another. The telescope was moved between the two exposures so that Polaris was on a different lens of the IFU for each exposure. The raw and subtracted images are shown in Figures 9.4 and 9.5.

With this arrangement, the background sky flux is the same as it would be on a larger telescope, as the IFU lenses are each 8 arc-minutes across. However, as Polaris is a point source, the data is equivalent to that from a H$\simeq$17 star on an 8 m telescope in terms of photon arrival rates, readnoise, instrument background level, cosmic rays, hot pixels and other noise sources. The only difference is that the inter-OH sky brightness will be lower at a more favourable site than Cambridge.

The total throughput (from above the Earth's atmosphere to a file on disk) determined from this observation is 8%, slightly higher than the laboratory measured value described in Section 9.2.1.

The above measurements of CIRPASS's throughput suggest that the instrument will perform as expected. The value stated for the throughput is proportional to

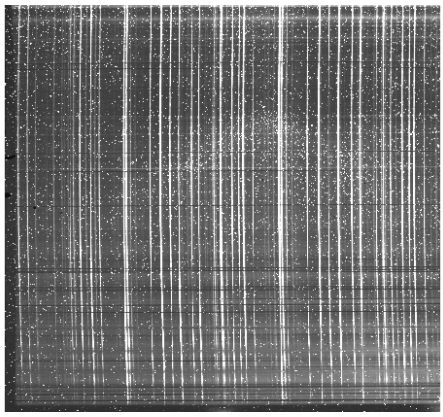

Figure 9.4: *Raw Polaris data obtained using a 5.5 mm telescope in Cambridge.*

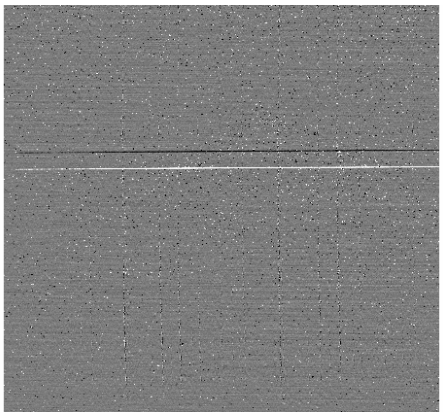

Figure 9.5: *Reduced data from the Polaris observations with a 5.5 mm telescope.* The sky subtraction was via beam-switching and, as can be seen, was very successful.

the gain used for the detector's readout electronics. The gain value also affects the stated noise performance in electrons. The gain was determined experimentally and is believed to be correct (Section 6.3.5). However, a more accurate indicator of the instrument's performance is the signal-to-noise obtained on a fainter astronomical object, where the detected photon rate is closer to the sensitivity limit of the instrument. This was the motivation for characterising CIRPASS using a small amateur telescope in Cambridge, as described in Section 9.7.

9.2.4 Uniformity of IFU and fibre slit

Observations of the OH background were used to quantify the relative performance for objects incident on different lenses of the IFU. The entire night sky spectrum obtained from each lens (or equivalently, fibre in the slit) was summed, using optimally extracted fibre spectra. Each lens should have received the same total counts from the sky, enabling their relative throughputs to be determined. Figure 9.6 shows the relative throughput for each of the fibres in the slit and Figure 9.7 shows a histogram of the same data. Figure 9.8 shows the reconstructed IFU image of the relative fibre throughputs. The calibration fibres have been smoothed out for these figures. There are a few fibres that have significantly lower than average throughputs, and a few that have slightly higher throughputs.

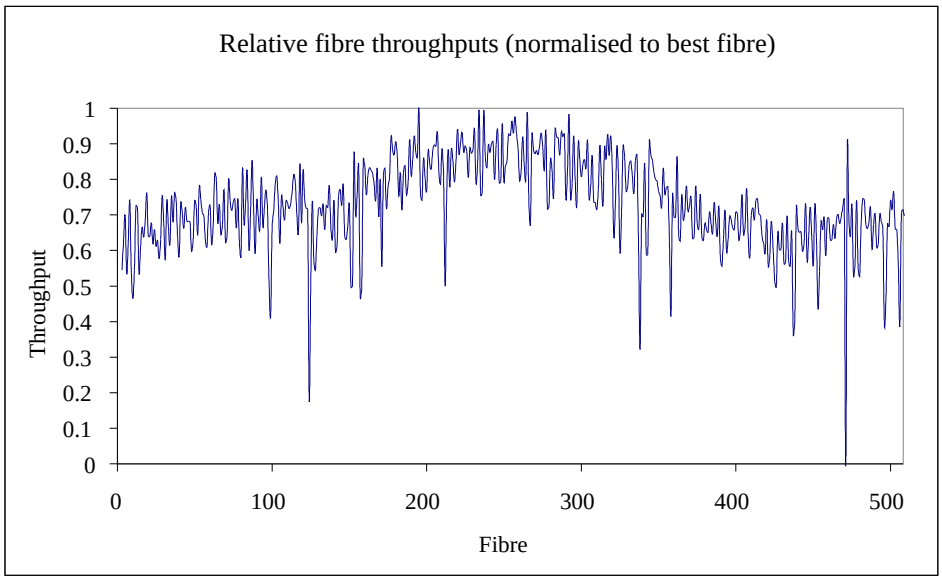

Figure 9.6: *Relative throughputs for each of the fibres in the slit.*

There appears to be a smooth variation of throughput with position in the slit, with the centre of the slit providing the best throughput. This should not be caused by vignetting within the camera or the spectrograph as the light beam is always narrower than any aperture. One explanation for the overall shape is that stray light from adjacent fibres contributes to a measured fibre's signal.

The throughput measurements presented above were obtained by averaging over the central range of fibres.

9.3 Optical quality

The spectra were focussed on the detector by moving the detector assembly, which can tilt the detector in two planes as well as changing its overall height. Thus, the number of degrees of freedom available is sufficient to allow uniform focus across the detector, even though the camera is chromatic. Figure 9.9 shows two typical arc line profiles in the dispersion direction, one for the centre and one for the edge of the detector, the profiles have FWHMs of 1.5 and 2.2 pixels respectively. Figure 9.10 shows typical line profiles in the fibre slit direction and the profiles have FWHMs of 1.8 and 3.0 pixels, for the centre and edge of the detector respectively. Figure 9.11 shows an arc line image taken with the calibration fibres, where the average line width is 1.98$\pm$0.22 pixels in the dispersion direction and 2.00$\pm$0.30 in the slit direction. The Zemax model for the camera optics predicted that 95% of the ensquared energy from a point source would lie within a 2 by 2 pixel box for 95% of the detector

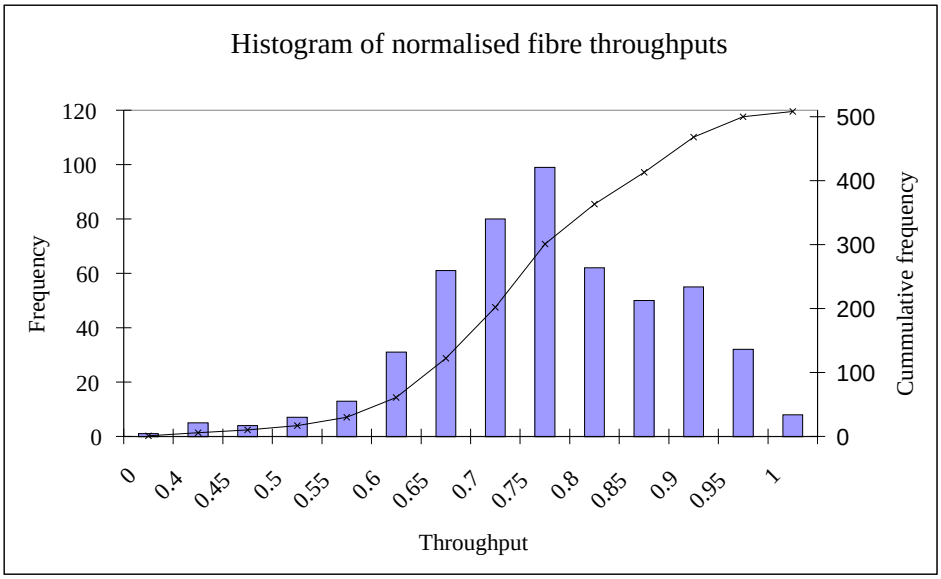

Figure 9.7: *Histogram showing the distribution of the normalised fibre throughputs.*

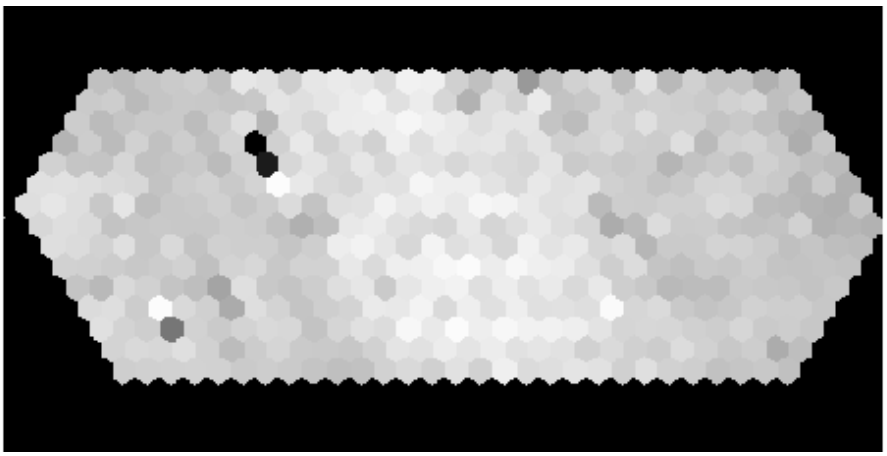

Figure 9.8: *IFU image, showing the fibre throughputs relative to the best fibre.*

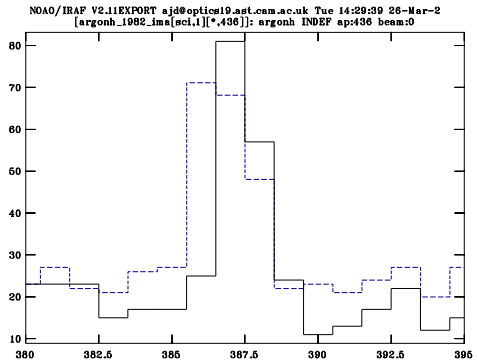

Figure 9.9: *Arc line profile in the dispersion direction.* The solid black line is a representative profile from the central section of the detector, the dotted blue line is a representative profile from the edge of the detector.

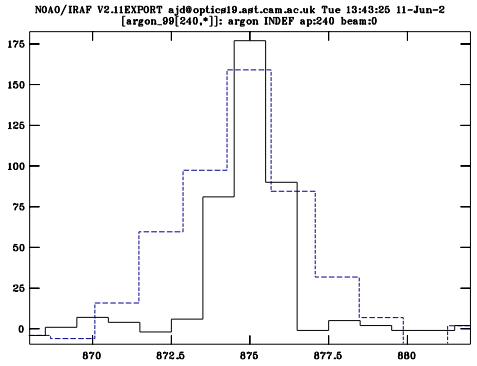

Figure 9.10: *Arc line profile in the fibre slit direction.* The solid black line is a representative profile from the central section of the detector, the dotted blue line is a representative profile from the edge of the detector.

Wavelength range	Filter combination	Background (e^-/pix/s)
Long J	Camblock 1 + 2	0.12
Short H	Camblock 1 + 3	0.13
Long H	Camblock 1	2.00

Table 9.2: *CIRPASS measured thermal backgrounds.* These values are detector dark subtracted.

area, suggesting that the performance of the optics is as expected. The predicted spot profiles from Zemax for the camera are given in Figure 9.12.

9.4 Instrument background

The cold room was operated at a constant −40°C, once the initial background testing had been carried out. A temperature of −40°C was chosen as this temperature could be automatically regulated. Operating at a temperature of −45°C (close to the cold room's performance limit) would require the hot gas regulation to be switched off, making the cold room temperature susceptible to changes in the external temperature of the laboratory. The thermal background was measured by placing the lens cap over the IFU so that a grey body at room temperature was observed, as well as the intrinsic background from the instrument. The backgrounds obtained, and used for the signal-to-noise calculations, are given in Table 9.2. The Long H performance in Table 9.2 is for camblock 1 located in the detector box. The performance is better

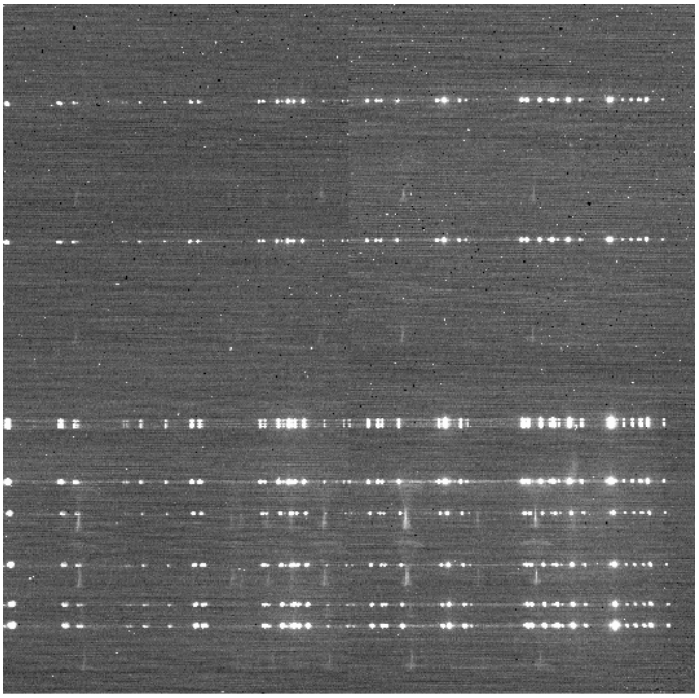

Figure 9.11: *Typical arc line image taken with the calibration fibres.*

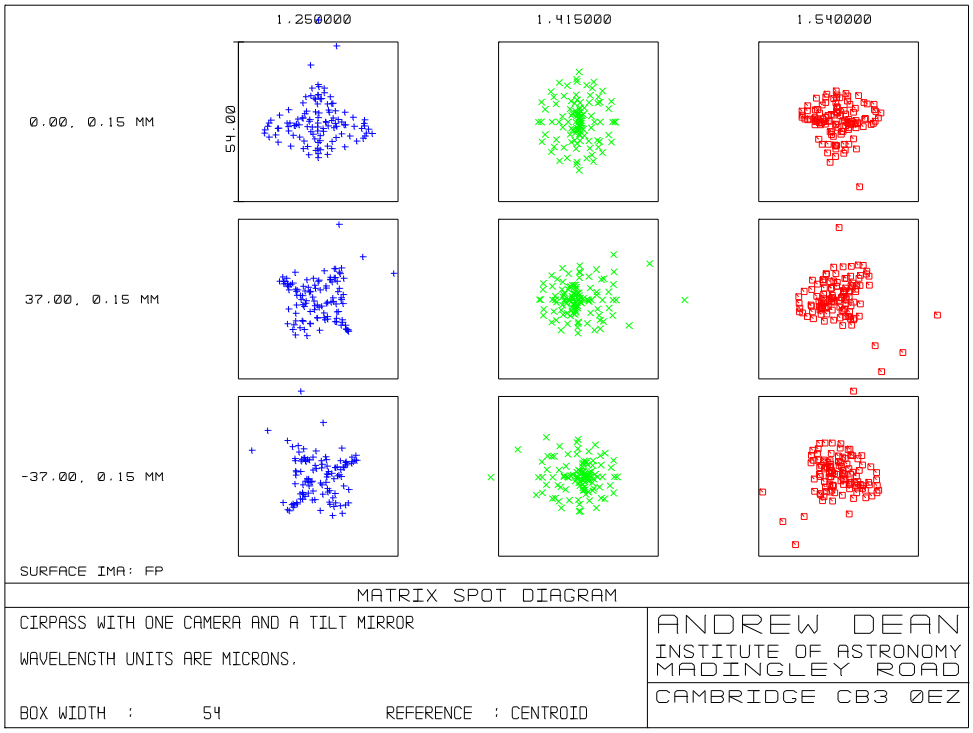

Figure 9.12: *Zemax predicted camera spot profiles, as a function of wavelength and position on the detector.* (Wavelength varies from left to right, detector position from top to bottom.)

than that given in Table 3.2 where camblock 1 was located in the filter wheel to allow the performance of each filter to be measured. With camblock 1 in the filter wheel, the detector can see the 'warm' (∼100 K) filter wheel and associated support, which would otherwise be blocked.

9.5 Temperature stability

Measurements of the temperature stability of the system were made using the position of the OH sky lines on the detector as a reference. A number of short-exposure (15 minute) OH observations were taken and the cold room temperature was logged at 5 minute intervals over the course of all the OH observations. The OH spectral images were cross-correlated with the first image to determine their positional shifts with time; the results are shown in Figure 9.13. The corresponding variation of the cold room temperature with time is shown in Figure 9.14. The position of the OH lines clearly follows the cold room temperature, which had a 0.7°C temperature cycle. In normal operation the cold room temperature remains constant to 0.1°C (Section 3.4). With this temperature stability, the position of an OH sky line on the detector remained fixed to an accuracy of better than 0.04 pixels for the duration of a $2\frac{1}{2}$ hour observation. This is sufficiently high to have little effect on the optical quality of the images and hence on the spectral resolution obtained or the accuracy of the fibre extraction algorithm.

9.6 CIRPASS signal-to-noise performance

A model was set up to determine the expected signal-to-noise (S/N) performance of CIRPASS. The detected object signal, S, can be predicted using Equations (9.1), (9.2) and (9.3).

$$F = F_o \times 10^{-\frac{m}{2.5}} \tag{9.1}$$

$$\gamma = F\frac{(\lambda \times 10^{-6})}{hc} \tag{9.2}$$

$$S = \gamma A_{Tel}\frac{\Delta\lambda}{10000}\frac{\epsilon}{100}t \tag{9.3}$$

Equation (9.1) gives the object flux, F (W/m^2/μm), for a point source of magnitude m, where F_o is the flux for a 0 magnitude object at that wavelength. Values

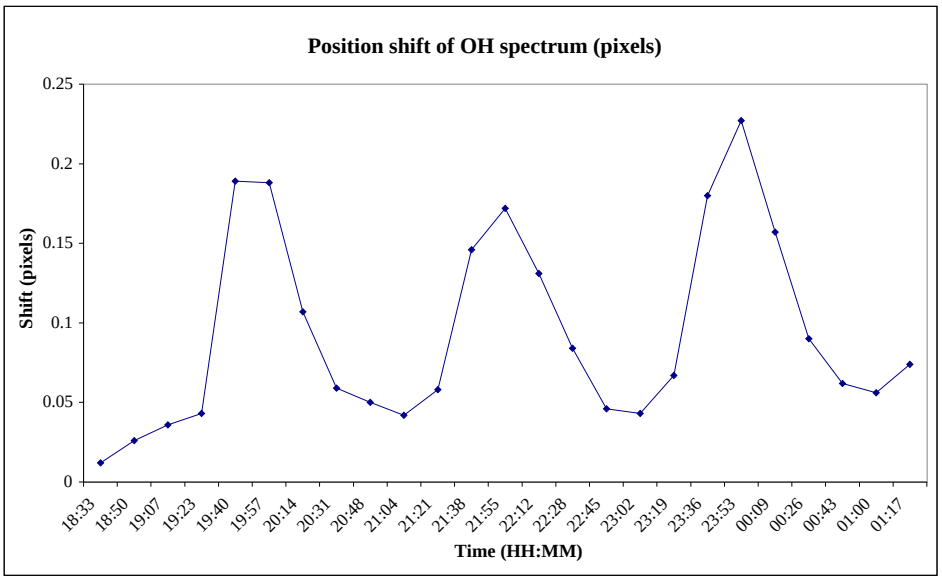

Figure 9.13: *Position of the OH spectra on the detector with time, as a function of the cold room temperature.*

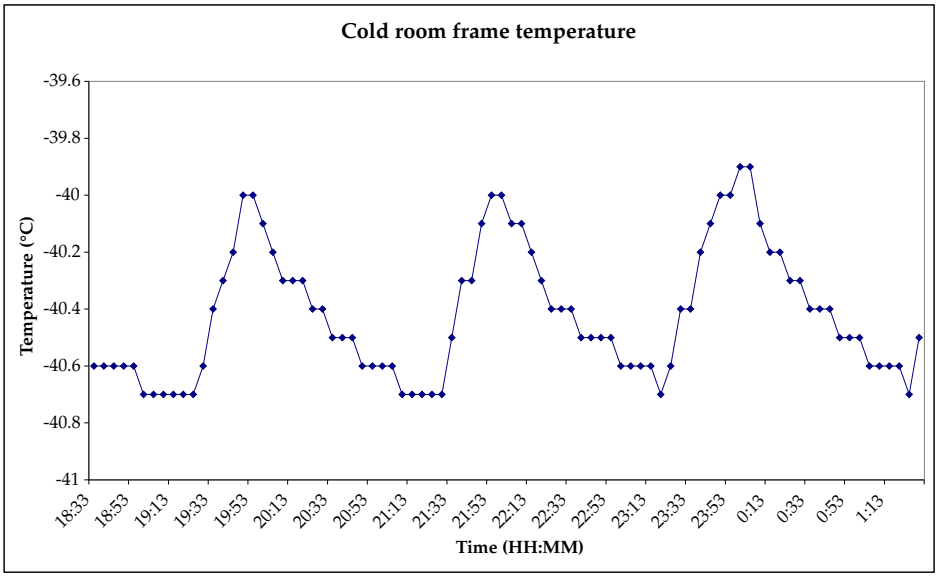

Figure 9.14: *Variation of the cold room temperature with time, for the same period shown in Figure 9.13.*

for F_o of 3.21×10^{-9} W/m^2/μm for J (1.25 μm) and 1.08×10^{-9} W/m^2/μm for H (1.65 μm) were used (MacKenty, 1997). The flux was converted to a photon rate γ (photons/s/m^2/μm) using Equation (9.2), where λ (μm) is the wavelength being observed, h (Js) is Planck's constant and c (m/s^2) is the speed of light. The object counts, S (e$^-$/SRE) are then given by Equation (9.3), where A_{Tel} (m^2) is the telescope area, $\Delta\lambda$ is the wavelength coverage of 1 spectral resolution element (SRE) (Å), ϵ (%) is the combined throughput of the instrument and telescope and t (s) is the total

exposure time. The object counts are assumed to be independent of the number of lenses receiving object light and are determined by summing over the relevant SREs.

The model includes noise contributions from the object and all background signals, including scattering within the instrument. The sensitivity achieved also depends on the number of lenses receiving object light, n_{lens}, or equivalently, the number of SREs summed to determine the object flux. Summing over lenses degrades the S/N performance as the noise contribution from the background signal is increased.

The total noise on an observation, N (e^-) is given by Equation (9.4).

$$N^2 = S + \beta\left(C_{inst} + D + B + R^2\right) \tag{9.4}$$

where C_{inst} (e^-) is the total detected counts from the instrumental inter-line continuum, D (e^-) is the total dark current, B (e^-) is the total thermal background and R (e^-) is the total readnoise. β is a background subtraction factor that quantifies the accuracy of the background subtraction. The observing pattern is assumed to be one observation of the object and one of the background, hence β=2. β=1 represents perfect background subtraction. (The background observation could also contain object data if a beam-switch observing pattern were adopted. This approach would result in a factor of $\sqrt{2}$ improvement in the S/N achieved, provided the object were sufficiently small to allow observation with a different part of the IFU.)

The background components in Equation (9.4) were calculated using the following formulae:

$$\begin{aligned}
C_{inst} &= n_{lens}(C_{sky} + C_{scat}) \\
C_{sky} &= c_{sky} A_{Tel} A_{Lens} \frac{\Delta\lambda}{10000} \frac{\epsilon}{100} t \\
C_{scat} &= \gamma_{sky} IFU_{lens} A_{lens} A_{Tel} \frac{\psi}{100} \frac{p_{sre}}{p_{det-fib} p_{det-disp}} \Lambda \frac{\epsilon}{100} t \\
p_{sre} &= p_{disp} p_{fib} \\
\Lambda &= \frac{p_{det-disp}}{p_{disp}} \frac{\Delta\lambda}{10000} \\
D &= d p_{sre} n_{lens} t \\
B &= b p_{sre} n_{lens} t \\
R &= r\sqrt{2 n_{lens} p_{sre}}
\end{aligned}$$

where, C_{sky} (e^-) is the detected interline continuum from the sky and C_{scat} (e^-) is the detected continuum from the scattered total sky background. c_{sky} (photons/s/m^2/arcsec^2/μm) is the intensity of the night sky continuum and

the Maihara et al. (1993) value of 590 photons/s/m^2/arcsec^2/μm was used. γ_{sky} was obtained from Equations (9.1) and (9.2), using the Herbst (1994) values for the sky brightness of J=15.2 and H=14 mag/arcsec^2. These magnitudes include the contribution from the OH sky lines and the inter-line continuum. IFU_{lens} is the total number of lenses in the IFU and A_{lens} (arcsec^2) is the area of an IFU lens on the sky. CIRPASS has hexagonal lenses, hence their area is $\frac{\sqrt{3}}{2}w^2$ where w (arcsec) is the lens diameter (measured across parallel edges). ψ (%) is the scattering within the instrument and Λ (μm) is the total wavelength coverage of the spectrograph. p_{sre} is the number of pixels in a spectral resolution element, and is composed of p_{disp} pixels in the dispersion direction and p_{fib} pixels in the cross-dispersion direction. $p_{det-disp}$ is the total number of detector pixels in the dispersion direction and $p_{det-fib}$ is the total number of detector pixels in the fibre slit direction. d (e$^-$/pix/s) is the detector dark current and b (e$^-$/pix/s) is the thermal background from the instrument. Fowler sampling was assumed, to reduce the readnoise to r e$^-$/read, from an NDR readout mode (5 reads were assumed with a single readout having a readnoise of 17 e$^-$). The factor of $\sqrt{2}$ in the equation for R is necessary as the measured object counts are deduced from two readouts of the detector. (The detector is read out at the start and end of an observation. The first readout determines the reset level and the second contains the object signal.) The signal-to-noise ratio obtained is then given by $\frac{S}{N}$.

A spreadsheet was set up based on the above equations. The spreadsheet calculates the S/N obtained using the input parameters discussed above. Table 9.3 summarises the instrument configuration contained in the spreadsheet, which also uses the thermal backgrounds presented in Table 9.2. The input parameters can easily be changed in the spreadsheet to match the object and sky magnitudes and any variation in the performance of the instrument.

The limiting broadband magnitudes obtained assuming a flat spectral energy distribution, for a 3 hour observation of a point source resulting in a S/N of 5, are presented in Table 9.4. Values are given for object light entering 1, 4 and 7 lenses. These numbers of lenses give an increasingly larger contiguous area on the IFU, provided the object is optimally located. The number of IFU lenses receiving light from a point source depends on the IFU scale chosen and the seeing. The equivalent line fluxes per SRE are given in Table 9.5. For comparison, the expected Hα line flux from a galaxy at redshift z=1, with a star formation rate (SFR) of 1 $M_\odot$/year would be 1.5×10^{-17} ergs/s/cm^2. (Bunker, private communication, and using the prescription of Kennicutt (1983)). This flux would give a S/N of 10 in a 2 hour exposure with CIRPASS on an 8 m telescope.

Parameter	Symbol	Value	
Telescope diameter	d_{tel}	8	m
Exposure time	t	10800	s
Diameter of lens on sky	w	0.36	arcsec
Spectral resolution	$\Delta\lambda$	4.4	Å/SRE
Pixels per SRE	p_{sre}	4	pixels
Number of lenses	n_{lens}	490	lenses
Throughput (CIRPASS)	ϵ_{cirp}	8	%
Throughput (telescope)	ϵ_{tel}	67	%
Readnoise (via Fowler sampling)	r	7.6	e^-/read
Dark current	d	0.05	e^-/pix/s
Scattering	ψ	18	%

Table 9.3: *Instrument and telescope parameters used when determining the S/N performance of CIRPASS.* (The total throughput, ϵ (%), is given by: $\epsilon = \frac{\epsilon_{cirp} \times \epsilon_{tel}}{100}$)

Wavelength band	Number of object lenses		
	1	4	7
J	21.3	20.5	20.2
Short H	20.3	19.6	19.3
Long H	19.3	18.6	18.3

Table 9.4: *CIRPASS limiting magnitudes for a S/N of 5 from a 3 hour exposure, a flat spectral energy distribution is assumed.*

Wavelength band	Number of object lenses		
	1	4	7
J	4.4	8.8	11.6
Short H	3.6	7.1	9.4
Long H	9.0	18.0	23.8

Table 9.5: *CIRPASS limiting line fluxes (10^{-18} ergs/cm^2/s) per 4.4 Å SRE, resulting in a S/N of 5 from a 3 hour exposure.*

Noise source	J=21.3 H=19.3 (Long) Noise (e^-/pixel)	
Object	14.3	23.4
Sky continuum	14.6	14.6
Thermal background	36.0	147.0
Detector dark	23.2	23.2
DCS detector readnoise	10.7	10.7
Scattered OH (@18%)	32.3	37.5

Table 9.6: *Breakdown of the noise sources present in a 3 hour exposure.* The J and H magnitudes are those for a S/N of 5.

9.6.1 Noise performance

A breakdown of the various components contributing to the noise on a single observation with CIRPASS is given in Table 9.6. As can be seen, the dominant noise source for a 10800 second exposure is from the thermal background for both J and H observations. The poor background performance in long H clearly has a significant impact on the noise performance of the instrument. The noise from the thermal background in long H is 4 times larger than that from the scattered OH, the second largest contributor. If Fowler sampling were not adopted, then the DCS detector readnoise would be 24 e^-/pixel, which is in line with the combined noise from the thermal background, dark, scattered OH and sky continuum for a 262 s exposure in H and a 2009 s exposure in J. Thus, as the optimal data reduction strategy depends on whether the observations are readnoise or background limited (Section 8.4), it will depend on the length of the observation.

The specified thermal background for both J and long H, with the appropriate filters, was 0.05 e^-/pix/s. If these backgrounds were achieved, but the performance otherwise unchanged, the limiting magnitudes would be J=21.4 and H=20.5.

The scattered OH provides the second most significant contribution to the noise sources. If the OH were masked, effectively reducing the scattering to 0% but with the thermal background at its current value, the limiting magnitudes for a 3 hour observation with a S/N of 5, become J=21.5 and H=19.3. (The H performance actually improves by 0.03 magnitudes with no scattering.) The instrumental interline continuum is equivalent to 4471 photons/s/m^2/arcsec^2/μm with 18% scattering in H, compared with the potential 590 photons/s/m^2/arcsec^2/μm with no scattering.

With both 0% scattering and a background of 0.05 e^-/pix/s, the limiting magnitudes become J=21.7 and H=20.8, an improvement of J=0.4 and H=1.5 over those currently obtained. Thus, reducing the thermal background is more important than

masking the OH for H band observations, with the current relatively high thermal background. For the J band observations, where the thermal background is not as dominant, the improvement in the limiting magnitudes is marginally better from OH masking than from reducing the background. For both bands, however, a more significant gain is made by masking the OH once the thermal background has been reduced to a level comparable with the detector dark current.

The noise present on CIRPASS data is one factor that limits the instrument's sensitivity. The above calculations provide a guide to the expected performance but do not take into account systematic errors that may be present, both in the model or intrinsic to the observing procedure. For example, if the measured gain were inaccurate, then the throughput and readnoise would also be inaccurate, furthermore, the accuracy of the background subtraction was not known. The possibility of systematic errors provided further motivation for characterising CIRPASS using a small telescope in Cambridge. The noise present in a reduced object image, from Cambridge observations, was used to fully quantify the performance of the instrument (Section 9.7). The sky observations contain object data of known magnitude, allowing the S/N ratio obtained by CIRPASS to be measured independently of the detector gain or system throughput.

9.7 Commissioning observations using an 8 inch telescope in Cambridge

In order to test CIRPASS's on-sky performance a small telescope was used in Cambridge. The telescope was an 8-inch Celestron on a ALTER D-6 equatorial mount[1]. A combination of a Linos Photonics and Kanya framework was assembled to support CIRPASS's IFU and fibre feed, the Celestron and a Star-light Xpress MX5 CCD guiding system. Figure 9.15 is a photograph of the assembly being set up for an evening's observing outside the laboratory in Cambridge.

The versatility of CIRPASS meant that it could be operated on a small telescope by simply changing the fore-optic's magnifying lens. A 48 mm focal length magnifier was used to match the Celestron to the IFU, giving an image size of 15.75″ per lens and a field size of 9.71′ x 3.94′. The collecting area of the Celestron is 1553 times less than that of an 8 m telescope; thus, the same object flux would be obtained from an object 8 magnitudes fainter on the larger telescope, but with the same sky

[1]The mount was purchased from Green Witch Astronomy.

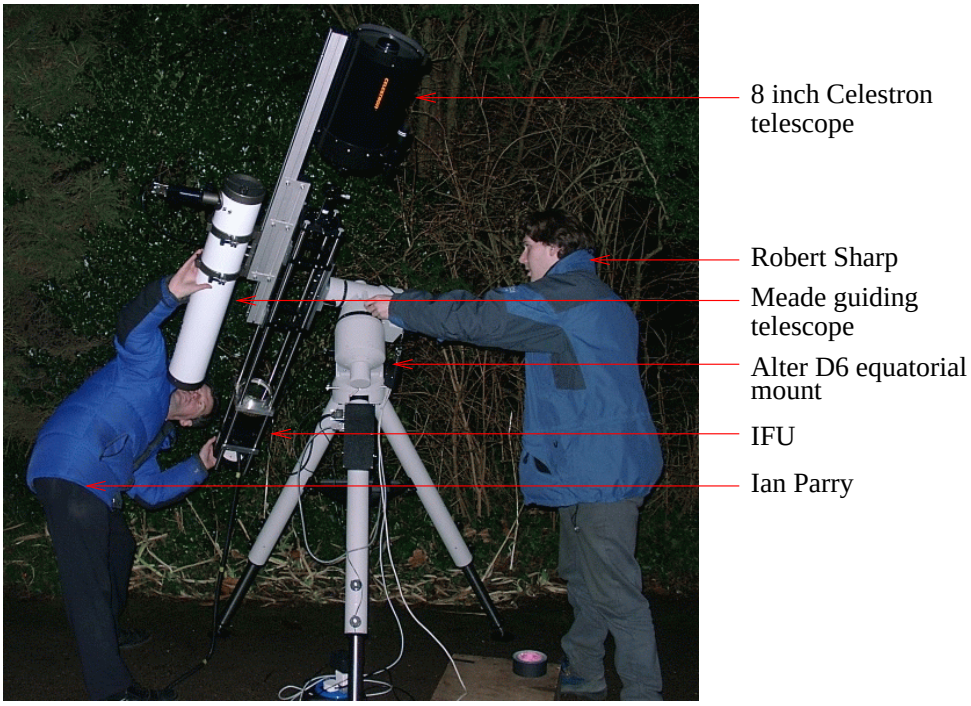

Figure 9.15: *The telescope arrangement used with CIRPASS for Cambridge test observations.*

background signal (assuming the sky background were the same at both sites).

CIRPASS was assembled and operating in the laboratory in Cambridge and the configuration was as it would be at a telescope. The refrigeration plant was maintaining the cold room at a temperature of -40 ± 0.1°C. The instrument control electronics and computers were moved into a 'control-room' section of the laboratory. No use was made of external computing facilities, that is, the instrument was running completely stand-alone. Data obtained was reduced using the custom written CIRPASS pipeline, in order to determine the functionality of the software in a telescope environment.

Observations were made over a few nights. The first night was used to align the optical components (the Celestron, CCD guide system and finder telescope) and to assess our data reduction software. Bright objects, Jupiter, Pollux and Arcturus were observed for this purpose. The quick-look data reduction software worked well, producing reconstructed images of the IFU in under 30 s. Consequently, it was a straightforward task to align the IFU with the Celestron and finder telescope. Figure 9.16 shows a beam-switched IFU image on Jupiter and Figure 9.17 shows the extracted spectrum. The strong absorption beyond 16200 Å is due to methane. Atmospheric water absorption can be seen at the short wavelength end of the spectrum. Figure 9.18 shows the observed Arcturus spectrum.

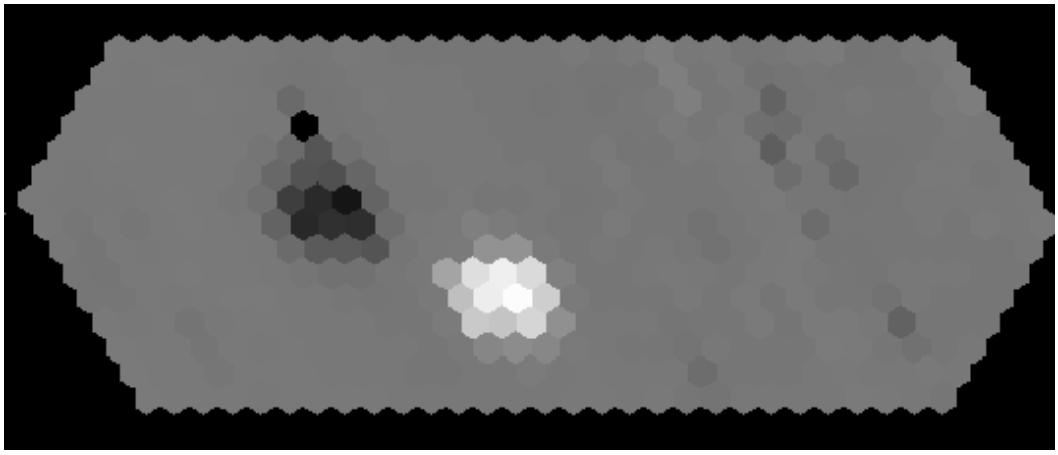

Figure 9.16: *Reconstructed IFU image of the beam-switched Jupiter observations.*

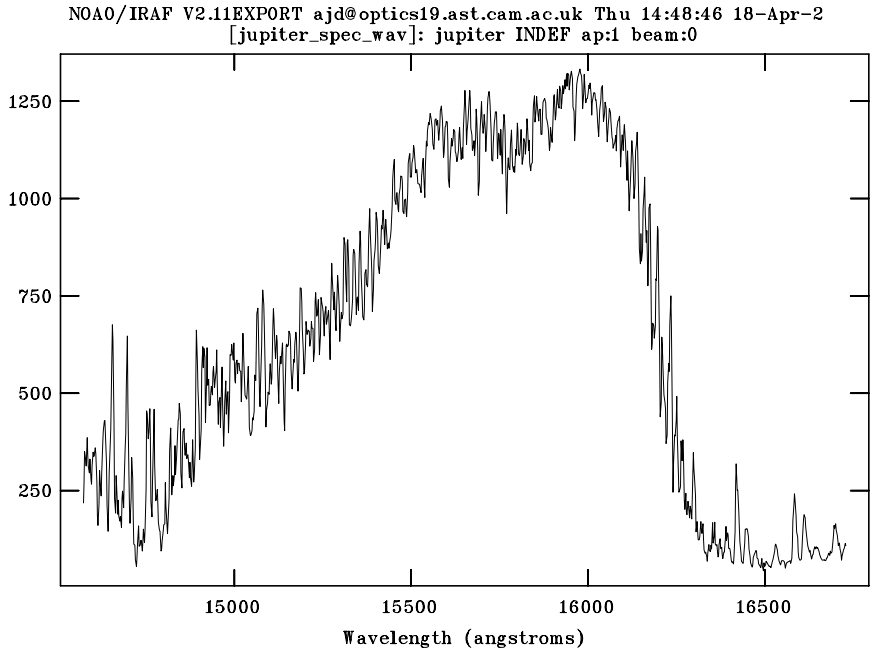

Figure 9.17: *Spectrum of Jupiter obtained from a 180 s Exposure.*

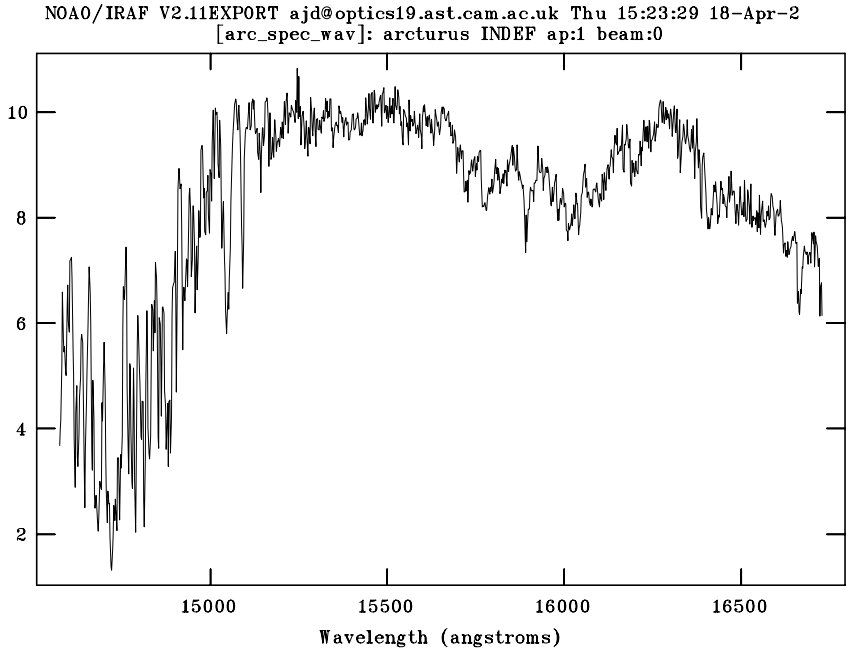

Figure 9.18: *Spectrum of Arcturus obtained from a 1800 s exposure.*

The process of assembling the telescope outside the laboratory (by passing the fibres through a convenient window), was time-consuming. We also had problems with dew forming on the Celestron and a very bright infrared security light illuminating the telescope. For these reasons, subsequent observations were made with the telescope inside the laboratory, but looking out of an open window. This considerably limited the area of observable sky. There were, however, plenty of stars in the region available that could be tracked for two hours.

Observations were again made of Polaris, but over the full wavelength range available with CIRPASS. The resulting spectrum is presented in Figure 9.19.

Observations were also made of HIP 3006, a F8, V=7.14 star (H$\simeq$6). This data was used to determine CIRPASS's on-sky S/N performance. A beam-switch observing approach was adopted, comprising 6 individual observations each lasting 600 s. Thus the spectrum obtained, presented in Figure 9.20, is from a 1 hour total observation. The throughput measured from the HIP 3006 detected counts was 6% and is the combined throughput of the Celestron telescope and CIRPASS.

Figure 9.21 is the spectrum obtained from a sky-subtracted area of blank sky, which has no systematic error giving a false non-zero flux level. The noise present in this spectrum is completely consistent with Poissonian errors, demonstrating that the sky-subtraction for CIRPASS worked correctly.

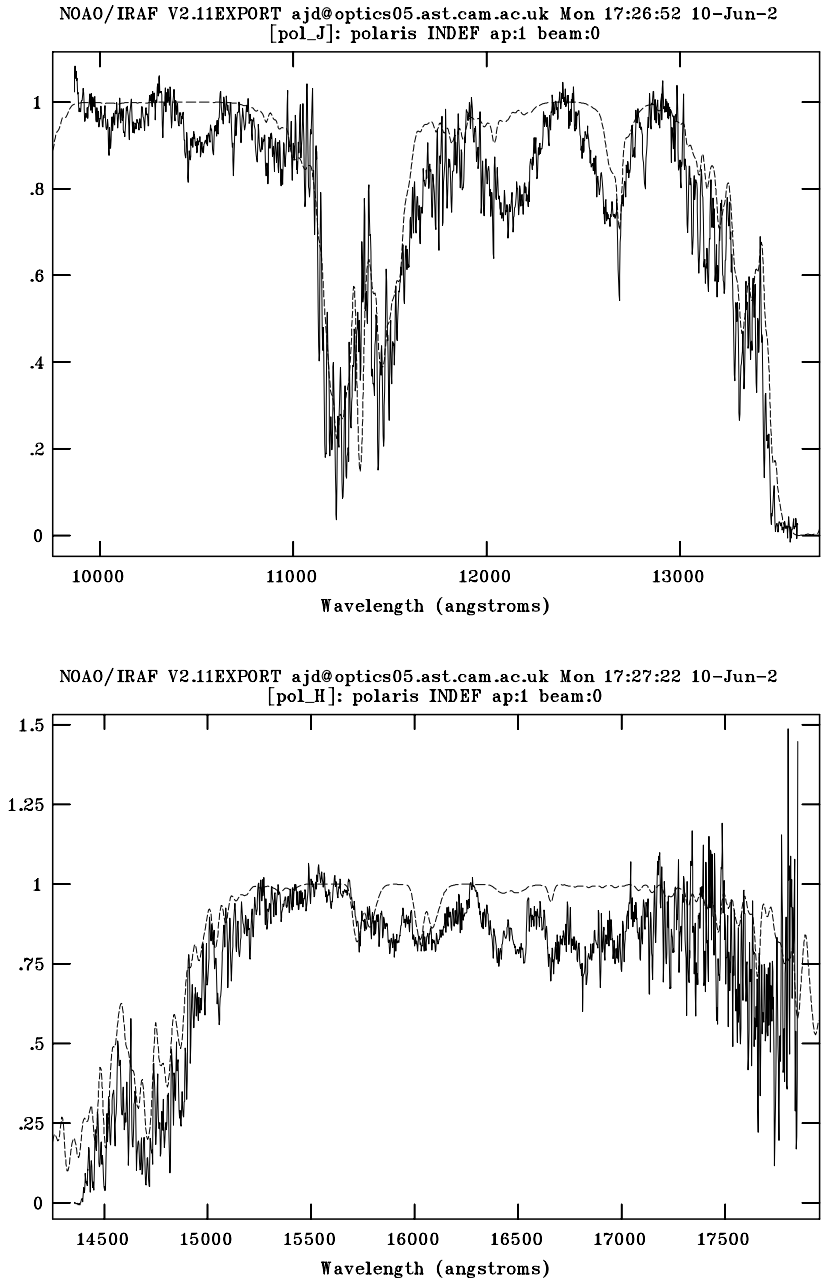

Figure 9.19: *J and H band spectra of Polaris.* The spectra are from a 40 s total exposure, for each of the four observations required to cover the whole wavelength range. The dotted line shows the Mauna Kea atmospheric transmission to the power of 5, suggesting that for these observations, the Cambridge sky was approximately 5 times poorer than that usually present at Mauna Kea.

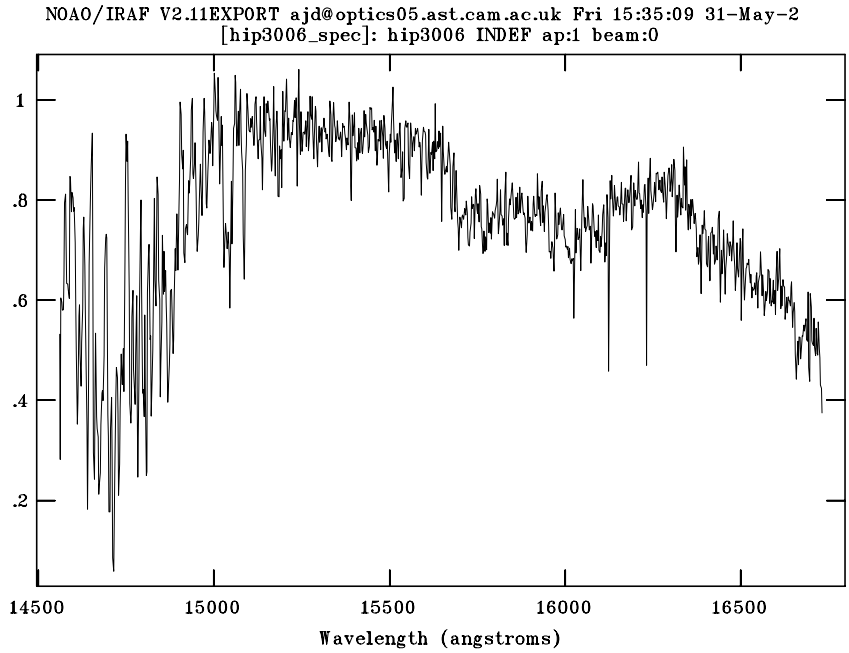

Figure 9.20: *The spectrum obtained from a 1 hour observation of the star HIP 3006.*

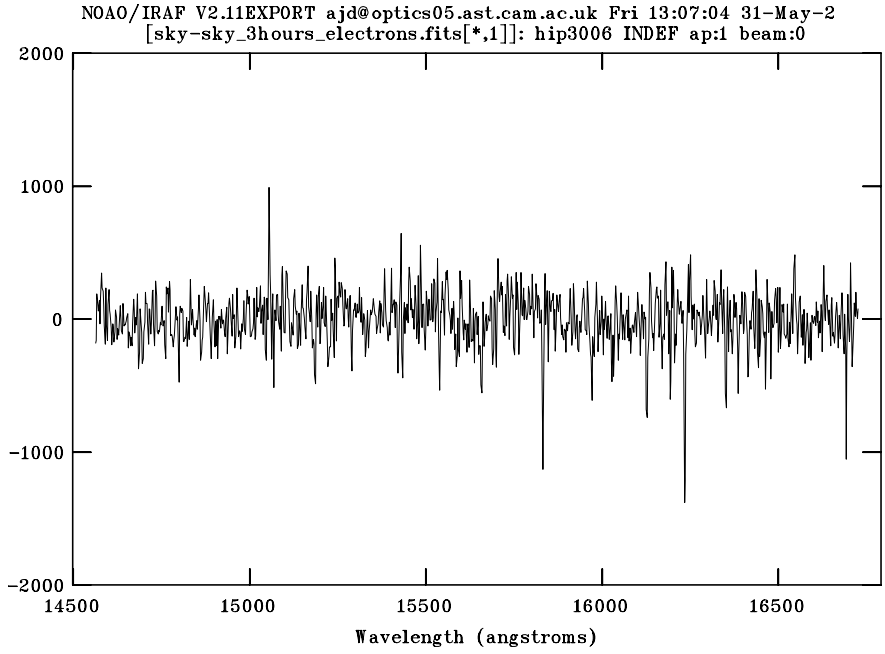

Figure 9.21: *Noise spectrum extracted from a 1 hour total sky observation.*

For Figure 9.21 the spectral units are detected photons per 2.2 Å bin (1 pixel wide at the detector). Observation of an emission line with a flux of 3.7x10^{-21} W/m^2 on a 8 m telescope with 6% throughput, would give 1000 detected photons in the line. With a 2 pixel SRE, this line would appear as a spike at 500 photons superimposed on the noise spectrum, which corresponds to a S/N ratio of 5. This line flux corresponds to a broadband magnitude of H=20.27. The determined performance is better than the S/N of 4.5 predicted by the model for this magnitude, background subtraction strategy, and a throughput of 6% (Celestron plus CIRPASS). Thus, the noise present in CIRPASS data is overestimated by the model. The model's deliberate use of the most pessimistic values for the instrument's thermal background and amount of scattered OH is the most likely cause of the discrepancy.

The Cambridge observations, therefore, suggest that the on-sky performance of CIRPASS is slightly better than was modelled.

CHAPTER 10

SUMMARY, CONCLUSIONS AND FURTHER WORK

10.1 Instrument description

The thesis has covered the design, construction and performance of the Cambridge Infrared Panoramic Survey Spectrograph (CIRPASS). CIRPASS provides integral field spectroscopy from 0.9 to 1.8 μm, with a wavelength coverage of 0.225 μm per exposure. In order to minimise noise sources, the spectrograph operates in a cooled enclosure at -40°C, and has the capability to remove, both in hardware and software, the dominant sky background from OH line emission. CIRPASS was developed from the COHSI spectrograph and a number of improvements were incorporated, including a larger integral field unit and a HAWAII 1K detector (Chapter 1).

10.2 CIRPASS fibre components

The CIRPASS spectrograph has a fibre slit, fed from a 499 element IFU that can sample the telescope focal plane at a number of different scales. A new fibre feed was successfully built for CIRPASS following techniques similar to those used for the COHSI and SPIRAL fibre feeds. CIRPASS is a versatile instrument that can easily be matched to a wide variety of telescopes. An interface was built to connect CIRPASS to the Gemini-S Telescope. This interface provides remote alignment of CIRPASS with the telescope, the facility to change image scale on the IFU, and illumination of the IFU with calibration sources (Chapter 2).

10.3 CIRPASS background sources and noise minimisation

The thermal background detected by CIRPASS was modelled, assuming blackbody emission from the instrument. The analysis showed that a significant thermal background would be detected, particularly from radiation with wavelengths above 1.8 μm. To counter this, new filters were designed for use with CIRPASS. In addition, a large part of the instrument that would otherwise operate at room temperature was cooled to -40°C.

An industrial cooling system, using an insulated enclosure maintained at -40 ± 0.1°C, was adopted. The entire spectrograph and cryogenic camera were operated in this cooled enclosure, which has external dimensions of $\sim 2\times3\times1.5$ m. Temperature-regulated liquid refrigerant was used to cool the enclosure, while a fan inside the cold room ensured a uniform temperature throughout. The chosen cooling solution was highly successful, relatively cheap and caused no technical problems, compared with an alternative solution of a vacuum-tight, LN_2-cooled cold room.

The background signal detected by CIRPASS was also minimised using filters. The performance of the filters purchased for CIRPASS was, however, slightly below specification resulting in a higher background than desired. Cooling to -40°C significantly reduced the thermal background detected by the instrument, and reduced the impact of the below standard filter. New filters are awaited (Chapter 3).

10.4 Spectrograph and OH suppression

The CIRPASS spectrograph was built using the large optics of the COHSI suppressor and forms a R$\sim$3100 spectrum on a mask surface. The mask allows hardware suppression of the OH sky lines, reducing the amount of scattered light within the spectrograph. CIRPASS was commissioned without suppression masks to allow the OH night sky to be fully quantified and optimal masks to be made. If the OH sky were suppressed in hardware, the reduction in background from scattered OH would mean an increase in limiting magnitude of J=0.2 and H=0.03, as CIRPASS has 18% scattering. This improvement in performance is lower than may intuitively be expected, as the dominant noise source in CIRPASS is from the thermal background and not scattered OH (Chapters 4 and 9).

10.5 Cryogenic camera

The spectrum on the mask surface is imaged via a cryogenic camera and the spectral resolution at the detector is high enough to allow software OH suppression. The camera is newly built and operates in the cooled environment at −40°C. The camera is cooled using liquid nitrogen and the detector temperature achieved is 86 K, with a stability of better than 0.5 K. No attempt was made to correct chromatic aberrations when designing the camera, allowing rapid construction through easily available optical materials. The chromatic nature is corrected by tilting the detector in the dispersion direction. The detector mount provides for focussing the camera and was successfully implemented using cryogenic stepping motors.

Operating the camera in the −40°C cold room caused problems with its O-ring sealed joints, particularly those used at the LN_2 ports, which experience temperatures below −100°C. O-rings specified to work to at least −60°C were required for all joints. It was also necessary to heat and insulate the O-ring joints at the LN_2 ports to maintain their temperature above −30°C, particularly during an LN_2 fill. This solution worked well but is not ideal, favouring a redesign of the joint (Chapter 5).

10.6 Detectors

CIRPASS uses HAWAII infrared detector arrays from Rockwell Scientific. The performance of the 1K detector array used to commission the instrument was quantified and found to be in reasonable agreement with that stated by Rockwell. The quantum efficiency of the CIRPASS detector used for the tests presented in this thesis, however, appears to be at the lower end of the stated efficiency of 50 to 80%. The detector readnoise was slightly higher than expected from previous experience with CIRPASS's detector readout electronics. As a result, a number of improvements to this system are planned. The camera was designed for use with a HAWAII 2K array, which would double the wavelength coverage currently available in one observation. The 1K detector will be replaced with a 2K once its performance has been fully characterised (Chapter 6).

10.7 Instrument and data reduction software

Instrument control and data reduction software were specifically written for CIRPASS to allow optimal use of the instrument to be made at the telescope. The instru-

ment control software provides an integrated environment from which all features of the instrument can be accessed. One program is used to adjust the instrument configuration, communicate with the telescope and initiate the data taking process. The program also provides a high level scripting language to allow specific observing scenarios to be predefined and initiated with a simple command (Chapter 7).

A flexible data reduction pipeline was written. The pipeline contains instrument-specific tasks that turn the raw data from CIRPASS into the Euro 3D standard format for data from IFS instruments. The pipeline also contains tasks for further reduction of the data, that are applicable to any data in the Euro 3D format. Extracting the spectra from each fibre in the CIRPASS slit, and reconstructing the image incident upon the IFU, were significant components of the pipeline newly written for CIRPASS. An optimal fibre extraction algorithm was developed, the performance of which was tested on data from the instrument and found to work well. The IFU reconstruction software was successfully coded in a general form that does not contain instrument-specific parameters; the geometry of the IFU to be reconstructed is obtained from the input 3D data. The pipeline also contains components that flat field and wavelength calibrate the data.

The data reduction pipeline was coded in a highly modular fashion. For this reason, the data reduction procedure can be specified before the observation commences and changed afterwards. This enabled a 'quick-look' mode to be implemented for use at the telescope. This minimal pipeline rapidly produces reconstructed IFU images and is used to ensure that the instrument is functioning correctly (Chapter 8).

10.8 Instrument performance

The expected performance of CIRPASS was modelled. The model contains the measured performance of individual components of CIRPASS and includes noise contributions from the thermal background, scattered OH, readnoise of the detector, and the object and sky brightness. The accuracy of the model was determined by observing the Cambridge night sky with CIRPASS attached to a small telescope. Observations of bright objects were used to check the overall functionality of the instrument and its control and data reduction software. A spectrum of Polaris was obtained for the entire J and H bands, which confirmed that the instrument control software and the quick-look data reduction pipeline were working well.

The star HIP 3006 (H$\simeq$6) was observed with CIRPASS for 1 hour from Cambridge,

and is equivalent to observing a H=14 star with an 8 m telescope. The signal-to-noise achieved in these observations was measured and compared with that predicted by the model. The on-sky observations gave a slightly better performance than expected. The limiting magnitudes for CIRPASS, in a 3 hour exposure, resulting in a signal-to-noise of 5 on an 8 m telescope are J=21.3 and H=19.3. The equivalent line fluxes are J=4.4×10^{-18} ergs/s/cm^2 and H=9.0×10^{-18} ergs/s/cm^2. These values are from the model and are, therefore, conservative.

The dominant background contribution in CIRPASS is the thermal background from the instrument. The filters used by CIRPASS are below specification and are the cause of the higher than expected background. A potential improvement of J=0.1 and H=1.2 in limiting magnitudes would be made with filters that perform to specification. If the OH were also masked, in addition to achieving the lower thermal background, CIRPASS's limiting magnitudes would become J=21.7 and H=20.8. A superior quality HAWAII 1K detector was installed immediately prior to CIRPASS being shipped to Gemini South, promising further performance improvements (Chapter 9).

10.9 Conclusions

CIRPASS has been successfully developed and tested. It is a new and unique infrared spectrograph combining OH suppression and integral field spectroscopy. The performance of CIRPASS is competitive and exceeded expectations. Exciting scientific observations should be possible with CIRPASS on an 8 m telescope.

APPENDIX A

ACRONYMS

AAT: Anglo-Australian Telescope
AO: Adaptive Optics
ADC: Analogue to Digital Converter
CCD: Charged Coupled Device
CIRPASS: Cambridge Infra-red PAnoramic Survey Spectrograph
CMOS: Complementary Metal-Oxide Semiconductor
COHSI: Cambridge OH Suppression Instrument
DCS: Double Correlated Sampling
DLAs: Damped Lyman-α Systems
DN: Data Number. The digital output from the detector hardware and software readout system that quantifies the number of photons detected by each pixel.
ESO: European Southern Observatory
FITS: Flexible Image Transport System
FMOS: Fibre Multi Object Spectrograph
FPU: Focal Plane Unit
FRD: Focal Ratio Degradation. A property of optical fibres whereby light emerging from a fibre has a faster focal ratio than that entering it.
FWHM: Full Width Half Maximum
GNIRS: Gemini Near Infrared Spectrograph
GOHSS: Galileo OH Suppression Spectrograph
GUI: Graphical User Interface
HAWAII: HgCdTe Astronomical Wide Area Infrared Imager
HST: Hubble Space Telescope
ICU: Instrument Control Unit
IFS: Integral Field Spectroscopy
IFU: Integral Field Unit
ISAAC: Infrared Spectrograph And Array Camera

ISS: Instrument Support Structure
LINERs: Low Ionisation Nuclear Emission Region Sources
LN_2: Liquid Nitrogen
MEF: Multi Extension Fits (file format)
MOS: Multi-Object Spectroscopy
MPFS: MultiPupil Field Spectrograph
NDR: Non Destructive Read
NIR: Near InfraRed
NIRMOS: Near InfraRed MultiObject Spectrograph
OHS: OH-suppression Spectrograph
PC: Personal Computer
PCB: Printed Circuit Board
PID: Proportional-Integral-Derivative controller. PID controllers are used to eliminate the need for continuous operator attention when maintaining, for example, the temperature of a device using an electrical heater. The controller will maintain a user defined set-point by measuring the response of the system to an external agent and then adjusting the power or time that the external agent is applied.
QE: Quantum Efficiency (Percentage of photons detected compared with photons incident on a detector.)
QSO: Quasi-Stellar Object
ROIC: Read Out Integrated Circuit
RRR: Read Reset Read
SAURON: Spectroscopic Areal Unit for Research on Optical Nebulae
SFR: Star Formation Rate
SHBD: Spectral Hole Burning Device
SMIRFS: Spectroscopic Multiple InfraRed Fibre System
S/N: Signal-to-Noise
SPIRAL: Segmented Pupil/Image Reformatting Array of Lenslets
SRE: Spectral Resolution Element
TCS: Telescope Control Software
TEIFU: Thousand Element Integral Field Unit
TIGER: Traitement Intégral des Galaxies par l'Etude de leurs Raies
UIST: UKIRT Imager SpecTrometer
UKIRT: UK Infra-Red Telescope
ULIRGs: Ultra-Luminous Infrared Galaxies
UV: Ultra Violet

VLT: Very Large Telescope

APPENDIX B

DEFINITIONS

J: 1.15 to 1.35 μm
Short J: 1.15 to 1.25 μm
Long J: 1.25 to 1.35 μm
H: 1.45 to 1.80 μm
Short H: 1.45 to 1.60 μm
Long H: 1.60 to 1.80 μm
K: 2.0 to 2.4 μm

APPENDIX C

SUPPLIER DETAILS

Alusett Limited
Units F & G,
Wykeham Industrial Estate,
Moorside Road,
Winchester,
Hampshire
SO23 7RX
U.K.
Tel: +44 (0) 1962 842424
`http://www.alusett.co.uk/`

Alusett offers a complete, custom design and manufacturing service for all types of enclosure, using a range of aluminium extrusions and patented connectors.

Barber and Clarke Ltd.
65 Oakes Rd,
Bury St. Edmunds,
Suffolk
IP32 6PU
U.K.
Tel: +44 (0) 1284 70 20 50
`http://www.barber-and-clarke.com`

Suppliers of air conditioning and refrigeration solutions.

Barnwell Services Ltd
Reginald Road,
Smethwick,
West Midlands
B67 5AS
U.K.
Tel: +44 (0) 121 429 8011
`http://www.barnwell.co.uk/`

A distributer of fluid sealing products.

Celestron
2835 Columbia Street,
Torrance,
CA 90503
USA
Tel: +1 310 328 9560
`http://www.celestron.com`

Manufacturer of amateur telescopes.

Cortex Controllers Ltd.
50, St Stephen's Place,
Cambridge
CB3 0JE
U.K.
Tel: +44 (0) 1223 368000
`http://www.cortexcontrollers.com/`

Cortex design and manufacture complete solutions for industrial video non-contact measurement and motion control fields.

Eurotherm Limited
Faraday Close,
Durrington,
Worthing,
West Sussex
BN13 3PL
U.K.
Tel: +44 (0) 1903 268500
`http://www.eurotherm.co.uk`

Eurotherm provides process control and automation solutions.

Green Witch Astronomy
Unit 6,
Dry Drayton Industries,
Scotland Rd,
Dry Drayton,
Cambridge,
Cambridgeshire
CB3 8AT
U.K.
Tel: +44 (0) 1954 211288
`www.greenwich-observatory.co.uk`

Supplier of amateur astronomy equipment including telescope, telescope mounts and CCD cameras.

Linos Photonics UK Ltd.
2 Drakes Mews,
Crownhill,
Milton Keynes,
Buckinghamshire
MK8 OER
U.K.
Tel: +44 (0) 19 08 26 25 25
`http://www.linos-photonics.co.uk`

A supplier of optomechanical components.

Optical Surfaces Limited
Godston Road,
Kenly,
Surrey
CR8 5AA
U.K.
Tel: +44 (0) 208 668 6126
`http://www.optisurf.com/`

A U.K. supplier of optical components and instruments including flats, spheres, aspherics, paraboloids, toroids and windows. They specialise in large optics, beam expanders and collimators.

PerkinElmer Life Sciences Ltd
PerkinElmer House,
204 Cambridge Science Park,
Cambridge
CB4 0GZ
U. K.
Tel: +44 (0) 1223 437400
`http://lifesciences.perkinelmer.com/index.asp`

Supplier of the Astrocam 4100 controller for the HAWAII 1K array.

Phytron
1347 Main Street,
Waltham
MA 02451
USA
Tel: +1 781 647 3581
`http://www.phytron.com/`

Phytron are a German company who supply stepping motors, stepping motor controls units, and positioning systems.

Pico Technology Limited
The Mill House,
Cambridge Street,
St Neots,
Cambridgeshire
PE19 1QB
U.K.
Tel: +44 (0) 1480 396 395
`http://www.picotech.com/`

A supplier of PC based oscilloscopes, data loggers and data logging software (Picolog).

Polymicro Technologies, LLC
18019 N. 25th Ave.
Phoenix,
Arizona 85023-1200
USA
Tel: +1 602 375 4100
`http://www.polymicro.com/`

Polymicro Technologies, LLC is a manufacturer and developer of micro-tubing, optical fibres, and related products for niche applications throughout the world.

Rockwell Scientific
1049 Camino Dos Rios,
Thousand Oaks,
CA 91360
USA
Tel: +1 805 373 4545
`http://www.rockwellscientific.com/`

The manufacturer of the HAWAII 1K and HAWAII 2K infrared focal plane array detectors.

Schott Glas
Business Segment Optics for Devices,
Hattenbergstr. 10,
55122 Mainz,
Germany
Tel: +49 (0) 6131/66-28 31
`http://www.schott.com`

A supplier of optical glasses.

Starlight Xpress Ltd.
The Office,
Foxley Green farm,
Ascot Road,
Holyport,
Berkshire
SL6 3LA
U.K.
Tel: +44 (0) 1628 777126
`http://www.starlight-xpress.co.uk/`

Supplier of astronomical and industrial CCD cameras.

Stebon Ltd
Unit 2c,
Chase Park Industrial Estate,
Ring Road,
Burntwood,
Staffordshire
WS7 8JQ
U.K.
Tel: +44 (0) 1543 677211
`http://www.stebon.co.uk/`

Manufacturers of Hybrid Stepper and Brushless DC servo motors.

THERMO RGL
Richardson Grating Laboratory,
705 St. Paul Street,
Rochester,
NY 14605
USA
Tel: +1 585 262 1331
`http://www.gratinglab.com/`

THERMO RGL design and manufacture diffraction gratings for telecommunications, photolithography, spectroscopy and astronomy.

BIBLIOGRAPHY

Allan A., Allington-Smith J., Turner J., Johnson R., Miller B., & Valdes F. G. 2001. *IFU Data Products and Reduction Software*, in ASP Conf. Ser. 238: Astronomical Data Analysis Software and Systems X, Vol. 10, 459+

Allington-Smith J. & Content R. 1998. *Sampling and Background Subtraction in Fiber-Lenslet Integral Field Spectrographs*, PASP, 110, 1216

Bacon R., Adam G., Baranne A., Courtes G., Dubet D., Dubois J. P., Emsellem E., Ferruit P., Georgelin Y., Monnet G., Pecontal E., Rousset A., & Say F. 1995. *3D spectrography at high spatial resolution. I. Concept and realization of the integral field spectrograph TIGER.*, A&AS, 113, 347+

Bacon R., Copin Y., Monnet G., Miller B. W., Allington-Smith J. R., Bureau M., Marcella Carollo C., Davies R. L., Emsellem E., Kuntschner H., Peletier R. F., Verolme E. K., & Tim de Zeeuw P. 2001. *The SAURON project - I. The panoramic integral-field spectrograph*, MNRAS, 326, 23

Becker T., Roth M. M., & Schmoll J. 2000. *3-D Spectroscopy with Fibers: Extraction Methods and their Limitations (Poster)*, in ASP Conf. Ser. 195: Imaging the Universe in Three Dimensions, 544+

Beckett M. G. 1995. *High Resolution Infrared Imaging*, PhD thesis, Institute of Astronomy

Bell E. F. & Kennicutt R. C. 2001. *A Comparison of Ultraviolet Imaging Telescope Far-Ultraviolet and Hα Star Formation Rates*, ApJ, 548, 681

Boehm P. 2001, World Wide Web, `http://www.aip.de./Euro3D/`

Bunker A. J., Warren S. J., Clements D. L., Williger G. M., & Hewett P. C. 1999. *Limits on the star formation rates of z>2 damped Lyα systems from Hα spectroscopy*, MNRAS, 309, 875

Bushouse, H. *et al.* . 1996, World Wide Web, `http://iraf.noao.edu/iraf/web/ADASS/adass_proc/adass_95/bushouseh/bushouseh.html`

Bushouse H., Skinner C., MacKenty J., Axon D., & Stobie E. 1998. *The STScI NICMOS Calibration Pipeline*, in NICMOS and the VLT: A New Era of High Resolution Near Infrared Imaging and Spectroscopy, Pula, Sardinia, Italy, June 26-27th 1998 ESO Conference and Workshop Proceedings 55, 1998, Wolfram Freudling and Richard Hook eds.,p. 18, 18+

Cheung C. Y. 2001, World Wide Web, `http://fits.gsfc.nasa.gov/`, email-fits@fits.gsfc.nasa.gov

Connolly A. J., Szalay A. S., Dickinson M., Subbarao M. U., & Brunner R. J. 1997. *The Evolution of the Global Star Formation History as Measured from the Hubble Deep Field*, ApJ, 486, L11

Content R. 1996. *Deep-Sky Infrared Imaging by Reduction of the Background Light. I. Sources of the Background and Potential Suppression of the OH Emission*, ApJ, 464, 412+

Cowie L. L., Songaila A., Hu E. M., & Cohen J. G. 1996. *New Insight on Galaxy Formation and Evolution From Keck Spectroscopy of the Hawaii Deep Fields*, AJ, 112, 839+

Cuby J. G., Lidman C., Moutou C., & Petr M. 2000. *ISAAC at the VLT: one year later*, in Proc. SPIE Vol. 4008, p. 1036-1047, Optical and IR Telescope Instrumentation and Detectors, Masanori Iye; Alan F. Moorwood; Eds., Vol. 4008, 1036–1047

Dubbeldam M., Content R., Allington-Smith J. R., Pokrovski S., & Robertson D. J. 2000. *An Integral field unit for the Gemini near-infrared spectrograph*, in Proc. SPIE Vol. 4008, p. 1181-1192, Optical and IR Telescope Instrumentation and Detectors, Masanori Iye; Alan F. Moorwood; Eds., Vol. 4008, 1181–1192

Eisenhauer F., Tecza M., Mengel S., Thatte N. A., Roehrle C., Bickert K., & Schreiber J. 2000. *Imaging the universe in 3D with the VLT: the next-generation field spectrometer SPIFFI*, in Proc. SPIE Vol. 4008, p. 289-297, Optical and IR Telescope Instrumentation and Detectors, Masanori Iye; Alan F. Moorwood; Eds., Vol. 4008, 289–297

Ellis R. S., Colless M., Broadhurst T., Heyl J., & Glazebrook K. 1996. *Autofib Redshift Survey - I. Evolution of the galaxy luminosity function*, MNRAS, 280, 235

Ennico K. A. 1998. *Near Infrared Faint Object Spectroscopy*, PhD thesis, Institute of Astronomy

Ennico K. A., Parry I. R., Kenworthy M. A., Ellis R. S., Mackay C. D., Beckett M. G., Aragon-Salamanca A., Glazebrook K., Brinchmann J., Pritchard J. M., Medlen S. R.,

Piche F., McMahon R. G., & Cortecchia F. 1998. *Cambridge OH suppression instrument (COHSI): status after first commissioning run*, in Proc. SPIE Vol. 3354, p. 668-674, Infrared Astronomical Instrumentation, Albert M. Fowler; Ed., Vol. 3354, 668–674

ESO/DMD User Support Group. 2001, World Wide Web, `http://www.eso.org/observing/etc/bin/gen/form?INS.MODE=swspectr+INS.NAM%E=isaac`

Finger G., Mehrgan H., Meyer M., Moorwood A. F., Nicolini G., & Stegmeier J. 2000. *Performance of large-format HgCdTe and InSb arrays for low-background applications*, in Proc. SPIE Vol. 4008, p. 1280-1297, Optical and IR Telescope Instrumentation and Detectors, Masanori Iye; Alan F. Moorwood; Eds., Vol. 4008, 1280–1297

Fowler A. M. & Gatley I. 1990. *Demonstration of an algorithm for read-noise reduction in infrared arrays*, ApJ, 353, L33

Gallego J., Zamorano J., Aragon-Salamanca A., & Rego M. 1995. *The Current Star Formation Rate of the Local Universe*, ApJ, 455, L1

García-Lorenzo B., Arribas S., & Mediavilla E. 2000. *INTEGRAL: A Simple and Friendly Integral Field Unit Available at the WHT*, The Newsletter of the Isaac Newton Group of Telescopes (ING Newsl.), issue no. 3, p. 25-28, 3, 25

Garnett J. D. & Forrest W. J. 1993. *Multiply sampled read-limited and background-limited noise performance*, in Proc. SPIE Vol. 1946, p. 395-404, Infrared Detectors and Instrumentation, Albert M. Fowler; Ed., Vol. 1946, 395–404

Geballe T. 2001, World Wide Web, `http://www.gemini.edu/sciops/instruments/nirspec/nirspecIndex.html`

Glazebrook K., Blake C., Economou F., Lilly S., & Colless M. 1999. *Measurement of the star formation rate from Hα in field galaxies at z=1*, MNRAS, 306, 843

Glazebrook K., Ellis R., Colless M., Broadhurst T., Allington-Smith J., & Tanvir N. 1995. *A faint galaxy redshift survey to B=24*, MNRAS, 273, 157

Haynes R., Content R., Turner J., Allington-Smith J. R., & Lee D. 1998. *SMIRFS-II: multiobject and integral-field near-IR spectroscopy at UKIRT*, in Proc. SPIE Vol. 3354, p. 419-430, Infrared Astronomical Instrumentation, Albert M. Fowler; Ed., Vol. 3354, 419–430

Hecht J. H., Ramsay Howat S. K., Walterscheid R. L., & Isler J. R. 1995. *Observations of variations in airglow emissions during ALOHA-93*, Geophys. Res. Lett., 22, 2817

Herbst T. M. 1994. *Numerial evaluation of OH-suppression instruments*, PASP, 106, 1298

Hines C. 1960. *Internal atmospheric gravity waves*, Can. J. Phys., 38, 1441

Hodapp K. 2000. *Near-infrared detector arrays: current state of the art*, in Proc. SPIE Vol. 4008, p. 1228-1239, Optical and IR Telescope Instrumentation and Detectors, Masanori Iye; Alan F. Moorwood; Eds., Vol. 4008, 1228–1239

Hofmann R., Thatte N. A., Tecza M., Eisenhauer F., & Lehnert M. 2000. *LUCIFER-MOS: a cryogenic multi-object infrared spectrograph for the LBT*, in Proc. SPIE Vol. 4008, p. 1094-1102, Optical and IR Telescope Instrumentation and Detectors, Masanori Iye; Alan F. Moorwood; Eds., Vol. 4008, 1094–1102

Hora J. 1997, World Wide Web, `http://www.ifa.hawaii.edu/instrumentation/quirc/quirc.html`

Iwamuro F., Motohara K., Maihara T., Hata R., & Harashima T. 2001. *OHS: OH-Airglow Suppressor for the Subaru Telescope*, PASJ, 53, 355

Johnson R. A., Irwin M., Dean A. J., & Parry I. R. 2002. *Extracting closley packed spectra*, in prep., to be published in PASP

Jorden P. R., Deltorn J.-M., & Oates A. P. 1994. *Nonuniformity of CCDs and the effects of spatial undersampling*, in Proc. SPIE Vol. 2198, p. 836-850, Instrumentation in Astronomy VIII, David L. Crawford; Eric R. Craine; Eds., Vol. 2198, 836–850

Keller C. U. 2000. *5,000 by 5,000 Spatial by 15,000 Spectral Resolution Elements: First Astronomical Observations with a Novel 3-D Detector*, in ASP Conf. Ser. 195: Imaging the Universe in Three Dimensions, 495+

Kennicutt R. C. 1983. *The rate of star formation in normal disk galaxies*, ApJ, 272, 54

Kenworthy M. 1998. *The Development of New Techniques for Integral Field Spectroscopy in Astronomy*, PhD thesis, Institute of Astronomy

Kenworthy M. A., Parry I. R., & Taylor K. 1998. *Integral field units for SPIRAL and COHSI*, in Proc. SPIE Vol. 3355, p. 926-931, Optical Astronomical Instrumentation, Sandro D'Odorico; Ed., Vol. 3355, 926–931

Kozlowski L. J., Montroy J. T., Cabelli C. A., Cooper D. E., Chen A. C., Bostrup G. L., Bai Y., Vural K., Hodapp K., & Hall D. N. 2000. *Visible and infrared detectors at Rockwell Science Center*, in Proc. SPIE Vol. 4008, p. 1240-1253, Optical and IR Telescope

Instrumentation and Detectors, Masanori Iye; Alan F. Moorwood; Eds., Vol. 4008, 1240–1253

Krabbe A., Weitzel L., Kroker H., Tacconi-Garman L. E., Cameron M., Thatte N. A., Samann G., Boeker T., Genzel R., & Drapatz S. 1995. *3D: a new generation imaging spectrometer*, in Proc. SPIE Vol. 2475, p. 172-183, Infrared Detectors and Instrumentation for Astronomy, Albert M. Fowler; Ed., Vol. 2475, 172–183

Le Fevre O., Saisse M., Mancini D., Vettolani G. P., Maccagni D., Picat J. P., Mellier Y., Mazure A., Cuby J. G., Delabre B., Garilli B., Hill L., Prieto E., Voet C., Arnold L., Brau-Nogue S., Cascone E., Conconi P., Finger G., Huster G., Laloge A., Lucuix C., Mattaini E., Schipani P., Waultier G., Zerbi F. M., Avila G., Beletic J. W., D'Odorico S., Moorwood A. F., Monnet G. J., & Reyes Moreno J. 2000. *VIMOS and NIRMOS multi-object spectrographs for the ESO VLT*, in Proc. SPIE Vol. 4008, p. 546-557, Optical and IR Telescope Instrumentation and Detectors, Masanori Iye; Alan F. Moorwood; Eds., Vol. 4008, 546–557

Lee D. 1998. *New Techinques in Astronomical Spectroscopy for 8 metre Telescopes*, PhD thesis, Durham University

Lee D., Haynes R., & Skeen D. J. 2001. *Properties of optical fibres at cryogenic temperatures*, MNRAS, 326, 774

Lilly S. J., Le Fevre O., Hammer F., & Crampton D. 1996. *The Canada-France Redshift Survey: The Luminosity Density and Star Formation History of the Universe to z∼1*, ApJ, 460, L1

Lilly S. J., Tresse L., Hammer F., Crampton D., & Le Fevre O. 1995. *The Canada-France Redshift Survey. VI. Evolution of the Galaxy Luminosity Function to z∼1*, ApJ, 455, 108+

Lorenzetti D., Cortecchia F., Vitali F., Cascone E., D'Alessio F., Ellis R. S., Fiorani A., Mancini D., Parry I. R., Pedichini F., Scaramella R., & Speziali R. 2000. *GOHSS (Galileo OH subtracted spectrograph): a progress report*, in Proc. SPIE Vol. 4008, p. 703-713, Optical and IR Telescope Instrumentation and Detectors, Masanori Iye; Alan F. Moorwood; Eds., Vol. 4008, 703–713

MacKenty J. W. *et al.*. 1997. *NICMOS Instrument Handbook Version 2.0*, World Wide Web, `http://www.stsci.edu/instrument-news/handbooks/nicmos/NIH.html`, (Baltimore: STScI)

Maihara T., Iwamuro F., Yamashita T., Hall D. N. B., Cowie L. L., Tokunaga A. T., & Pickles A. 1993. *Observations of the OH airglow emission*, PASP, 105, 940

Maihara T., Ohta K., Tamura N., Ohtani H., Akiyama M., Noumaru J., Kaifu N., Karoji H., Iye M., Dalton G. B., Parry I. R., Robertson D. J., Sharples R. M., Ren D., Allington-Smith J. R., Taylor K., & Gillingham P. R. 2000. *Fiber multi-object spectrograph (FMOS) for the Subaru Telescope*, in Proc. SPIE Vol. 4008, p. 1111-1118, Optical and IR Telescope Instrumentation and Detectors, Masanori Iye; Alan F. Moorwood; Eds., Vol. 4008, 1111–1118

Maillard J. P. 1995. *3D-Spectroscopy with a Fourier Transform Spectrometer*, in ASP Conf. Ser. 71: IAU Colloq. 149: Tridimensional Optical Spectroscopic Methods in Astrophysics, 316+

Martini P. & DePoy D. L. 2000. *Optimal resolutions for IR spectroscopy through the OH airglow*, in Proc. SPIE Vol. 4008, p. 695-702, Optical and IR Telescope Instrumentation and Detectors, Masanori Iye; Alan F. Moorwood; Eds., Vol. 4008, 695–702

McLean I. S. 1997. *Electronic Imaging in Astronomy: Detectors and Instrumentation* (John Wiley & Sons)

McLean I. S. & Chaffee F. H. 2000. *Instrumentation for the Keck Observatory*, in Proc. SPIE Vol. 4008, p. 2-7, Optical and IR Telescope Instrumentation and Detectors, Masanori Iye; Alan F. Moorwood; Eds., Vol. 4008, 2–7

McLean I. S., Graham J. R., Becklin E. E., Figer D. F., Larkin J. E., Levenson N. A., & Teplitz H. I. 2000. *Performance and results with the NIRSPEC echelle spectrograph on the Keck II telescope*, in Proc. SPIE Vol. 4008, p. 1048-1055, Optical and IR Telescope Instrumentation and Detectors, Masanori Iye; Alan F. Moorwood; Eds., Vol. 4008, 1048–1055

Moller P. & Warren S. J. 1998. *HST images of a galaxy group at z=2.81, and the sizes of damped Lyα galaxies*, MNRAS, 299, 661

Murray G. J., Allington-Smith J. R., Content R., Dodsworth G. N., Dunlop C. N., Haynes R., Sharples R. M., & Webster J. 2000. *TEIFU: a high-resolution integral field unit for the William Herschel Telescope*, in Proc. SPIE Vol. 4008, p. 611-622, Optical and IR Telescope Instrumentation and Detectors, Masanori Iye; Alan F. Moorwood; Eds., Vol. 4008, 611–622

Offer A. R. & Bland-Hawthorn J. 1998. *Rugate filters for OH-suppressed imaging at near-infrared wavelengths*, MNRAS, 299, 176

Oliva E. & Origlia L. 1992. *The OH Airglow Spectrum - a Calibration Source for Infrared Spectrometers*, A&A, 254, 466+

Osterbrock D. E., Fulbright J. P., & Bida T. A. 1997. *Night-Sky High-Resolution Spectral Atlas of OH Emission Lines for Echelle Spectrograph Wavelength Calibration. II.*, PASP, 109, 614

Osterbrock D. E., Fulbright J. P., Martel A. R., Keane M. J., Trager S. C., & Basri G. 1996. *Night-Sky High-Resolution Spectral Atlas of OH and O_2 Emission Lines for Echelle Spectrograph Wavelength Calibration*, PASP, 108, 277+

Parry I. R., McMahon R. G., King D., & Horton A. 2002, World Wide Web, `http://www.ast.cam.ac.uk/~optics/dazle/`

Perryman M. A. C. & Peacock A. 2000. *The Astronomical Potential of Optical STJs*, in ASP Conf. Ser. 195: Imaging the Universe in Three Dimensions, 487+

Pettini M., Boksenberg A., & Hunstead R. W. 1990. *Metal enrichment, dust, and star formation in galaxies at high redshifts. I - The z = 2.3091 absorber toward PHL 957*, ApJ, 348, 48

Pettini M., Shapley A. E., Steidel C. C., Cuby J., Dickinson M., Moorwood A. F. M., Adelberger K. L., & Giavalisco M. 2001. *The Rest-Frame Optical Spectra of Lyman Break Galaxies: Star Formation, Extinction, Abundances, and Kinematics*, ApJ, 554, 981

Ramsay S. K., Mountain C. M., & Geballe T. R. 1992. *Non-thermal emission in the atmosphere above Mauna Kea*, MNRAS, 259, 751

Ramsay Howat S. K., Ettedgui-Atad E., Bennett R. J., Bridger A., Content R., Ellis M. A., Hastings P. R., Strachan M., Wall R., & Wells M. 1998. *UIST: an imaging spectrometer for the UK Infrared Telescope*, in Proc. SPIE Vol. 3354, p. 456-467, Infrared Astronomical Instrumentation, Albert M. Fowler; Ed., Vol. 3354, 456–467

Roche N., Ratnatunga K., Griffiths R. E., Im M., & Neuschaefer L. 1996. *Angular sizes and luminosity evolution of faint galaxies*, MNRAS, 282, 1247

Rosa-González D., Terlevich E., & Terlevich R. 2002. *An empirical calibration of star formation rate estimators*, MNRAS, 332, 283

Roth K. C., Guyon O., Chun M., Jensen J. B., Jorgensen I., Rigaut F., & Walther D. M. 2001. *Hokupa'a Performance and Point Spread Function Characterization*, American Astronomical Society Meeting

Rousselot P., Lidman C., Cuby J.-G., Moreels G., & Monnet G. 2000. *Night-sky spectral atlas of OH emission lines in the near-infrared*, A&A, 354, 1134

Singh B. & Thomas III J. H. 1998. *Handbook of Vacuum Science and Technology* (Academic Press), p470

Smail I., Ellis R. S., Fitchett M. J., & Edge A. C. 1995. *Gravitational lensing of distant field galaxies by rich clusters - II. Cluster mass distributions*, MNRAS, 273, 277

Steidel C. C., Adelberger K. L., Giavalisco M., Dickinson M., & Pettini M. 1999. *Lyman-Break Galaxies at $z \gtrsim 4$ and the Evolution of the Ultraviolet Luminosity Density at High Redshift*, ApJ, 519, 1

Storrie-Lombardi L. J., McMahon R. G., & Irwin M. J. 1996. *Evolution of neutral gas at high redshift: implications for the epoch of galaxy formation*, MNRAS, 283, L79

Taylor K. & Atherton P. D. 1980. *Seeing-limited radial velocity field mapping of extended emission line sources using a new imaging Fabry-Perot system*, MNRAS, 191, 675

Tody D. 1993. *IRAF in the Nineties*, in ASP Conf. Ser. 52: Astronomical Data Analysis Software and Systems II, Vol. 2, 173+

Wilkinson A., Sharples R. M., Fosbury R. A. E., & Wallace P. T. 1986. *Stellar dynamics of CEN A*, MNRAS, 218, 297

Wolfe A. M., Turnshek D. A., Smith H. E., & Cohen R. D. 1986. *Damped Lyman-alpha absorption by disk galaxies with large redshifts. I - The Lick survey*, ApJS, 61, 249